Electron tomography and microscopy on semiconductor heterostructures

D i s s e r t a t i o n

zur Erlangung des akademischen Grades

d o c t o r r e r u m n a t u r a l i u m

(Dr. rer. nat.)

im Fach: Physik

eingereicht an der

Mathematisch-Naturwissenschaftlichen Fakultät

der Humboldt-Universität zu Berlin

von

M.Sc. Michael Niehle

Präsident der Humboldt-Universität zu Berlin

Prof. Dr. Jan-Hendrik Olbertz

Dekan der Mathematisch-Naturwissenschaftlichen Fakultät

Prof. Dr. Elmar Kulke

Gutachter/innen:
1. Prof. Dr. Henning Riechert
2. Prof. Eric Tournié
3. Prof. Dr. Günter Möbus

Tag der mündlichen Prüfung: 19.09.2016

Zusammenfassung

Elektronentomographie weist eine geringe Verbreitung in der Forschung an epitaktischen Halbleiterheterostrukturen auf, obwohl die Nanotechnologie zusehens kleinere und zunehmend dreidimensional (3D) strukturierte Baugruppen anstrebt. Der letzte Aspekt erfordert den Einsatz von Tomographie mit einer Ortsauflösung von wenigen Nanometern, um den Zusammenhang von Realstrukur und Bauteileigenschaften in relevanten Materialsystemen zu verstehen. In der vorliegenden Arbeit wird die Elektronentomographie konsequent auf ein epitaktisches III-Sb Schichtsystem, das auf Si aufgewachsen worden ist, und auf eine 3D (In,Ga)N/GaN-Heterostruktur angewendet. Das Hauptaugenmerk liegt auf der Analyse der räumlichen Anordnung und Struktur ausgedehnter Kristalldefekte und ihrer Wechselwirkung. Die 3D Rekonstruktion offenbart Details, die ausschließlich der Elektronentomographie zugänglich sind.

Eine grundlegende Voraussetzung für die erfolgreichen Tomographieuntersuchungen ist die Probenherstellung mittels fokussiertem Ionenstrahl, was als unerlässliches Werkzeug herausgestellt wird. Eine gezielte Objektauswahl und -orientierung erfolgt unter Verwendung eines vielseitigen Zweistrahlmikroskops, das ein Rasterelektronen- und ein Rasterionenmikroskop in einem Gerät vereint. Des Weiteren ermöglicht dieses Gerät die Herstellung geeigneter Probenformen und -abmessungen, die durch die Komplexität der Mikrostruktur gefordert werden. Rastertransmissionselektronenmikroskopie wird zur Aufnahme tomographischer Daten eingesetzt. Das große Sichtfeld stellt sich als Vorteil heraus.

Der Schwerpunkt der Arbeit liegt auf einer umfassenden Mikrostrukutrcharakterisierung der antimonidbasierten Heterostruktur. Nanoporen, ein Beispiel für 3D Defekte, werden identifiziert, welche in diesen mit Molekularstrahlepitaxie hergestellten Proben unerwartet sind. Die Elektronentomographie erlaubt es, die räumliche Anordnung und die Abmaße der Pore sowie deren facettierte Form detailliert zu bestimmen. Die Grenzfläche zwischen Substrat und Schicht stellt ein Beispiel für einen 2D Defekt dar. Die Abscheidung von AlSb geht dem Lagenwachstum des stark gitterfehlgepassten GaSb auf Si voraus, was zu eingebetteten AlSb Inseln an der III-Sb/Si Grenzfläche führt. Die Morphologie und die Positionen der Inseln werden mit Elektronentomographie bestimmt. Darüber hinaus entsteht ein Netzwerk von Fehlpassungsversetzungen an der Grenzfläche zwischen Inseln und Substrat. Ergänzende Untersuchungen an der Tomographieprobe mittels (Raster-) Transmissionselektronenmikroskopie ermöglichen es, den Zusammenhang zwischen Inseln und dem Auftreten von Liniendefekten, die das Schichtsystem durchlaufen (Durchstoßversetzungen), bzw. Unreglemäßigkeiten in den Fehlpassungsversetzungsnetzwerken herauszustellen. Als Voraussetzung für die Entstehung von Durchstoßversetzungen werden 60°-Versetzungen an der Grenzfläche betrachtet, die vor dem Zusammenwachsen der Inseln eingebaut werden. Die bloße Verbindung der Fehlpassungsversetzungsnetzwerke während des Zusammenwachsens kann die Beobachtungen von Ort und Anzahl der Durchstoßversetzungen nicht erklären. Abschließend wird die räumliche Anordnung der eindimensionalen (1D) Liniendefekte durch den gesamten Schichtstapel mittels Tomographie herausgestellt. Die Wechselwirkung mit Antiphasengrenzen wird unterstrichen. Ungewöhnliche Verläufe von Liniendefekten werden anhand des Tomogramms erklärt. Dazu zählt das Auftreten von Dislokationen auf {110} Gitterebenen, von Liniensegmenten parallel zur Grenzfläche und von solchen, die sich scheinbar entlang der Wachstumsrichtung vor und zurück bewegen. Die 3D Darstellung erlaubt die eindeutige Beobachtung von Wechselwirkungsorten. Eine Verwechslung mit Versetzungen, die sich nur zufällig entlang der Beobachtungsrichtung überschneiden, wird vermieden.

Der Einschluss von (In,Ga)N in GaN basierten Nanosäulen wird mit Elektronentomographie detailliert charakterisiert. Das Tomogramm zeigt, dass (In,Ga)N-Lagen unterschiedlicher Dicke und unterschiedlichen Indiumgehalts auf verschiedenen Facetten der 3D Struktur eingebaut werden. Diese Information lässt sich ausschließlich mit der Elektronentomographie gewinnen, weil die Geometrie der schräg wachsenden Säulen eine besondere Herausforderung darstellt.

Zusammenfassend demonstriert die vorliegende Arbeit die Analyse von ausgedehnten Kristalldefekten aller Dimensionalitäten in komplexen Heterostrukturen mittels Elektronentomographie und -mikroskopie. So werden eindeutige Einblicke in die Entstehung von Defekten während des Kristallwachstums und in Wechselwirkungsmechanismen von Defekten ermöglicht. Über die bloße 3D Darstellung von Defekten hinaus erlaubt die Elektronentomographie mikrostrukturelle Objekte zu erklären und zu verstehen – insbesondere in Verbindung mit komplementären Untersuchungen an ein und derselben Probenstelle.

Abstract

Electron tomography exhibits a very poor spread in the research field of epitaxial semiconductor heterostructures in spite of the ongoing miniaturization and increasing three-dimensional (3D) character of nanostructured devices. The latter aspects necessitate a tomographic approach at the nanometre scale in order to understand the relation between the structure and the properties of respective material systems. In the presented thesis, electron tomography is rigorously applied to a laser based on an epitaxial stack of III-Sb layers on Si and to an (In,Ga)N/GaN nanocolumn heterostructure. The main goal is the analysis of the spatial arrangement of extended defects and their interaction. The 3D reconstructions reveal details that are uniquely accessed by electron tomography.

A fundamental prerequisite for the successful tomography investigations is the focused ion beam based specimen preparation which is emphasized as indispensable tool. A specific target selection and orientation succeeds by the application of a versatile dual-beam microscope including a scanning electron microscope and a focused ion beam. Moreover, the fabrication of an adequate specimen shape and size is feasible which satisfies the requirements imposed by the complexity of the microstructure. Scanning transmission electron microscopy is selected for the tomographic data acquisition. The provided wide field of view is a great advantage.

The focus lies on a comprehensive microstructure characterization of the antimonide based heterostructure. A type of 3D defects, namely nanopores, is revealed which is unexpected for the growth by molecular beam epitaxy. Electron tomography provides a detailed insight into its spatial position and dimension as well as its faceted morphology. The interface between the substrate and the layer is principally a planar (2D) defect. The initial deposition of AlSb precedes the layer-by-layer growth of highly lattice mismatched GaSb on Si resulting in buried, nanometre sized AlSb islands at the interface. Their morphology and location is determined by the tomographic investigation. Furthermore, a misfit dislocation network is formed at the interface between each island and the substrate. The correlation of islands to the origin of threading dislocations and to failures in the misfit dislocation network succeeds by applying complementary (scanning) transmission electron microscopy investigations of the same sample volume. The presence of 60° dislocations at the interface before island coalescence appears to be required for the formation of threading dislocations. The mere match of misfit dislocation networks during coalescence does not account for the number and distribution of observed line defects. Finally, the 3D arrangement of threading dislocations penetrating through the complete layer stack, i.e. line defects (1D), is reconstructed from the tomographic data. The interaction with anti-phase boundaries is highlighted. Peculiar dislocation line directions are unravelled by electron tomography, that is, the origin of lines on {110} lattice planes, of line segments parallel to the heterostructure interface and of such appearing to move back and forth with regard to the growth direction is explained. The 3D representation enables the unambiguous observation of reaction nodes. The confusion due to dislocations that coincidentally overlap in projections along a single viewing direction, is avoided.

The detection of (In,Ga)N insertions on GaN nanocolumns is carried out by electron tomography. A facet dependent (In,Ga)N layer thickness and a variable amount of incorporated indium are deduced from the tomogram. The inclined growth of nanocolumns toward the surface normal imposes geometric constraints which designates electron tomography as unique choice to access this information.

In conclusion, electron tomography and microscopy are shown to reveal extended defects of all dimensionalities in complex heterostructures and thus provide unambiguous insights into the defect formation during growth and into defect interaction mechanisms. Exceeding the mere 3D presentation of defects, electron tomography is used to explain and understand microstructural features, especially in conjunction with complementary observations of one and the same specimen site.

Table of Contents

List of Figures

Abbreviations

2D	two-dimensional
3D	three-dimensional
ADF	annular dark-field
AFM	atomic force microscopy
APB	anti-phase boundary
APD	anti-phase domain
ART	algebraic reconstruction technique
BSE	back-scattering electron
BF	bright-field
CBED	convergent beam electron diffraction
CSL	coincidence site lattice
DF	dark-field
fcc	face centred cubic
FIB	focused ion beam
HAADF	high-angle annular dark-field
HOLZ	higher order Laue zone
LED	light emitting diode
MBE	molecular beam epitaxy
MFD	misfit dislocation
QWs	quantum wells
SAD	selected area diffraction
SAG	selected area growth
SE	secondary electron
SEM	scanning electron microscopy
SF	stacking fault
SIRT	simultaneous iterative reconstruction technique
STEM	scanning transmission electron microscope
TD	threading dislocation
TDS	thermal diffuse scattering
TEM	transmission electron microscope
WBDF	weak-beam dark-field
WBP	weighted back-projection

1. Introduction

The realization of tomography in a transmission electron microscope (TEM) has initially been established in biology [1, 2]. Since, the method is simply addressed as electron tomography. Biological samples attenuate the intensity of the incident electron beam exponentially. The intensity distribution in an image reflects variations in the transmitted sample thickness and mass density. Therefore, the resulting image information presents a mass-thickness contrast [3]. This contrast mechanism is used in x-ray based clinical diagnostics, too, especially in computed tomography. The general public is nowadays familiar with this tomography application which dates back to the 1970s [4]. Electron tomography opens the access to a length scale of several nanometres while x-ray tomography covers the dimension of tens to hundreds of micrometres [5].

The development of electron tomography for materials science has started not until the beginning of the present millennium. Koster *et al.* [6] published the first result showing silver particles in a zeolite support. In general, there are two challenges which have to be faced in materials science. Firstly, the predominant work with crystalline materials gives rise to diffraction contrast. This contrast mechanisms violates prerequisites for the tomographic reconstruction of three-dimensional (3D) objects from two-dimensional (2D) projections. Secondly, the treatment of compact materials that contain atoms with high atomic numbers Z, imposes a limit to the maximal specimen thickness in contrast to the carbon ($Z = 6$) dominated biological research objects. The application of high-angle annular dark-field (HAADF) scanning transmission electron microscopy (STEM) and energy-filtered transmission electron microscopy (EFTEM) have tackled these challenges [7]. Rare examples for the choice of the energy dispersive x-ray (EDX) signal in STEM point to a further route to realize electron tomography in materials science [8–10]. Reviews on electron tomography in materials science have followed fast after first achievements [5, 11–15].

Today, chemists and materials scientists routinely apply electron tomography to examine the distribution of particles in porous supports. The latter consist of materials with small atomic number. The former are often considered for the use as catalysts and they exhibit a rather high atomic number. A dedicated review on this application of electron tomography is published, for instance, by Friedrich *et al.* [13]. The respective samples present an ideal object for HAADF imaging based electron tomography. The particles provide a good contrast and they inherently serve as markers for the crucial alignment of images in a tilt series. The investigation of small three-dimensional objects that are easily dispersed on a carbon support, present a similar situation. Nanowires belong to these objects. The disclosure of the outer morphology of nanowires [16–18] and the determination of axial or radial chemical structures within nanowires [19–21] has been demonstrated. Beside the mere distribution of nanoparticles, structural features of these objects have also been revealed by electron tomography like voids [22] or tetrapod shapes [23]. Most complex morphologies are accessed in the case of dendritic structures [24]. Eventually, atomic resolution in electron tomography is

achieved at dispersed nanoparticles and -rods [25–28]. On the other hand, the morphology of porous materials like catalyst supports themselves has been under investigation [29–32]. The rather large specimen thickness does not impose a limitation in this case.

In contrast to the previous examples, there is only a small number of electron tomography investigations applied to compact, crystalline materials. These comprise the analysis of embedded quantum dots (QDs) and precipitates as well as buried interfaces. The faceting of Si/Ge QDs in Si and InAs QDs in GaAs has been retrieved by Yates *et al.* [33] and Inoue *et al.* [34], respectively. An example for the arrangement of InAs QDs in GaAs has been published by Hernández-Saz *et al.* [35]. The 3D arrangement of particles or precipitates in polycrystalline intermetallic alloys has been subject of electron tomography analyses [11, 36]. Buried interfaces have been regarded with respect to their roughness in 2D grown ZrO_2/In_2O_3 stacks [37] and in electronic devices [38]. Furthermore, the evaluation of thin buried layers in electronic devices has been demonstrated by electron tomography [8, 39–41]. The so far listed tomography results in materials science are mostly based on information acquired by HAADF STEM or by energy filtered transmission electron microscopy (EFTEM) as presented in the review article of Midgley and Weyland [7]. In any case, experiments aim at the acquisition of chemical information.

One strength of transmission electron microscopy is the revelation of microstructural defects like dislocations. In the previous examples, information on dislocations are suppressed due to the avoidance of diffraction contrast. Indeed, the required imaging modes violate a prerequisite for 3D tomographic reconstructions. The intensity does not vary monotonically with thickness. Moreover, the contrast depends on the orientation of the crystalline specimen. Nevertheless, there are four examples revealing the arrangement of line defects. The first work by Barnard *et al.* [42] discovers two dislocation types and their course in a GaN sample. Tanaka *et al.* [43, 44] have investigated the mechanical response of silicon after indenting and after bending a sample by electron tomography. They have allocated the glide systems to the revealed dislocations. A more recent contribution of Mussi *et al.* [45] dwells on the investigation of screw dislocations in olivine. Eventually, the outlined scarcity of examples suggests that electron tomography on compact, crystalline materials has not become a routine characterization tool.

On the other hand, the fabrication of ever smaller semiconductor heterostructures for electronic devices demands the control over the microstructure on a nanometre scale. Beside the device miniaturization, trends of 3D device designs gain importance. The unambiguous characterization and the understanding of the microstructure requires more and more 3D analyses as the projections in microscopy disguise structural properties or are even misleading. The goal of this thesis is formulated against the background of the spread of *electron tomography in materials science* – especially with regard to *compact semiconductors* – and the significance of a *3D understanding of the microstructure*.

The application of electron tomography on semiconductor heterostructures that are relevant for optoelectronic devices, presents the materials science aspect of this work. Two III-V heterostructures are under investigation as case studies. The antimonide based epitaxial layer structure fabricated on Si wafers is an example for a planar heterostructure (cf. section A.1). It is considered for the application as infrared laser. A comprehensive characterization by electron tomography and by complementary TEM/STEM investigations elucidates its microstructure and does justice to the complex, spatial defect arrangement. In particular, the

occurrence and interaction of point defects (0D), dislocations (1D), planar defects like interfaces and anti-phase boundaries (2D) and volume defects (3D) are faced. In contrast to the planar film, (In,Ga)N/GaN nanocolumns present an example for a three-dimensionally grown material system (cf. section A.2). The peculiar geometric arrangement necessitates the unique access via electron tomography in order to address an open question on the relation of optoelectronic properties and the 3D chemical structure on a nanometre scale.

The second focus of this thesis affects methodical challenges. As a prerequisite, a focused ion beam-scanning electron microscope (FIB-SEM) and the electron tomography are introduced at the Paul-Drude-Institut für Festkörperelektronik (PDI) within the frame of this work. The versatile FIB-SEM device is the key to the preparation of adequate specimens for tomographic investigations. This significance comprises the site specific object selection, the isolation of the object in a certain specimen shape and its particular orientation. Moreover, the specimen has to be mounted on a needle-shaped specimen post. The information from specimens are collected in a tilt series of STEM micrographs. The selection of an adequate TEM/STEM signal for the tilt series acquisition must be considered for the individual questions to the material systems. The specimen thickness, especially with respect to the presence of antimony with its high atomic number ($Z = 51$) and the crystal orientation demand special attention.

In the following, the structure of the thesis is outlined. The next chapter gives a brief overview on the fundamentals that are touched throughout the text. The fundamentals comprise two parts. The properties of III-V materials and their epitaxial growth on wafers with dissimilar crystal structure are described in the first one. The second one addresses electron tomography in a broader sense. The preparation of adequate specimens by FIB and pitfalls of this method are pointed out. The STEM and its imaging modes are introduced. Eventually, the basics of axial tomography are summarized.

Afterwards, chapter 3 is dedicated to the experimental realization. Firstly, the challenges of individual specimen requirements imposed by the scientific question are solved by the application of the FIB-SEM device. Secondly, preliminary information for the acquisition of a tilt series are retrieved. This information includes the correlation of the crystallographic orientation and the tomogram and the evaluation of an adequate signal for the tilt series.

The successive chapter 4 presents the largest part of the thesis which treats the microstructure of the III-Sb heterostructure on Si. The first section dwells on the nature of a 3D defect that is revealed in the initial GaSb layer. The second section treats the interface toward the substrate and the AlSb nucleation layer. The interface of the large misfit (Al,Ga)Sb/Si material system is essential for the understanding of threading dislocations through the epitaxial film. The final section explains the spatial arrangement of line defects within the several micrometre thick antimonide layer stack. The mobility of dislocations by means of conservative and non-conservative motion and obstacles to their motion are considered. The latter two sections highlight interactions of dislocations with anti-phase boundaries and with other line defects.

Chapter 5 contains the investigation of the (In,Ga)N/GaN nanocolumn sample. The presence of the deposited (In,Ga)N layer and the qualitative differences in the indium content is elaborated for the various facets of the 3D object. Eventually, the conclusion terminates the thesis. Additional information on the samples under investigation and some crystallographic relations are presented in the appendix.

2. Fundamentals

2.1. Integration of III-V semiconductors

The materials under investigation are epitaxial heterostructures that comprise III-V compound semiconductors. In order to exploit their attractive properties and to simultaneously rely on established technology, III-V materials have to be combined with dissimilar materials. This combination gives rise to structural defects that affect the optical and optoelectronical properties of the heterostructures. The following section addresses fundamental properties of the III-V crystal structure and the description of line defects. The formation of the epitaxial interface in a heterostructural system is treated thereafter.

Most of the following sections include information based on well established and documented knowledge. The Landolt-Börnstein series [46] and the International Tables of Crystallography [47] are named as valuable compendia. The visualization of atomic structure models is realized with Diamond 3.1 (© Crystal Impact GbR).

2.1.1. Properties of III-V semiconductors

The class of semiconductors compounded of group III and group V elements exhibits two different crystal structures: sphalerite (or zinc-blende) and wurtzite structure. These are displayed in figure 2.1. The regarded group III elements (red) comprise aluminium (Al), gallium (Ga) and indium (In). Nitrogen (N), phosphorus (P), arsenic (As) and antimony (Sb) belong to the considered group V elements (blue). The bonding character of the III-V semiconductors is predominantly covalent [48]. The III-nitrides form wurtzite structured crystals. The structure is perspectively illustrated in the top of figure 2.1(a) along the hexagonal $[\bar{1}\bar{1}20]$ direction. It belongs to the hexagonal space group $P6_3mc$ (no. 186). Both atom sorts are organized in their own nets of equilateral triangles parallel to the basal or (0001) plane. The lattice parameters are commonly denoted a and c corresponding to the unit cell edges parallel and vertical to the basal plane, respectively. Constituent atoms are tetrahedrally coordinated which is underlined by the green polyhedra.

Figure 2.1(b) illustrates the sphalerite structure which belongs to space group $F\bar{4}3m$ (no. 216). The upper left image presents a perspective view of the cubic unit cell approximately along the [010] direction. The lattice constant a corresponds to the length of the unit cell edges. The red atoms apparently belong to a face centred cubic (fcc) Bravais lattice. The position of blue atoms belong to a second fcc lattice that is shifted by $\frac{1}{4}$ of the space diagonal. The atoms in the sphalerite structure are tetrahedrally coordinated, too. The right upper image displays the cubic unit cell with green coordination polyhedra along a $\langle 110 \rangle$ direction. This view facilitates the comparison to the wurtzite structure. In fact, the two sorts of atoms are arranged in triangular nets as well. These are found parallel to the four symmetry equivalent $\{111\}$ planes.

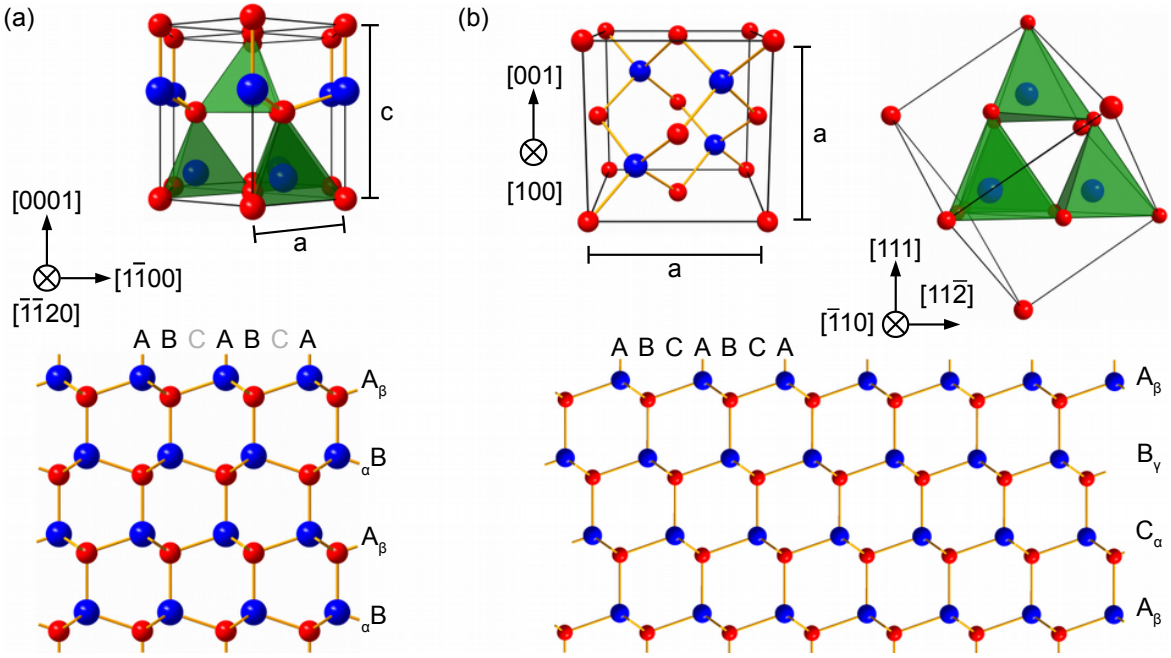

Figure 2.1. Crystal structure of III-V compound semiconductors: The upper images show perspective views of (a) the wurtzite and (b) the sphalerite unit cell. Red atoms are related to group III and blue ones to group V elements throughout the present work. The lower images describe the same structures but with respect to the stacking of densely packed planes of atoms.

The lattice planes with the triangular atom arrangement corresponds to the densest packing of spheres in a plane. An instructive description of both structures succeeds by the stacking of these planes. The lower images in figure 2.1 shows the projection of the wurtzite and the sphalerite structure onto a $\{\bar{1}\bar{1}20\}$ and onto a $\{110\}$ plane, respectively. In this viewing direction, the three distinct positions A, B and C are labelled. Atoms in a densely packed layer are located in one of these positions which is marked in the right. Greek lettering is used for the group III atoms. In that way, the two structures are distinguished by the stacking sequences of densely packed lattice planes: wurtzite $...ABABAB...$ and sphalerite $...ABCABC...$ or regarding the double layers of III-V atoms $...A\alpha B\beta A\alpha B\beta A\alpha B\beta...$ and $...A\alpha B\beta C\gamma A\alpha B\beta...$, respectively. The pairs of atoms in these projections are often referred to as dumbbells. Their orientation strictly alternates in subsequent layers of the wurtzite structure which is reflected by the 180° rotation of the coordination tetrahedra around the [0001] axis, too. In the sphalerite structure, the dumbbells keep their orientation.

Neither the 6_3mc nor the F$\bar{4}$3m space group have a centre of inversion which gives rise to the occurrence of polar directions. Pairs of group III and group V atoms in equal positions (e.g. $A\alpha$) are considered as dipoles that define polar axes along the [0001] and the [111] direction in figure 2.1. The lack of inversion symmetry implies the possibility of inversion domains and anti-phase boundaries introduced during crystal fabrication.

The ambition to investigate heterostructures of III-V semiconductors is owed to their electronic and optical properties (see, e.g., [51]). The diagrams in figure 2.2 illustrate the band gap E_g and the lattice constants of III-V semiconductors. The coloured background indicates the correspondence of energies to the visible electromagnetic spectrum. Red light

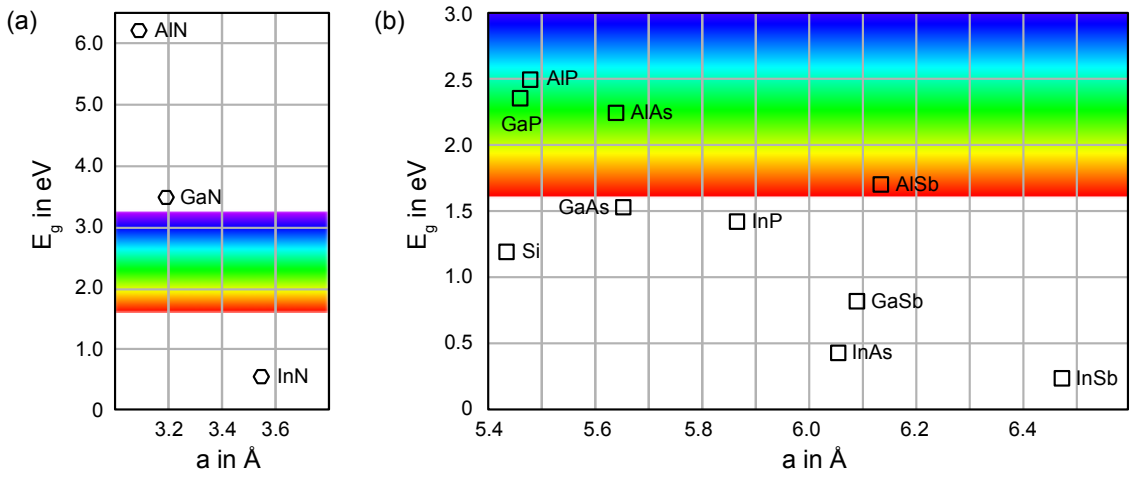

Figure 2.2. The band gap E_g and the lattice constant a of III-V compound semiconductors and silicon is displayed (adapted from [49] and [50], respectively). Hexagonal and square symbols are representative for the respective crystal structures.

(wavelength $\lambda = 780\,\text{nm}$) is found at the lower energies and blue light ($\lambda = 380\,\text{nm}$) at higher energies. Si is added to the diagram as reference. It exhibits the diamond structure (space group no. 227 $Fd\bar{3}m$) which is obtained from the sphalerite structure by filling all atom positions with the same element. Tailoring the optical properties requires to select compounds with an adequate E_g. The diagrams show the value for binary compounds. Ternary and quaternary compounds of the displayed III-V materials allow to tune E_g. Limitations arise in some cases due to the miscibility (see, for instance, [52]). Current research dwells on the realization of distinct spectral regimes for several applications. Some examples comprise ternary systems of (In,Ga)N which are explored for light emitting diodes (LED) [53, 54], heterostructures of quaternary (Al,Ga)(As,Sb) and (In,Ga)(As,Sb) alloys for infrared devices (sensors, lasers) [55–57] and superlattices of ternary (Al,Ga)As and GaAs as quantum cascade lasers emitting in the terahertz regime [58]. Beside the optical functionality, the electronic properties, for instance of GaN, are in the focus of high-frequency and high-power applications [59].

The working reliability of the crystalline III-V compounds sensitively depends on their microstructure. These deviations from an ideal single crystal comprise three-dimensional (3D), two-dimensional (2D), one-dimensional (1D) and point (0D) defects. Examples of 3D defects are precipitates/clusters, pores/voids or cracks. Stacking faults (SF), twin boundaries and interfaces are named as examples for 2D defects beside the anti-phase boundary mentioned above. Interstitial, substitutional or antisite atoms or vacant atom positions in the crystal belong to the 0D defects. Dislocations represent the 1D defects. They are described in the following in some detail for the fcc structure. The textbooks of Kelly and Knowles [60], Weertman and Weertman [61] and Hirth and Lothe [62] are pointed out as references for the explanations and as source for further details.

A dislocation is described by its line direction $\vec{l}(\vec{r})$ and by its Burgers vector $\vec{b}$. The position vector $\vec{r}$ underlines that the line direction is not constant. The angle between $\vec{b}$ and $\vec{l}$ determines the character of the dislocation. An edge dislocation is characterized by the

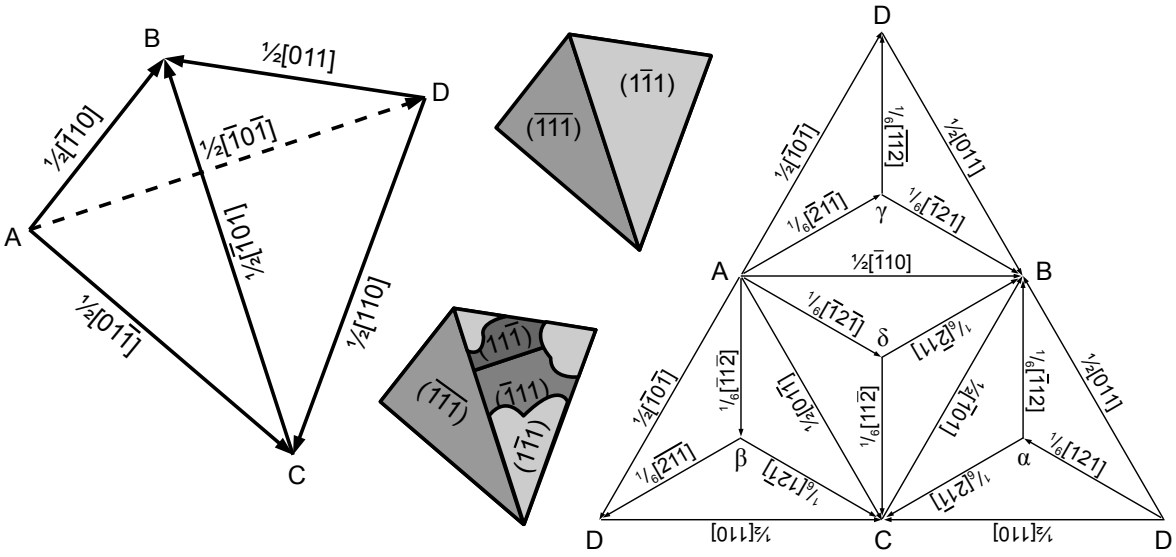

Figure 2.3. Illustration of the Thompson tetrahedron [63]: Burgers vectors' relations of perfect dislocations are shown in the perspective sketch. The small tetrahedra exhibit the same orientation. They demonstrate the indexation of the tetrahedron faces. The partial dislocations are depicted in the elevation sketch of the tetrahedron. (Convention of indexation adapted from Hirth and Lothe [62])

perpendicular and a screw dislocation by the parallel orientation of the two vectors. The dislocation is called mixed type for all other cases where $0° < \measuredangle(\vec{b}, \vec{l}) < 90°$. Furthermore, perfect and partial dislocations are distinguished. A perfect one requires $\vec{b}$ to be a lattice translation vector. The Burgers vector of a partial dislocation is not a lattice translation vector but points to a high symmetry site within the lattice. The Burgers vector is conserved along the dislocation line. Dislocations end at surfaces or in nodes. Burgers vectors of dislocations that react in a node always sum up to zero if the convention is made that all $\vec{l}$ point toward the node. The movement of a dislocation in a plane that is spanned by $\vec{b}$ and $\vec{l}$, is called conservative. Conservative motion occurs in glide planes which are usually planes with the highest packing density. The mobile dislocation is glissile. If $\vec{l}$ does not lie in a glide plane, the dislocation will be sessile. A motion of such dislocations is non-conservative and occurs due to dislocation climb.

A systematic description of dislocations in fcc materials has been introduced by Thompson [63] in order to describe dislocation reactions. The author has proposed an instructive aid that has become known as Thompson tetrahedron. It is illustrated in figure 2.3. The complete set of perfect $\frac{1}{2}\langle 110\rangle$ and partial $\frac{1}{6}\langle 112\rangle$ dislocations is contained for the primary $\{111\}\langle 110\rangle$ glide systems. Thompson has used the capital and Greek letters to address the dislocations. They mark the start and end point of the Burgers vector. Actually, it is more general than the application of arrows and the selection of directions. The dislocations will be glissile if $\vec{l}$ and $\vec{b}$ belong to one of the four glide systems. In contrast, there are sessile line defects which include, for instance, the perfect edge/90° or Lomer dislocation and the Frank partial (Aα, Bβ,... $\hat{=}\frac{1}{3}\langle 111\rangle$) dislocations. Frank dislocations occur after the nucleation of point defects on $\{111\}$ lattice planes. The formation of Lomer dislocations are subject of the discussion in section 4.2.

The energy of a dislocation line is proportional to $|\vec{b}|^2$. Therefore, the dissociation of a perfect dislocation in a bulk fcc structure, e.g. CD $\rightarrow$ Cα + αD, is expected because

$$\left|\frac{1}{2}[110]\right|^2 = \frac{1}{2} > \left|\frac{1}{6}[\bar{2}\bar{1}1]\right|^2 + \left|\frac{1}{6}[\bar{1}\bar{2}\bar{1}]\right|^2 = \frac{1}{3}. \tag{2.1}$$

On the other hand, this reaction creates a SF bordered by the partial dislocations. The required SF energy limits the separation of the two partial dislocations.

An extension to the concept of the Thompson tetrahedron has to be made for the sphalerite structure which is the combination of two fcc lattices. The presence of double layers (A_β, B_γ and C_α; see figure 2.1) provides two distinct positions of the dislocation lines on {111} planes. The bonds within the double layer or between two double layers can be broken. These two locations are referred to as glide and shuffle set, respectively.

Defects of all dimensionalities are encountered in chapter 4 and are described in more detail where necessary.

2.1.2. Heteroepitaxy of III-V semiconductors

The combination of different III-V materials as well as their integration in established silicon technology is faced to challenges which are traced back to the interfaces of the heterostructures. The epitaxial deposition of layers (epilayers) on single crystalline substrates is considered in the following. Provided that the interface is chemically stable and that a direct growth without intermediate layer is possible, the similarity of crystal symmetry, lattice constants and bonding character promotes the successful formation of a smooth heterostructure interface and a single crystalline layer. A mismatch of the structures entails the formation of defects like threading dislocations (TD) which can work, for instance, as path for leakage currents in opto-/electronic devices [64, 65]. The crystal structures and the lattice constants as presented in figures 2.1 and 2.2 are taken into account.

The impact of symmetry is regarded at first. The combination of cubic, covalent materials allows a one-to-one match of covalent bonds at the interface for equally oriented substrate and layer. This applies for III-V heterostructures as well as for the integration of III-V semiconductors on Si. A cube-on-cube growth can be realized in this case, i.e. $(001)_S \parallel (001)_L$ and $[100]_S \parallel [100]_L$ (S and L denote the substrate and epilayer). The combination of the wurtzite structured III-V heterostructures with cubic materials fits symmetrically for the bonding of atoms on the hexagonal (0001) and the cubic (111) surfaces with the in-plane orientation $[11\bar{2}0] \parallel [1\bar{1}0]$. The orientation relationship implies that the wurtzite lattice constant a has to be compared to the spacing of the {110} lattice planes $d_{110} = a/\sqrt{2}$ in the cubic structures.

Si has an inversion centre in contrast to the sphalerite structure and, hence, it does not exhibit a polar axis. The heteroepitaxy of polar III-V materials on non-polar substrates is prone to the formation of inversion domains and anti-phase boundaries in the epilayer. This aspect is considered in sections 4.2.2 and 4.3.

On the other hand, the match of lattice constants has to be considered for the formation of an epitaxial interface. The realization of heterostructures with exactly the same lattice dimensions requires lattice constant engineering with ternary or quaternary alloys. In gen-

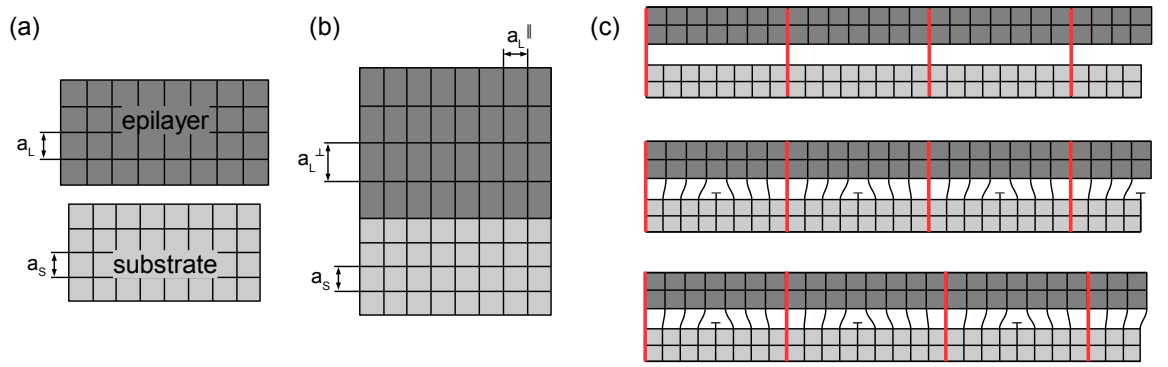

Figure 2.4. Models for epitaxial interfaces (c) Semi-coherent interfaces and in large misfit heterostructures where lattice constant is commensurable (middle) or incommensurable (bottom).

eral, a mismatch between the substrate and the layer exists and the epitaxial film reacts to this difference. The initial situation is displayed in figure 2.4(a). An interface between two lattices with different lattice constants has to be established. The first case is depicted in figure 2.4(b). It occurs for materials with a small lattice mismatch. Promising combinations emerge from the comparison of semiconductors in figure 2.2(b). The semiconductors with the lattice constant around 6.1 Å are already mentioned above. GaP and AlP are predestined for the integration on Si. The schematic shows a coherent interface between the substrate and the compressively strained epilayer ($a_L > a_S$). In consequence, the layer becomes tetrahedrally distorted, i.e. $a_L^{\perp} > a_L^{\parallel}$. This pseudomorphic growth works until a critical thickness is reached which depends on the lattice mismatch f and the elastic properties of the involved materials [66, 67].

$$f = \frac{a_S - a_L}{a_S} \tag{2.2}$$

The exceeding of the critical thickness causes the introduction of misfit dislocations (MFD) into the layer. They nucleate at the surface and leave threading segments within the layer [68]. An attempt to suppress this route of TD formation is the introduction of a buffer layer. Either this layer exhibits a certain thickness to allow for the annihilation of defects by dislocation interactions or it is designed to as template to match the lattice constants of substrate and epilayer. For instance, the lattice constants of Si and GaAs have been mediated by the application of a graded $Si_{1-x}Ge_x$ buffer layer [69]. Alternatively, the filtering of TDs by strained layer superlattices or the post growth treatment by thermal cycling has been considered (see, e.g. [70]).

The integration of highly mismatched systems is also feasible by the formation of a coincidence site lattice which is depicted in figure 2.4(c) [71]. The upper image illustrates the existence of lattice planes (red lines) that are in register before the contact of substrate and layer is established. If the quotient of the lattice constants

$$\frac{a_S}{a_L} = \frac{m}{n} \qquad m, n \in \mathbb{N} \tag{2.3}$$

is representable by m and n, a coincidence site lattice (CSL) can be formed. The crystal lattices are commensurable. The CSL period is $m \cdot a_L = n \cdot a_S$. The middle image shows

the merged crystals with a semi-coherent interface. A MFD is introduced within each period of the CSL, i.e. a periodic MFD network is created. The spacing of MFDs s is expressed by equation 2.3 or by means of f and the Burgers vector

$$s = \frac{\vec{b}_{\parallel}}{f}. \tag{2.4}$$

$\vec{b}_{\parallel}$ is the Burgers vector component parallel to the interface plane and perpendicular to the MFD line direction. Usually, the situation is less ideal and the lattices are incommensurable. m and n only approximate the lattice constant quotient. One solution is the occasional alternation of the coincidence distance realized by $m+1$ and $n+1$ lattice planes [72]. Otherwise there remains residual stress which is considered in section 4.3.2.1. Beyond, the CSL idea extends the possibilities to combine materials with different symmetries of adjoining lattice planes (see, for instance, [73]). The formation mechanism of a MFD network is discussed in section 4.2. The dislocations at the heterostructure interfaces are treated with respect to the Thompson tetrahedron. This simplification ignores the dissimilar materials because the Burgers vector is defined with reference to the ideal bulk lattice. A correct description would require the model of grain boundary dislocations [74].

The eventually formed interfaces sketched in figure 2.4 are tacitly established at a fixed temperature. A mismatch in thermal expansion coefficients introduces a lattice mismatch during the sample cooling after growth. Additionally required MFDs have to nucleate at the surface and move toward the interface. An estimate of the thermally induced strain is given in section 4.3.2.1 for the epitaxy of GaSb on Si(001).

Beside the 2D growth mode, there are material combinations and growth regimes where 3D structures establish on the substrate surface instead of closed layers. Considering the free surface energy of the substrate γ_S, the layer γ_L and the free energy of the interface γ_I, the following inequations characterize the 3D (Volmer-Weber) and the 2D layer-by-layer (Frank-van-der-Merwe) growth mechanism, respectively [69].

$$\gamma_S < \gamma_L + \gamma_I \tag{2.5}$$

$$\gamma_S > \gamma_L + \gamma_I \tag{2.6}$$

The 3D growth regime is exploited, amongst other things, in order to circumvent the formation of threading dislocations. The 3D objects exhibit a free surface which allows to expand the lattice and reduce the epitaxially and thermally imposed strain [75]. Furthermore, the dislocations tend to be as short as possible in order to minimize the energy according to their length. The 3D object provides more options for a dislocation to terminate at a surface. Two competing approaches toward 3D structures, namely nanowires, have been considered. The self-organized growth where inequation 2.5 is valid, and the growth through the holes in a mask on a prepatterned substrate [75].

In the presented work, two heteroepitaxial material systems are considered as case studies. They are described in appendix A. One system corresponds to a large misfit system that forms a MFD network. The other one is an example for the selected area growth (SAG), i.e. the 3D growth by the application of a mask.

2.2. Electron tomography

This section treats electron tomography and the necessary prerequisites which are encountered in this thesis, i.e. the focused ion beam (FIB) and the STEM. The first section describes the FIB which is an indispensable tool for the preparation of specimen. They are the foundation for the subsequent tomographic studies. The understanding of the FIB is essential in order to prepare specimen of appropriate quality and in order to judge preparation induced artefacts. The second section addresses the STEM. The working principle and image conditions are shortly introduced. The STEM and the purposeful selection of an adequate signal present the base for the acquisition of a tomographic tilt series. Finally, a section briefly discusses the principles of axial tomography carried out in a TEM/STEM.

2.2.1. Focused ion beam

The development and investigation of focused ion beams ranges back to the 1970s. A survey of original works on field ionization sources is found in Orloff *et al.* [76]. Nowadays, focused ion beams are routinely used in scanning microscopes which are commercially available as mature devices. To be precise, these devices are scanning FIB microscopes but they are commonly addressed simply as FIB. Applications of the FIB comprise the field of failure analysis, substrate patterning by removing or depositing material and the TEM sample preparation (see for instance [77, 78]). Beyond, the FIB is inherently a microscope which is also used due to its characteristic imaging capabilities.

In 2003, nearly all FIBs have been based on gallium (Ga) emitters according to Orloff *et al.* [76]. Recent trends expand the spectrum of emitters by the application of gaseous materials. On the one hand, the helium ion microscope enables a higher resolution than the Ga FIB which is beneficial for imaging or milling of very small and well defined sample volumes [79, 80]. On the other hand, the xenon plasma FIB provides higher beam currents to remove material more efficiently than the Ga FIB [81, 82]. The latter development is interesting for failure analysis on length scales of several 100 µm.

The capability to prepare TEM specimens is essential for the realization of the presented experiments. The FIB allows a site specific preparation with a resolution of less than 1 µm. A target object is selected, isolated in an advantageous specimen geometry and mounted on an adequate specimen holder or support. In the following, these actions are describe in a general manner along with the basic working principle of the FIB. In subsequent chapters, particular details of FIB sample preparations are described and discussed with respect to challenges of actual experiments.

Setup of the dual-beam FIB-SEM device

The specimen preparation is carried out in the JIB4501 dual-beam microscope (JEOL Ltd.) located at the PDI. It is addressed in the fundamentals part as its design is paradigmatic for dual-beam devices. The schematic in figure 2.5 depicts the setup of the microscope. An SEM and an FIB column are mounted in one vacuum chamber. The optical axes of both microscopes ideally coincide at the sample surface. They are inclined to each other by 52°. The working distance of the SEM as well as of the FIB is 18 mm leaving sufficient space for

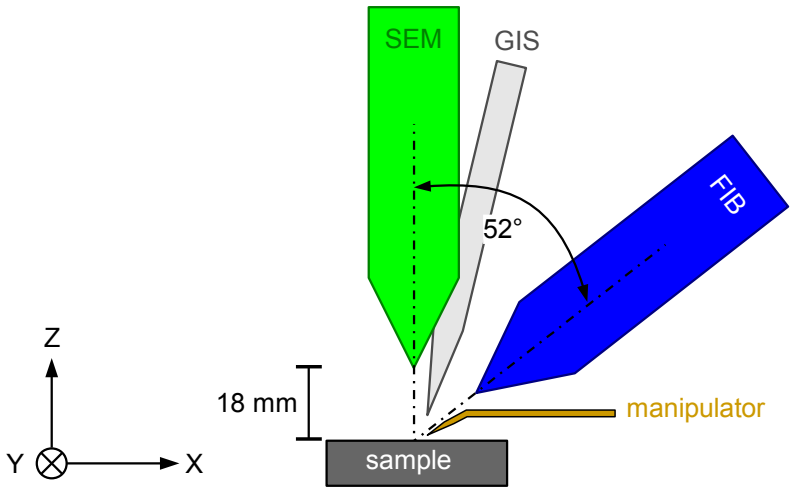

Figure 2.5. Schematics describe the arrangement of the focused ion beam (FIB) and the scanning electron microscope (SEM) in one vacuum chamber. The gas injection system (GIS) and the manipulator complete the device for the purpose of TEM specimen preparation.

the versatile sample stage. The stage offers six degrees of freedom. Beside the translational X-, Y- and Z-axis, there is a fine-Z-axis mounted on the tiltable stage in order to move any sample location into the eucentric height. The tilt axis T is normal to the image plane of figure 2.5 and ideally intersects the coincidence point of SEM and FIB. The tilt is variable from $-10°$ to $54°$ so as to allow a view under normal incidence onto the sample with both the SEM and the FIB. A continuous azimuthal rotation around the fine-Z-axis completes the flexibility. Two gas injection systems (GIS) allow the deposition of carbon and tungsten by an electron or ion beam induced process (see below). Finally, a manipulator (Kleindiek Nanotechnik GmbH) is attached to the chamber to move micrometre-sized sample pieces with a precision of several tens of nanometres.

The SEM is indispensable for the orientation of the specimen and for the *in situ* lift-out technique which is described below. An Everhart-Thornley- and a back-scattering electron detector are available to image the sample by both the secondary electron (SE) and the back-scattered electron (BSE) signal, respectively. The textbook of Reimer [83] is named for details about SEM and respective detection methods. The SE signal caused by ions is captured by the Everhart-Thornley-detector, too, in order to use the FIB for imaging. Beside this common feature, the layouts of the electron microscope and of the ion microscope exhibit significant differences which are hardly perceived during routine work. Some details are described in the following in order to solidify the notion of an ion microscope based on gallium.

The Ga emitter is schematically depicted in figure 2.6(a) according to the technical datasheet of the manufacturer [84]. In fact, the arrangement of electrical contacts, an isolating ceramic socket and a tungsten filament are similar to electron emitters for the SEM and the TEM. A tungsten (W) needle is attached to the filament which is actually found in field emission sources of electron microscopes, too. In addition, a spring like Ga reservoir is mounted at the end of the W tip. Liquid Ga is wetting the surface of the W needle. A heating current through the filament is not needed for the working state because the melting

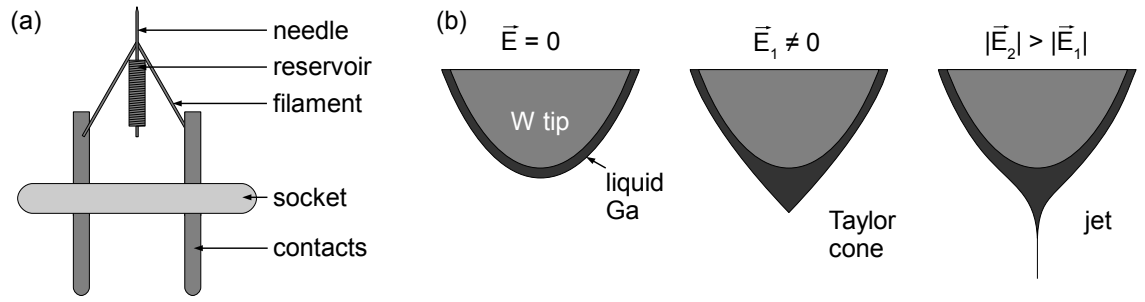

Figure 2.6. (a) The schematic depicts the design of the Ga^+-ion emitter (adapted from [84]). (b) The liquid Ga wets the W needle. A Taylor cone forms at the apex of the needle in an applied electric field $\vec{E}$. At a sufficient field strength field ionization occurs and Ga^+-ions are emitted from the tip of the Taylor cone.

point of Ga is around room temperature. The low melting point, an ideal surface tension and the chemical compatibility to tungsten feature Ga as the ideal material for a liquid metal ion source (LMIS). The evolution of the wetting Ga film at the tip of the W needle in an electrical field $\vec{E}$ is illustrated in figure 2.6(b) according to the *in situ* TEM observations of, for instance, Benassayag *et al.* [85]. The equilibrium shape transforms to a Taylor cone [86] in the presence of an electric field. The highest field strength at the fine tip cause the ionization of Ga-atoms which are ejected from the liquid and accelerated toward the extraction electrode. It is remarkable that Ga^+-ions are predominantly created in the narrow applicable extraction voltage range. A too high voltage causes the collapse of the shape and leads to a jet of Ga [85]. A comprehensive description of the LMIS including the choice of ideal emitter materials and the physical working principle is published by Forbes [86].

After passing the extraction aperture the Ga^+-ions are accelerated with a selectable voltage U of 3 kV to 30 kV. In contrast to electrons, the ions have a much higher mass M while the absolute value of the charge q is the same. Their non-relativistic velocity v

$$v = \sqrt{\frac{2qU}{M}} \tag{2.7}$$

is smaller by the factor $\sqrt{M/m_e} = 356$ where m_e is the electron mass. This difference justifies the application of electrostatic lenses for the ion optical system. The manipulation of the particle path by magnetic lenses with a magnetic flux density $\vec{B}$ is inefficient because the responsible Lorentz force $\vec{F}_L$

$$\vec{F}_L = q(v \times \vec{B}) \tag{2.8}$$

depends on the velocity v. A further consequence of the low velocity concerns the beam broadening due to Coulomb repulsion [87]. A detailed theoretical elaboration on ion optics as well as on the LMIS is collected by Orloff *et al.* [76].

Interaction of the Ga^+-ion beam with sample material

The development of preparation strategies and the judgement of artefacts introduced during preparation require knowledge on the interaction of the Ga^+-ion beam and the sample mate-

rial. Ions loose their energy during their travel through the material by different interaction mechanisms [76, 88, 89]. Finally, they come to rest at a certain depth. The empirical quantities are the stopping power and the range. It is characteristic of ions to accumulate in the Bragg peak of the related Bragg curve (see figure 3.1 or e.g. [90]). (Here, the term "Bragg peak" is not related to the diffraction phenomenon.) The site specific specimen preparation relies on interactions that transfer momentum to sample atoms which are ejected from the sample surface. The operations milling and polishing are based on this sputtering effect. The creation of secondary electrons presents a second interaction effect which allows FIB imaging and the ion beam assisted deposition (IBID) procedure. For both purposes, the interactions must take place near the surface. The 30 kV ions reach depths several tens of nanometres in amorphous materials. Respective material dependent calculations have been usually carried out with the TRIM simulation package [91–93]. Kempshall *et al.* [91] demonstrate that the calculation is imprecise for crystalline materials by comparing imaging as well as milling in and off zone axis conditions. Consequently, this channelling effect allows an even deeper penetration of ions. In greater depth, hit atoms are not released through the surface but they are displaced from their ideal crystal lattice positions. These events lead to an amorphisation layer after a sufficient ion dose which has a thickness that depends on the accelerating voltage and on the sample material [88, 94, 95]. The figure to characterize the effect of material removal is the sputter yield. It measures how many atoms are removed per incident Ga^+-ion and depends on the incidence angle toward the surface [92]. A maximum occurs at 80° in the case of flat surfaces. The sputter yield must be reconsidered for geometrical constraints of uneven surfaces. Sputter atoms in a deep trench will redeposit at the side walls and eventually limit the maximal aspect ratio of a trench. The beam current and the scanning route influence this ratio [96].

The FIB is a charged particle probe. Consequently, the sample must be conductive to avoid charging. Alternatively, charge neutralization must be realized by supplying negative charges from an electron flood gun or the SEM [97].

Artefacts of preparation and specimen damage

The greatest drawback of TEM specimen preparation by FIB is the introduction of an amorphised damage layer and the implantation of Ga. This aspect is elaborated in sections 3.1 and 4.1.2.2. FIB polishing with low accelerating voltage or with Ar^+-ion polishing are discussed as counteractions in detail. Beside these measurements, Kato [94] reports on a chemical etching step to remove amorphous material which works for selected materials.

A common problem of the lamella fabrication is the curtaining effect [77]. The lamella surface exhibits grooves along the ion beam direction that occur first after the rough milling. The application of low beam currents, i.e. a better defined probe, reduces these initial grooves. They reappear on a finer scale during polishing. They are avoided by an alternating reorientation of the FIB parallel to the lamella surface [98]. Furthermore, they are diminished by the application of an amorphous protective layer at the top of the lamella [99].

So far, physical consequences of the interaction with Ga^+-ions are addressed. The chemical reactivity of Ga has to be considered as well. The Ga-V compound semiconductors appear to be particularly affected [100]. Figure 2.7 illustrates the attempt to isolate ordered

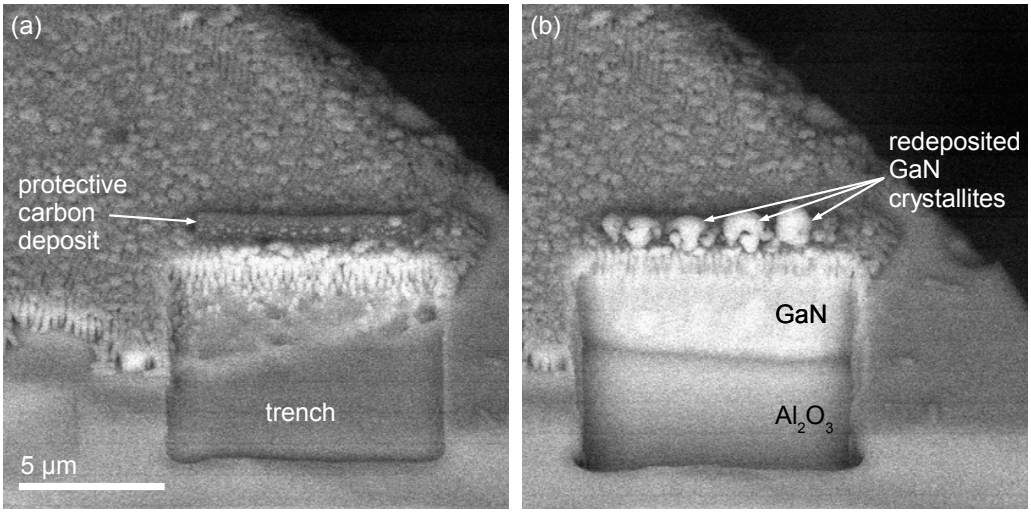

Figure 2.7. The BSE SEM images of are acquired under an incidence angle of 52° toward the sample surface. (a) Contours of a trench in front of the protective carbon deposit are visible after a short time of milling. (b) The final trench offers a view onto the specimen cross-section.

GaN nanocolumns within a lamella. A stripe of protective carbon is deposited on top of the sample. An emerging trench is visible in figure 2.7(a) below the carbon deposit. The completed trench allows an oblique view onto the sample cross-section as shown in figure 2.7(b). It reveals the GaN template layer grown on an Al_2O_3 substrate. The occurrence of micrometre-sized crystallites aside the trench is remarkable. It is assumed that the N-atoms released during sputtering react with the long tails of the Ga^+-ion beam profile in the vicinity of the milled area. The characteristic ion beam profile results from repulsive Coulomb interactions among the ions [101]. Challenges due to the regrowth of GaN are addressed in section 3.1. This effect is observed in GaAs and GaSb processing, too, but in a less pronounced manner.

The presence of Ga at the bottom of the lamella, on the specimen support and in the protective layer is emphasized because of two experiences encountered during initial experiments. Figure 2.8(a) presents a layer of Ga covering a TEM lamella. This situation happens after an attempt to polish the lamella with Ar^+-ions. The lamella is partly situated in the shadow of the specimen support with regard to the ion beam. The left side appears to be cleaned by the ion beam. The top and the right side are covered by two smooth layers. It is assumed that the support heated up and the liquid Ga wetted the lamella. This observation reminds of the Ga emitter described above and in figure 2.6. The double layer is owed to the one-time repetition of the polishing attempt. Figure 2.8(b) displays a TEM image of a lamella which has been heated to 400 °C. Ga is boiled out of the protective carbon layer. The Ga creeps over the lamella surface and reacts with the sample material to form the observed faceted crystallite in the right of the image. The amount of Ga is significant and must be considered in respective experiments in future.

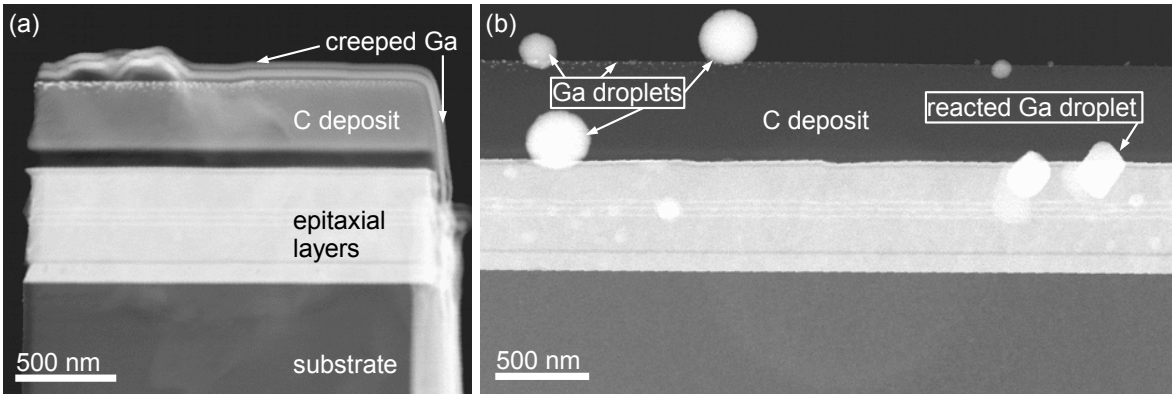

Figure 2.8. The dark-field STEM images show lamellae that have been faced to heat input after FIB preparation. (a) The copper specimen support of the lamella has been heated by an Ar^+ ion beam during the attempt of post FIB preparation treatment. (b) The lamella has been heated to 400 °C during an *in situ* TEM experiment.

Ion beam induced deposition (IBID)

The JIB4501 is equipped with two GIS providing tungsten hexacarbonyl $W(CO)_6$ and phenanthrene $C_{14}H_{10}$ as precursor gases for tungsten and carbon deposition, respectively. The deposition operation is based on the ion- or electron beam induced decomposition of the precursor molecules. The nozzles for the gas inlet are approached to the sample surface. Adsorbed molecules are cracked by secondary electrons or by excited surface atoms which are generated by the scanned ion or electron beam, or by the direct interaction with the incident beams. Utke *et al.* [93] have controversially discussed which mechanism dominates the decomposition of precursor molecules. They explain the significantly higher deposition rate of IBID by excited surface atoms which transfer energy to adsorbed precursor molecules. Hence, the deposition with the FIB is preferred for the sake of speed.

The deposition of tungsten and carbon is applied during the specimen preparation which is described in the next paragraph. Carbon deposits are used as protective layers that preserve objects close to the sample surface from ion beam damage. Of course, the ions would destroy a several tens of nanometre thick surface layer at the start of the deposition process. Therefore, an initial 100 nm thick layer of carbon is required which is realized by electron beam induced deposition or by the evaporation of carbon onto the whole sample with a carbon coater (see section 3.1).

Routine steps of specimen preparation

The *in situ* lift-out technique is an established procedure to prepare lamellae for TEM investigations. The advantage over conventional preparation methods is the capability to extract a selected target object (see e.g. [102–104]). This routine procedure is illustrated in figure 2.9.

The destructive quality of the FIB necessitates the deposition of a protective stripe of carbon as shown in figure 2.9(a). The FIB image is acquired in normal incidence. It prevents the damage of the target object which can be a three-dimensional feature as well as an object buried below a smooth surface. The repeated imaging of the surface with the FIB is indis-

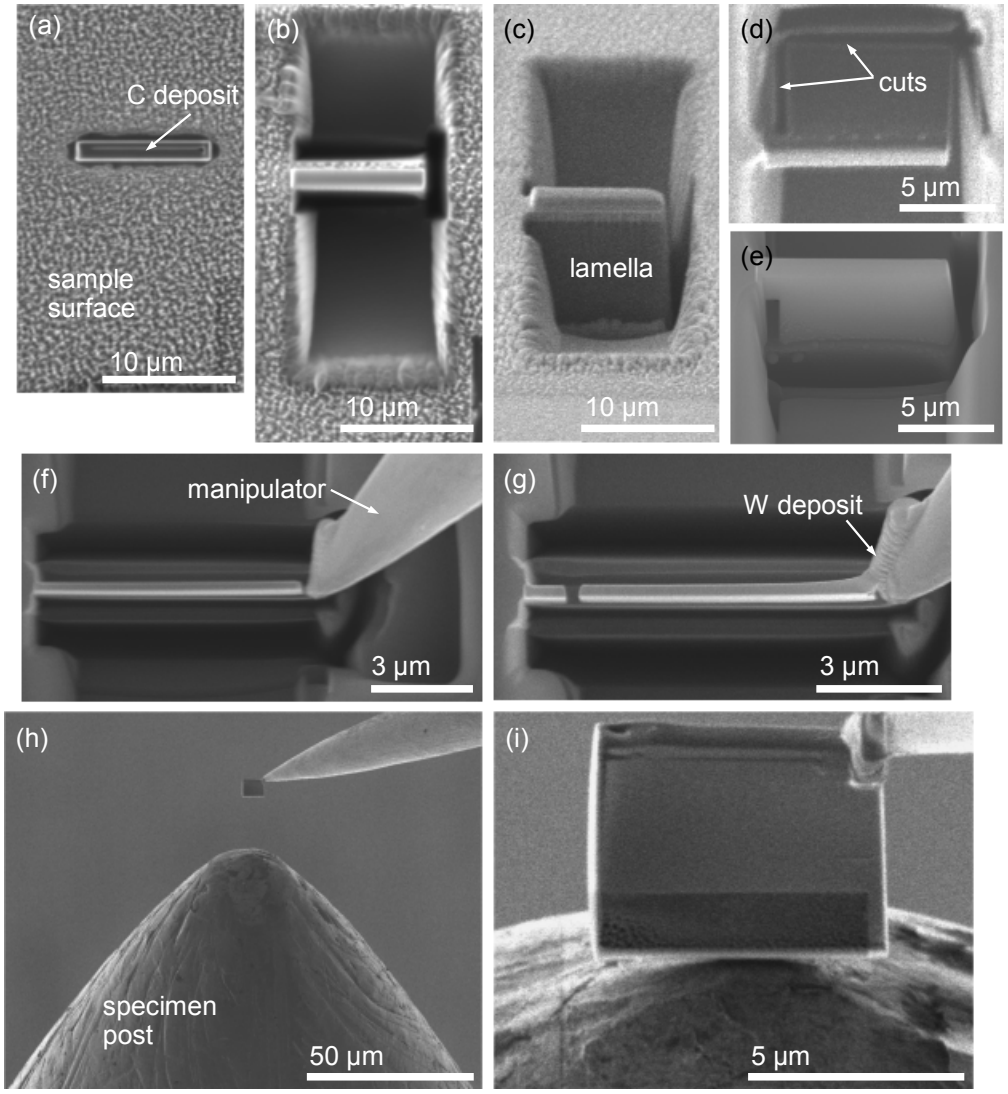

Figure 2.9. The SEM and FIB images images illustrate steps of the routine lift-out procedure for the preparation of TEM specimen.

pensable for the lift-out procedure. Figures 2.9(b) and (c) present a FIB and a SEM image taken under normal incidence and under an angle of 52° toward the sample normal, respectively. These images illustrate trenches that are milled with the FIB. They isolate a lamella below the protective stripe. A finer milling step with the sample tilted by some degrees succeeds to realize plane-parallel lamella surfaces. Redeposition impedes the formation of side walls parallel to the beam direction. The stage has to be titled by approximately $\pm 2°$ to expose the side to the beam. This tilt value depends on the material as well as on the depth and width of the trenches.

The specimen stage is tilted by 52° for the next step in order to image one side of the lamella with the FIB. The bottom and most of the sides of the lamella except for a small bridge are cut free from the sample material. Figure 2.9(d) shows the result as seen by the FIB. Figure 2.9(e) presents the SEM view after tilting back to the original stage position.

This view is important to ensure the completeness of the bottom and side cuts. Afterwards, the needle of the manipulator is approached to the lamella. It is found that an additional trench at the side facilitates the positioning and the bonding of the needle. The SEM views along the original surface normal in figures 2.9(f) and (g) depict the attachment of the lamella to the manipulator. The former image demonstrates the positioned manipulator beside the lamella. In the latter image, the needle is glued to the lamella by the deposition of tungsten. Then, the remaining bridge is cut and the lamella is ready for the lift-out.

The lamella has to be transferred to an adequate support for TEM investigations. Here, a specimen post with a base diameter of 1 mm is used in order to mount the specimen onto a dedicated tomography holder. The oblique FIB view onto the lamella and the specimen post in figure 2.9(h) illustrates the approach of the manipulator with the attached lamella to the support. The careful placement is shown in figure 2.9(i). The attachment by tungsten and the cut-off from the manipulator complete the lift-out procedure. Finally, the lamella must be trimmed and polished to the desired and adequate shape for the TEM/STEM investigation. The modification of the routine lift-out procedure and the individual solutions of tackled challenges in this work are presented in section 3.1.

2.2.2. Scanning transmission electron microscopy

In the present work, all the raw data for electron tomography investigations are acquired by the use of a scanning transmission electron microscopy (STEM) signal. The large field of view and the suppression of diffraction contrast are the general advantages for the application of STEM based electron tomography in materials science. The suitability of the incoherent high-angle annular dark-field (HAADF) signal has been emphasized by Midgley and Weyland [7]. Beyond, valuable information is provided in bright-field STEM [105] which needs careful consideration for the application in electron tomography. Both methods are described below and readdressed in the course of the subsequent chapters presenting the experimental results.

In addition to the electron tomography measurements, complementary measurements are carried out applying the TEM mode. The extracted information relies on the specific exploitation of the electron diffraction conditions. Throughout the text, the acronyms TEM and STEM are related to imaging modes that comprise a parallel and a serial (scanned) acquisition of data, respectively. The Bragg condition

$$n \cdot \lambda = 2 d_{hkl} \sin \theta_B \tag{2.9}$$

relates the diffraction information originating from a set of lattice planes ($h\ k\ l$) with spacing d to the Bragg diffraction angle θ_B. The latter quantity depends on the electron wave length λ . The integer n points to harmonics of the spatial frequency $k = 1/d_{hkl}$. TEM methods that are applied in this work comprise selective area diffraction (SAD) and convergent electron beam diffraction (CBED), dark-field (DF) and weak-beam dark-field (WBDF) imaging and high-resolution TEM (HRTEM) imaging. Necessary details of these methods which are required for the understanding of the experimental data, are explained along with the respective results. Reference is made to the textbooks of Hirsch *et al.* [106], Williams and Carter [3] and Reimer [107] for further elaborations on these topics.

It is remarked that a dedicated textbook for STEM is still missing although it has a comparable long-standing history as TEM. The status quo of STEM developments and applications is summarized in a collection of topical contributions edited by Pennycook and Nellist [108]. In contrast, TEM imaging and diffraction techniques are comprehensively published in many textbooks. Therefore, an own section for respective fundamentals is omitted.

Principle of reciprocity and bright-field STEM

The success of STEM is essentially promoted by the introduction of an electron field emission gun (FEG). Crewe *et al.* [109] pioneered the development of dedicated STEM systems. Figure 2.10(a) presents the simplest setup according to the authors initial realization. Their original intention has been to exceed the mere use of "information about the electron-scattering properties of a specimen" which has been applied for TEM imaging in that time. They have incorporated an electrostatic spectrometer and a photomultiplier tube in place of the detection system. In that way, they reached chemical information with a lateral resolution of 3 nm. The development of dedicated STEMs lingers on. The realization of aberration correction for the probe forming lens allows increased beam currents and reduced spot sizes [110]. Chemical maps with atomic resolution are possible using the electron energy loss signal after the introduction of these improvements [111].

Beside the dedicated STEMs, the combination of STEM and TEM in one machine is widely spread providing the advantages of both methods. The manifold magnetic lenses and deflection coils in such machines allow to focus the beam in the specimen plane or to spread it for a parallel illumination implementing the STEM and TEM mode, respectively [112]. The scanning is realized by a periodic signal applied to deflection coils.

The quantitative interpretation of BF images acquired in TEM has a long tradition (see e.g. [3]). It is based on simulations of contrast features arising from microstructural objects like dislocations or SFs. It has been outlined in the 1970s that BF STEM images contain valuable information on the microstructure as well. Maher and Joy [114] have imaged respective defects. They have emphasized that an interpretation can be based on TEM contrast simulations if the principle of reciprocity holds. Figure 2.10(b) illustrates this principle according to the overview article of Humphreys [113] in the ray diagram of a simplified microscope setup. In TEM, the specimen is illuminated by the source image formed by the condenser system. The semi-convergence angle of the illumination is α_i. The signal originating from one point in the specimen is captured on a parallel detector from an angular range $2\alpha_o$ that is defined by the objective aperture. If reciprocity holds between STEM and TEM, the ray path can be reversed for the STEM case. That is, a point source is placed at the pixel position leading to the illumination of a point on the specimen under the probe semi-convergence angle α_p. The signal from this point is detected under the detection angle $2\alpha_d$ and must be equal to the pixel intensity value from the TEM case. The rigorous equivalence of respective apertures and lenses including their spherical aberrations has been underlined by Humphreys [113]. The obvious problem will arise from the very small detection angle if $\alpha_d \stackrel{!}{=} \alpha_i$. STEM images are very noisy under these conditions as only a small portion of the incident electrons is detected.

Practically, conditions are chosen for TEM and STEM imaging as shown in the upper and lower sketch of figure 2.10(c), respectively. An approximately parallel illumination

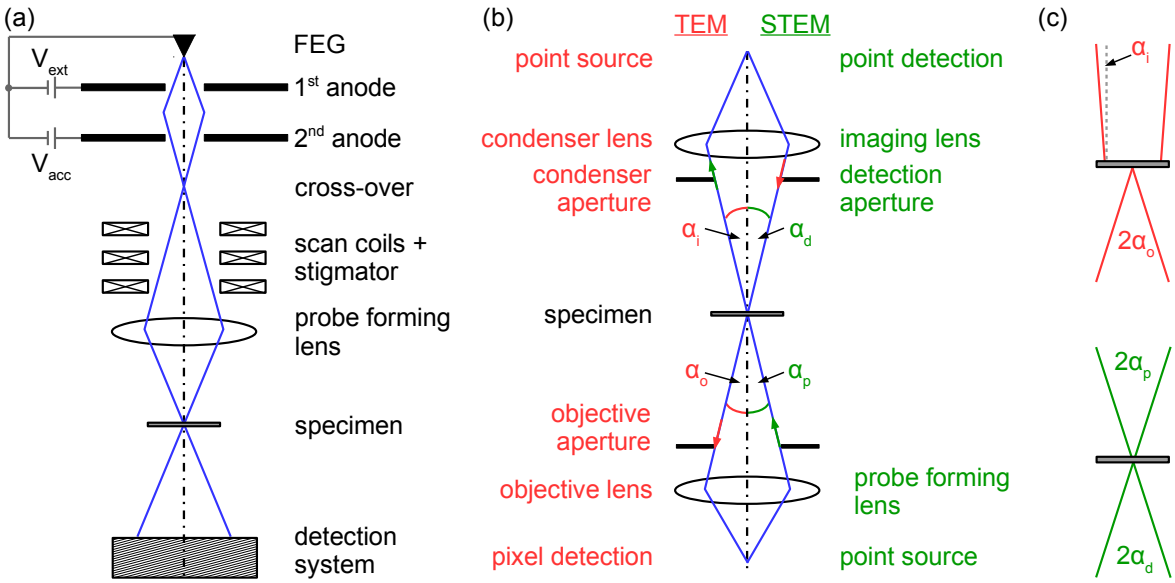

Figure 2.10. (a) The schematic depicts the setup of the original dedicated STEM with a FEG electron source (adapted from [109]). (b) The principle of reciprocity is illustrated on the schematic beam paths in a simplified TEM/STEM setup (according to Humphreys [113]). (c) The comparison of the different angles α_i has to be related to the situation used in practice. The upper sketch represents the typically parallel illumination in a TEM and the convergent beam condition in a STEM.

with α_i as small as possible is applied for phase contrast images in TEM. The condition $\alpha_p = \alpha_d$ is usually applied for STEM imaging to avoid the intensity loss by a small detection angle in the reciprocity case. The set of imaging lenses (cf, e.g., manual of the JEM2100F [112]) transfers the STEM signal to the detector. These lenses define a virtual camera length to determine α_d in addition to the usual aperture. In respect of the dedicated STEM in figure 2.10(a), the changeable camera length corresponds to a variable distance between the detection system and the specimen.

More recently, Phillips *et al.* [115, 116, 117] have returned to the interpretation of defects in BF STEM images with the necessary contrast simulations which have been claimed by Maher and Joy [114]. Beside the calculation of dislocation and SF contrast under different imaging conditions, Phillips *et al.* [115] have outlined characteristics of BF STEM imaging that provide essential advantages for investigations presented in sections 3.2.3 and 4.3. These benefits become manifest in the reduction or even suppression of diffraction contrast features that are typical of TEM images - bending and thickness contours as well as depth dependent oscillations along dislocation lines. In that way, defects are imaged over large areas with a homogeneous contrast which is the prerequisite for subsequent tomographic analyses presented in sections 3.2.3 and 4.3. Furthermore, STEM provides a wider field of view and a larger penetration capability than TEM [118]. This aspect is important to trace dislocations in several 100 nm thick and several micrometre wide lamellae.

A qualitative explanation for the suppression of diffraction contrast features is described by figure 2.11 according to, for example, [107]: The usual concept of the Ewald sphere in reciprocal space is employed. The parallel illumination in TEM is represented by the red part of the Ewald sphere construction. The direction of a single wave vector characterizes the

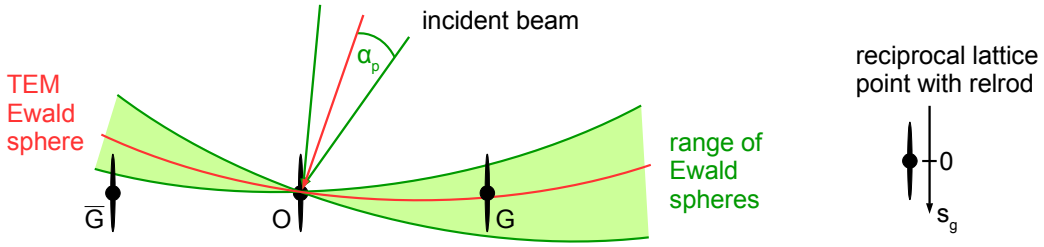

Figure 2.11. The concept of the Ewald sphere is illustrated for a section through reciprocal space. The parallel illumination is represented by the red line that intersects the origin O (corresponding to the direct beam) and the relrod along a reciprocal lattice point G (corresponding to a diffracted beam) in the schematically presented two-beam case. The green range of Ewald spheres depicts the case of a convergent beam illumination.

incident beam. The intersection position with a reciprocal lattice vector or the accompanying relrod is characterized by the excitation error s_g. In the ideal two beam case, only the direct beam and one diffracted beam related to the depicted intersection contribute to the image contrast. The BF and DF images exhibit contrast oscillations with a characteristic spacing that depends on s_g. The oscillations occur due to the Pendellösung which describes the intensity oscillation of the two beams. The convergent STEM illumination is decomposed into a set of incident beams with differently oriented wave vectors. In consequence, there is a set of Ewald spheres (green) that intersect a larger part of the relrod. The resulting signal includes the summation over a range of s_g. The characteristic intensity oscillations blur with an increasing convergence angle.

High-angle annular dark-field STEM

So far, α_d has been considered for the detection of the BF STEM signal. It is tacitly expected that $0 < \alpha_d \leq \alpha_p$. It has to be underlined that BF TEM/STEM provides a mass thickness contrast for the case of amorphous specimen and that it is routinely employed for electron tomography in biology. Materials science deal with crystalline substances and are, therefore, faced to electron diffraction which superimposes further contrast mechanisms to the mass thickness contribution. The DF STEM signal offers valuable information to overcome the limits of tomography in materials science [7]. The application of a ring shaped detector [119, 120] enables the selection of electrons scattered into an angular range from the inner θ_{in} to the out collection angle θ_{out}. These angles are defined by the dimension of the annular dark field (ADF) detector and the camera length. The detector dimensions and its position are fixed. Hence, the collection angle range is varied by the selection of the camera length: the shorter the camera length the higher the scattering angle of selected electrons. The setup is schematically shown in figure 3.12 which is explained below in section 3.2.3.

The arrangement for the high-angle annular dark-field (HAADF) condition is of great interest because the signal can be treated as incoherent. In the case of low collection angles the coherent interaction of diffracted beams prevails. The influence of thermal diffuse scattering (TDS) exceeds the coherent contribution at a sufficiently high θ_{in}. Hartel *et al.* [121] calculated respective conditions and formulated boundary conditions for an incoherent signal in HAADF mode. They derived a power law for the relation of the intensity I_{HAADF} from the

atomic number Z of the scattering atomic species.

$$I_{HAADF} \propto Z^n \tag{2.10}$$

Therefore, the HAADF STEM is known as Z-contrast imaging. Typical conditions require $\theta_{in} \geq 60\,\mathrm{mrad}$ and $\theta_{in} > 3\alpha_p$. The exponent n depends on θ_{in} [121] and lies between 1.7 and 1.8 for the selected camera lengths applied for the presented results.

Pennycook [122] has illustratively described the formation of an incoherent signal. He has underlined that the incoherency occurs due to the choice of the detector because the initial probe as well as its state within the material are highly coherent. Furthermore, the choice of a bright-field detector reflects a diffraction contrast at the same time. Indeed HAADF STEM image contrast simulation has been based on the calculation of coherent Bloch waves by several groups (see [123]). There, the localized 1s states along atom columns [124, 125] predominantly contribute to the high-angle signal due to their broad distribution in reciprocal space, i.e. in the diffraction or detector plane, while the detector spatially filters out the coherent interaction with 2s and higher order states far from the atomic column [122]. Consequently, the description of electron scattering is based on 1s states as usually done for HRTEM [125]. On the other hand, TDS becomes more pronounced at high-angles. It destroys the coherency of the electron wave field. TDS appears due to the interaction of the electrons with phonons which happens incoherently due to the thermal character. Conclusively, the amount of TDS intensity increases with thickness at the expense of the coherent 1s intensity [122]. This is the comprehensible essence of the accurate, mathematical description discussed in earlier studies (see, e.g., [121]).

These considerations on incoherency and the HAADF signal are focused on crystals illuminated along a low-indexed zone axis. The prevailing 1s-states give rise to the notion of channelling. Geuens and Dyck [125] have pointed out that the validity of the 1s-model is limited to zone axis condition and small beam or specimen tilts. The subsequently excited non-1s states are less efficiently scattered to large angles [123] and the I_{HAADF} drops. This dechannelling effect limits the validity of equation 2.10. Chemically homogeneous, crystalline material exhibits heterogeneous HAADF contrast due to different orientations (polycrystals) or strain fields (dislocations or interfaces) which leads to dechannelling effects [126–128]. Furthermore, the intensity is, in general, different for the amorphous and crystalline phase of a material [129]. These aspects are important for the chemical interpretation of the HAADF signal.

2.2.3. Basics of tomography

The origin of the tomographic problem has been formulated by Radon [130] already in 1917. The author treated the 2D integral transform of a function f which is known as Radon transform $\mathcal{R}$ today. The comprehensive mathematical description can be found, for instance, in the original work [130] or embedded in an extended treatment presented by Deans [131]. The problem is illustrated by equation 2.11 and figure 2.12.

$$\mathcal{R}f = \int_L f(x,y)ds \tag{2.11}$$

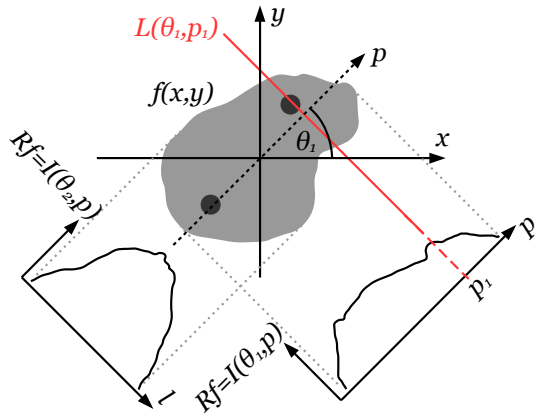

Figure 2.12. The principle of the Radon transform $\mathcal{R}$ is schematically depicted. The projection of an object function f along the direction defined by θ corresponds to a line in Radon space.

The object function $f(x, y)$ is integrated along all straight lines L that are parametrised by an angle θ and the radial coordinate p. f is defined for the 2D space of real numbers $(x, y) \in \mathbb{R}^2$. The challenge consists of the inversion or $\mathcal{R}f$ because, regarding tomography, there is a set of images in the first instance. They correspond to intensity line profiles $I(\theta_i, p)$ which are represented around the object $f(x, y)$ in figure 2.12. The profiles correspond to the integration of f along lines $L(\theta_i, p)$ with the same orientation given by θ_i. An important practical demand on the images has to be made in order to enable the unambiguous inversion. Images must be projections of f, that is, $I(\theta, p)$ is proportional to the integration of a physical property along $L(\theta, p)$. In general, this requirement is hardly met in the case of transmission electron microscopy as discussed in detail by Hawkes [132]. Nevertheless, the successful application of electron tomography in biology features the method as valuable tool since the initial work of DeRosier and Klug [1]. Here, the mass-thickness contrast that governs BF images of amorphous specimen [3], exhibits a monotonic dependence of I from the mass-density distribution [132]. The situation is fundamentally changed in the case of crystalline materials. The occurrence of diffraction contrast violates the projection requirement. Electron tomography has been essentially promoted in materials sciences since the routine application of Z-contrast/HAADF STEM where diffraction contrast is suppressed [7]. The selection of adequate STEM imaging conditions for electron tomography is further discussed in section 3.2.2.

An exact inversion of the Radon transform is practically impossible due to the discrete sampling of image points as well as a limited number N of tilt angles θ_i and a limited tilt range. If N images are acquired in equidistant tilt steps about a single tilt axis and about $\pm 90°$, the resolution d in the plane perpendicular to the tilt axis is limited to

$$d = \frac{\pi \cdot D}{N} \tag{2.12}$$

as derived by Crowther *et al.* [133]. D is the size of the object of interest. A further restriction must be considered if the maximal tilt angle α is smaller than 90°. This limitation entails the "missing wedge" problem leading to the elongation of the reconstructed object

perpendicular to the tilt axis and to the viewing direction at 0°. An elongation factor e_x has been defined by Radermacher and Hoppe [134]:

$$e_x = \sqrt{\frac{\alpha + \sin\alpha\cos\alpha}{\alpha - \sin\alpha\cos\alpha}}. \tag{2.13}$$

The index x marks the direction of the elongation in a Cartesian object space if y is the direction of the tilt axis and z the viewing direction at 0°. These experimental limitations are regarded in available algorithms to reconstruct the 3D volume of the object.

3D reconstruction algorithms

Fourier based algorithms have been applied in the first electron tomography reconstructions [1, 135]. Fourier methods appear to be naturally suited due to their relationship to the Radon transform [131]. The electron micrographs are assumed to be projections. Then, the 2D Fourier transform of the micrograph corresponds to a central slice through the 3D Fourier transform of the object. These prerequisites are described by Crowther *et al.* [133] and are since known as the "projection requirement" or the "central slice theorem". Hence, the procedure is based on the sampling of the 3D Fourier space from 2D Fourier transforms of micrographs taken along different directions. The gaps in Fourier space have to be interpolated [133, 136]. Finally, the object reconstruction is the inverse 3D Fourier transform.

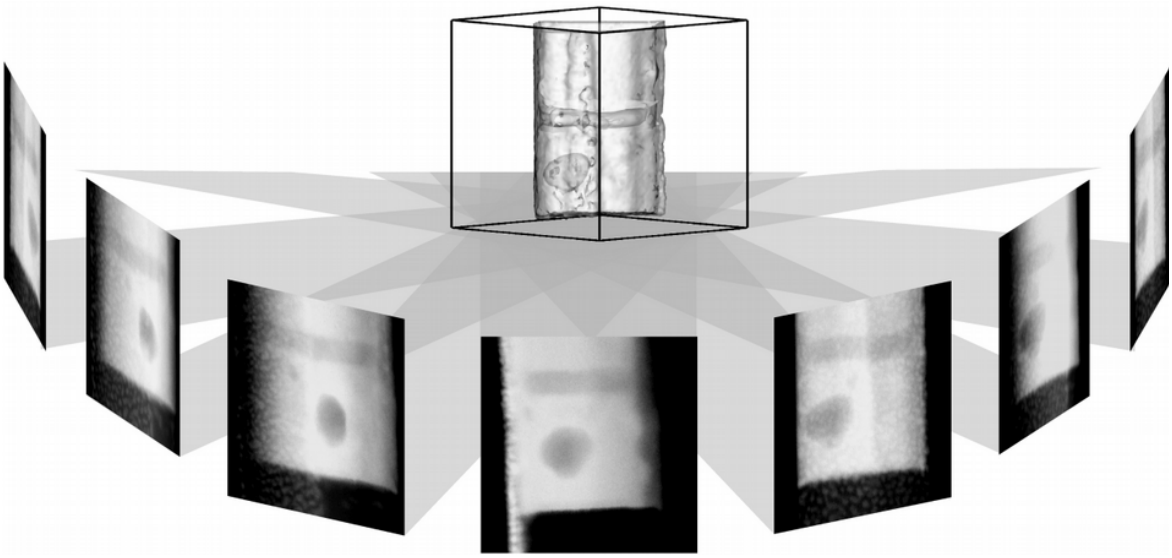

Figure 2.13. The back-projection of the image intensity into the reconstruction volume (centre)

Alternatively, there is a couple of direct reconstruction methods that operate exclusively in real space. The initial back-projection method goes back to the work of Hart [137]. Figure 2.13 illustrates the principle where a series of aligned images is arranged around the reconstruction volume of the object. The image points with their intensity values are continued as rays into the volume along the respective directions of the image orientation. The superposition of rays from all images in the object volume represents the back-projection

reconstruction. A backlash of this direct method occurs due to the oversampling of low spatial frequencies. They cause a blurring of the reconstruction (see, e.g., [7]). The blurring is suppressed by a weighting function that enhances high spatial frequencies. The resulting weighted back-projection (WBP) is a combination of a direct and Fourier method because the weighting function is applied in Fourier space [138].

Beside the widely spread WBP, the direct method of the simultaneous iterative reconstruction technique (SIRT) has been routinely applied since computation capacity has not been a limitation anymore [13]. The SIRT has been introduced by Gilbert [139]. It is shortly described following the authors proposal of the additive variant. The case of an image series acquired about one single tilt axis is assumed. Here, the volume reconstruction is decomposed into a 2D problem as depicted in figure 2.12. Slices perpendicular to the tilt axis are calculated according to equation 2.14 from line intensities $I(\theta, p)$ of the respective images.

$$f_{ij}^{q+1} = max\left[f_{ij}^{q} + \frac{\sum I_{\theta p}}{\sum L_{\theta p}} - \frac{\sum R_{\theta p}^{q}}{\sum N_{\theta p}}, 0\right] \tag{2.14}$$

f_{ij}^{q} is assigned to the q^{th} iteration of the reconstructed object function. The replacement of (x, y) by the integers i and j is owed to the discrete sampling of the experiment. The discrete coordinates of pixels in the projections are θ and p. The object addressed by i and j in one slice of the 3D object is called a voxel instead of pixel. The reprojection of the q^{th} object iteration is R^q. $L_{\theta p}$ is the length of the ray through the reconstruction volume and $N_{\theta p}$ the number of voxels along this path. $I_{\theta p}$ and $R_{\theta p}^{q}$ are weighted by $L_{\theta p}$ and $N_{\theta p}$, respectively. The sums are calculated over all rays that intersect the reconstruction point (i, j). The expression $max[..., 0]$ represents the preliminary knowledge that the object function is positive which is not exploited by the Fourier method [139]. In the original proposal of the SIRT, f^0 is set to the mean value of I. The usage of an initial reconstruction (e.g. a back-projection) instead of the mean intensity accelerates the convergence of the SIRT algorithm. Gilbert [139] have pointed out that the SIRT algorithm passes a minimum for the similarity of the original projection and the reprojections and diverges afterwards. Mostly, 10 to 15 iterations are sufficient to achieve the minimum.

The alternative iterative algorithm of the algebraic reconstruction technique (ART) which has been proposed beforehand [140], is mentioned for completeness. It is less robust against projection errors than the SIRT algorithm [139]. Regarding the Fourier method, the SIRT reaches a better reliability of reconstructed features in case of a limited tilt range or coarse tilt steps. With respect to the WBP, the SIRT results are less noisy [7, 37]. On the other hand, the introduction of further preliminary knowledge possibly prefers other algorithms than the SIRT. Atomically resolved electron tomograms present impressive examples. Atomic resolution has been demonstrated by Scott *et al.* [27] and Chen *et al.* [28] who utilize equal slope tomography, and by Aert *et al.* [25] and Goris *et al.* [26] who describe an algorithm based on compressive sensing. The former reconstruction method comprises a Fourier approach [141]. The latter exploits the sparsity of atoms in the reconstructed volume and requires only a view projections along low indexed zone axes [28]. Both methods exceed the resolution limit given by equation 2.12.

Visualization and segmentation

The visualization as well as the analysis of 3D data, i.e. the output of the reconstruction algorithms, requires an adequate representation. One possibility is the decomposition of the reconstructed volume in a suite of 2D slices which is well known from clinical computed tomography. These slices are easily displayed on a screen, sheet or any planar surface. They show different grey values of the tomogram voxels that are intersected. Distances and shapes are conveniently accessed in the plane of the slices. Here, the 3D notion of the object is lost. In order to evoke a spatial impression for the observer, the object of interest needs some surface which reflects a virtual light source and creates shadows. In addition, the perspective of some frame, e.g. the edges of a cube, support the notion of three-dimensionality (see central image in figure 2.13). The definition of representative surfaces is attempted by the selection of a single grey value (isosurface representation) or by the semitransparent representation of several grey values that are colour coded. The semitransparency provides an insight into the reconstruction volume and allows to grasp the spatial arrangement of objects. In general, different perspectives onto the volume are needed. Printed on paper, a choice of images is needed. Of course, the live manipulation of the object on a computer screen is easier and more instructive in order to establish a 3D notion.

The evaluation and representation of tomograms with weak contrasts or with a high noise level necessitates alternative ways to highlight objects contained in the volume. The process of object isolation within the 3D data is called segmentation. In biological data sets, the manual segmentation is often indispensable to outline the objects of interest [142]. In materials sciences, rare examples are found (e.g. [143]). The procedure is carried out in slice images where contours are pasted along traces of the object. This task is extremely laborious and, hence, motivates alternative approaches. An automated segmentation is, for instance, realized with the discrete algebraic reconstruction procedure (DART) [144, 145]. The prior knowledge of the number of different, homogeneous phases in the object is included in the algorithm. The number of grey values in the reconstruction is limited and the segmentation is inherently done.

3. Experimental realization

This chapter is dedicated to the experimental realization of the electron tomography investigations. The first section deals with challenges of the specimen preparation by FIB. It is outlined that different scientific questions require adapted strategies to tackle respective challenges. The second section describes the selection of appropriate STEM imaging modes for the acquisition of tilt series of micrographs. The aspects of specimen thickness and crystallographic orientation are emphasized.

3.1. Case specific sample preparation by FIB

The SEM/FIB dual-beam microscope is outlined as indispensable tool for the preparation of specimens suited for electron tomography. The JIB4501 at the PDI is applied for the specimen fabrication except for one example for which the predecessor, the JIB 4500, is used. In this section, procedures and strategies are presented and discussed that meet the specific requirements of different tomography experiments. The versatility of the FIB based preparation allows to adapt the three key characteristics of the specimen for the cases studied in this work. Firstly, the size and the shape are controlled to enable the transmission of electrons through the material over a specimen tilt range as high as possible. Secondly, the local resolution permits the isolation of selected targets within the specimen. Finally, the flexibility of the sample stage provides the possibility to align specific crystallographic orientations with respect to the tilt axis of the TEM tomography sample holder. The necessity to carefully regard these three aspects and to modify the preparation a posteriori to initial tilt series acquisitions is emphasized throughout the following sections.

The demand for a protective layer on top of the prospective lamella is described in section 2.2.1. Several attempts for the preparation of tomography specimens have to be undertaken due to the moderate success rate. Therefore, it is found to be more efficient to deposit an initial protective layer on the whole sample with a carbon coater (model CC7650 - Quorum Technologies Ltd.) instead of the local electron beam induced carbon deposition. Afterwards, the fast growth of a carbon stripe with the FIB is immediately started. Besides, the whole sample is protected against surface damages caused by FIB imaging. The higher penetration depth of the electron beam is sufficient to still reveal objects buried below the initial protective carbon coating with a layer thickness of up to 100 nm. Calculations with the TRIM software package [146] show that the 30 kV Ga^+-ions have an accumulation peak at 23 nm depth in carbon.

Amorphous carbon is advantageous for electron tomography due to its low atomic number $Z_C = 6$. Residual protective material around the material of interest hardly reduces the maximal specimen thickness which can penetrated by the electron beam. This aspect becomes particularly clear in the case of ensembles of free-standing 3D objects that have to be embedded in protective carbon. Consequently, carbon is preferred over the usual deposit

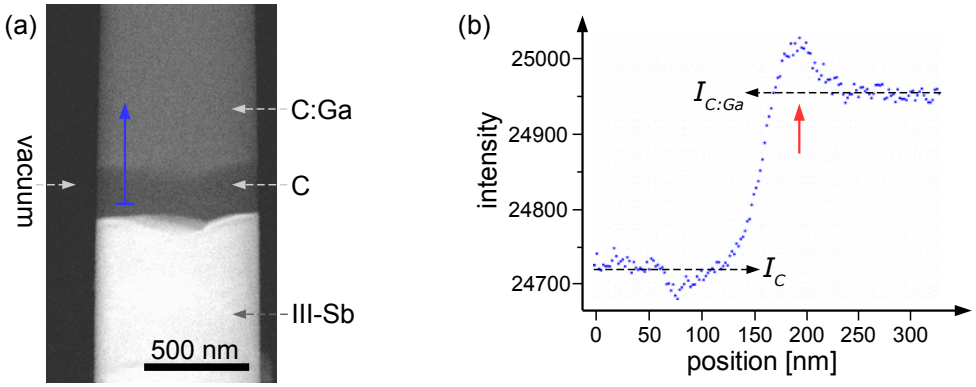

Figure 3.1. The estimate of the Ga content in the protective C layer is based on the HAADF image (a). An intensity line scan is displayed in (b) according to the position marked by the blue arrow.

material platinum which would obscure details or would severely limit the maximal specimen thickness. Thermally evaporated carbon is expected to form a layer of pure carbon. But the Ga-ion beam assisted deposition from phenanthrene leads to the incorporation of Ga. The quantitative evaluation of the HAADF image in figure 3.1 allows to judge whether the resulting effective atomic number Z_{eff} is significantly higher than Z_C. The image in figure 3.1(a) shows the cross-section of a III-Sb layer stack with the deposited carbon layers on top. A clear contrast between the thermally evaporated carbon C and the FIB deposited carbon C:Ga is observed. The blue arrow marks the position of the line plot shown in figure 3.1(b). Intensity values from pure carbon I_C and from Ga contaminated carbon $I_{C:Ga}$ layers are the actual digital readouts. The dark signal from the detector I_{dark} is measured in absence of the sample, i.e. in the vacuum ($I_{dark} = 24430$). It causes an intensity offset over the whole image. The specimen thickness along the line plot is expected to be constant. The red arrow indicates an intensity maximum which is related to the Bragg-peak of the stopping power. Accelerated ions loose kinetic energy during the interaction with the irradiated solid until they come to rest. The accumulation in a specific depth occurs due to the highest energy loss at low kinetic energies [90].

The intensity I in the HAADF image is related to the atomic number Z by a power law [121]:

$$I \propto Z^{1.8}. \tag{3.1}$$

The exponent is specific for the applied collection angle range of 80 mrad to 210 mrad. The consideration of intensity ratios circumvents the dependence of the absolute intensity on imaging parameters, e.g. beam current and dwell time. The measured values have to be corrected by I_{dark} as described by Rosenauer *et al.* [147]. An effective atomic number Z_{eff} is obtained with respect to the intensity due to pure carbon I_C.

$$\frac{I_{C:Ga} - I_{dark}}{I_C - I_{dark}} = \left(\frac{Z_{eff}}{Z_C}\right)^{1.8} \tag{3.2}$$

The measurement yields $Z_{eff} = 8.3$ which is only slightly higher than the value for pure carbon and remarkably smaller than the expected value of Ga. Therefore, the FIB deposited carbon is regarded as suitable for the embedment of 3D structures that are composed of GaN.

In addition to equation 3.1, the actual HAADF intensity depends on the atomic density and on the specimen thickness. The thickness is constant for both intensity values. Z_{eff} has to be regarded as function of the atomic density. At this point, the work of Igaki *et al.* [148] is mentioned. They have systematically investigated the Ga content in FIB deposited carbon. They have found a Ga concentration of 13% by energy dispersive spectroscopy for carbon deposits that have been grown under comparable conditions.

3.1.1. Needle-shaped specimens for tomography

Ideally, a data set for a tomographic investigation comprises projections of the specimen from a tilt over 180°. Therefore, it is intended to manufacture a specimen that is sufficiently thin for electron transmission in all viewing directions reached by the goniometer rotation from −90° to 90°. Beyond, a constant thickness facilitates (S)TEM contrast interpretation and, eventually, the 3D evaluation of the tomogram. The ideal specimen has the shape of a cylinder. Of course, the needle-shaped specimen has to contain the object of interest. The isolation of a 3D defect by the FIB-based preparation is illustrated in figure 3.2. An initial lamella is prepared by the lift-out method (see section 2.2.1 and [103]) and mounted on the specimen post for the tomography sample holder. The lamella is looked upon after an initial polishing step with Ga ions at 30 kV in the STEM. The specimen thickness is approximately 400 nm at this stage. Figure 3.2(b) shows a part of a BF STEM image revealing the 3D defect. The distance of the object toward the lamella edges is determined. The intermediate STEM imaging is indispensable because the object is embedded in the dense GaSb layer and cannot be observed in the SEM. Afterwards the lamella is trimmed to a needle as depicted in figure 3.2(c). Depending on the target size of the object and the specimen, it is advised to iteratively repeat the position control by STEM imaging as done in this example. The BF STEM image of the final specimen is displayed in figure 3.2(d). The diameter is estimated to be 150 nm. The actual shape of the needle cross-section is discussed in section 4.1.2.2.

It is worth to discuss improvements to the described preparation procedure. The visibility of the target object in the SEM or, alternatively, markers created at the lamella surface would avoid the time consuming, repeated position control with the STEM. Hernández-Saz *et al.* [95] proposed a series of FIB milled dots as markers below the layer of interest. The damage of the substrate below the object of interest is regarded as critical because it is expected to cause a bending of the final needle-shaped sample. The inclusion of FIB deposited tungsten markers within the protective C layer is used in later attempts instead. The marker dimension is similar to the proposal of Hernández-Saz *et al.* [95]. The usage of markers allows in any case a more reliable position control than the mere measurement of distances to the lamella edges that vanish during trimming. The stability of the ion optics is crucial for the position control independent of the discussed target preparation strategies. First experiments including the preparation presented in figure 3.2 are carried out with the predecessor SEM/FIB device of the JIB4501, namely the JIB4500. Beam shifts during the fine polishing steps with FIB - especially at low accelerating voltages - cause a loss of position control at the required resolution of approximately 10 nm. Eventually, a very low success rate has to be accepted as a consequence.

Beside the exact site-specific preparation, the damage layer at the specimen surface has to be considered. The final machining with Ga^+-ions at accelerating voltages of 3 kV to

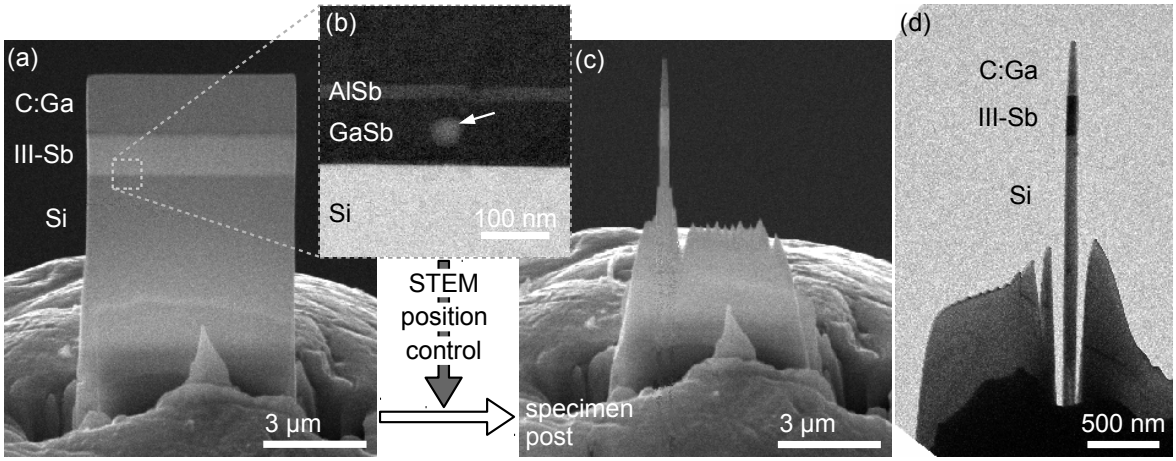

Figure 3.2. (a) SEM image of a TEM lamella mounted onto a tomography specimen post. (b) BF STEM image: The buried object of interest is located in the STEM. (c) The lamella is cropped in order to confine the 3D defect within a needle-shaped specimen. (d) BF STEM image of the prepared specimen for the tomographic investigation.

5 kV is applied throughout the presented tomography experiments. These conditions reduce the amorphised damage layer to only several nanometres [94, 95]. On the other hand, a residual amount of Ga is implanted deeper into the crystalline material [88]. Therefore, a final polishing step with Ar ions at low accelerating voltages is suggested. Inoue *et al.* [34] have finalized a needle-shaped GaAs specimen with an embedded InAs quantum dot with 500 V Ar^+-ions. In fact, this is a promising strategy which, nevertheless, has to be carefully adapted to the respective task.

Initial results are presented in figure 3.3. The precision ion polishing system (PIPS) from Gatan Inc. is applied for the Ar^+-ion milling at 500 V. An adapter to mount the tomography specimen post in the PIPS has been manufactured by the mechanical workshop of PDI. It is shown in figure 3.3(a) along with the schematic arrangement of the Ar^+-ion guns toward the specimen. The impact angle α_{imp} can be varied from $-10°$ to $10°$. Figures 3.3(b) and (c) show (S)TEM micrographs of needle-shaped III-Sb stacks on a vicinal Si(001) substrate. The phase contrast image in figure 3.3(b) presents the needle edge at the transition from the substrate to the epitaxial layer at atomic resolution. An 8 nm thick amorphised layer on Si substrate is observed. The GaSb appears to sputter preferentially compared to the substrate. The problem of material dependent sputter yields occurs between different antimonide layers, too. Figure 3.3(c) illustrates this aspect for the comparison of GaSb, AlSb and In(As,Sb) (QWs). A higher α_{imp} suppresses this problem which also occurs during FIB milling [98]. The surface roughening of homogeneous material as seen in figure 3.3(c) at the GaSb buffer layer imposes a further limitation to the Ar^+-ion polishing. It is mentioned that a similar roughening happens after Ar plasma treatment of a Si needle using the Solarus plasma cleaner (Gatan Inc.).The latter procedure is claimed to remove FIB sample preparation damage in the case of Y:ZrO_2 and MgB_2 by Hata *et al.* [149].

Consequently, a final polishing with Ar^+-ions is regarded as valuable step to remove a Ga containing, amorphised damage layer on the specimen. The application under the described conditions for the final trimming step is not recommended. Hence, the intended size and

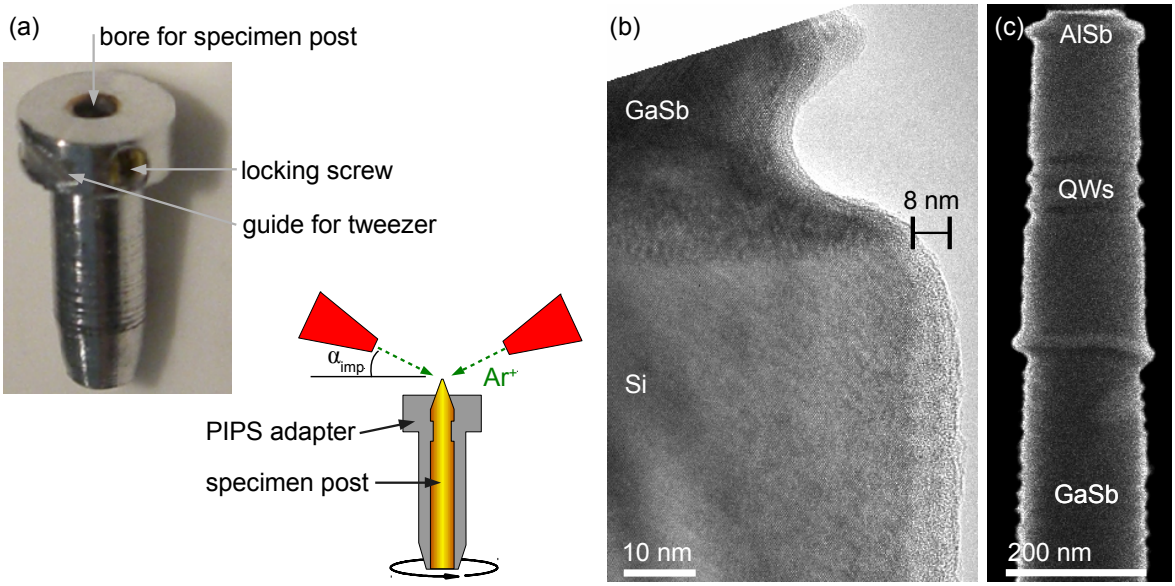

Figure 3.3. (a) An adapter for the Gatan PIPS allows to mount tomography specimen posts. The schematic illustrates the geometry during the sputter process. Ion guns (red) with impact angle α_{imp}. A needle-shaped specimen is imaged that has been refined by Ar ion polishing at 0.5 kV: (b) The HRTEM image is acquired near the interface between GaSb and Si along a <110> direction. (c) The ADF STEM image of the III-Sb layer stack depicts the silhouette of the needle-shaped specimen.

shape of the specimen has to be defined during FIB preparation at accelerating voltages as small as possible.

3.1.2. Alignment of an in-plane direction with the tomography tilt axis

Isolation of an interface

The sample preparation for the 3D investigation of interface features must regard the size of relevant features. Zhong *et al.* [37] studied the chemical roughness of buried interfaces in a ZrO_2/In_2O_3 layer stack where the topography is studied over an area of approximately 1800 nm^2. This example fits well into a needle-shaped specimen with the interface plane perpendicular to the tilt axis. Here, the presented case aims at the investigation of several buried AlSb islands at the interface between the Si substrate and the GaSb buffer layer. The area of interest is about one order of magnitude larger and does not match to the previous specimen geometry.

The alignment of the III-Sb/Si interface parallel to the tilt axis is required to tackle the new task. (Details about the sample structure are given in section A.1). Figure 3.4 illustrates the modified preparation of a needle-shaped specimen. The sample is vertically inserted into the microscope chamber. The FIB is orthogonally directed onto the sample edge. The bird's eye view by the SEM is shown in figure 3.4(a). It displays the cross-section of the sample. The surface appears under a shallow incidence angle as well but is out of foucus due to the fastly increasing depth. The white dashed line emphasizes the shape of the lift-out lamella. The black dashed line marks the shape of the prospective needle-shaped specimen. The lamella from the cross-section is mounted to a tomography specimen post as depicted in the SEM

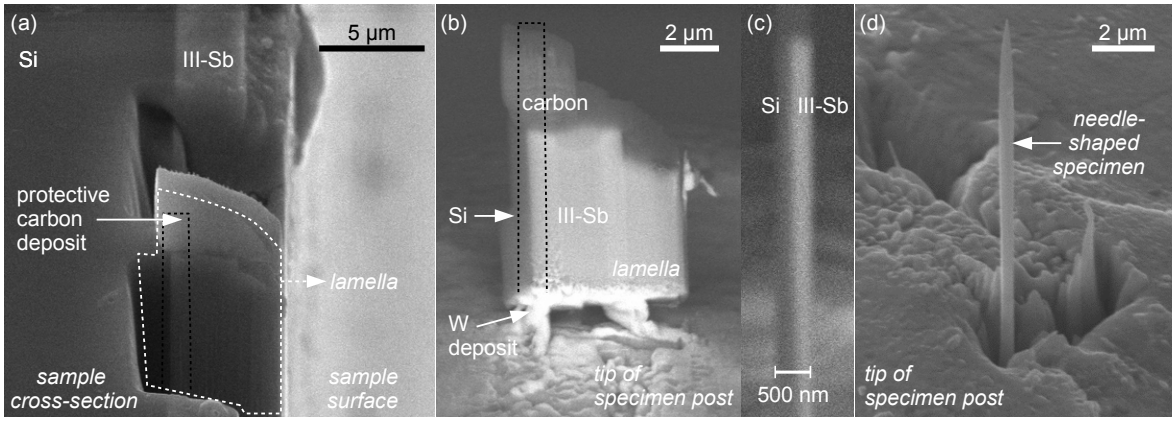

Figure 3.4. The SEM images illustrate the fabrication of a needle-shaped specimen parallel to the interface. (a) The SE image of the sample cross-section in the left part and the glancing view along the sample surface (right) is captured in a bird's eye view. (b-c) The atomic number sensitive BSE images enable the control of the interface position at 20 keV acceleration energy. (c) The last possible check of the progress before reducing the acceleration voltage for the FIB and the SEM. (d) The final specimen milled at 3 kV exhibits a sharp tip.

BSE image in figure 3.4(b). The chemical sensitivity of the BSE signal allows to distinguish between the Si substrate and the GaSb buffer layer. Hence, it allows to control the position of the milling areas during the transform to a needle-shaped specimen as demonstrated in figure 3.4(c). The SE SEM image of the final preparation result is presented in figure 3.4(d). The specimen tip is very sharp after the final FIB milling at 3 kV which has completely consumed the protective carbon deposit. In this case, the loss of the deposit during the final polishing step is not regarded as drawback because the objects of interest are situated along the whole needle and not only below the surface.

Alignment of the [1$\bar{1}$0] orientation to the tilt axis

A more demanding task requires the alignment of a defined crystallographic orientation to the tilt axis. The parallel alignment of a $\langle 110 \rangle$ direction and the tilt axis turns out to be necessary after initial tomography experiments exploiting diffraction contrast (cf. section 3.2.3). In fact, this requirement is met by a refinement of the procedure to isolate an interface. First of all, the target direction has to be identified and to be correctly oriented. Beyond, a large, plane-parallel lamella is needed because objects of interest stretch over the whole III-Sb stack thickness (cf. section A.1). Furthermore, the targeted lateral scale does not fit into a needle prepared along the growth direction either.

Figure 3.5(a) shows the SE SEM view onto the edge of a piece of sample. One sample corner and a perpendicular edge are observed in the right image part. Si exhibits two distinct cleavage planes which are easily told apart. These planes are of {110} and {111} type [150]. An aluminium cube manufactured by the PDI mechanical workshop is used as aid for the sample orientation. The two schematic cubes in the centre of figure 3.5 describe its application. They are depicted as a dice with its common pips to facilitate the spatial notion. The piece of sample is fixed with its (1$\bar{1}$0) cleavage plane parallel to a cube edge. In the presented case, the miscut direction is successfully guessed from the inclination of the

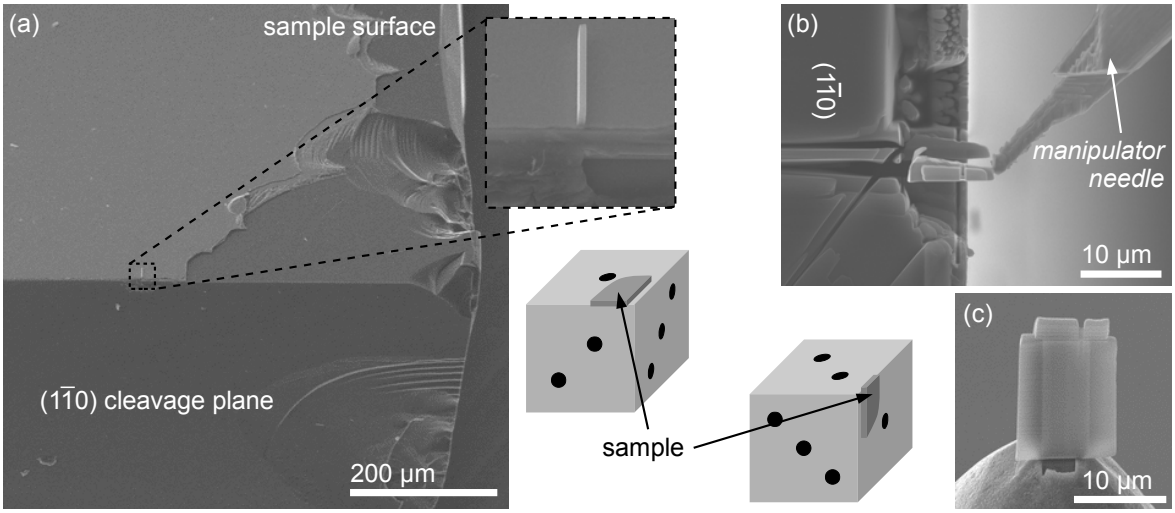

Figure 3.5. The alignment of the [1$\bar{1}$0] direction with the tilt axis for the tomographic data acquisition relies on the recognition and orientation of crystallographic directions. (a) The cleavage plane facilitates this task. A cubic aid allows to precisely orient the cleavage plane toward the ion beam direction. A lamella is lifted out from the aligned sample cross-section (b) and mounted on the tomography specimen post (c).

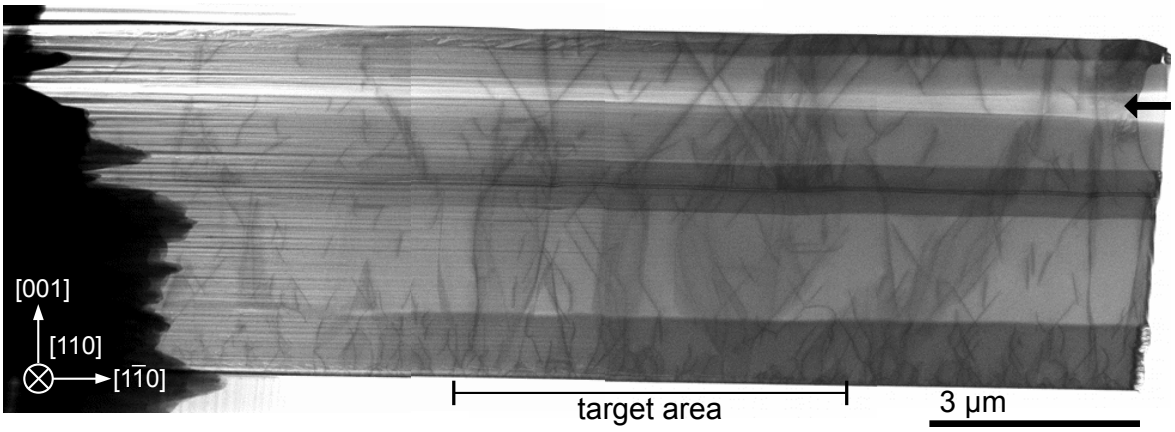

Figure 3.6. An overview of the TEM lamella as montage of four BF STEM images. The brightness and contrast level of single images is adapted to match at adjacent micrographs. Dark contrast lines reflect the presence of defects. The black arrow marks the result of a misplaced milling area (see text).

cleavage planes toward the sample surface. If the wrong side is chosen, the targeted direction will deviate from the tilt axis by the miscut angle. At first, the sample surface is mounted perpendicular to the ion beam in order to deposit a protective carbon stripe as shown in the inset of figure 3.5(a). Trenches to shape a lamella are milled in this orientation, too. Afterwards, the "dice" is reoriented to perform a precise tilt by 90°. In that way, the [1$\bar{1}$0] direction points upward and the sample is viewed along the lamella direction and parallel to the interface as shown in figure 3.5(b). A second protective deposit is applied on the cross-section before the lamella is glued to the manipulator needle. Figure 3.5(c) shows the lamella mounted onto a tomography specimen post. The small notch at the top is caused by a misplaced milling area and has to be considered later on. The final thinning of the lamella

is carried out in the direction perpendicular to the layer stack in order to avoid preferential sputtering. The specimen post is mounted horizontally for this purpose.

Figure 3.6 presents a bright-field STEM image of the whole lamella that has been prepared for the tomographic investigation. It is not the final status before the tilt series acquisition. A further polishing step has been applied. The image is composed of 4 single recordings in order to cover the full length of 15 µm. The black ragged edge in the left marks the bottom side which is attached to the sample post. The lamella has initially been thinned with the Ga^+-ion beam directed from the right which is indicated by the residual "curtaining" next to the bottom. The bright band in the upper image part (bold arrow) shows the effect of the erroneously positioned milling area. There, the lamella possesses a smaller thickness. The fine polishing steps have been carried out in the orthogonal direction removing the former curtaining within the target area. The chemical information about the different antimonide layers is contained in the BF STEM image beside the desired diffraction contrast from line defects. The Si substrate is located at the lower image edge and appears white due to the contrast settings. The stacking sequence of the sample is described in section A.1. It is remarkable that the surface quality influences the visibility of the layer structure as observed in the comparison of the right and left image parts.

3.1.3. Target preparation of an inclined nanocolumn

This section treats the most demanding FIB specimen preparation for a tomographic investigation. The low-dimensional GaN based heterostructures which are described in section A.2, have to be isolated and oriented with their preferential growth direction to the tilt axis of the goniometer. The indispensability of a tomographic approach is highlighted in figure 3.7. An idealized highly symmetric shape of a hexagonal nanocolumn is shown in the sketches. The inclusion of In on different facets can be studied by standard cross-sectional samples as long as a highly symmetric surface justifies the consideration of projections from one low-indexed direction (cf., e.g., [151–153]). The schemes in figure 3.7(a) and (b) illustrate such a situation for core-shell nanocolumns with a hexagonal symmetry that grow epitaxially on a substrate with a high symmetry surface orientation. A plan-view specimen reveals the layer structure on facets in the [0001] zone which is outlined in the right of figure 3.7(a). The section perpendicular to a side facet allows to analyse the layer sequence grown on the side walls as well as on the top and pyramidal facets which is demonstrated in figure 3.7(b). Here, this case corresponds to one of the $\langle 11\bar{2}0 \rangle$ zone axes. In contrast, this does not work for the perpendicular orientation which provides a $\langle 1\bar{1}00 \rangle$ viewing direction. The layers then lie inclined toward the imaging direction. The presented sample exhibits the less symmetric $(11\bar{2}2)$ surface and nanocolumns that grow along the [0001] direction, i.e. inclined toward the surface normal. This arrangement is schematically illustrated in figure 3.7(c). Standard cross-sectional samples result in specimen foils perpendicular to the surface. Accessible zone axes are the unfavourable $[1\bar{1}00]$ and the high indexed $[\bar{1}\bar{1}23]$ direction. The actual morphology of the nanocolumns is unknown and the analysis of projection images requires assumptions on the habit similar to the idealized representations in figure 3.7.

As a consequence of this geometrical situation, conventional TEM projections are insufficient to characterize the abundance of In in (In,Ga)N layers on different facets. Therefore, a method is described in the following that enables the analysis of the nanocolumns' morphol-

ogy and the In content on different facets. The presented strategy comprises the orientation and isolation of the target nanocolumn which is described in this section, and the data acquisition for electron tomography which is discussed in the subsequent sections. The strategy commences with the adaptation of sample preparation by FIB with respect to the requirements of electron tomography. The faced challenges are grouped in requirements imposed by the tomography experiment and such imposed by the treatment of the material system with Ga^+-ions. At this point, it has to be emphasized that the presented procedure of sample preparation works at the limit of the used Ga^+-ion based dual beam device.

The first group defines the aspired orientation of the sample at the tomography pin. The rotation around the surface normal $\vec{n}$ for the acquisition of the tilt series is not feasible. The thickness that electrons have to penetrate, would be too high if the nanocolumns (diameter of circa 180 nm) are imaged along the $[\bar{1}\bar{1}23]$ direction. Beyond, the highest material contrast between (In,Ga)N layers and GaN is realized by looking approximately parallel to the $\{1\bar{1}00\}$ planes. The distinct contrast improves the tomographic results by means of SNR. Consequently, the nanocolumn axis, i.e. the [0001] direction, is ideally aligned with the tilt axis to view all $\langle 11\bar{2}0\rangle$ and $\langle 1\bar{1}00\rangle$ directions.

The second group deals with the interaction characteristics of the charged Ga^+-ion beam with GaN and Al_2O_3. The latter material is an isolator and charges up which impedes the position control of the milling area or disables imaging at all. The former material is prone to heavily recrystallize and/or redeposit when etched by the Ga^+-ion beam (cf. section 2.2.1). In the following, the different steps of the successful preparation are described.

In a first step, the whole sample is coated with thermally evaporated carbon to protect the surface against ion beam damage like in the former examples of antimonide samples. In addition, the carbon layer improves the conductivity of the surface. Afterwards, carbon is deposited by GIS-FIB in two distinct directions. The inset in figure 3.8(a) schematically illustrates the two deposited carbon stripes. The one labelled "A" offers the common protection against ion beam damage during the lift-out procedure. The one labelled "B" is aligned with the preferential growth direction of the nanocolumns. Later on, it serves as protection during machining the sample along the direction that is adapted to the sample geometry. Figure 3.8(a) shows the SEM view onto the sample surface after both steps of carbon deposition. A major optimization of the lift-out procedure concerns the processing of GaN with

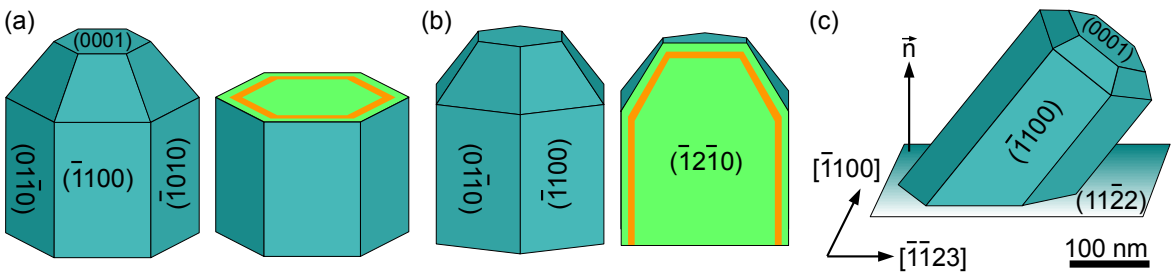

Figure 3.7. The schematic depicts hexagonal GaN nanocolumns that grow along the high symmetric [0001] direction. If this direction is aligned with the sample surface normal, conventional TEM plan-view (a) and cross-sectional specimens (b) provide information about layers inserted on the bounding facets (orange). (c) The inclined growth of nanocolumns complicates the access to this information.

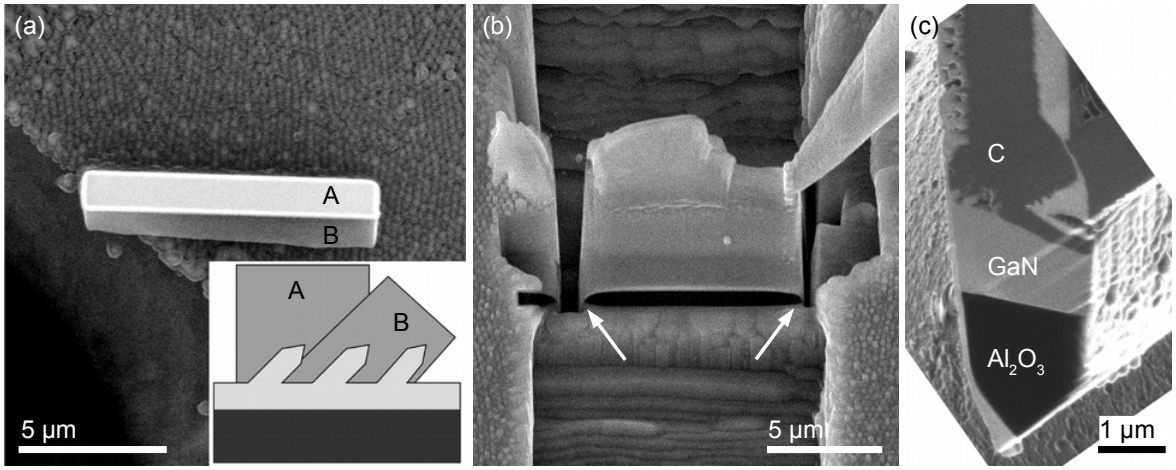

Figure 3.8. (a) The SEM image shows two protective carbon layers A and B. The inset schematically demonstrates the arrangement of the layers with respect to the nanocolumn orientation. (b) SEM image: The lamella glued to the manipulator needle/tip is cut free except for two spots (arrows) where GaN is redeposited. (c) The FIB scan over the ion beam polished cross-section of the lamella reveals the chemical structure of the sample with the Al_2O_3 substrate, the GaN template with the GaN based nanocolumns on top and the protective carbon layer. The occurrence of redeposited GaN is described in the text.

an Ga^+-ion beam. Figure 3.8(b) presents a more than 2 µm thick lamella immediately before the removal from the sample. The large thickness is owed to the size of nanocolumns projected along the $[\bar{1}\bar{1}23]$ direction. The manipulator needle is attached and slits to detach the lamella are cut. Two arrows mark regrown GaN at the lower trench which has been cut first. This reconnection impedes the lift-out. The pronounced tendency of GaN redeposition or recrystallization in the vicinity of a milling area is underlined by figure 3.8(c) and by figure 2.7. The former image is recorded from the polished lamella's cross-section with the FIB. It highlights the chemical structure. In contrast to the polished area, the remaining lamella surface (oblique view, right image part) is covered with a rough layer. The insulating Al_2O_3 appears black due to the positive charging by Ga^+-ions and the consequent reduction of the secondary electron signal. The carbon deposition appears in dark grey and is embedded in GaN represented in light grey. The left rim of the Al_2O_3 substrate evidences a coverage with GaN, too. Obviously, the left side of the lamella has been opposite to the side from which the final trench has been applied. Hence, the reconnection of the lamella with the substrate has to be prevented. Here, the generous and "iterative" cutting of trenches solves the problem. Iterative means, the sample has to be rotated by 180° for several times in order to successively establish the bottom cut to free the lamella from both sides under 52°. In that way, the symmetric Al_2O_3 wedge at the bottom of figure 3.8(c) is established. The initial trenches to define the lamella are created equally deep for this procedure. It is noticed that the low sputter yield of Al_2O_3 limits the attainable depth of the trenches or the lamella height, respectively. Finally, the GaN redeposition gives a further reason to thoroughly embed the GaN nanocolumns in carbon. It prevents the random growth of GaN crystallites at the nanocolumns surface. In figure 3.8(c), the inclined nanocolumns on top of the GaN template are visible. Voids have remained during carbon embedment. The successful coverage of the low-dimensional objects only works where the distance between nanocolumns is suf-

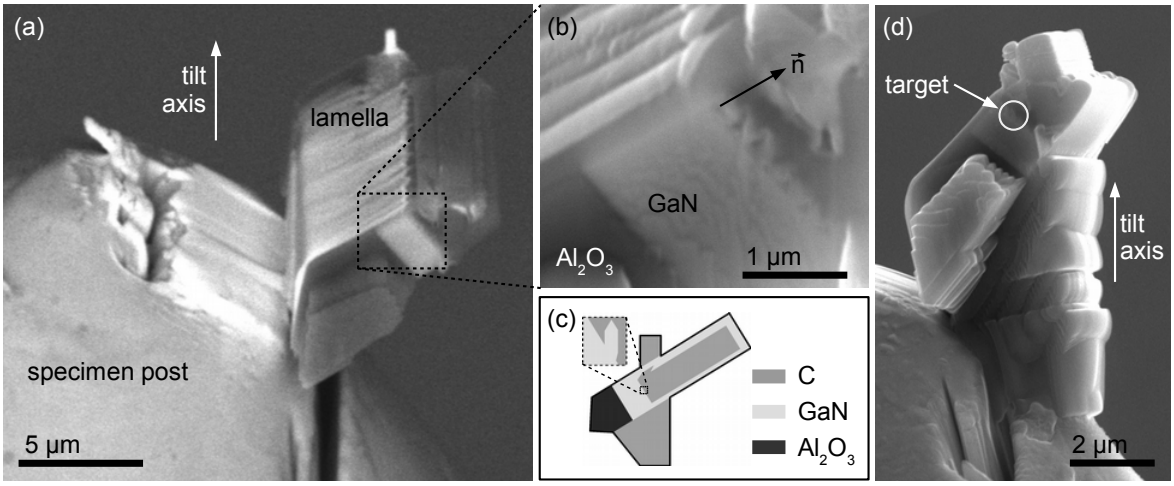

Figure 3.9. (a) SEM BSE image of the attached raw lamella and (b) a magnified extract showing the aligned nanocolumns in polished cross-section of the lamella. The BSE signal is sensitive to the chemical composition. (c) The sketch of the lamella cross-section with the correct nanocolumn alignment points to the need for a further carbon deposition as filling material. (d) The final raw lamella with the carbon filling is imaged by secondary electron SEM.

ficiently large. Later experiments have been carried out with an embedment of nanocolumns in liquid epoxy and the subsequent bake-out. This way is promising for ordered arrays of nanocolumns with a homogeneous morphology. Of course, the visibility of nanocolumns in the FIB or electron microscope is impeded. The consequent loss of local control is unacceptable for the presented sample of inclined nanocolumns.

The lamella is attached to the tomography sample holder post (figure 3.9(a)) under the maximal stage tilt angle of 54°. The chemically sensitive BSE SEM view in figure 3.9(a) and (b) show the lamella after tilting back to 0°. The nanocolumns are nearly aligned with the axis of the specimen post as shown in the enlarged cross-section of the lamella in figure 3.9(b). In fact, a tilt of 4.4° is missing. This aspect is discussed later in section 5.1. The SEM views in figures 3.9(a) and (b) are actually bird's eye views, i.e. only the projection of the specimen post axis is found vertically in the images. The schematic in figure 3.9(c) depicts the situation with the vertical axis orientation within the image plane. The illustration of the chemical composition demonstrates a further step before isolating the target object in the final specimen shape. The hollow wedge below the region of interest in the direction of the later tilt axis has to be filled to support the final specimen. The post is turned *ex situ* by 90° to access this wedge for carbon deposition. The result is shown in figure 3.9(d). This step will be unnecessary if a lamella is cut in the final direction from the very beginning of the preparation. The corresponding attempt has not been successful due to the redeposition of GaN. In contrast, this strategy works well for low "correction" angles. For instance, the alignment of the low-indexed [001] axis with the tilt axis for tomography is carried out for the vicinal Si(001) substrates (4° miscut) which are faced in the preceding sections.

The raw lamella with its carbon support is reduced to a 280 nm thick and 1.3 µm wide lamella. The isolation of a target nanocolumn in a needle has not been attempted although it might be very helpful. The simple reason is the balance between success rate and the limited possibility to reach the necessary position refinement in the FIB-SEM to separate

the too close nanocolumns. On the other hand, the periodic arrangement of SAG objects facilitates the targeting because positions of nanocolumns can be guessed. At this point it has to be remarked that a FEG-SEM integrated in the dual-beam system would offer enhanced capabilities to localize target objects.

This last example of specimen preparation highlights the versatile and unique capabilities of the FIB-SEM instrument. It provides the access to the characterization of more and more complex 3D structures at the nanoscale. Probably, a dedicated operator will be needed in future to assemble necessary experience and to be equipped with an adequate amount of time.

3.2. Tilt series acquisition for tomographic reconstructions

The TEM/STEM experiments are performed at the JEOL electron microscope 2100F of the PDI. The machine is equipped with a field emission electron source and it is operated at an acceleration voltage of 200 kV. A BF and ADF STEM detector and a CCD camera are attached for image recording. TEM and STEM provide a vast choice of imaging modes. In order to select an adequate signal for electron tomography, the applicability of imaging modes must be carefully considered with regard to the complete tilt series. Crucial questions concern the signal dependence on sample thickness and crystallographic orientation. Moreover, the knowledge on the orientation is needed for the evaluation of tomograms. The following section deals with the exploitation of specimen orientation. Afterwards, the conditions for the acquisition of a tilt series applying the HAADF signal are evaluated. The last section is dedicated to BF STEM imaging for electron tomography using the strain contrast around dislocation lines.

3.2.1. Crystallographic orientation of the tomogram

The assignment of crystallographic orientations to the tomogram requires a preceding determination of the viewing directions. Figure 3.10 demonstrates the procedure to obtain corresponding information. The SAD pattern of the specimen is used to estimate the deviation from a low indexed zone axis at perpendicular tilt angles. The centre of the Laue circle (CLC) is observed on the fluorescent screen of the TEM. For demonstration, a recorded diffraction pattern is shown in figure 3.10(a). The presented example originates from a needle shaped specimen. The superposition of Si and III-Sb spots is apparent. Spots with like indices are deflected under a higher Bragg angle for Si which has got the smaller lattice constant. The experimental data is compared to the calculated diffraction pattern in figure 3.10(b). The JEMS software package [154] enables the superposition of two patterns and to respect a tilt away from a low indexed zone. In that way, the deviation from the [110]

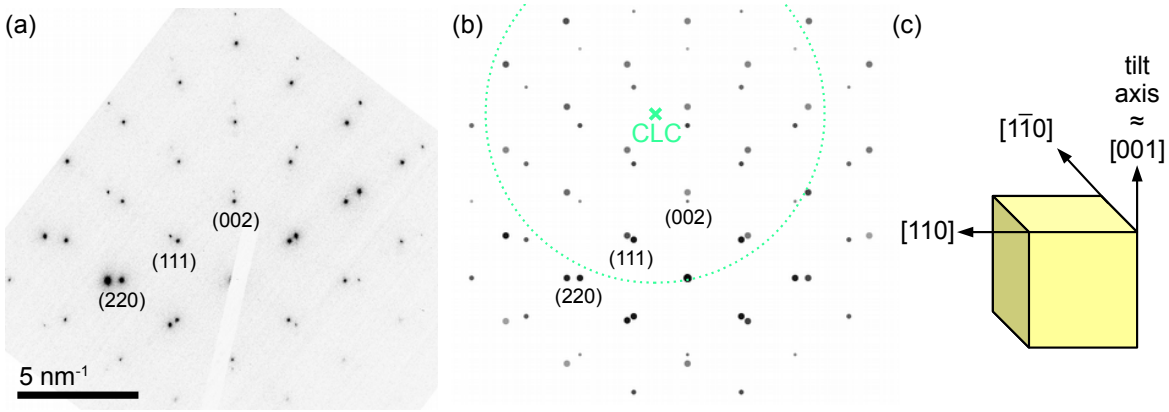

Figure 3.10. (a) The SAD pattern (inverted grey scale) of a needle shaped specimen shows the superposition of substrate and layer diffraction spots. The corresponding goniometer tilt angle α is required for the later allocation of crystallographic directions to the reconstructed volume which is schematically depicted in (c). (b) The comparison to a calculated diffraction pattern allows to estimate the deviation to the closest low indexed zone. For this, the position of the CLC must be observed.

direction is estimated to be smaller than 1°. Finally, the direction along the tilt axis needs to be evaluated. In the presented case, the deviation of the [001] direction from the tilt axis is found to be nearly 1°. Applying these information, crystallographic directions are assigned to the edges of the reconstructed volume which initially possesses a tetragonal form. The result is schematically depicted in figure 3.10(c). In fact, the precision of the needle orientation is limited by the accuracy during FIB sample preparation. In the following, small deviations of 1° and less are not explicitly indicated in subsequent figures for simplicity. The tomography sample holder (Fischione Model 2050 [155]) is manually tilted to approach a low indexed zone as close as possible while the nominal microscope goniometer tilt angle remains at 0°. In addition to the ±90° goniometer tilt capability, the single axis holder allows a manual, continuous rotation over 360°. An exact alignment of a crystallographic orientation and the tilt axis for tomographic data acquisition would require a triple axis holder in order to compensate the limited accuracy by the FIB lift-out technique.

3.2.2. Meeting the projection requirement

The HAADF STEM signal has been identified as suitable choice for transmission electron tomography in materials science [7]. In fact, the monotony of the intensity as a function of the sample thickness exhibits a limited validity. Figure 3.11 presents HAADF STEM images of a wedge shaped lamella. The images are recorded with the ADF detector at different camera lengths resulting in the variation of the collection angle ranges. The displayed detection angles are nominal values from the manufacturer's manual [119]. A specimen with a wedge angle of 15° has been prepared with the FIB. Hence, the thickness t along the beam direction is determined from the distance x to the edge by $t = x \cdot \sin 15°$. The specimen exhibits the cross-section of the laser structure grown with a thick GaSb buffer layer on Si(111) (sample D, see section A.1). Intensity plots are extracted from each micrograph along the marked arrows and displayed beneath the respective image. The red graphs belong to Si, the blue ones to GaSb and the green ones to the protective carbon deposit C:Ga. The intensity originating from GaSb passes a maximum at the thickness of 400 nm in the case of the smallest detection angles. That means, a contrast inversion occurs and the demand for monotony is not fulfilled. At the same time, the graphs of Si and C:Ga remain monotonic. But they intersect each other which does not happen for higher collection angles. In the middle micrograph of figure 3.11, the lighter element curves are approximately linear and the Si intensity remains higher than the one of the deposited layer. The GaSb signal stays monotonic until 0.7 µm thickness. At the highest collection angles, all three materials present an approximately linear behaviour with thickness. The decreasing intensity at high scattering angles is qualitatively explained by the Rutherford atomic scattering factor [3]. Leaving the dwell time of the scanning probe constant, the reduced intensity at high collection angles results in worse signal to noise level.

The selection of adequate imaging conditions for HAADF STEM tomography has to respect the experimentally obtained relations from figure 3.11. In principal, the highest collection angles ensure the monotonic intensity variation with thickness as well as with the atomic number Z. In practice, the smallest possible collection angle is chosen because noise deteriorates the tomographic results. In the case of GaSb, the selection of the ADF collection angle range 60 mrad to 160 mrad for a thickness below 400 nm. Furthermore, the acquisition

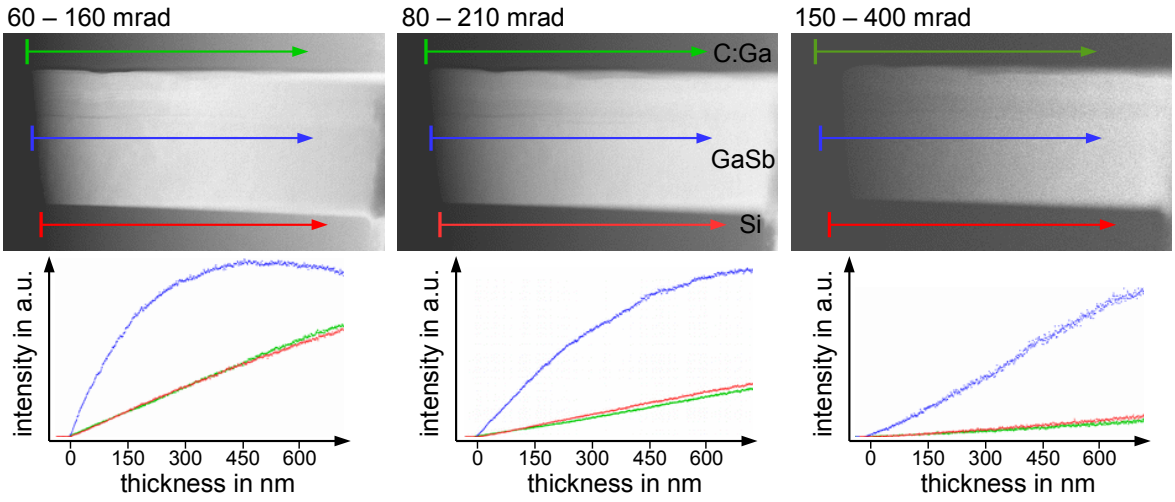

Figure 3.11. The wedge-shaped cross-section specimen of sample D helps to identify suitable imaging conditions for the tilt series acquisition using the STEM HAADF imaging mode. The relation between intensity and specimen thickness as well as intensity and average atomic number is presented as intensity line profiles. Images are acquired with the specimen not aligned to a zone axis.

time of a single image should be as short as possible to reduce image disturbances due to experimental instabilities, e.g. stage drift or magnetic stray fields.

If the cupping artefact [156] has to be avoided, the requirements will be even stricter. The signal has to be linear over the whole thickness range of interest. The decreasing slope of the intensity results in an underestimation of Z in the centre of thick objects. Linearity will also be necessary for all present materials if phases of different Z have to be distinguished, i.e. the intersection of graphs must not occur within the targeted thickness range. Consequently, the measurements according to figure 3.11 suggest that a three-dimensional, element sensitive analysis of a HAADF tilt series requires a careful consideration of the physical signal characteristic and the instrumental detection conditions. The collection angle has to be adjusted to the elemental composition of the material and the specimen thickness. Finally, it has to be underlined that the investigation of compact and crystalline high Z materials like GaSb is in comparison to, for instance Si, more challenging because of the thickness limitation.

The investigation of compact crystalline material imposes a further challenge. The HAADF intensity arising from a crystal is known to be enhanced for viewing directions along low indexed zone axes. This effect has been attributed to channelling (see, for instance, Cowley and Huang [126]). The effect has been very clearly shown by Yu *et al.* [129] who compared the contrast between amorphous and crystalline Si, i.e. chemically identical material. Crystalline Si tilted off a low-indexed zone axis has appeared even darker than the amorphous part. The simultaneous presence of an amorphous and a crystalline phase of the same material would lead to different grey values in the reconstructed volume in spite of the same atomic number and specimen thickness. The orientation dependent signal intensity of crystalline material implies that the element sensitive analysis of the tomogram requires phases with equal Bravais lattices and an epitaxial alignment. Samples presented in this work meet these requirements.

Assuring the proper imaging conditions, a tilt series of micrographs is acquired. Parameters for the acquisition are provided along with the presented data in chapter 4 and chapter 5. The DigiScan™ II scan generator and the Gatan Microscopy Suite® (GMS) are used for STEM image recording. Images of any tilt series require two processing steps. They have to be laterally aligned in order to exhibit the projection of the tilt axis at the same position in all images. A distinctive object or a marker are extremely beneficial for this task. A further step affects the grey scale of the images. The varying intensity due to orientation dependence necessitates a normalization. The grey scales are shifted to an arithmetic mean intensity. This procedure presumes that the number of atoms in the projected volume is constant which is true as long as the specimen remains in the field of view. The IMOD software package is applied for the image processing [157, 158].

3.2.3. Information beyond the projection requirements: dislocation imaging

Undoubtedly, there is a great interest in the 3D arrangement of line defects. They significantly influence the mechanical and electrical properties of heterostructures. In general, the line direction $\vec{u}$ of a dislocation has to be known in order to determine its character. Assumptions, e.g. about the preferred glide plane, have to be made if $\vec{u}$ is deduced from projections. The situation will become too complex to make such assumptions if defects interact with each other or with planar defects and if non-conservative defect motion is included. The departure from common glide planes occurs in the latter two cases. The spatial relations of defects provide necessary information to understand their mobility and, finally, their behaviour during device operation.

The selection of an adequate TEM/STEM signal for dislocation imaging sensitively depends on the crystal orientation. Therefore, the specimen layout is a posteriori reworked in FIB sample preparation after initial experiments (cf. section 3.1.2). The HAADF STEM signal has been selected to suppress diffraction contrast effects in order to be exclusively sensitive to the average atomic number of the material and to the thickness. On the contrary, the dislocation imaging requires diffraction contrast and, moreover, demands to retain adequate conditions over the whole tilt range. Of course, this situation violates the requirements for the reconstruction algorithms. The consequences will be discussed in section 4.3.1.3.

The first choice for the imaging of dislocations is the weak-beam dark-field (WBDF) TEM technique. It reveals defects as narrow line features with high defect contrast. In fact, Barnard *et al.* [42, 159, 160, 161] have applied this method for the tomographic investigation of dislocations in epitaxial GaN layers. Here, an accurate alignment of the selected diffraction vector with the tilt axis has to be maintained. This precision is hardly guaranteed by mounting the sample with the FIB system. A triple tilt axis sample holder facilitates to meet this requirement as presented by Hata *et al.* [162]. Another drawback of WBDF tomography are dynamical contrast features like thickness and bend contours as well as contrast oscillations along defect lines inclined toward the image plane. They lead to artefacts in the tomogram which obscure details from line defects. The combination of WBDF with the precession of the electron beam has been shown to reduce the dynamical character of the contrast mechanism [45].

Tanaka *et al.* [43, 44] have overcome the challenges of TEM tomography like the WBDF method by applying ADF STEM. Figure 3.12(a) depicts the geometric configuration: The

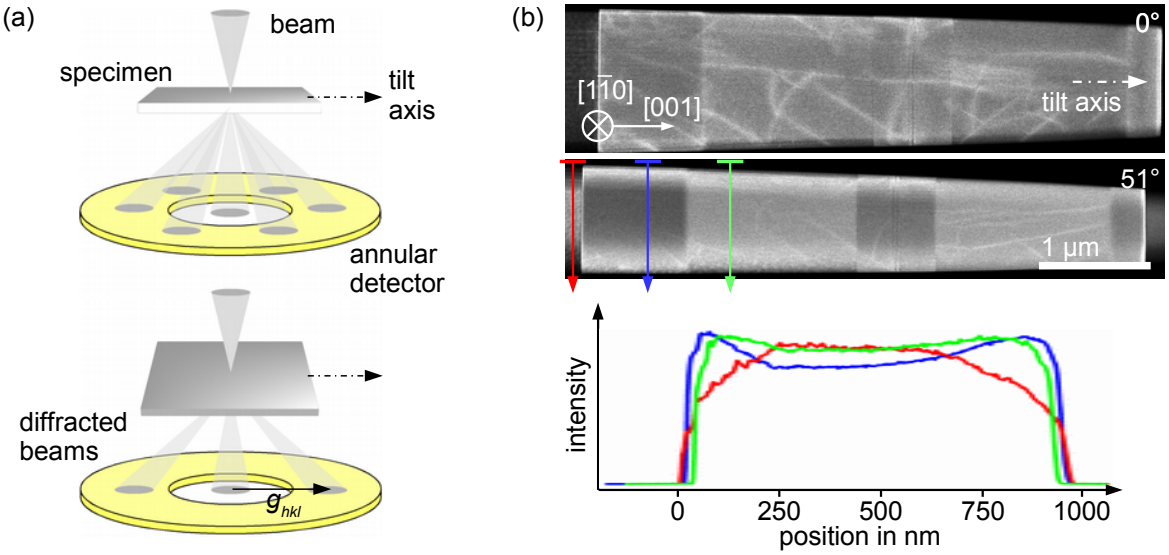

Figure 3.12. (a) ADF STEM detection geometry: A low indexed zone axis of the specimen and the incident beam are aligned in the upper scheme. In the lower one the specimen is tilted away from such a zone axis. (b) ADF STEM images for two different tilt angles: The inversion of contrast is highlighted by the intensity profiles across the lamella.

convergent incident beam is diffracted by the crystalline specimen. The divergent diffracted beams result in diffraction discs in the plane of the annular detector. The upper scheme illustrates the case where the viewing direction is aligned with a low indexed zone axis of the specimen. Many spots are excited. In contrast, the lower scheme presents the usual case at an arbitrary tilt angle with a small number of excited spots. The approximate alignment of the tilt axis with a reflection g_{hkl} that is sensitive to the strain field of the dislocations, ensures defect visibility during the whole tilt series. The orientation requirement of the diffraction vector is less demanding than for WBDF. The divergent beam leads to an averaging over excitation errors in the vicinity of the targeted diffraction spot (see, e.g., [107] 319ff.). By the way, this is the reason for the suppression of contrast features due to dynamical diffraction [107, 161]. Beyond, STEM provides a larger specimen area to be imaged at once which will prove to be necessary in the experiment presented below.

So far, the ADF-signal should be adequate for the tomography of dislocation lines. But the aspect of contrast inversion with thickness which is discussed in section 2.2.2, imposes a further limitation [39]. Figure 3.12(b) shows two ADF STEM images of a 1 µm wide lamella in the [1$\bar{1}$0] orientation and tilted by 51°, respectively. The line scans along the arrows demonstrate the reversal of the contrast with increasing thickness for GaSb and AlGaSb (blue and green line profile, respectively). This example shows the dependence of the intensity-thickness relation from the average atomic number. The maximum intensity has not been exceeded for the silicon substrate (red line profile) in the far left image part, yet. Increasing the collection angle shifts the inversion to higher thicknesses but approaches the high-angle regime where diffraction contrast is strongly attenuated.

Finally, the BF STEM offers a signal that is sensitive to the targeted line defects. It tackles problems due to a changing thickness whether they originate from dynamical diffraction or from absorption. Figure 3.13 presents images from a BF STEM tilt series of the 1 µm wide

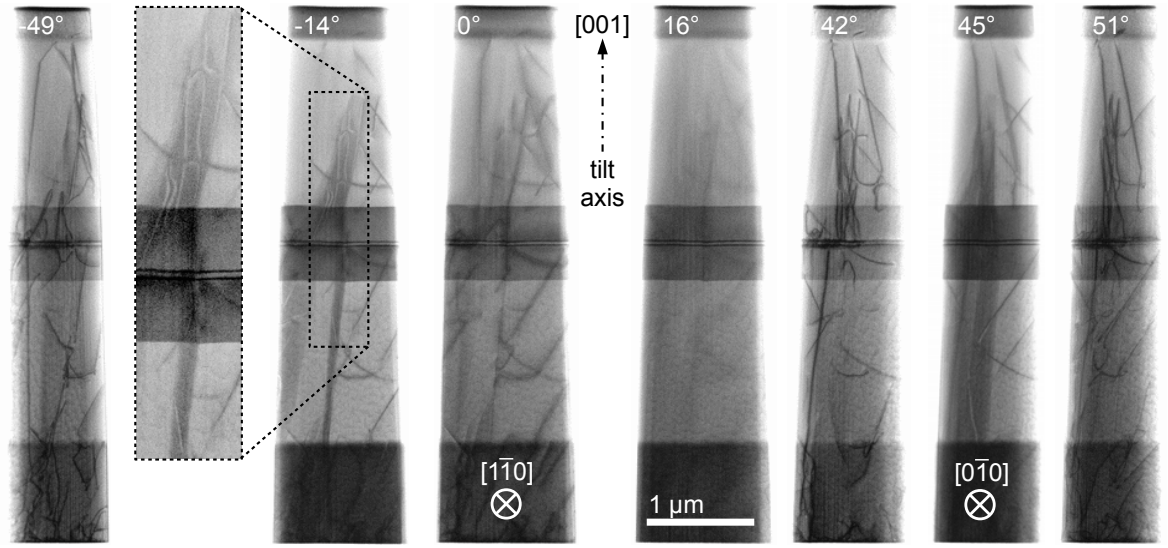

Figure 3.13. The BF STEM images originate from a series taken with the tilt axis nearly parallel to the [001] direction. That way, a systematic row of reflections along g_{002} remains excited over the whole tilt range. The development of contrast features is described in the text.

lamella from figure 3.12. The tilt axis has been approximately aligned with the [001] crystal orientation. The deviation accounts for 1.2° resulting in a precession of the [001] direction around the tilt axis. The whole tilt series includes information on the composition of the layers. An absorptive contribution I_{abs} to the BF STEM intensity I expressed by a simple exponential decay law is expected.

$$I_{abs} = I_0 \exp(-\frac{t}{\lambda}) \tag{3.3}$$

This contribution depends on the material thickness t and a material specific mean free path λ. I_0 is the intensity of the incident beam. Actually, den Broek *et al.* [156] discussed the thickness dependent HAADF intensity based on an exponential intensity decay of the transmitted beam, i.e. as complementary signal to the BF mode. They have assumed to collect the scattered intensity with the ADF detector which approximately holds for several tenths of nanometre thickness depending on the material.

The STEM micrographs acquired at −49°, 42° and 51° provide the desired dislocation contrast with excellent clarity. At 0° features appear slightly blurred. At tilts of −14° and 46° two unwanted incidences occur. Broad dark bands extend within the sample which widen over a certain tilt range. Obviously, they arrive from planar defects that are analysed in section 4.3.1.1. Attempts to three-dimensionally reconstruct these defects have failed. Nevertheless, their detection is, generally, valuable as will be discussed below. The second obstacle is imposed by the reversal of the dislocation line contrast when superimposed with the occurring planar defect. The contrast enhanced inset next to the −14° micrograph emphasizes the contrast inversion. It counteracts the accumulation of intensity at the location of the dislocation in the back-projection volume during the tomographic reconstruction.

Furthermore, at most tilt angles, the dislocation lines are out of contrast or appear blurred

or very faint (see, for instance, the micrograph at 16°). Conclusively, the selected g_{002} diffraction vector has a poor sensitivity for the investigated defects. Presented high contrast cases are assumed to arise due to the excitation of sensitive reflections in the proximity of low indexed zone axes or in higher order Laue zones (HOLZ).

The best condition is realized by the selection of a {220} reflection which has been proven to be sensitive to dislocations with a parallel component of the Burgers vector in silicon [43, 44]. In order to align the tilt axis with the $(2\bar{2}0)$ diffraction vector, the geometry for the FIB sample preparation must be modified (cf. section 3.1.2). The whole prepared specimen is surveyed in a BF STEM image (figure 3.6). A selection of images from the tilt series is shown in figure 4.31. Apparently, this lamella provides access to a much larger sample volume than the rather needle-shaped specimen from figures 3.12 and 3.13. This specimen size matches the scale on which microstructural interactions take place.

4. Reconstruction of 3D-, 2D- and 1D-defects in planar III-Sb heterostructures

This chapter is dedicated to the characterization of epitaxial III-Sb layers grown on vicinal Si(001) substrates by TEM methods with special emphasis on electron tomography. A comprehensive notion of the material system is developed which does justice to the complex microstructure of these heteroepitaxial structures. Firstly, section 4.1 addresses the characterization of a 3D defect that is discovered in the GaSb buffer layer. In section 4.2, the focus is directed to the interface (2D defect) between the Si substrate and the GaSb buffer layer which comprises an AlSb nucleation layer. In third place, section 4.3 dwells on the three-dimensional arrangement of threading dislocations (1D defects) and their interaction planar defects (2D).

4.1. Electron tomography on a nanopore embedded in GaSb

Three-dimensional defects are revealed in the investigation of epitaxial III-Sb heterostructures on Si substrates. The first part of the experimental results presents the identification of the defect type. Afterwards, a single 3D defect isolated in a needle-shaped specimen is regarded. The acquisition of a tilt series and the observation of the defect along the accessed directions are described. Finally, the tomographic analysis of the image series outlines the morphology of the defect under investigation. The subsequent discussion is divided into a part that dwells on the formation of the pore and a part on technical aspects of the experimental performance. Part of the presented results is published in [163].

4.1.1. Experimental results

4.1.1.1. Identification of the 3D defects

At first, the type of the 3D defect is determined preceding the detailed analysis of its morphology. Two experimental approaches are described in the following. The object is recorded in the TEM BF mode as displayed in figure 4.1(a). The image is acquired with the objective lens defocused. Fresnel fringes appear around the target object under these conditions. These contrast oscillations do neither occur at the interface to the Si substrate nor at the boundaries of the AlSb layer. The formation of Fresnel fringes is based on the difference in the mean inner potential of two adjacent materials [3]. Hence, the defect volume contains material that differs significantly from the GaSb host matrix or it is empty. Indeed, the defocus contrast has been applied to reveal voids in thick specimens [164].

A quantitative estimate of the defect content succeeds by the evaluation of HAADF signal intensity. Figure 4.1(b) presents an HAADF image of a needle shaped specimen which allows the observation in orthogonal directions. The intensity profile along the blue line is

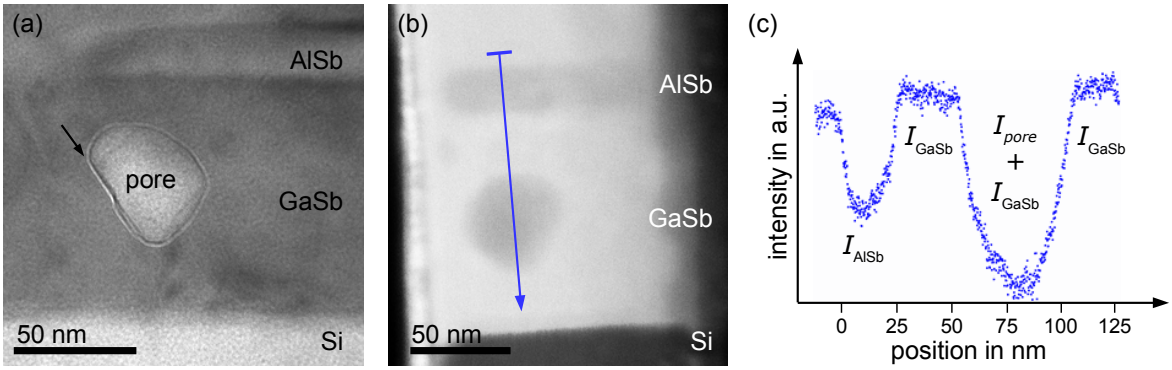

Figure 4.1. (a) The defocused BF TEM image exhibits strong Fresnel contrast around the 3D defect (Fresnel fringes marked by black arrow). (b) The HAADF image taken from a tilt series (cf. figure 4.2) shows Z- and thickness contrast. (c) The intensity profile along the line marked in (b) is displayed.

shown in figure 4.1(c). The origin of the local intensity minima is assigned to the AlSb layer I_{AlSb} and to the overlap of the 3D object (3DO) and GaSb $I_{3DO} + I_{GaSb}$, respectively. The maximal extension of the 3D object along the viewing direction amounts to 50 nm. This value is obtained from the view in the perpendicular direction (cf. figure 4.2). Of course, the total specimen thickness of 150 nm is extracted from this image, too. The following inequations are set up regarding the graph of figure 4.1(c):

$$I_{AlSb}(150\,\mathrm{nm}) < I_{GaSb}(150\,\mathrm{nm}) \tag{4.1}$$

$$I_{3DO}(50\,\mathrm{nm}) + I_{GaSb}(100\,\mathrm{nm}) < I_{AlSb}(150\,\mathrm{nm}). \tag{4.2}$$

The considered thicknesses fall into the linear regime of the HAADF signal intensity (cf. figure 3.11). Therefore, the intensity from both the AlSb layer and the GaSb buffer can be split into

$$I_{III-Sb}(150\,\mathrm{nm}) = I_{III-Sb}(50\,\mathrm{nm}) + I_{III-Sb}(100\,\mathrm{nm}). \tag{4.3}$$

The linearity allows to extend and conclusively transform inequation 4.2 to

$$I_{3DO}(50\,\mathrm{nm}) < I_{AlSb}(50\,\mathrm{nm}). \tag{4.4}$$

Consequently, the average atomic number must be lower than for AlSb according to equation 2.10. The only material with a lower atomic number Z available during growth is pure aluminium. At the growth temperature of more than 500 °C, it will form a crystalline or polycrystalline precipitate. The resulting formation of additional spots in SAD patterns has not been observed. The dissolution of the substrate and subsequent Si migration are excluded because indications of interface instabilities are not observed. Eventually, the 3D object must be vacant or filled by residual gases from the growth chamber. In the following, it is treated and referred to as pore.

4.1.1.2. Tilt series acquisition of an isolated 3D defect

A tilt series of the needle-shaped specimen of sample B (cf. section A.1) is acquired applying the HAADF STEM imaging mode. A selection of images is presented in figure 4.2. The tilts

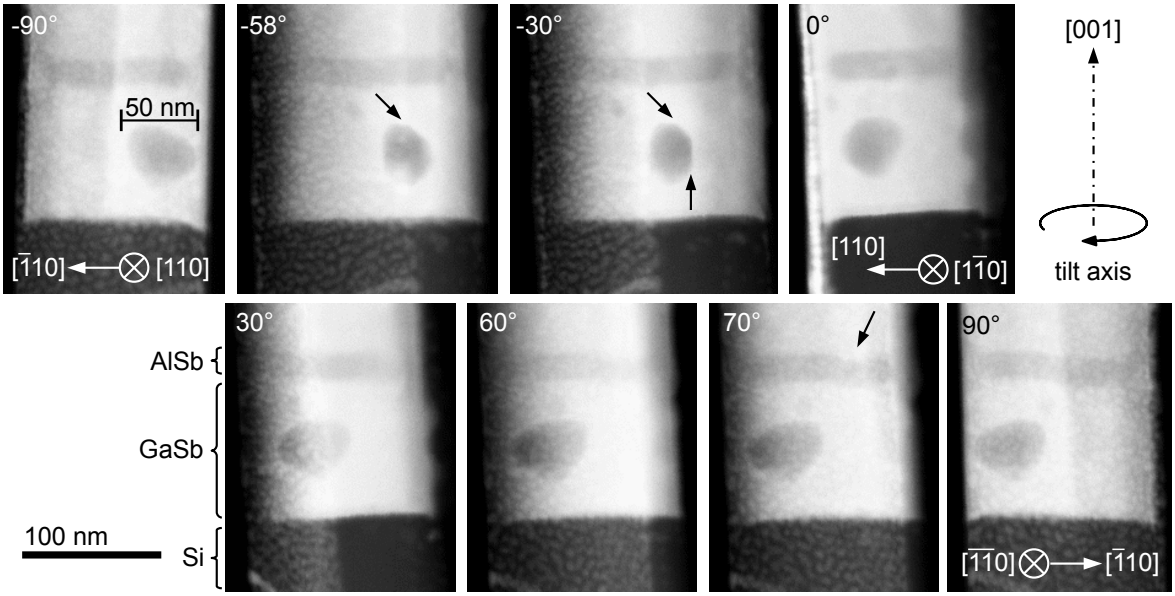

Figure 4.2. The presented micrographs are extracted from an HAADF STEM tilt series. A 3D defect is situated within the GaSb buffer layer that has been grown on a vicinal Si(001) substrate. It is terminated by an AlSb barrier layer. The corresponding tilt angles label the images.

of the goniometer are used as labels in the figure. The tilt about $\pm 90°$ is carried out in steps of 2°. Frames with a size of 2048 x 2048 pixels are acquired using a dwell time of 20 µs at each imaged point which results in an acquisition time of approximately 90 s per frame. The sampling rate is chosen to be 1.3 Å per pixel, that is, the field of view amounts to nearly 270 nm.

The specimen shape deviates remarkably from the intended cylindrical or conical form of a needle which is inferred from the change of the projected diameter. Obviously, the width of the object is larger in the micrograph at −30° than at 0° or 90°. The maximal thickness that must be penetrated by the electron beam reaches 170 nm. A collection angle range of 60 mrad to 160 mrad is regarded as suitable according to figure 3.11.

The [001] direction and the tilt axis are inclined to each other by $(0.8 \pm 0.2)°$. The axis of the needle-like specimen itself exhibits an inclination toward the [001] orientation and precesses on a cone with an opening semiangle of circa 4° around the tilt axis. This aspect is obvious from figure 4.2 where the specimen edge is vertical at $\pm 90°$ and inclined by 4° at 0°. The indication of crystallographic orientations follows vertical and horizontal directions in the images in a good approximation and is applied in the tomographic reconstruction later on.

As prerequisite for the 3D evaluation of the tilt series, the 3D defect appears to be confined within the specimen, that is, effects due to the interaction with the specimen surface are not expected. Furthermore, it is observed that the defect does neither touch the AlSb layer nor the Si substrate. Beyond, valuable hints on the morphology of the spatial defect as well as of the AlSb barrier are obtained. The perpendicular views at −30° and 60° suggest an anisotropic expansion. All together the object of interest appears roundish except for particular views that point to a faceted boundary (black arrows in −30° image). In the

70° micrograph, a discontinuity in the AlSb layer is marked by an arrow. This feature is mostly obscured by a bright vertical band occurring during the tilt series. A damage layer at the (110) surface of the specimen is apparent from the speckle-like contrast features. It is separated from the volume of interest at 0°. The damaged surface overlays an increasing part in the projected image with progressing tilt angle toward ±90°.

4.1.1.3. 3D analysis of the pore shape

In the following, the results of the 3D reconstruction from the HAADF STEM tilt series data (figure 4.2) are presented. The tomogram is calculated with the WBP algorithm from the aligned tilt series. Figure 4.3 shows the isosurface visualization of the reconstructed volume which is cropped to equal sizes in all three orthogonal directions. Colours red, green and blue are used consistently to facilitate the recognition of crystal directions or lattice planes, respectively. The faces of the resulting cube are aligned to the {100} lattice planes of the cubic crystal system. The specimen appears smooth due to binning of the raw data preceding the reconstruction. Besides, objects containing less than 20 voxels are deleted in the representation. The images (a) - (c) are montages of two semitransparent isosurfaces. One represents the outer specimen shape and the pore and the other one is selected to show the AlSb barrier layer. The Si substrate is not visible under the chosen conditions. The semitransparency enables the view into the specimen volume. In contrast, figure 4.3(d) is an opaque isosurface.

A 4° inclination of the interface with respect to the (001) lattice plane is resolved in the

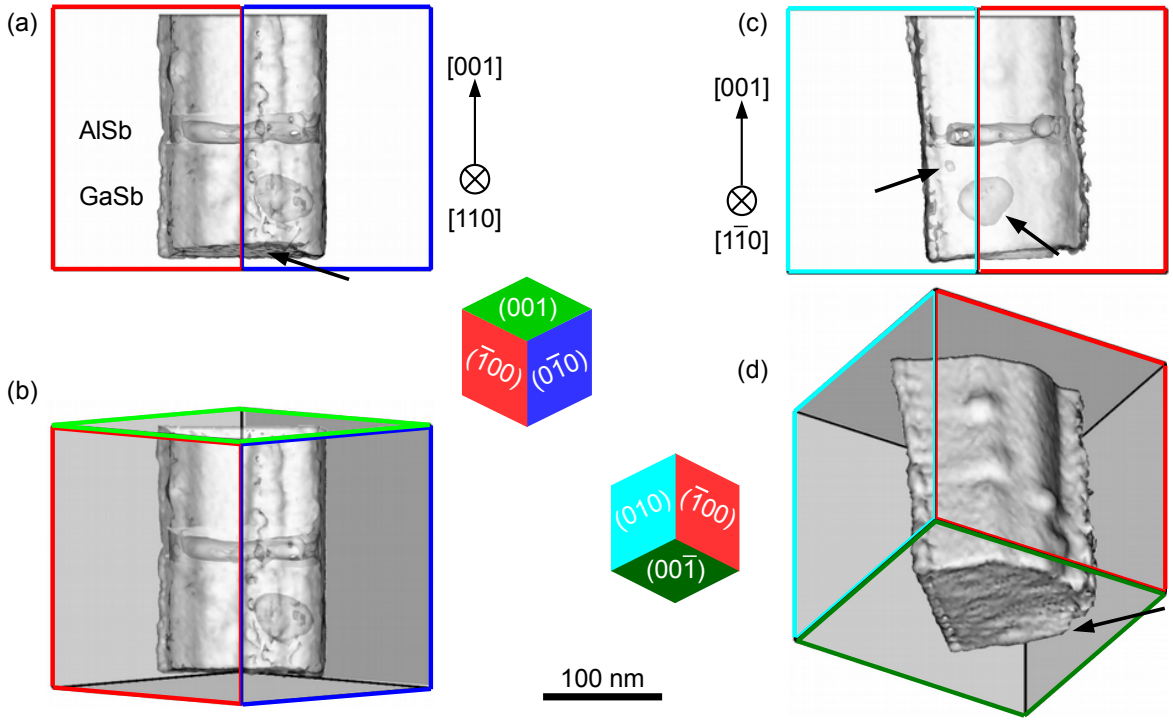

Figure 4.3. The isosurface representation of the reconstructed volume: (a) - (c) The semitransparent visualization of two grey values shows both the pore and AlSb layer within the outer specimen shape. (d) The opaque isosurface depicts the specimen surface morphology.

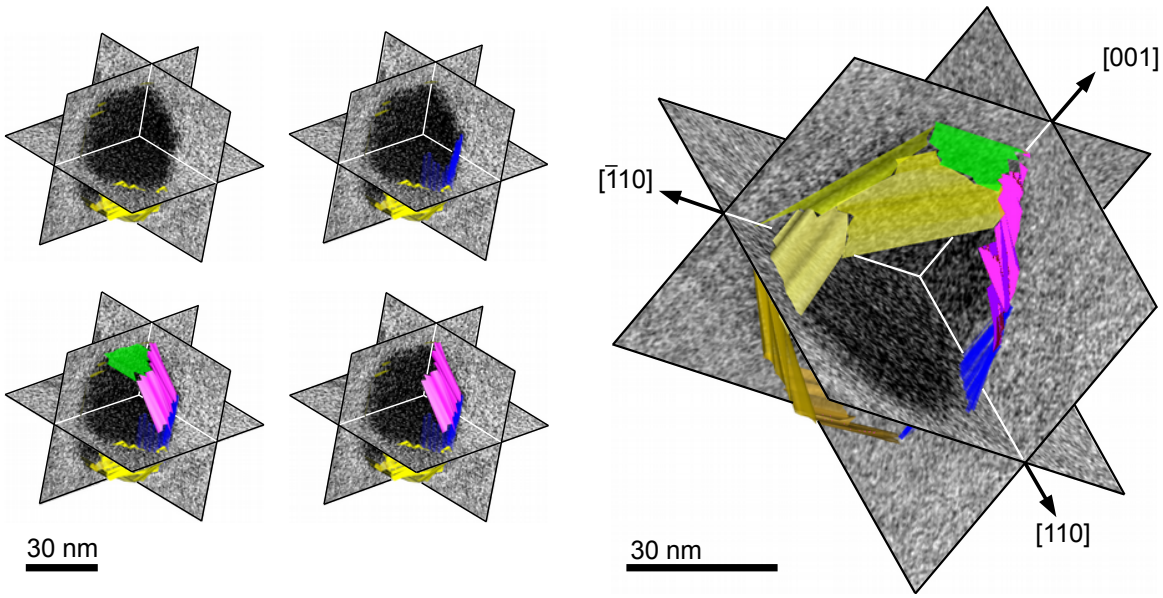

Figure 4.4. The rendering of the pore morphology: Relation of the rendered surface to orthogonal slices through the reconstructed volume. Colours green, pink and blue indicate three facets which are considered in more detail (cf. figure 4.5). Facets in yellow complete the rendered pore.

tomogram (figure 4.3) which complies with the substrate miscut. Figure 4.3(a) shows the view along the [110] direction, i.e. the respective view to the projection at −90° goniometer tilt (cf. figure 4.2). This perspective onto the 3D isosurface provides the view onto the interface to the substrate under a shallow angle (arrow). The tilt of the [001] axis toward the [$\bar{1}\bar{1}$0] direction by 4° in figure 4.3(b) realizes the edge on view of the interface and puts the original substrate normal in the vertical image direction. The angular resolution is demonstrated to be better than 4° with this result.

The view along the [1$\bar{1}$0] orientation in 4.3(c) reveals a smaller pore (upper arrow) with a size of approximately 10 nm. So far, it has been obscured by the speckles of the surface damage on the (110) in both the tilt series. Aware of this feature, the image alignment preceding the reconstruction has been significantly improved for the subsequent analysis. The lower arrow in the figure points at a concavity in the pore surface. The surface of the specimen appears to have a decoration of droplet like objects. Additional to the speckles causing damage layer on the (110) face, big drops at the surface are recognized in figure 4.3(d). The opaque isosurface highlights objects on the specimen surface. Beside the droplets, ridges along the [001] direction are disclosed, for instance at the edge of the (110) plane. The thick ridge in the right of the image explains the bright vertical band occurring throughout the tilt series. The lower arrow points to a ridge that overlays the substrate. Finally, it is apparent that the intended conical or cylindrical form has not been realized.

Figure 4.4 illustrates the generation of a manually rendered model of the pore and its relation to slices through the reconstructed volume. Besides, the illustration conveys a 3D notion of the pore. Three mutually orthogonal slices reflect the grey scale data of the 3D volume. The small images in the left demonstrate the successive addition of rendered facets. The rendering procedure is based on the search and on establishing straight intersection lines

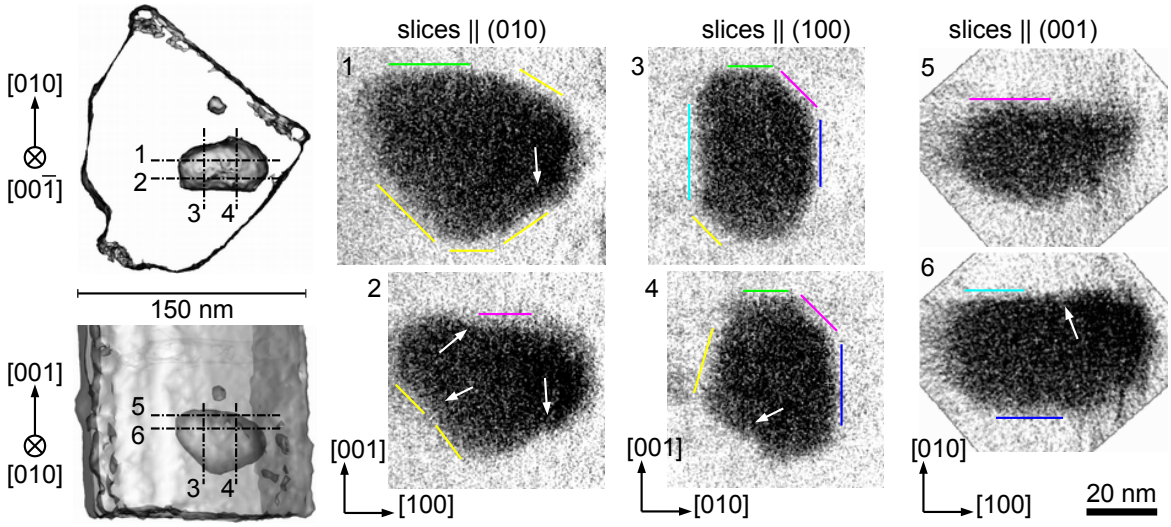

Figure 4.5. Slices parallel to {100} lattice planes are exploited for the determination of facets. The pink, green and blue lines are traces of facets that are explained in detail. The isosurface representation in the left illustrates the location of the slices.

between the slice and a pore facet. The IMOD software package [157, 158] allows to create slices in arbitrary directions. This versatility is beneficial for a careful 3D data evaluation applying this procedure, i.e., slices intersecting perpendicularly through a facet facilitate their determination. Finally, the shape of the pore boundary is predominantly rendered by the model. The large image in the right of figure 4.4 presents the result with three distinct facets in green, pink and blue. These are paradigmatically discussed in more detail while the semitransparent facets in yellow are shown for completeness. The front is left open allowing a look inside and supporting the spatial perception. Parts remaining without rendered surface belong to very small facets or are simply roundish edges. Whether an edge exhibits a nanofaceting or is continuously round, exceeds the resolution capability.

The laborious colouring of the facets is indispensable for the subsequent index determination which is outlined in figure 4.5. The isosurface representations in the left describe the location (dot and dash lines) of the slices shown in the right. Indeed, the [00$\bar{1}$] perspective onto the isosurface is inaccessible during the experiment. It completes the notion about the spatial arrangement of the two pores. The indices ($h\ k\ l$) of the green, pink and blue facets are determined from slices parallel to {001} lattice planes as illustrative example. The slices represent grey values averaged from five subsequent slices in order to improve the signal to noise ratio. The direction of the intersection line $[u_1\ v_1\ w_1]$ between a facet and a slice are deduced with the knowledge about the slice orientation. Obtaining a second, linear independent direction $[u_2\ v_2\ w_2]$ from a further slice allows to calculate the normal to the facet or the indexation of the lattice plane, respectively, by equation B.8. It is hardly possible to allocate intersection lines to a certain facet without the previous tracing and application of colours due to the complex morphology of the pore. The results for the green, blue and pink facet that are comprehensively deduced from figure 4.5, are summarized in table 4.1.

The distinctively developed facets comprise four {100} and two {110} planes. Less pronounced facets like two {111} and several higher indexed ones, i.e. h,k or $l > 1$, are

facet colour	slice ∥ (100) $[u\ v\ w]$	slice ∥ (010) $[u\ v\ w]$	slice ∥ (001) $[u\ v\ w]$	facet $(h\ k\ l)$
green	[010]	[100]		(001)
blue	[001]		[100]	$(0\bar{1}0)$
pink	[011]	[100]	[100]	$(0\bar{1}1)$

Table 4.1. Examples of facet index $(h\ k\ l)$ determination from slices through the 3D reconstructed volume (cf. figure 4.5).

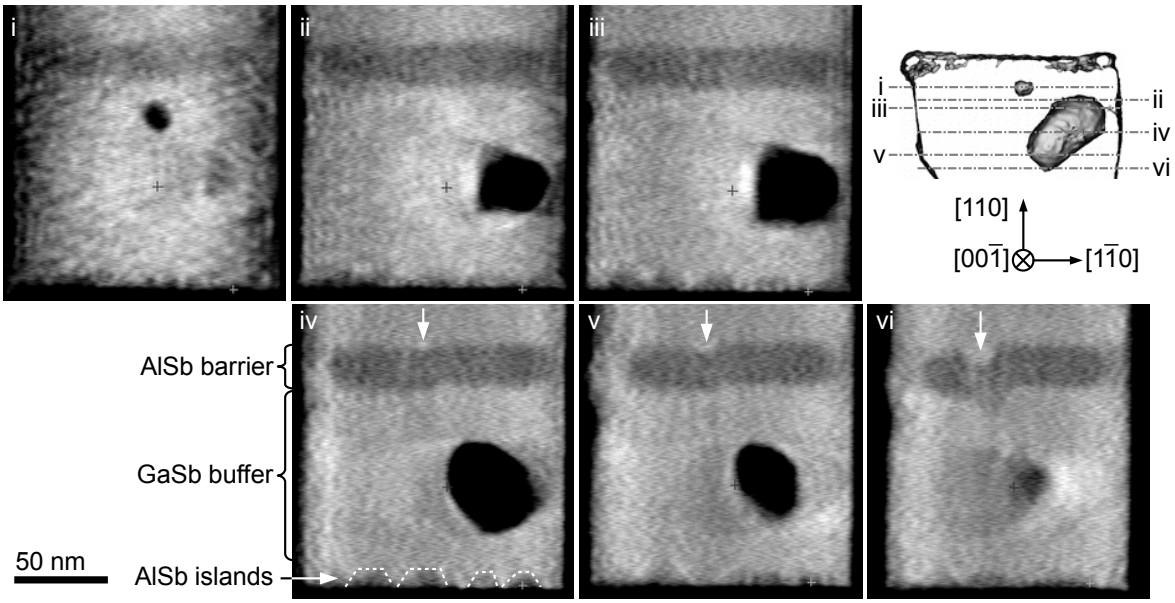

Figure 4.6. Extreme contrast representation of (110) slices through the pore and the AlSb barrier layer. Vertical arrows mark a discontinuity of the barrier layer. The AlSb nucleation layer becomes perceptible at the interface under these contrast settings.

suggested from the analysed data. The reliability decreases with the size of facets. A complicating aspect arises due to concavities mentioned above with respect to the isosurface representation. White arrows in figure 4.5 point at further concave sites which interrupt facets. On the other hand, the absence of GaSb twins as known from SAD observations excludes an erroneous indexation due to the presence of a differently oriented crystal variant. All facets belong to one cubic coordinate system.

Finally, the very limit of information content is exploited. The raw data is binned by 8×8 pixels and the contrast is maximized. The result is shown in figure 4.6. The isosurface presentation in the upper right highlights the positions of slices i - vi. The signal-to-noise (SNR) ratio is apparently increased regarding the slices in figure 4.5. On the other hand, the binning reduces the resolution. In addition to the pore that appears completely in black, information about volumes filled with AlSb are gained. Slices i - iii show a smooth AlSb barrier above the two pores. The other three slices demonstrate the presence of a step or groove (white arrows) in this layer. A small part seems to be downcast. Furthermore, slices

ii - vi reveal the islands of the AlSb wetting layer. These have been marked by dashed lines in slice iv. The last aspect gives rise to the tomographic investigation of the interface between Si substrate and buffer layer including the AlSb islands which is presented in section 4.2.

4.1.2. Discussion

4.1.2.1. Formation of pores in GaSb epilayers

The discussion of the pore formation requires an idea of their localization within the heterostructure stack and a proof that they have not accidentally occurred in the investigated sample. In fact, their presence is unexpected for the intended layer-by-layer grown heterostructure. The following paragraphs address the localization, an idea for a formation mechanism and the implications of the morphological analysis. The experimental findings are discussed according to the publication of the results in [163]. The significance for future growth experiments and the device performance is discussed at the end of section 4.3.

Localization of pores

The occurrence of a pore in the III-Sb heterostructure on vicinal Si(001) which has been recorded in a tilt series (figure 4.2), is not an exemption. All samples listed in table A.1 except for sample F show the emergence of pores. Figure 4.7 presents ADF STEM images of sample cross-sections. Samples A and D have been grown on nominal Si(001) and Si(111) substrates, respectively. The other heterostructures are deposited on vicinal Si(001) wafers. The thickness of the GaSb buffer layer is different for samples A and B and samples C and D, respectively. Sample E presents a different sequence of III-Sb layers. The attention is drawn only to the initial superlattice of AlSb and GaSb layers. All samples presented in figure 4.7 have the presence of an AlSb layer in common. The lateral distribution of pores appears heterogeneous. Their distances among each other vary between less than 100 nm up to the order of 1 µm. On the other hand, their position along the growth direction is common to all samples presented in figure 4.7. Pores occur below the AlSb barrier layer independent of the substrate choice and the GaSb buffer layer thickness. As a consequence, the formation during the coalescence of the initial 3D growth (cf., for instance, [165]) is excluded.

Pores are not observed in sample F which does not exhibit an AlSb layer. Furthermore, the observation of a heterostructure with the same design like samples A, B and C but grown on GaSb(001) does not show pores either in spite of the AlSb layer presence. An additional distinctive feature in the images of figure 4.7 is highlighted for the following discussion. The collection angle of the ADF STEM image of sample C is smaller than in the other cases. The remaining diffraction contrast resulting under the applied imaging conditions (cf. section 3.2.3) reveals microstructural features that are attributed to dislocation lines.

The remarkably rough interfaces and surface of sample D originate from the presence of twins. Twinning is characteristic for the growth of III-Sb on Si(111). Steps at interfaces and the surface of the other three samples are addressed later on in section 4.3.2.1.

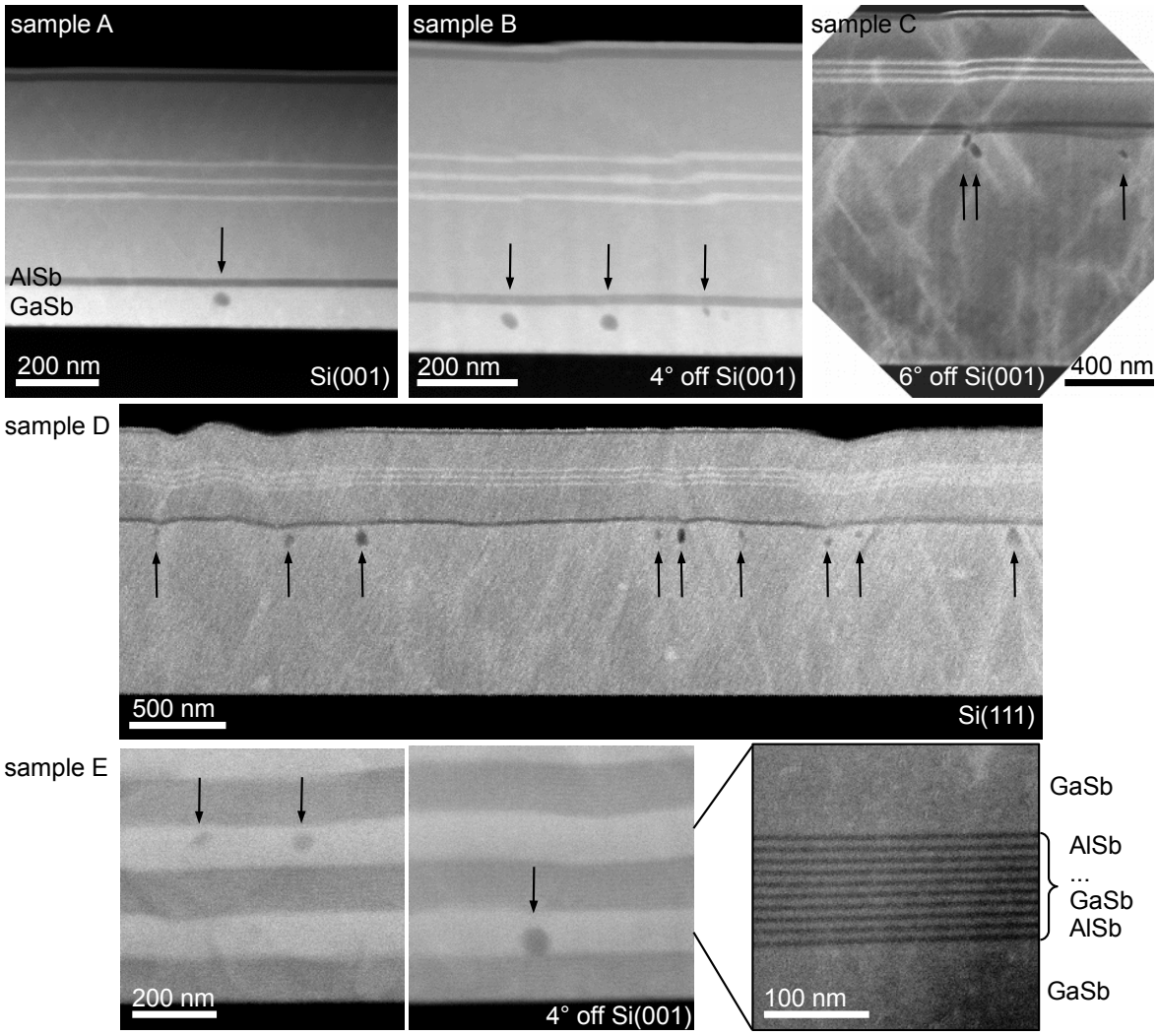

Figure 4.7. HAADF STEM images are captured in order to determine the location of pores in heteroepitaxial III-Sb multilayers. They are grown on nominal Si (001) (sample A) and on vicinal Si(001) with 4° (sample B) and 6° miscut (sample C) toward the [110] direction as well as on Si(111) substrates (sample D). In contrast to the overview images, only the AlSb-GaSb superlattice near the interface to the 4° miscut Si(001) substrate are shown for sample F in the lower row of images. Black arrows mark the pores. The image contrast settings exclusively shows the III-Sb layers while the Si substrate and the protective carbon layers appear in black.

Origin of pores

It is assumed that a significant number of point defects is incorporated into the GaSb layer under the applied Sb-rich MBE growth conditions. Following hypothesis is suggested starting from this assumption. It is schematically depicted in figure 4.8. There is an excess of vacancies that exceed the thermodynamically stable concentration. Hence, there is a driving force that moves the vacancies toward the sample surface in order to annihilate. The diffusion of vacancies precedes slower than the advance of the growth front. The deposition of the AlSb layer presents an obstacle to the vacancy migration toward the surface. Instead of annihilating at the surface, the vacancies accumulate below the AlSb barrier and, eventu-

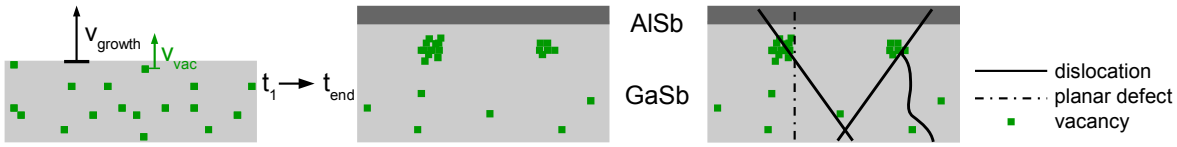

Figure 4.8. The schematics describe a model of pore formation. During GaSb buffer growth (t) excess vacancies are introduced in the epitaxial layer. The vacancies annihilate at the surface in order to establish an equilibrium concentration. The growth front moves faster than the vacancies ($v_{vac} < v_{growth}$). The insertion of an AlSb layer presents an obstacle for vacancies and stops their motion (t_{end}). The vacancies cluster and create voids. the right scheme extends the idea by nucleation sites defined by dislocations and planar defects.

ally, condensate in pores. This final situation is exclusively observed in samples exhibiting an AlSb barrier layer (figure 4.7). Samples with a composition gradient from GaSb to the (Al,Ga)(Sb,As) cladding layer appear free of pores. The disability to pass the AlSb thin film is suggested to have an electrostatic reason. Murarka and Peckerar [166] and Tahini *et al.* [167] have considered charged point defects in semiconductors. A repulsive electrostatic field has to be created. It is speculated that accumulated charges at the AlSb layer which owns the highest band gap of 1.61 eV [55] in the layer stack, are the origin of such a field. The range into the GaSb buffer defines the distance of the pore toward the barrier. The function of the AlSb as barrier to point defects might be beneficial in order to suppress defect motion during operation of the finalized laser device.

A further aspect in the nucleation location of pores is the lateral position. The determination of nucleation sites by dislocations or planar defects is taken into consideration. The left scheme in figure 4.8 presents the respectively extended model. Anticipating the correlation of the step revealed by the tomographic data (figure 4.6) with a planar defect (cf. section 4.3), there is a hint to the coincidence of a pore with a planar defect. The image of sample C in figure 4.7 gives a further hint to the coincidence of pores with dislocations. The absence of pores below the AlSb layer deposited on a homoepitaxially grown GaSb buffer layer which appears widely free of defects, is in agreement with this notion of nucleation sites.

So far, a shortcoming of the presented model has to be pointed out. The consideration of vacancy condensation neglects the fact that the compound semiconductor GaSb consists of two different atom species. Consequently, there are two types of vacancies: V_{Ga} and V_{Sb}. The growth under Sb-rich conditions suggests that the assumed excess vacancies belong to only one type. The nucleation of these point defects belonging to only one fcc sublattice in the sphalerite structure implies the excess of atoms from the other fcc sublattice. These have to remain as precipitate within the pore or have to be emitted as interstitials into the crystal lattice. Several nanometre sized precipitates are experimentally ruled out (cf. section 4.1.1.1) whereas a small remaining wetting layer on the pore bounding surfaces might be undetected in the case of the experimental sensitivity. Regarding the stay of resulting interstitials, the publication of Vardya and Mahajan [168] provides an interesting option beside the simple movement toward the surface. The authors describe a mechanism of dislocation climb which is based on the absorption of point defects (interstitials or vacancies) at the dislocation core. The mechanism is based on the inherent function of a dislocation as sink and source for point defects. Moreover, the authors underline that pairs of vacancies or intersti-

tials have to be accumulated at once because a single absorbed point defect is energetically highly unfavourable. In order to have a concrete example, Sb interstitials Sb_i and V_{Ga} are assumed. That is, V_{Ga} have to be emitted into the GaSb buffer layer if dislocations climb by absorption of Sb_i. In this example, further vacancies are provided for the growth of pores and an interaction mechanism of pores and dislocations is implied.

Final pore morphology

The detailed analysis of the pore morphology provides insights into the energetics of a stable crystal form. The dominance of $\{100\}$ and $\{110\}$ facets is deduced from the tomographic evaluation of the tilt series. In contrast, pores bound by $\{111\}$ planes in sphalerite structured materials have been reported by Huang *et al.* [169] and Jäger and Jäger [170]. The former work describes tetrahedral etch pits in GaSb that are overgrown subsequent to the etching step with arsenic. The latter work deals with voids in GaP that form in annealing experiments of dopant diffusion. Considerations of energetically stable habits of sphalerite structures belong to a long lasting discussion. Cahn and Hannemann [171] argued that the surfaces with the lowest density of dangling bonds are energetically favourable. Sectioning the bulk GaAs crystal parallel to $\{111\}$ is the simplest realization of this proposal. This is in accordance with the findings of the afore mentioned publications [169, 170]. A further aspect is introduced by the polar character of the $\{111\}$ surfaces. Harrison [172] addresses this problem and finds the perfect cleavage planes $\{110\}$ in GaAs as energetically favourable surface. The strong ionic bonding contribution in III-V compound semiconductors necessitates an equivalent presence of group III and group V elements in the surface plane [173]. This argument agrees with the revealed $\{110\}$ facets of the pore but contradicts the presence of $\{100\}$ surfaces. Ideas of energetically favoured surfaces must be extended by possibilities of surface reconstructions. These include the reduction of dangling bonds, the local rearrangements of surface and near surface atoms as well as the incorporation of adatoms. It is assumed that foreign adatoms are negligible under the MBE growth conditions. But excess Sb atoms may be responsible for the formation of a stable reconstruction of a $\{100\}$ surface of GaSb [174] which explains the presence of respective pore facets.

Qualitatively, the presence of $\{100\}$ and $\{110\}$ facets conveys the notion of a form that approximates a sphere (see figure 4.9). The dimensionless sphericity Ψ allows to quantitatively compare the similarity of 3D objects to a sphere. The surface A of the object is related to its volume V by

$$\Psi = \frac{\pi^{\frac{1}{3}}(6V)^{\frac{2}{3}}}{A}. \tag{4.5}$$

The smallest ratio of volume V and 3D object surface A is realized by a sphere and results in $\Psi = 1$ which corresponds to the minimization of the surface tension of the 3D object. Figure 4.9 shows different habits and their sphericity. Pure crystal forms like the octahedron ($\Psi = 0.67$), the cube ($\Psi = 0.81$) and the rhombic dodecahedron ($\Psi = 0.90$) which are formed by $\{111\}$, $\{100\}$ and $\{110\}$ facets, respectively, are less similar to a sphere than the habit with mixed forms. The example with $\{100\}$ and $\{110\}$ bounding planes of equal distance to the centre of gravity accounts for a sphericity of $\Psi = 0.94$. This consideration suggests a tendency to approximate a sphere. In contrast, the quantitative determination of the pore sphericity from the experimental data results in the significantly smaller value

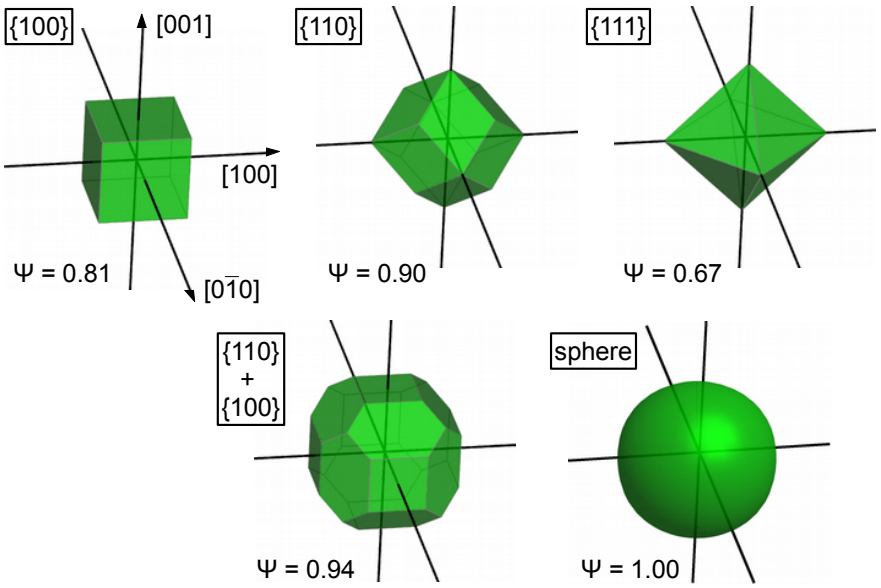

Figure 4.9. The notion about the pore morphology is supported by the visualization of different cubic crystal habits. The sphericity quantifies the similarity to a sphere.

of $\Psi = 0.85$. This contradiction is solved by the consideration of concavities in the pore morphology (arrows in figure 4.5). The coalescence of two pores is supposed which leaves these recesses in the surface. Hence, this fine detail has to be emphasized as valuable hint for the understanding of the pore shape.

The treatment of the pore as 3D body is convenient but the general difference between a usual, convex crystal form and a pore has to be mentioned. The concave surface of the crystal matrix surrounding the pore is the substantial matter. The approach is assumed to be valid as long as the bounding facets dominate over the impact of edges comparing a crystal and the pore. This limitation implies a possible size effect, i.e the size dependent change of the pore morphology.

4.1.2.2. Experimental performance and potential improvements

This section is dedicated to the discussion of technical aspects of the experiment. In the first place, advantages of the applied experimental conditions are highlighted. A critical consideration of resolution limits follows and, finally, potential improvements are outlined.

The specimen shape enables the acquisition of projections over the tilt range of 180°. Thereby, the missing wedge problem [143] and the elongation of the reconstructed volume [134] are circumvented. The silhouette of the specimen is directly observed in the reconstructed volume represented by, for instance, the isosurface viewed along the [00$\bar{1}$] direction (figure 4.5). Of course, this viewing direction is inaccessible in the microscope. It is exclusively attained in the visualization of the 3D evaluated data set. Consequently, irregularities caused by the specimen preparation are easily told apart from reconstruction artefacts.

A systematic decrease of intensity toward the centre of the specimen is not detected in figure 4.6. Hence, the selection of the HAADF imaging conditions with a collection angle range of 60 mrad to 160 mrad avoids the cupping artefact that has been described by den

Broek *et al.* [156]. This artefact arises from a non-linear increase of intensity with thickness and results in the underestimation of the intensity within the volume of interest. The maximal thickness of 170 nm encountered here remains approximately in the linear regime for GaSb which is consistent with the preliminary considerations illustrated in figure 3.11.

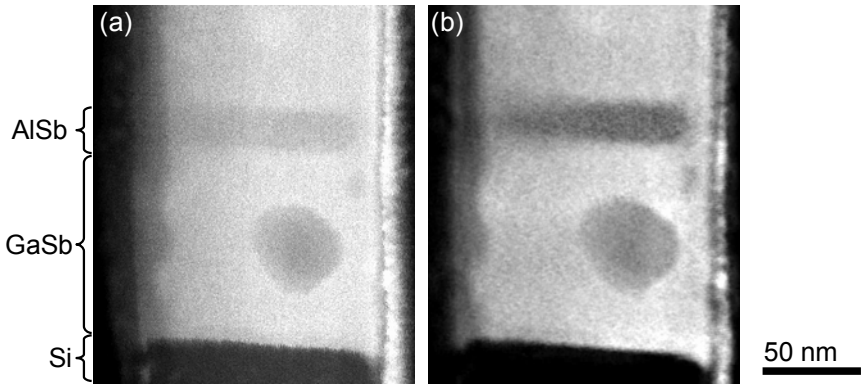

Figure 4.10. The HAADF image (a) is compared to the reprojection of the reconstructed volume (b). The direction of the reprojection corresponds to the viewing direction of the HAADF micrograph.

In figure 4.10(a) and (b), an HAADF image is compared to the reprojected volume in the respective direction. The general similarity is apparent, i.e. structural features are reproduced in the tomogram. The enhanced contrast in the reprojection image is in agreement with the intention of the polytropic montage [137] which has preceded the development of electron tomography. On the other hand, the spatial resolution is downgraded: The dark vertical border that parts the surface damage in the right from the specimen volume appears broader and blurred. The transition from the GaSb to the AlSb layer is less abrupt. Besides, this blurring exacerbates with increasing distance to the small pore. The overall loss of resolution is a consequence of data binning and low-pass filtering before the application of the reconstruction algorithm. These measurements are applied to reduce the noise in the tomogram. A compromise between resolution and SNR is made for the data evaluation. A further impact originates from inaccuracies of the image alignment and uncorrelated distortions in individual images. The distortions cause the gradient of blurring with respect to the small pore to which all images have been aligned.

The facet determination relies on the angular resolution in addition to the spatial resolution. The latter limits the size of detectable facets. The former is important to distinguish between crystallographic planes separated by a certain angle α. In principal, the determination of angles in the tomogram can be inaccurate because of residual image distortions and the wrong allocation of tilt angles to the individual frames. Matoba *et al.* [175] quantified deviations of the actual goniometer tilt and the computer readout. For the presented results, the deviation of the vicinal substrate surface from the (001) plane by 4° (figure 4.3) shows that the angular resolution is not a limitation for the discrimination of low indexed facets (hkl) with $h, k, l \leq 2$.

Finally, some approaches are supposed that improve the tomography performance. Three aspects are considered comprising the sample preparation, the data acquisition and the raw data evaluation:

1.) The investigation of the pore succeeded in spite of the damage layer on the (110) surface. Nevertheless, it is assumed that the avoidance of surface features is beneficial in order to reduce noise in the reconstructed volume. This damage layer occurred during SEM monitoring of the preparation progress with an acceleration voltage of 20 kV. The surface features might form due to electron beam induced redeposition of sputtered material or they are remains of molten material. Of course, the question arises why 20 kV electrons harm the material and the TEM investigations at 200 kV do not alter the material. Beam damage due to TEM investigations are not observed although three different tilt series have been acquired. The energy dependence of the interaction of charged particles with matter in SEM and TEM have been studied by Egerton *et al.* [176]. They have found that there is a minimum at energies in between the regimes of electron-electron and electron-nucleus interactions explaining the counterintuitive behaviour observed in this work. Moreover, the work of Yasuda *et al.* [177] suggests a careful consideration of electron beam induced creation and clustering of vacancies in GaSb. This effect is excluded as origin for pores during FIB based sample preparation because the pores are also observed in conventionally prepared specimen. In general, the aspect of irradiation damage in TEM and SEM observations has to be reconsidered for each object under investigation because the energy dependence is specific to the material system.

Two further preparation related points concern the size and the shape of the sample. A cylindrical specimen with a diameter as small as possible is aspired to focus on the object of interest. This reduction maximizes the control of the experiment, especially by excluding or reducing artefacts. This requirement is limited by the performance of FIB sample preparation. The resolution of the ion beam microscope, the precision of site control and the stability of the ion optics. The irregular shape of the presented specimen is, for instance, the consequence of beam drift during the intended transform of the specimen into a cylindrical object. Moreover, the reaction of the Ga-ion beam with the GaSb has to be kept in mind. Lugstein *et al.* [178, 179] described the reaction of GaSb as well as the formation of Sb nanowires under Ga ion irradiation. That is, a balance between specimen shaping and ion beam interaction with the sample has to be found in order to avoid surface features.

The second optimization proposal is related to the later image alignment of the tilt series. The introduction of markers allows a more precise image alignment as well as a correction of image distortions and the nominal tilt angle. Gold particles are applied in electron tomography on biological objects for this purpose [142] which might be feasible by a dip of the needle shaped specimen into an adequate suspension. The ultimate control and application of marker has been demonstrated by Hayashida *et al.* [180] who deposited tungsten dots with a helium ion microscope.

2.) The data acquisition in STEM benefits from shorter scan times. Random image distortions arise due to sample stage movements and magnetic disturbance fields. A higher beam current at the object plane is required for this improvement because a faster scan reduces the SNR. An enhancement of the beam current will occur if the microscope is equipped with a C_S-corrector for the condenser system or a higher gun brightness (e.g. a cold field emitter or a higher acceleration voltage [107]). The urgency to increase the beam current and to reduce the scan time will grow if larger collection angles for HAADF imaging are needed due to higher sample thicknesses or if an EDX signal has to be exploited for direct chemical maps. For instance, Kotula *et al.* [9] reported an acquisition time of 1 h for one EDX map in a tilt

series.

3.) The last aspect addresses the software based data evaluation. The necessary alignment of tilt series images preceding the 3D reconstruction relies on distinct features that are visible in subsequent images. Presented results are improved by the usage of the small pore instead of larger objects as the whole needle shape, the AlSb layer or the big pore. Consequently, a feature which is even smaller in size and which provides a stronger contrast in all images, contributes to an improvement of the tomogram. The digital image correction with help of a set of small markers has been described above.

4.2. The buried AlSb wetting layer

The 2D growth of GaSb on Si sensitively depends on the deposition of an initial AlSb layer. In fact, this wetting layer forms small islands which have been observed *ex situ* by atomic force microscopy (AFM) [181, 182]. In contrast to AFM investigations, electron tomography provides an insight into the volume of the completed heterostructure, i.e. AlSb islands are already overgrown by GaSb and the substrate is entirely covered. Hence, the final state of the interface is addressed by the tomographic investigation in this section. Three aspects motivate the consideration of the finalized heterostructure. The first two concern the stability of the AlSb islands. The GaSb coverage protects AlSb from easy oxidation [183] when the sample is exposed to air for *ex situ* experiments. Furthermore, a redistribution of AlSb is excluded. Neither the AlSb forms a solid solution with GaSb nor does the AlSb islands reshape during overgrowth. These phenomenons are reported for the overgrowth of InAs quantum dots with GaAs by García *et al.* [184] and Songmuang *et al.* [185]. Authors have described the reshaping of islands from an initial truncated pyramid to a doughnut like structure. Finally, the chemical stability of the interface between GaSb and Si is evident from the tomographic investigation. Vajargah *et al.* [165] have reported on the dissolution and roughening of the Si surface during immediate GaSb growth without an AlSb nucleation layer.

In the following, the experimental results are presented in three subsections. The acquisition of the tilt series is described at first. The subsequent analysis of the tomographic data reveals the distribution, size and shape of AlSb islands at the interface between the Si substrate and the III-Sb film. Afterwards, the dislocation structure is studied by STEM/TEM. It is correlated to the location of AlSb and, first and most important, to expected sites of island coalescence. The discussion dwells on the morphological island anisotropy and the crucial aspect of coalescence as source for threading dislocations. The last subsection discusses technical aspects of the tomographic experiment and of the microstructural analysis.

4.2.1. Experimental results

4.2.1.1. Tilt series around an in-plane direction of the interface

The conical specimen tip is tilted about 180° in steps of 2°. HAADF STEM images with 2048 x 1024 pixels are acquired at each tilt step with a sampling rate of 0.2 nm per pixel. The ADF collection angle range is set to 110 mrad to 300 mrad which ensures a predominantly linear behaviour of the intensity dependence on thickness for GaSb (cf. figure 3.11). Figure 4.11 presents five images from this series. The $[1\bar{1}0]$ direction is approximately aligned to the tilt axis. The deviation of both directions amounts to 1.5°. The maximal material thickness that has to be penetrated by electrons, is measured from the orthogonal viewing directions in figure 4.11 (images at tilt angles 0° and 90°). The HAADF signal fulfils the monotony requirement for the maximum of 180 nm thick GaSb shown in the projection along the [110] orientation. The $[00\bar{1}]$ direction comprises the maximal combined thickness of a 30 nm GaSb and a 80 nm Si layer which imposes the minor constraint due to the lower thickness as well as the lower average atomic number.

The HAADF image taken at a tilt angle of 4° shows the view edge-on to the III-Sb/Si

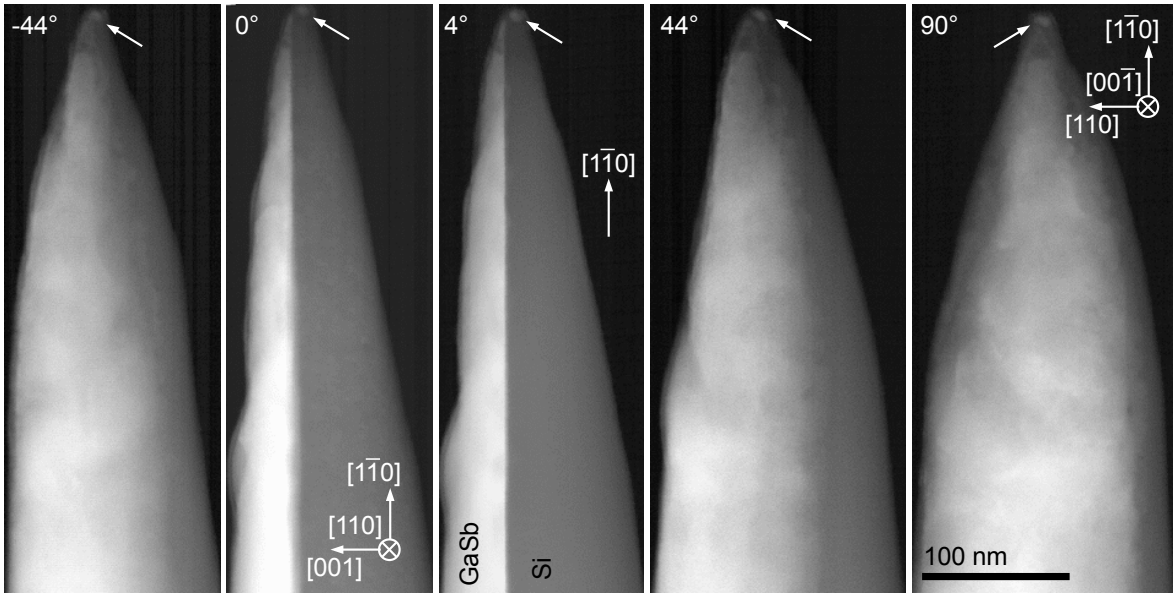

Figure 4.11. The HAADF STEM images are extracted from the 180° tilt series. They present the needle-shaped specimen along the low-indexed directions [110] and [00$\bar{1}$] at the tilt angles of 0° and 90°. The III-Sb/Si interface is observed edge-on at 4° tilt. The micrographs at ±44° show further tilt states. The location of AlSb islands is not unambiguously discerned.

interface which is not aligned to the [110] direction. Consequently, the miscut is established by the inclination of the surface normal toward the [110] direction and the substrate steps are predominantly oriented along the [1$\bar{1}$0] direction. Buried AlSb islands are not observable because islands are expected to overlap or to be homogeneously distributed. Moreover the obvious roughness and the thickness changes of the III-Sb layer obscure Z-contrast from single islands. Likewise, the observation of AlSb islands in the approximate view perpendicular to the interface (90°) is impeded. The Si substrate surface appears smooth compared to the epitaxial layer. Hence, the substrate related intensity does not contribute to short range contrast changes in the HAADF image taken along the [00$\bar{1}$] direction.

The analysis of the 3D defect in section 4.1 deals with homogeneous GaSb. In contrast, it has to be emphasized that the current problem requires to distinguish between three different materials, namely Si, GaSb and AlSb. The presence of an amorphised damage layer complicates this situation because the HAADF intensity from crystalline and amorphous material with the same chemical composition differs. Hence, the interpretation of figure 4.11 by chemical means is omitted except for the coarse distinction between substrate and GaSb dominated layer.

Finally, the attention is drawn to the bright blob on the specimen top. This feature is extremely valuable for an accurate alignment of the tilt series images.

4.2.1.2. Tomography of AlSb islands

The conical, needle-shaped specimen is reconstructed from the aligned series of images with the WBP algorithm. The SIRT algorithm results in a detrimental blurring at the heterostructure interface even after a small number of iterations. This effect is related to the

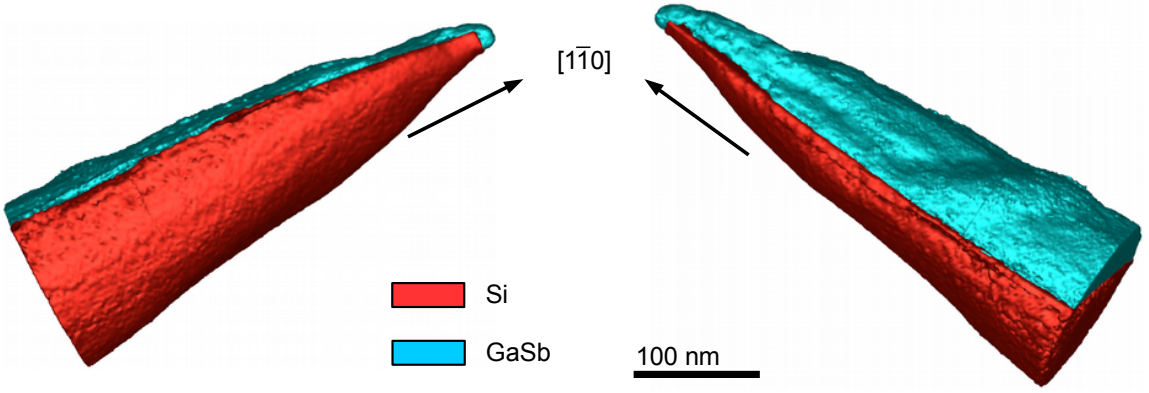

Figure 4.12. The isosurface visualisation of the reconstructed volume is presented in two inclined views onto the GaSb layer (blue) and the Si substrate (red). The two colours correspond to different grey values, i.e. the visualisation is a montage of two isosurfaces that illustrate differences in the roughness of the specimen surface.

high contrast artefact which occurs at abrupt, high differences in specimen mass density [12, 142, 186]. The reconstructed specimen is shown in figure 4.12 as a montage with two grey values represented in red and blue. The values display the Si and the GaSb surfaces, respectively. The two viewing directions convey a notion of the morphology. The FIB processing leads to an apparently smoother specimen on the Si substrate side. The GaSb exhibits an uneven surface. The very fine roughness on both sides is an artefact caused by noise in the tomogram. Beside physical aspects of specimen milling which explain material and orientation dependent effects of ion sputtering, a pronounced chemical sensitivity of GaSb to the Ga^+-ion beam is assumed. Therefore, it is more difficult to obtain an equally smooth surface without the protective carbon layer on both the GaSb layer and the Si substrate. However, the different thickness of substrate and layer within the needle is attributed to the limited control of the milling position during FIB preparation at 3 kV acceleration voltage.

The tomography data reveals the morphological character of the AlSb islands. They exhibit an anisotropic, lateral elongation and indications for coalescence. Statements are based on slices through the reconstructed volume which are presented in figures 4.13 and 4.14. The former figure presents a slice oriented parallel to the substrate surface and close to the interface, i.e. it is tilted away from the (001) plane by the amount of the substrate miscut. The identified and numbered AlSb islands are schematically sketched in the right of the figure along with the specimen silhouette. The predominant elongation of islands points along the [110] direction. It is remarked that this direction is perpendicular to the prevailing surface step direction. The lateral dimensions of AlSb islands range from 18 nm to 110 nm. In fact, their expansion amounts on average only to (36 ± 3) nm and (30 ± 3) nm in the [110] and the [1$\bar{1}$0] directions, respectively, unless there is an indication of coalescence. Concave parts in the perimeter are treated as such indications. Dashed lines in the scheme of figure 4.13 mark sites of coalescence. The long chain of island 10 is an illustrative example for the connection of three islands. The consideration of $\langle 110 \rangle$ directions appears natural because edges directed along the [110] and the [1$\bar{1}$0] orientation predominate at the interface.

Further observations from the slice through the tomogram in figure 4.13 concern the spec-

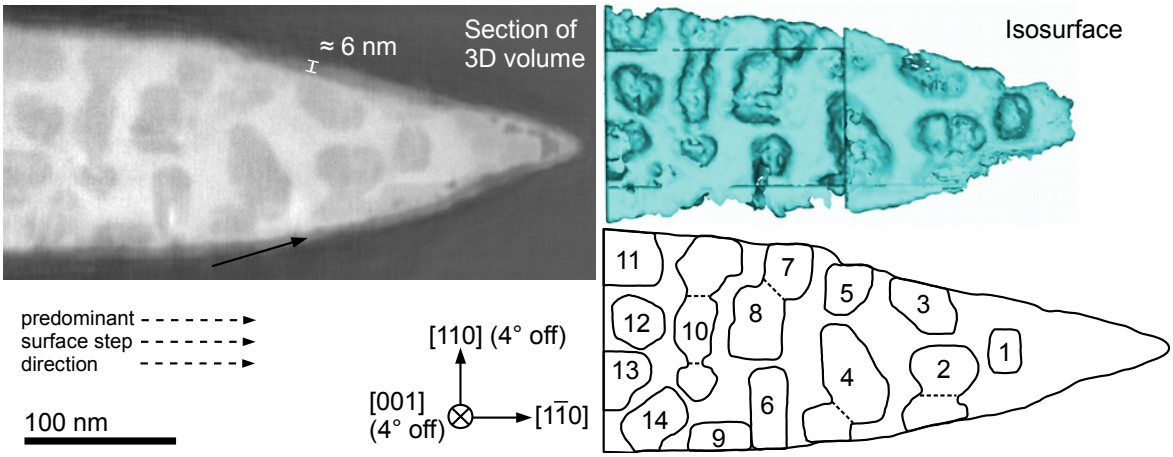

Figure 4.13. The left image presents a slice through the reconstructed volume parallel to the substrate surface. The distribution, the lateral size and shape of nucleated islands is accessible. The upper right isosurface presentation depicts the imprint of the AlSb islands within the GaSb layer. It conveys the 3D notion of the reconstructed volume. The scheme on the bottom right outlines the numbered islands along with the outer specimen shape.

imen constitution due to FIB preparation. The black arrow points to a grey rim bordering the section through the specimen. It is associated to the amorphised damage layer caused during FIB sample preparation and must not be confused with the similar grey value of the AlSb islands. The damage layer is approximately 6 nm thick. Beyond, a bulge of the amorphous layer into the specimen below island number 1 is outlined. The bright grey interspace represents GaSb which covers the islands as well as the substrate in between the AlSb islands. Bright features within the islands, e.g. in island number 6, are considered as artefact in the tomogram. Residual contrast from dislocation lines in the input tilt series for the tomographic reconstruction occurs along low indexed viewing directions (cf., for instance, [127] or section 2.2.2). This deviation from Z-contrast is assumed to cause this artefact. The isosurface in figure 4.13 illustrates AlSb island shapes as imprints into the GaSb layer. The isosurface presentation of the islands themselves and the subsequent morphological analysis is not possible with the reconstructed data.

Slices orthogonal to the heterostructure interface are extracted from the 3D volume and shown in figure 4.14. The (1$\bar{1}$0) slices depict the specimen cross-section perpendicular to the predominant direction of the FIB preparation or the tilt axis, respectively. The elliptical shape is a result of the different sputter rates of GaSb and Si. It clearly deviates from the intended circular cross-section. The sectioned AlSb islands are emphasized by dotted lines and labelled by the corresponding numbers introduced in figure 4.13. The interface of the III-Sb layer to the Si substrate appears smooth, i.e. a chemical reaction of Ga and Si and a subsequent roughening is not observed. A reshaping of AlSb during GaSb overgrowth is not observed either. Black arrows pointing downward mark notches in islands 2 and 10. They correspond to positions that are highlighted by dashed lines in the scheme of figure 4.13. That is, they agree with the findings on coalescence sites of islands from the lateral analysis.

Island heights range from 11 nm to 16 nm. Most islands exhibit a flat top facet parallel to the (001) lattice plane. Islands 2, 6, 8 and 12 differ from this top morphology. They show

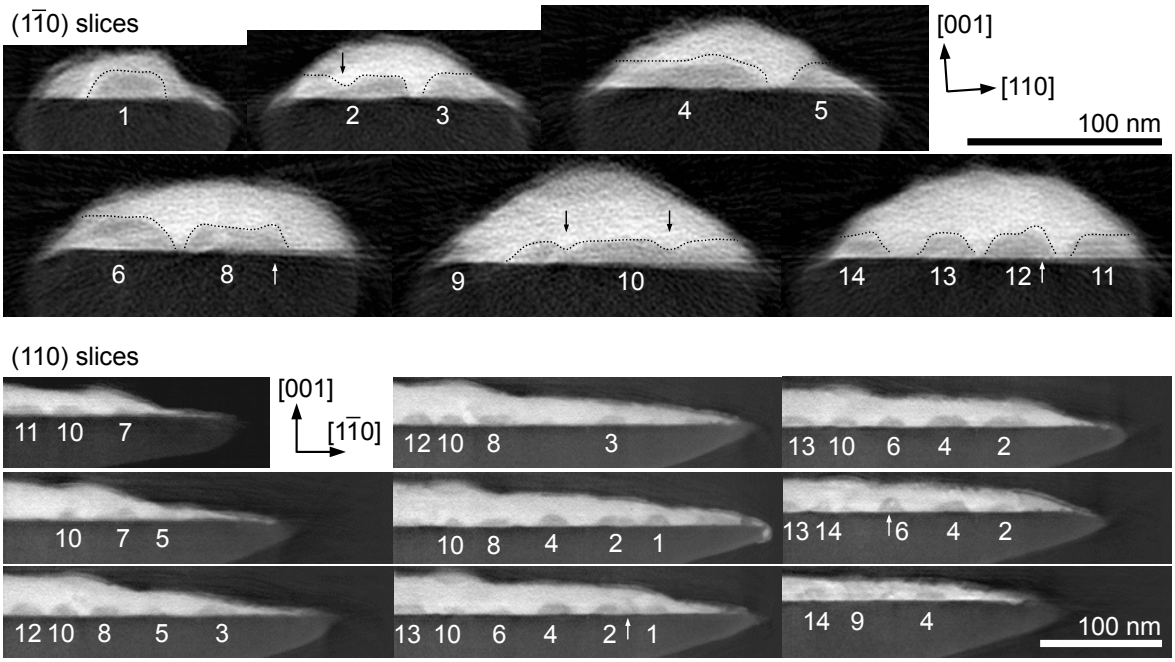

Figure 4.14. Slices parallel to the (1$\bar{1}$0) and (110) planes are extracted from the reconstructed volume. They provide information about side and top facets of the islands and their height along the growth direction. Black arrows indicate sites of AlSb island coalescence. White arrows mark islands with unusual heights.

peaks exceeding the average height of (12 ± 3) nm. Peaks are highlighted by white arrows pointing upward in figure 4.14. The side facets of the AlSb islands are always inclined with respect to the surface normal. $\{111\}$ planes are expected in accordance with the predominating $\langle 110 \rangle$ edges. Indeed, different inclinations are observed which implies the presence of side facets with higher indices. A quantitative determination of the higher indexation is beyond the scope of the data.

4.2.1.3. Microstructure analysis by STEM and TEM methods

TEM and STEM investigations are carried out in order to elucidate the microstructural features of the tomography specimen and, eventually, to correlate them to the findings of the tomographic analysis. It is anticipated that these measurements rely on specific crystal orientations. In this respect, the limitation due to the single available tilt axis of the tomography holder has to be reminded.

Figure 4.15 presents a HRTEM image of the specimen tip acquired approximately in the [110] zone axis. The resolution of the $\{111\}$ lattice planes is evident. A periodic contrast modulation (arrows) with a spacing of approximately 3.4 nm is observed along the interface. It is assigned to the presence of MFDs at the interface between the III-Sb layer and the Si substrate. A Burgers circuit is shown in the upper right image which depicts the magnified part marked in the micrograph by a dashed square. The deduced gap in the circuit points to the perfect dislocation with the Burgers vector $\frac{a}{2}[1\bar{1}0]$. The Fourier filtered images in the right correspond to the magnified part. The two sets of $\{111\}$ lattice planes are isolated in the middle and lower image. They verify the ending of two $\{111\}$ lattice planes at the

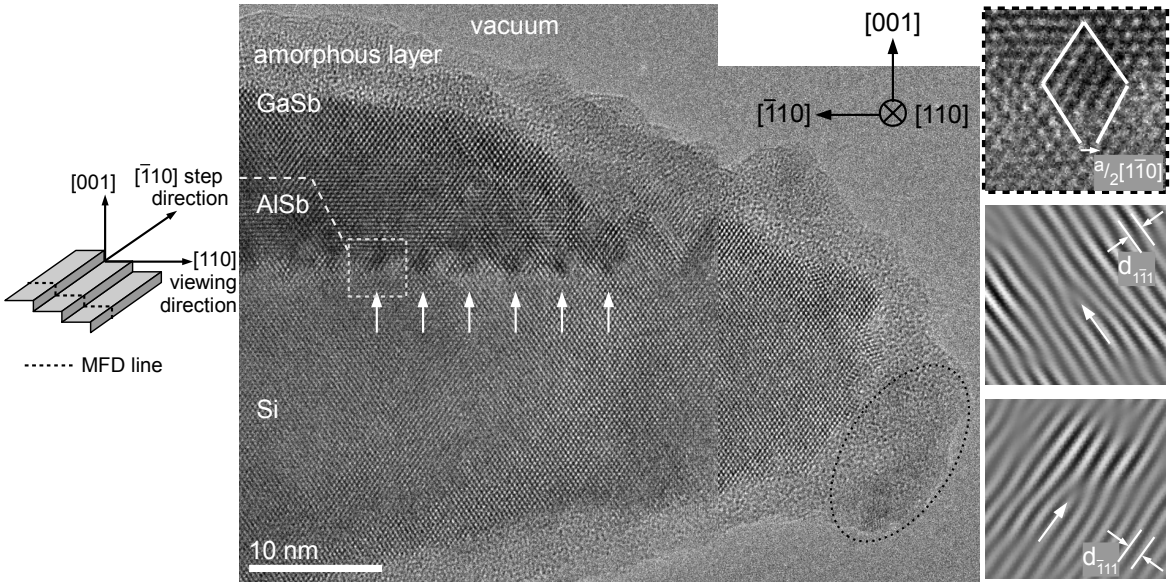

Figure 4.15. The HRTEM image is acquired from the apex of the conical specimen tip which exhibits a sufficiently thin thickness. The diamond and the zinc-blende lattices of the substrate and the III-Sb layer, respectively, are resolved along the [110] zone axis. The viewing direction is perpendicular to the predominant direction of surface steps. White vertical arrows highlight a contrast modulation along the interface. The diagonal arrows underline the termination of {111} lattice fringes.

interface (arrows) which is characteristic for Lomer or perfect 90° dislocations [187].

The viewing direction in figure 4.15 is perpendicular to the predominant direction of the surface steps which is inferred during the tilt series acquisition. Therefore, the interface is, in general, not imaged edge-on and the dislocations comprise segments parallel to the image plane in order to ascend the steps. Indeed, the periodic contrast features are broader than those ones observed by Kim *et al.* [182] regarding the width along the [001] direction. It is assumed that steps occur in the projected sample volume of the regarded area. The miscut is intended to create surface double steps on the Si(001) substrate. The average terrace width t_w results from the double step height $\frac{a_{Si}}{2}$ and the miscut angle

$$t_w = \frac{a_{Si}}{2 \cdot \tan 4^\circ} = 3.9\,\mathrm{nm} \tag{4.6}$$

where $a_{Si} = 0.543\,\mathrm{nm}$ is the lattice constant of Si. Consequently, more than one step is crossed along the viewing direction in a specimen of more than 10 nm thickness. In even thicker parts, the periodic contrast features become less pronounced. It is remarked that average terrace widths and the average spacing of MFDs exhibit a similar magnitude.

Finally, the HRTEM image underlines the benefits of the polishing step with Ga^+-ions at 3 kV during FIB sample preparation. The amorphous damage layer is easily discerned from the intact crystalline core of the specimen. The small thickness of approximately 6 nm is confirmed. It is remarkable that this layer is hardly thicker at the very tip where ions have arrived at 0° angle of incidence. The phase contrast is not sensitive to the chemical composition. Therefore, the white blob outlined by the arrows in the Z number sensitive HAADF images (figure 4.11) is not discerned in figure 4.15. Its expected location on the

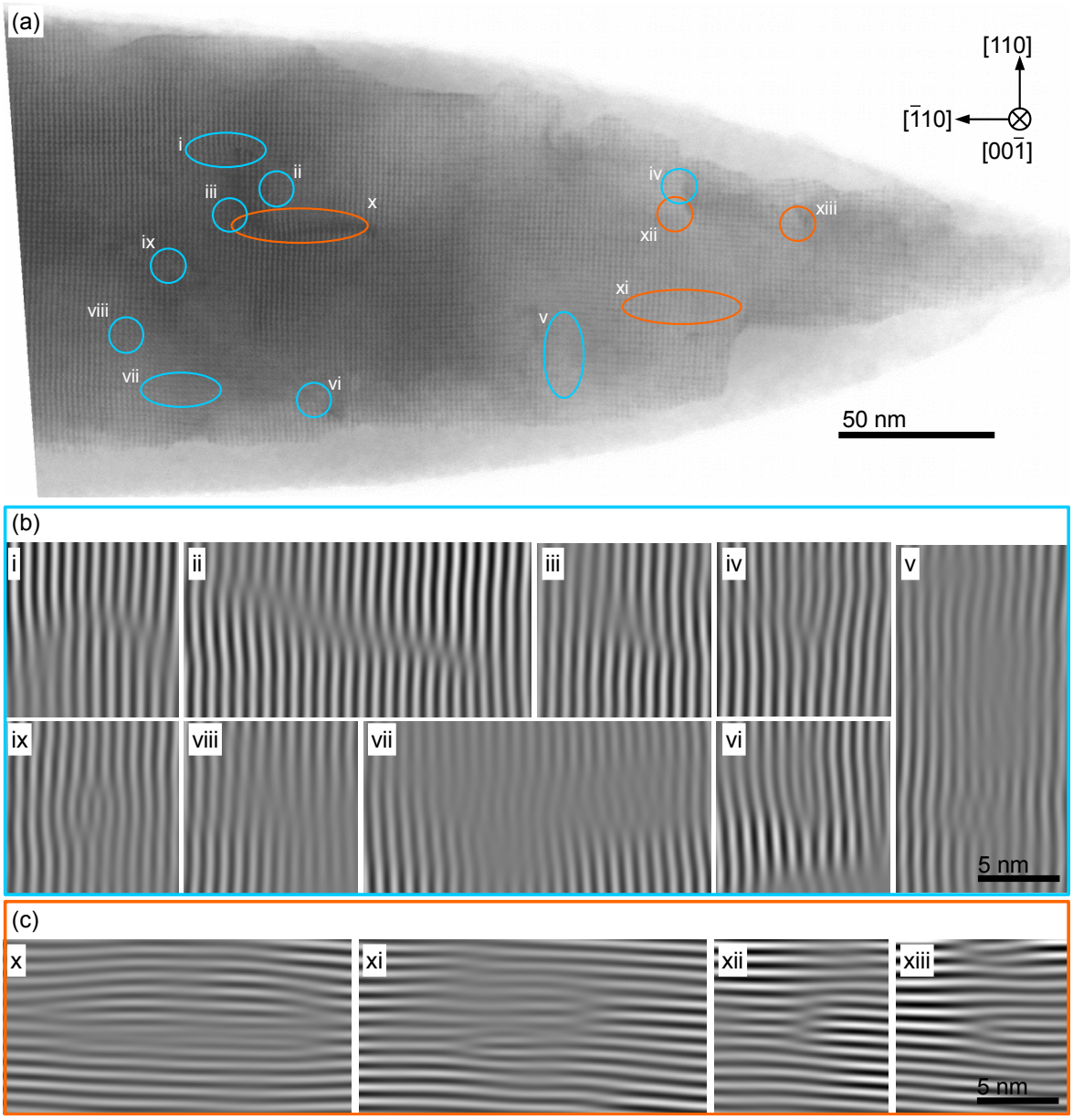

Figure 4.16. (a) This BF STEM image is acquired along the [00$\bar{1}$] direction. The superposition of the III-Sb layer with the Si lattice which is situated beneath the epitaxial film along the viewing direction results in a dominant Moiré contrast. Excerpts from the Fourier filtered BF STEM image are extracted to investigate lattice defects disturbing the Moiré period along the [$\bar{1}$10] (b) and the [110] direction (c).

Si substrate side is marked by a dotted ellipse. Obviously, the rearrangement of material during FIB preparation occurs at the specimen surface indicating chemical reactions with the milling Ga^+-ion probe beside a purely physical sputtering process.

The micrograph in figure 4.16(a) is acquired in BF STEM mode with the specimen oriented approximately along the [00$\bar{1}$] zone axis. Image details are dominated by pronounced Moiré fringes. They form a periodic pattern along the orthogonal [110] and [1$\bar{1}$0] directions with a spacing of 1.7 nm. The pattern appears perfect over large areas of the investigated

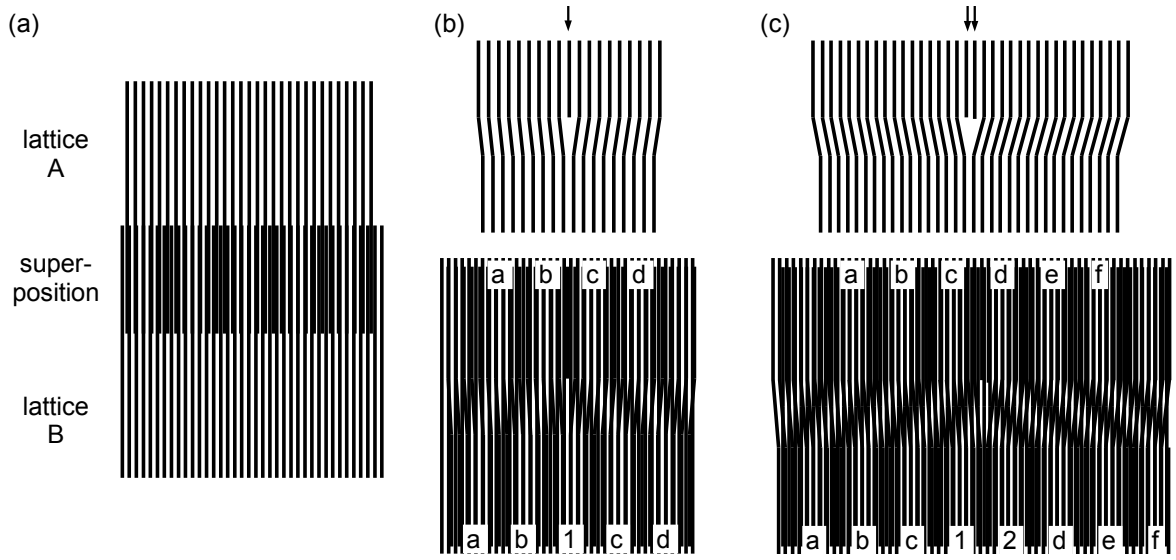

Figure 4.17. (a) The optical analogue of line sets with different spacings (A and B) explains the formation of Moiré patterns. The insertion of (b) one and (c) two extra half lines (arrows) reappears in the Moiré patterns shown in the bottom images.

specimen indicating a high ordering in the MFD network. Deviations from the periodicity of this Moiré pattern are used to determine the location of TDs. The two sets of fringes along the orthogonal directions are isolated in Fourier filtered images. The imperfections of the periodicity appears as terminating half-lines. Magnified parts of the filtered images are presented in figures 4.16(b) and (c). They present fringes parallel to the [110] and parallel to the $[1\bar{1}0]$ direction, respectively. The positions of defects are marked by blue and orange circles and ellipses in figure 4.16(a). Roman numbers label corresponding image parts and positions. The filtered images present a variety of faults in the periodic pattern. The simple case of one terminating black or white line is observed for instance in iv or vi. Furthermore, there are sets of fringes which are position shifted to each other along arbitrary line directions as most prominently seen in ii. A case of fringes that seem to be intercalated, is seen in x.

The location of TDs sensitively depends on the interpretation of the Moiré pattern presented in figure 4.16(a). Therefore, this contrast mode and its applications in electron microscopy are explained in more detail. Following explanations are restricted to translational Moiré patterns. Detailed descriptions of this well-established method can be found, for instance, in the textbooks of Williams and Carter [3], Reimer [107] and Hirsch *et al.* [106]. The initial situation is the superposition of two crystals A and B of different lattice constants as schematically illustrated in figure 4.17(a). Two descriptions of the contrast formation are found in literature. One point of view is based on diffraction theory [188]. A double diffracted beam interferes with the central beam in BF mode or with a single diffracted beam in DF mode. The resulting image shows a contrast modulation with the period d_M obtained from the difference of the reciprocal lattice vectors $\vec{g}_1$ and $\vec{g}_2$ as expressed by

$$d_M = |\vec{g}_M|^{-1} = |\vec{g}_1 - \vec{g}_2|^{-1} = \left| \frac{d_1 d_2}{d_2 - d_1} \right| . \tag{4.7}$$

The indices correspond to the diffracting lattice planes of crystal 1 and crystal 2, respectively. The presented heterostructure is composed of the two crystals Si and GaSb with lattice constants $a_{Si} = 0.543\,\text{nm}$ and $a_{GaSb} = 0.610\,\text{nm}$. The substrate is treated as rigid lattice and the antimonide layer as relaxed. The pseudomorphic case ($a_{Si} = a_{GaSb}$) is excluded due to the relaxation processes described below in section 4.2.2. The small difference of the AlSb and GaSb lattice constants is neglected. Here, the cube-on-cube orientation of the two materials is evident from SAD observations (cf. figure 3.10), i.e. lattice planes with the same indexation are parallel and the resulting Moiré patterns are of translational type. The Moiré period of 1.7 nm is explained by the coupling of the $\vec{g}_{220}$ reflections from Si and GaSb. The applied lattice plane spacings are $d^{220}_{Si} = a_{Si}/\sqrt{8} = 0.192\,\text{nm}$ and $d^{220}_{GaSb} = a_{Si}/\sqrt{8} = 0.216\,\text{nm}$.

The second description uses a simple optical analogue as model (figure 4.17). It is applied to understand the contrast features of figure 4.16. Figure 4.17(a) demonstrates the superposition of two line patterns with different line spacings which are superimposed. The surrounding of line coincidences appears brighter as sites where lines are shifted by approximately half of their spacing. In that way, the presence of a missing half plane and its effect on the Moiré pattern can be analysed. Figures 4.17(b) and (c) display the two cases of one and two extra half planes, respectively. Bassett *et al.* [188] were the first authors who systematically exploited this information. They deduced that the Burgers vector component perpendicular to the Moiré fringes causes N terminating half lines according to

$$N = \vec{g}_{hkl} \cdot \vec{b}. \tag{4.8}$$

Exceeding the optical analogue, the authors have claimed that the determination of the dislocation character is not possible. Both screw and edge dislocations entail N half lines as predicted from equation 4.8. In addition, Angelo *et al.* [189] have mentioned the requirement of an inclination of the dislocation line with respect to the interface in order to obtain a terminating half line. Of course, a dislocation confined at the interface and running through the whole specimen produces the terminating lines at the specimen edge. The Moiré pattern does not allow to distinguish whether the dislocation line is situated in the substrate or in the epitaxial layer. It is assumed that the Si lattice is free of dislocations and serves as reference lattice to form the Moiré pattern. Consequently, the presence of terminating half-lines is attributed to threading dislocations in the III-Sb layer.

$\vec{b}$	$\frac{1}{2}[110]$	$\frac{1}{2}[1\bar{1}0]$	$\frac{1}{2}[101]$	$\frac{1}{6}[1\bar{1}2]$	$\frac{1}{2}[211]$
$N(\vec{g}_{220})$	2	0	1	0	1
$N(\vec{g}_{2\bar{2}0})$	0	2	1	$\frac{2}{3}$	$\frac{1}{3}$

Table 4.2. The number N of terminating half-lines in translational Moiré patterns is expected for dislocations with Burgers vector $\vec{b}$ and the imaging vector $\vec{g}$.

In the first instance, the presented analysis is intended to reveal the approximate positions of threading dislocations which are, eventually, correlated with the location of AlSb islands. On second thoughts, it is worth to count the terminating half lines and obtain quantitative information about the Burgers vector $\vec{b}$. Exemplary values for N are listed in table 4.2. The

imaging vectors are $\vec{g}_{2\bar{2}0}$ and $\vec{g}_{220}$. A selection of Burgers vectors of perfect $\frac{1}{2}\langle 110\rangle$ and partial $\frac{1}{6}\langle 112\rangle$ dislocations that occur in sphalerite structure, are regarded.

Indeed, the observation of terminating half-lines in figure 4.16(b) and (c) reveals situations which agree with the preliminary considerations. For instance, the images iv and xii both exhibit one half-line and could belong to $\vec{b} = \frac{1}{2}[101]$. Another example is the case of two partials with Burgers vectors $\frac{1}{6}[1\bar{1}2]$ and $\frac{1}{2}[211]$ inducing the split up into $\frac{2}{3}$ and $\frac{1}{3}$ terminating half-lines as depicted in image ii. But this analysis must not be overstressed because, on the one hand, the determination of Burgers vectors is ambiguous and, on the other hand, the influence of faults in the MFD network has to be considered. The ambiguity is easily seen as the first example of images iv and xii is also explained by the other three $\frac{1}{2}\langle 110\rangle$ Burgers vectors with a component along [001]. The effect of the MFD network is discussed below. Only one important observation has to be reminded for the later argumentation. The case of two terminating half-lines does not occur. Therefore, the essential conclusion is that none of the 90° MFDs bend out of the interface and becomes a TD.

Eventually, figure 4.16(a) indicates the preservation of layer crystallinity. The missing Moiré fringes in the lower right points at an amorphised corner that is already supposed by the tomographic result presented in figure 4.13. The broader damage rim at the bottom in figure 4.16(a) is misleading because the sample is slightly tilted away from the normal of the interface to reach the $[00\bar{1}]$ orientation. The ragged crystal edge at the top is assumed to indicate the starting oxidation of AlSb. AlSb is prone to oxidisation in air [183].

The dark-field micrograph in figure 4.18(a) is acquired in TEM mode. The weak-beam imaging condition is sensitive to the strain field of the MFDs. The specimen is tilted 22° off the [110] zone axis. In this way, a condition is found where a strong excitation of the $(\bar{6}60)$ reflection is realized while the weak $(2\bar{2}0)$ spot is used for imaging. This $g_{2\bar{2}0}(\bar{g})$ diffraction condition is reached exclusively at the chosen goniometer tilt angle. The missing second tilt axis would relieve this restriction which allows only for the shallow view under 22° onto the interface between substrate and epitaxial layer.

The faint dotted lines represent the MFDs along the [110] direction. These MFDs are confined at the interface between substrate and layer which overlap along the imaging direction. They are assigned to one set of orthogonal MFDs forming a network composed of perfect 90° or Lomer dislocations. According to the formation model [190], the detected dislocations running along the [110] direction possess a $\frac{a}{2}[1\bar{1}0]$ Burgers vector, i.e., they are of edge type. The oscillation along the line occurs due to the depth dependence of the diffraction contrast intensity.

The traces of the MFD network are partly disturbed by bright diffraction contrast features caused by TDs. Their positions are consistent with the deduced faults in the Moiré pattern shown in figure 4.16(a). The latter are represented by small crosses. The array of blue and orange symbols is compressed in the vertical direction by a factor of $\sin 22° \approx 0.37$ to account for the tilting of the (001) plane. The agreement with features in the WBDF image has to be emphasized. The careful investigation of the MFD network reveals shifts in sets of parallel MFD lines. Respective boundaries are marked by green dashed lines. Furthermore, double arrows mark regions which appear free of TDs despite of faults in the MFD array. In these regions, the spacing of MFD lines lies in the range of 3.7 nm to 4.0 nm. The pixel size in the micrograph corresponds to 0.3 nm.

Besides, the WBDF image exhibits lots of diffraction contrast features that have to be told

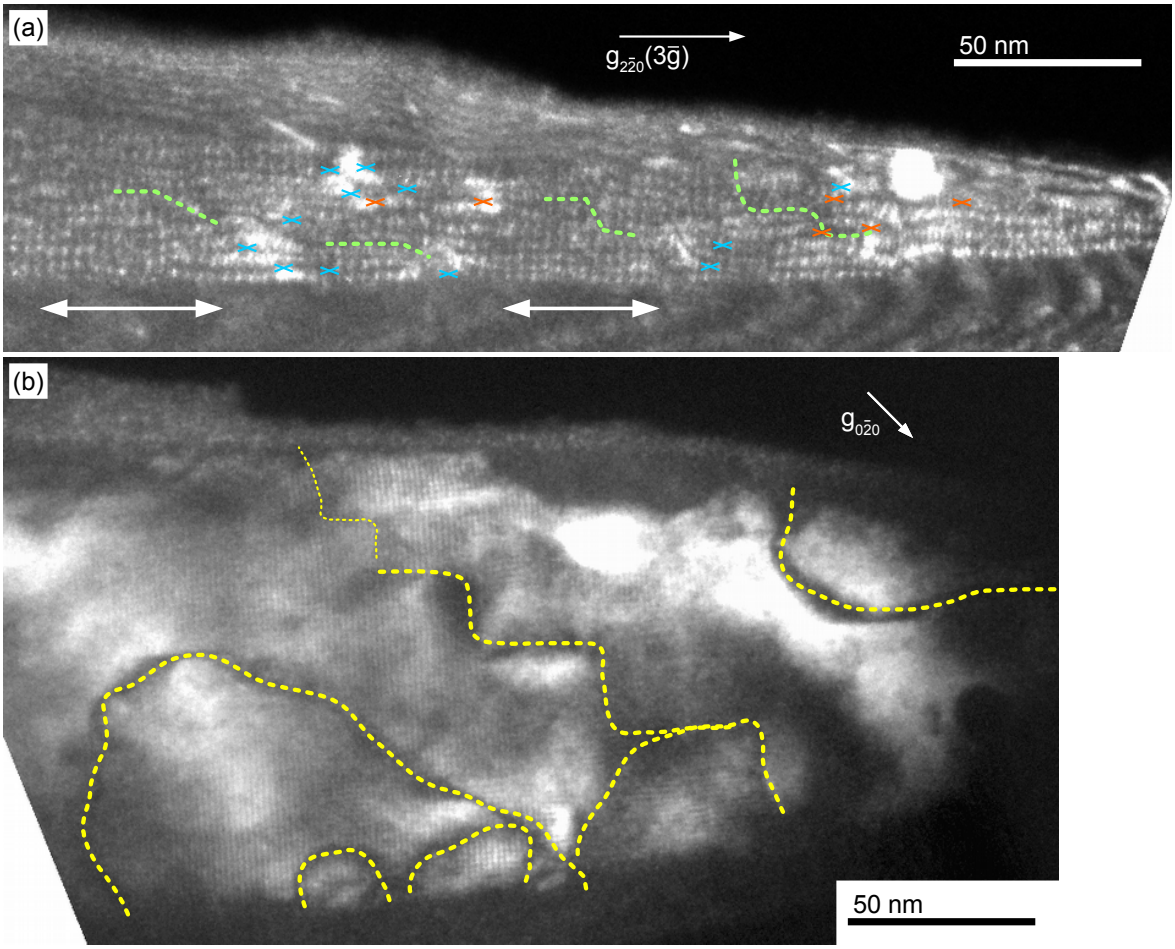

Figure 4.18. (a) The WBDF image applying a $g_{2\bar{2}0}(3\bar{g})$ condition reveals the MFD network. The interface between substrate and layer is imaged under an inclined view obtained by a 22° tilt away from the [110] zone axis. The correlated positions of the threading dislocations are marked by crosses. The green dashed lines outline shifts in the MFD network. (b) The TEM DF image with the $(0\bar{2}0)$ reflection excited reveals dark bended features that are related to APBs.

apart. The conical specimen shape causes thickness fringes along the isolated Si substrate which look like wood grain. Spotty details along the bright contours originate from preparation artefacts, e.g. redeposited crystallites composed of existing elements. Thickness fringes are present in the region of pure GaSb, too. Their much narrower spacing is related to the higher averaged atomic number.

The resolution of the micrograph is limited by both the inherent resolution of the WBDF mode and the compression of the interface under the shallow view direction. A lower value than 1.7 nm for the first limitation is proved by the fact that the shift of MFD fringes is observable. The interruption of MFD lines due to depth dependent intensity oscillations is regarded for the second limitation. The length of the interface along the [110] direction is known from the [001] views and the oscillations are counted, i.e. they have a period of approximately 10 nm projected into the interface plane. Features causing shifts on a shorter scale are not resolved in this direction.

The TEM DF image in figure 4.18(b) is captured with the $g_{0\bar{2}0}$ diffraction spot selected.

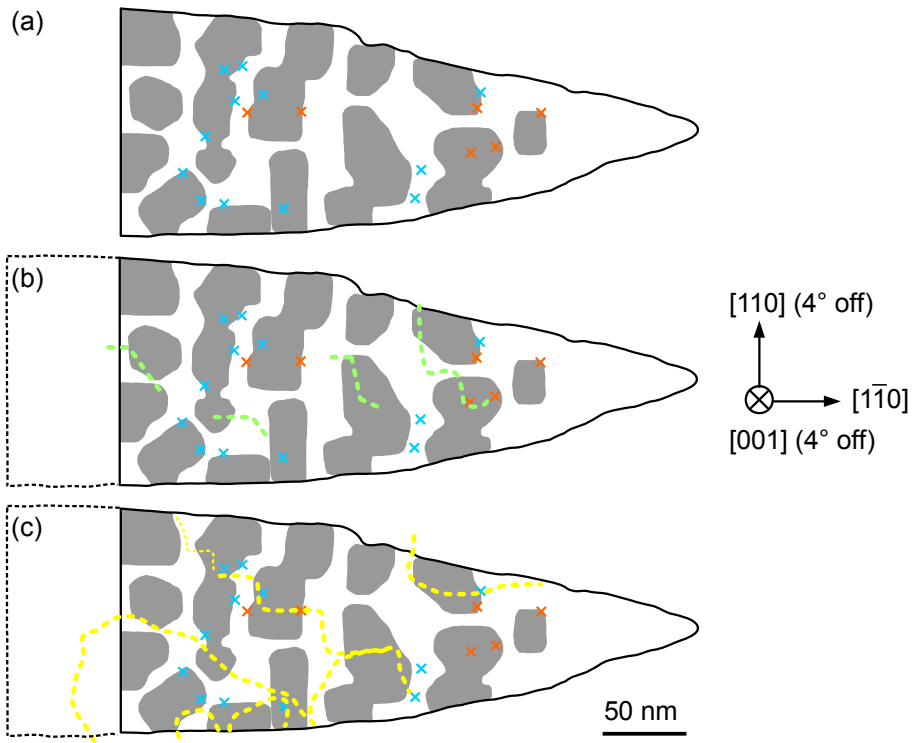

Figure 4.19. The location of AlSb islands which has been deduced from tomographic measurements is related to microstructural features acquired by complementary (S)TEM measurements. The silhouette of the specimen appears as black lines. The AlSb islands are filled grey areas. (a) The position of threading dislocation, (b) faults in one set of dislocations in the MFD network at the interface observed in the WBDF image and (c) the APBs suggested by the DF TEM image are superimposed to the silhouettes and the TD positions.

This imaging condition is assumed to be sensitive to anti-phase boundaries. Dark irregular bands are observed which are marked by yellow dashed lines. Due to the applied diffraction conditions, these dark objects are treated as a hint to anti-phase boundaries (APBs). The occasional widening of bands is attributed to an inclination of APBs with respect to the viewing direction. The DF image exhibits residual Moiré fringes. The slight tilt out of the [00$\bar{1}$] zone is not sufficient to completely attenuate this effect. In contrast, Moiré fringes are suppressed in the WBDF image taken at a tilt angle of 22° as observed in figure 4.18(a).

The experimental results are summed up in the schemes displayed in figure 4.19. The silhouette of the specimen is illustrated along with the lateral island shapes (grey areas). This information is obtained by the tomography investigation as outlined in figure 4.13. The image plane corresponds to the orientation of the original substrate surface. The schemes relate the location of AlSb islands with microstructural features which are revealed by complementary TEM and STEM measurements. Figure 4.19(a) correlates the results from the Moiré pattern analysis to the location of AlSb islands. Crosses mark the positions of threading dislocations. The prevailing presence at the edge of AlSb islands is evident. There are occasional defects superimposed on the islands location. The GaSb filled interspaces appear free of TDs except for two cases. The lateral expansion of islands during GaSb overgrowth is expected to proceed symmetrical on opposed island faces. That is, the location of island coalescence during the transition from the 3D to the 2D growth mode is in the middle between

two AlSb islands.

The black dashed line in the left of figures 4.19(b) and (c) belong to the larger investigated part of the specimen. The scheme of the former figure shows the location of shifted MFD lines by green dashed lines. The presence of these lines is attributed to further sites of coalescence (see discussion in section 4.2.2.2). Sites apart from notches and concavities which are revealed from the tomogram, point to smaller AlSb nuclei that merged to form the detected, 30 nm to 36 nm sized islands. This fact is learned although the information from the WBDF micrograph is rather fragmentary due to three points. The resolution from the observation under the shallow incidence is rather poor. The second set of MFD is not accessible. The network is obscured by strain contrast from TDs. The analysis of the interactions between TDs and the MFD shifts is impeded under these circumstances.

The APBs suggested by figure 4.18(b) are superimposed to the silhouette in figure 4.19(c). The correlation to island boundaries or the bisection of their distances is hardly observed. The detection of the contrast features near TDs is possible under the chosen diffraction condition, i.e. the $(0\bar{2}0)$ reflection is not sensitive to the TD strain fields. Therefore, the abundance of the dislocations in the vicinity of APBs is observed. The implications of these findings are discussed below.

A comment on the relation of results from the WBDF micrograph in figure 4.19(b) and from the DF image in figure 4.19(c) has to be made. The shape of green dashed line fragments is similar to segments of the APBs. The position agrees in several parts. The location of the APB at the interface is assumed to be offset from the broad contrast features originating from inclined APB parts. The expected inclination is dedicated to the fact that lots of APD annihilate within the first tens of nanometres of GaSb buffer growth (see, for instance, [191]). Therefore, a correlation of the MFD network shifts and the occurrence of APBs is suggested.

4.2.2. Discussion

Implications for the growth of III-Sb layers on Si are discussed in the following two sections. First, morphological features are under consideration. The island shape, the coalescence of islands and the meaning of the Si wafer miscut have to be faced. In the second section, the generation of TDs and their interaction with AlSb islands and the MFD network are addressed. Limiting factors and benefits of the experimental methods are regarded in the final section.

4.2.2.1. Anisotropic AlSb island growth and coalescence

A preferential growth direction of AlSb is suggested by the lateral shape analysis with respect to figure 4.13. It points along the [110] orientation. This direction is perpendicular to the prevailing surface steps along the $[1\bar{1}0]$ direction. The situation is schematically depicted by the right island shown in figure 4.20(a). This observation is unexpected with regard to the Schwöbel barrier imposed by surface steps. Schwöbel and Shipsey [192] have argued that crossing a surface step requires to overcome a potential barrier for atoms diffusing on a crystal surface. Consequently, atoms diffuse on terraces parallel to surface steps and arrive preferentially at island {111} facets that are not parallel to the steps. There, they are included on the island surface starting at the intersection line between side facet and Si(001) terrace. Thus, the growth along the step direction is promoted as illustrated in the middle of figure 4.20(a).

In fact, the experimental data hints to many island coalescences that have to occur due to an expansion in the direction perpendicular to the steps. Figure 4.20(b) shows the non-

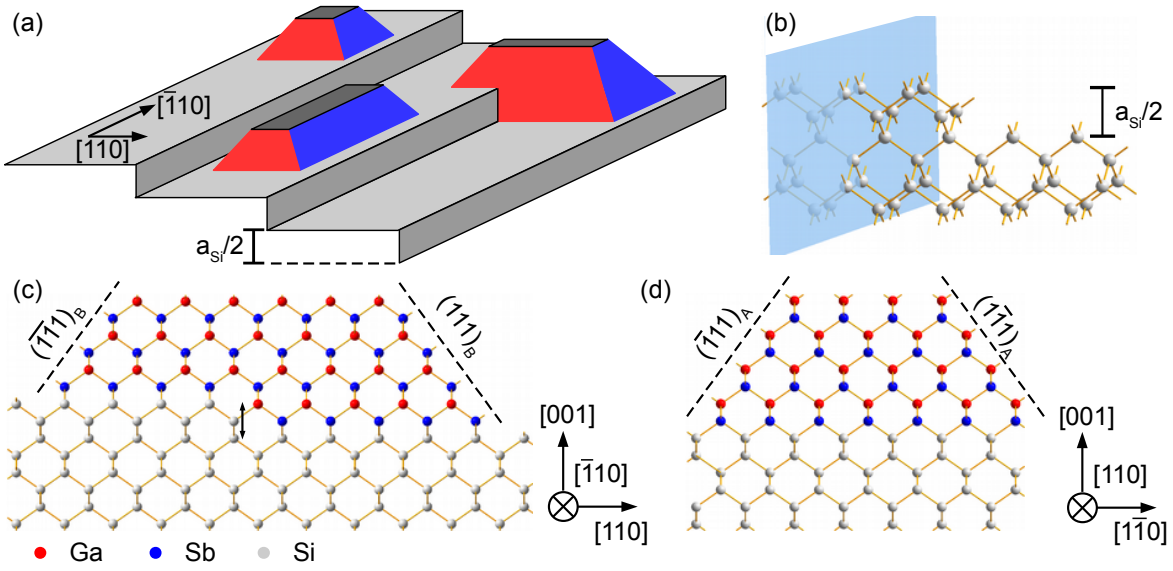

Figure 4.20. (a) The scheme presents three examples of lateral islands dimensions. Red and blue side facets correspond to Ga and Sb terminated $\{111\}_A$ and $\{111\}_B$ facets, respectively. (b) A double step on the unreconstructed Si(001) surface is illustrated. The blue plane marks the position of a {110} lattice plane. The idealized epitaxial continuation of the Si substrate with GaSb (starting with Sb) is presented along the orthogonal (c) $[1\bar{1}0]$ and (d) [110] directions. The double arrow highlights the double step.

reconstructed Si(001) surface with a double atomic step which has a height of half the Si lattice constant $\frac{a_{Si}}{2}$. The energetically favourable orientation of dangling bonds with respect to the surface step direction is known from literature [193], i.e. they lie in a $\{110\}$ plane parallel to the surface step. The applied Sb soak in the MBE chamber preceding the III-Sb growth start suggests that the first layer bonding to the Si substrate consists of Sb atoms. The epitaxial arrangement of GaSb atoms on the Si(001) surface with one double atomic step is illustrated by the ball-and-stick models of the interface in the perpendicular viewing directions $[\bar{1}10]$ and [110] presented in figures 4.20(c) and (d), respectively. The lattice mismatch between Si and GaSb is neglected for simplicity. This merely geometric construction reveals the chemical termination of $\{111\}$ side facets. It is assumed that stable surfaces prefer the lower number of dangling bonds which determines the intersecting position of $\{111\}$ planes through the bulk crystal. The Ga terminated $\{111\}_A$ and the Sb terminated $\{111\}_B$ facets occur pairwise. Adjacent side facets of the truncated pyramids exhibit different surface terminations as shown in figures 4.20(c) and (d).

Hence, the anisotropic expansion along the [110] direction is assigned to the preferential growth on $\{111\}_B$ facets. The isotropic growth on both types of $\{111\}$ facets would result in truncated pyramids like the one in the left of figure 4.20(a). Furthermore, Schwöbel barriers imposed by the substrate miscut are negligible for the discussion of island anisotropy. The average terrace width is one order of magnitude smaller than the respective island dimensions. The expansion of AlSb islands in the orthogonal direction would hint to APB and single atomic steps on the vicinal Si(001) substrate. Indeed, Akahane *et al.* [181] described AlSb islands elongated in both directions [110] and $[1\bar{1}0]$ on Si(001) substrate without miscut where single atomic steps prevail [193]. The preferential growth on $\{111\}$ planes terminated by group V elements is in agreement with observations by Kang *et al.* [194] (GaSb on GaAs(001) substrates) and by Ernst and Pirouz [195] (GaP on nominal and vicinal Si(001) substrates).

4.2.2.2. Coalescence of islands

The presented results distinctively show the coalescence of islands during the initial growth stage of the antimonide layer. The current notion supposes the creation of TDs due to a mismatch of MFD networks in different islands. The discovered number and distribution of TDs suggests mechanisms to connect networks without the emergence of dislocations. Models of island coalescence found in literature are summed up in the following paragraphs. Afterwards the implications of the experimental results are regarded with respect to existing and extended models.

Coalescence without the formation of threading dislocations

Figure 4.21 is dedicated to the matching of MFD networks without the emission of a TD. The initial state before coalescence occurs, is illustrated in figure 4.21(a). The island perimeters are illustrated as grey rims. One set of MFDs with the equilibrium distance d_1 is represented by black dashed lines. The orthogonal set is omitted for simplicity. The model for the MFD formation is described by Rocher and Snoeck [190]. It is based on the inclusion of perfect 90° dislocations at the lateral growth front i.e. along the [110] and the $[\bar{1}10]$ direction. The

Burgers vector of these Lomer dislocations $\vec{b}_{90^\circ}$ lies in the (001) interface plane together with the orthogonal line direction. Consequently, the dislocation does not belong to a common glide system of bulk sphalerite structure. These glide systems are bound to the $\{111\}$ planes outlined by the Thompson tetrahedron (see figure 2.3). Perfect dislocations of a common glide system are denoted 60° dislocations although they only form an angle of 60° in case of a respective line direction. This convention is convenient to distinguish the sessile Lomer and the glissile dislocations. $\vec{b}_{90^\circ} = \frac{1}{2}[110]$ is assigned to the sketched dislocation lines without loss of generality for the following considerations. In general, the parallel sets of MFDs in the two islands are shifted with respect to each other. Hence, the question arises how dislocation lines connect to each other without gliding when islands merge.

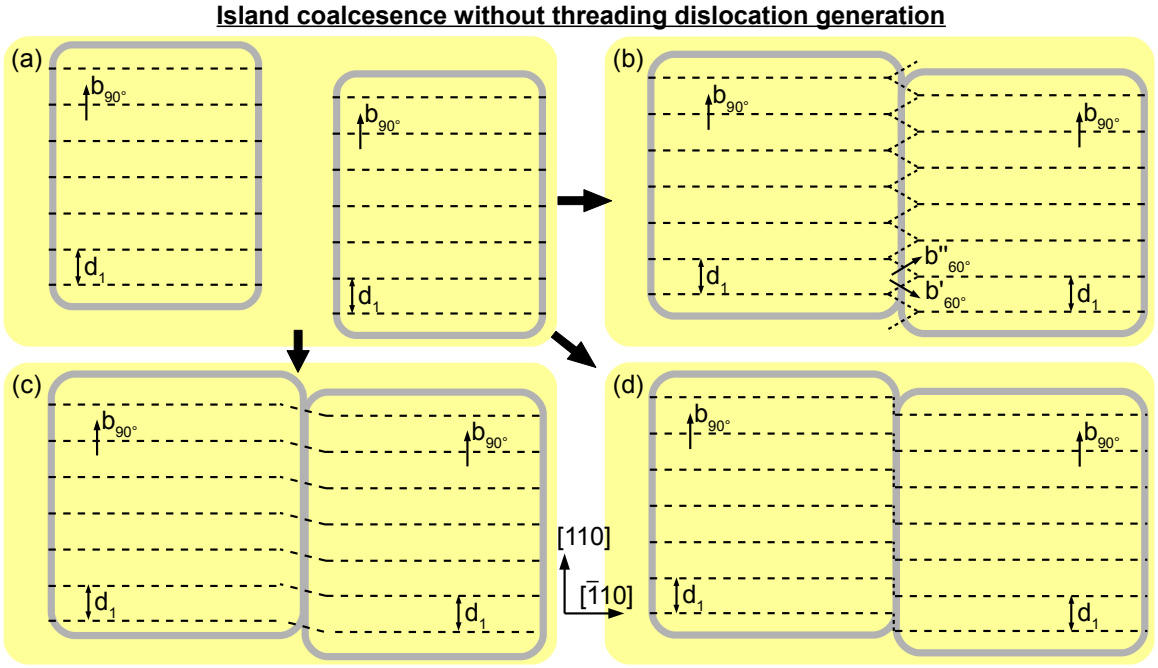

Figure 4.21. The schemes depict the island perimeter (grey rim) in the (001) interface plane. One set of the MFD network is represented by dashed lines with a equilibrium distance d_1 and the Burgers vector b_{90° of a perfect dislocation. (a) In general MFD networks of two islands are not in phase. (b) - (d) Different models for the behaviour of MFD networks during island coalescence have been proposed [194, 196, 197]. (Details are described in the text.)

Figure 4.21(b) represents a proposal of Zhu and Carter [196] who investigated the case of GaAs on Si(001). They actually studied the reaction of a 60° dislocation gliding to the interface and reacting with the 90° MFDs. Later Kang *et al.* [194] considered the insertion of 60° dislocation segments with $\vec{b}'_{60^\circ}$ and $\vec{b}''_{60^\circ}$ as mechanism to link the shifted sets of MFDs in two islands for the case of GaSb epitaxy on GaAs(001) substrates. The Burgers vectors must satisfy one of the following equations at the nodes.

$$\frac{1}{2}[110] = \frac{1}{2}[101] + \frac{1}{2}[01\bar{1}] \tag{4.9}$$

$$\frac{1}{2}[110] = \frac{1}{2}[10\bar{1}] + \frac{1}{2}[011] \tag{4.10}$$

The zigzag structure is dedicated to an energetically favourable configuration but requires a glide within the (001) plane as outlined by Zhu and Carter [196]. It is omitted by Kang *et al.* [194] keeping the glissile dislocation character of the 60° segments. The natural origin of an initial 60° dislocation at the coalescence line is considered below. Moreover, the authors distinguish between large MFD network shifts of approximately $\frac{d_1}{2}$ and small ones. In the latter situation, they assume the direct connection of MFDs with a slight bending as presented in figure 4.21(c). A different explanation for the observed shifts of $\frac{d_1}{2}$ is given by Komninou *et al.* [197] who dwell on the problem of GaAs growth on Si(001) substrate. The integration of polar GaAs on non-polar Si entails the formation of APBs. It is argued that the interaction of an APB with the MFD network requires the shift for symmetrical reasons. As a result, the connection is realized by short screw components placed within the APB at the interface between layer and substrate [197]. This situation is illustrated in figure 4.21(d).

The ideal linkage of MFD networks without the emission of TDs is considered because the density of threading defects is much lower than the density of coalescence sites. The finally established MFD network appears less disturbed in the presented heterostructure of GaSb on vicinal Si(001) compared to the case of GaAs on Si(001) (cf. micrographs in [196, 197]). The obvious difference is the shorter MFD spacing d_1 in the heterostructure with the higher lattice mismatch. To account for this perfection, mechanisms to align the MFD over long distances are regarded in addition to the models presented in figure 4.21. Bourret and Fuoss [198] studied the GaSb/GaAs system and introduced the idea of a "generalized Stranski-Krastanov mechanism". They observed a periodic interface corrugation that might be initiated by a thin alloyed layer of Ga(As,Sb) at the early growth stage before the island formation would start. A much simpler notion comprises the movement of MFDs within the (001) interface plane. This consideration violates the common idea of the sessile Lomer dislocations. The usual slip system in bulk fcc crystals requires the Burgers vector and the dislocation line to lie on a {111} lattice plane [62]. Rare examples for dislocation motion on {001} planes are presented, for instance, in [62, p.273] and in [199] for bulk fcc metals. The model introduced by Zhu and Carter [196] actually demands the (001) glide plane, too. Evidence for the movement of Lomer dislocations in the (001) interface plane is given by Qian *et al.* [200] who have investigated the growth of GaSb on GaAs(001). They observed that MFD nucleate at the island growth front with a spacing greater than d_1 and move inward during continued lateral island expansion to reach the equilibrium distance. On the other hand, the character of bonding at the heterostructure interface is assumed to be similar to the bulk layer and substrate material because both III-V and Si exhibit a covalent bonding. Hence, the origin of the stress to conservatively move a MFD or even a set of MFDs on the (001) plane is questioned.

Formation of threading dislocations during coalescence

A survey of proposed mechanisms for the generation of TDs is given in figures 4.22 and 4.23. The first case is a consequence of a different MFD spacing in networks. The equilibrium distance d_i depends on the height of an island [194]. Thus, two islands with d_1 and d_2 have to be connected as shown in figure 4.22(a). Kang *et al.* [194] investigated the growth of GaSb on GaAs(001). They have observed the termination of two half lines in Moiré patterns of plan view samples (cf. equation 4.8). Thus they have concluded that 90° dislocations

move out of the interface as depicted in the right part of figure 4.22(a). It is remarked that the pure edge character will be preserved if the dislocation line is kept as short as possible during subsequent growth.

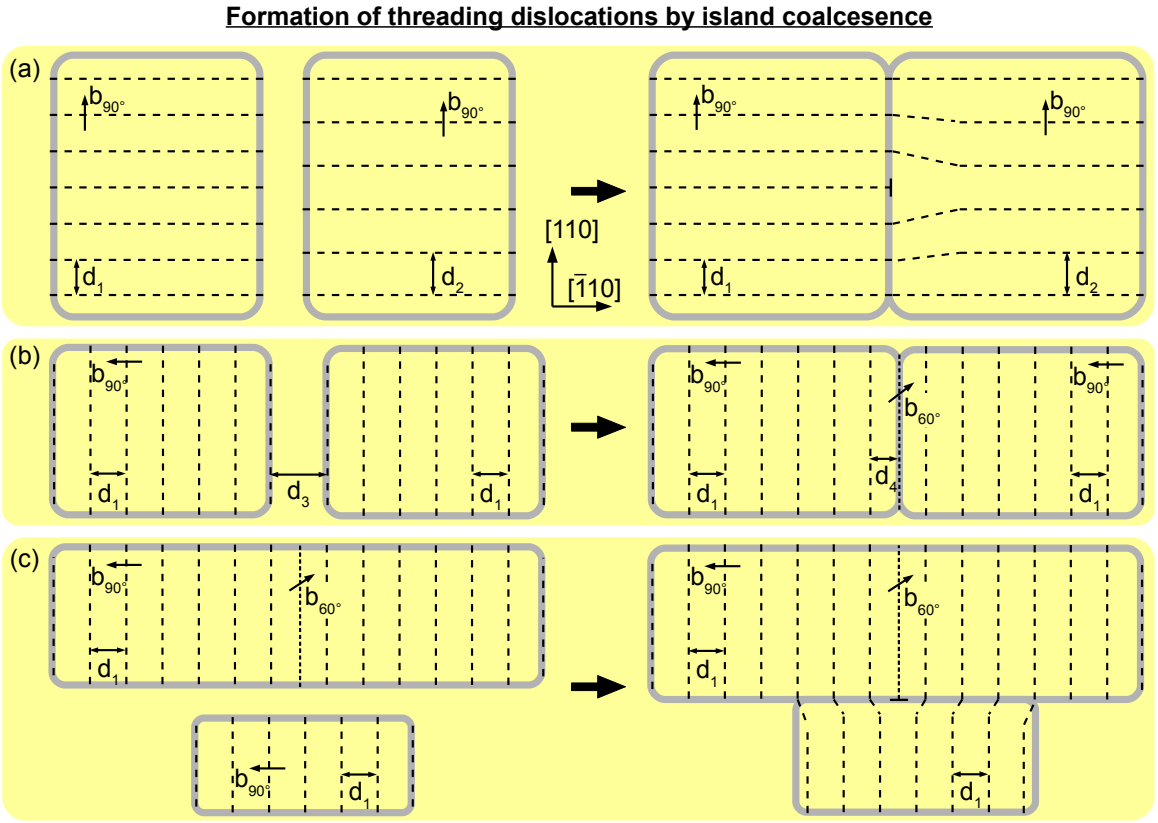

Figure 4.22. The schemes depict the island perimeter (grey rim) in the (001) interface plane. One set of the MFD network is represented by dashed lines equilibrium distance d_1 and the Burgers vector b_{90° of a perfect dislocation. (a) An island height dependent equilibrium distance d_2 is added according to [194]. (b)+(c) The insertion of a perfect 60° dislocation and subsequent implications are illustrated.

Except for this example, mixed type dislocations are usually observed to emanate from the interface. Three possible origins are discussed which are based on reports in literature. The first one is mentioned by Rocher and Snoeck [190] and illustrated in figure 4.22(b). If the distance between two islands d_3 is very small and if MFDs are just nucleated at the island edge, the remaining lateral stress $\sigma_{\parallel}$ will not suffice to form a further perfect edge dislocation. The spacing of the last two MFDs fulfils $d_3 < 2d_1$. The right scheme illustrates the insertion of a 60° dislocation at the interface passing through the coalesced island instead. This train of thought has to be completed because, so far, this does not give rise to a threading dislocation. Figure 4.22(c) describes the circumstance at a triple point during the coalescence with a third island. Here, the 60° dislocation cannot match one of the MFDs. Hence, it moves out of the interface plane as illustrated or has to react with one MFD whereupon a third line segment with a different Burgers vector is emitted into the layer. At this point, it is worth to consider the orthogonal set of MFDs and the model presented in figure 4.21(b). The mechanism to create a 60° dislocation according to figure 4.22(b) inherently

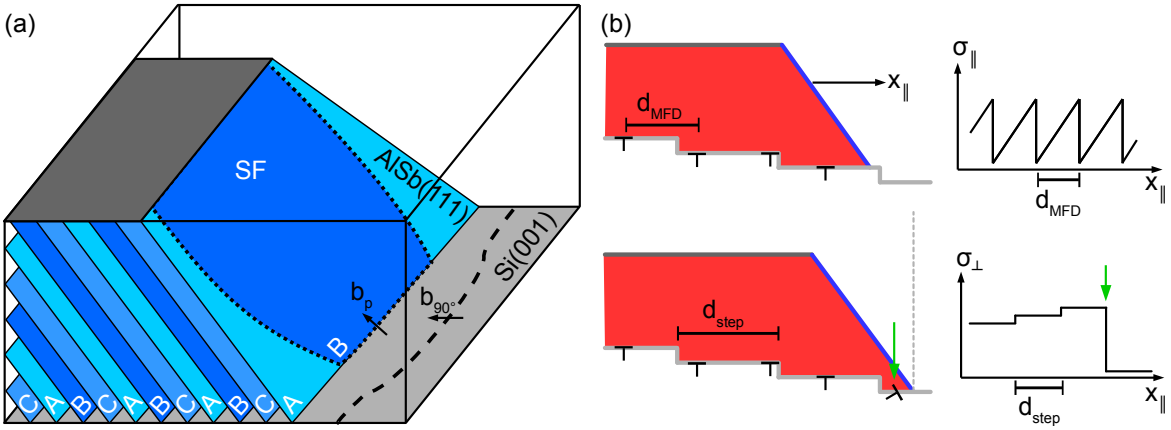

Figure 4.23. (a) The simplified scheme illustrates the interaction of a SF that randomly nucleates on the (111) growth front, and the MFD network. (b) The sketch depicts the extension of the island along $x_{\parallel}$. The diagrams schematically describe the development of the in-plane $\sigma_{\parallel}$ and out-of-plane $\sigma_{\perp}$ stress.

provides a dislocation to link the shifted orthogonal MFD networks. To be precise, the idea must be extended because alternating 60° segments ($\vec{b}'_{60°}$ and $\vec{b}''_{60°}$) are required.

The next two cases regard further sources fot the formation of 60° dislocations before island coalescence. Indirectly, they lead to TDs according to figure 4.22(c). Ernst and Pirouz [195] report on an unexpectedly high SF density in several heterostructures on Si(001) which start growing in a 3D mode. Later, islands coalesce to a closed film and 2D growth follows. The authors explain this phenomenon by the random inclusion of SFs on {111} side facets during initial island growth. They assume that layers at the growth front that nucleate in wrong positions on {111} planes, result in SFs which cover the complete side facet. Alternatively, the formation of SFs or twins is caused by impurities at the substrate surface as recently outlined by Madiomanana *et al.* [201]. These mechanisms are independent of the island coalescence. In fact, Qian *et al.* [200] state that the dislocation density in GaSb layers grown on GaAs(001) does not increase during island coalescence. Vajargah *et al.* [165] show SFs within AlSb islands deposited on Si(001). TDs are already formed during the initial 3D growth mode. At this stage, the SF only forms a dislocation line with the interface to the substrate. Again this idea must be further elaborated with regard to island coalescence. Figure 4.23(a) outlines that the SF is bound by TDs after the adjacent islands merged with the faulted one. In this case, a partial dislocation b_p is formed at the interface. Of course, a reaction with a MFD is thinkable, too. In addition, the nucleation of dislocation half-loops and their glide toward the interface [68] has to be considered as source for TDs after the closure of the epitaxial film. The driving force could originate from residual, accumulated strain similar to the case of figure 4.22(b). This option is discussed in section 4.3.2.1.

So far, the origin of TDs is discussed regardless of the Si(001) substrate miscut. The upper part of figure 4.23(b) describes the above discussed notion in terms of in-plane stress $\sigma_{\parallel}$. The island expands in the lateral direction $x_{\parallel}$ while $\sigma_{\parallel}$ increases to a critical value. The nucleation of a MFD at the intersection of interface and growth front relieves the stress. This procedure is periodically continued until islands coalesce. The application of a wafer miscut necessitates the consideration of an out-of-plane stress $\sigma_{\perp}$. Every time the growth front crosses a surface step $\sigma_{\perp}$ increases. Finally, the accumulated stress has to be plastically

relaxed by a dislocation. The Lomer MFD do not contribute to this relaxation. A dislocation with a Burgers vector component along the [001] direction is required which is most efficiently realized by 60° dislocations $\left(\vec{b} \in \left\{\frac{1}{2}[101], \frac{1}{2}[011], \frac{1}{2}[0\bar{1}1], \frac{1}{2}[\bar{1}01]\right\}\right)$. This situation is depicted in figure 4.23(b). Assuming ideal Si double steps and a terrace width of 3.9 nm, every 9 steps or after approximately 35 nm such a dislocation has to be included in case of the listed 60° dislocations. The alternating sign in the component along the [001] direction in equations 4.9 and 4.10 implies that the configuration proposed in figure 4.21(b) does not relief the out-of-plane strain due to the stepped substrate surface. Partial dislocations would be less effective but could contribute as well. On the other hand, they trigger the formation of a SF. Hence, there is a general need for dislocations at the interface in addition to the 90° MFD.

Comparison to experimental results

Eventually, a comparison of discussed models and the experimental facts is provided in the following. The analysis of the Moiré pattern according to figure 4.16 does not reveal TDs with a Burgers vector parallel to the (001) interface plane in the investigated specimen. As a consequence, the height distribution of the present islands does not account for different equilibrium distances d_i of MFDs which has been discussed with respect to figure 4.23(b). On the other hand, the height dependence of d_i could be saturated for the prevailing island heights. In addition to the Moiré analysis, a result from section 4.3 is anticipated. Dislocations with $\vec{b} = \frac{1}{2}[110]$ are rarely observed in subsequently grown layers although the investigated volume is much larger. Beyond, the detected dislocations are formed apart from the interface in dislocation reactions.

The presence of perfect 60° or partial dislocations at the interface is a necessary consequence of the deduced TDs. The determination of their segments within the (001) plane is inaccessible due to the unique sample holder tilt axis limiting possible imaging conditions. Nevertheless, they are excluded as cause for the observed half period shifts in MFD networks which are outlined in figure 4.18(a). On the one hand, those segments are expected to run along the intersection lines of {111} glide planes with the interface. The irregular courses would imply a non-conservative motion parallel to the (001) planes before meeting the interface. The motion within the interface plane is hindered by the presence of the MFDs. On the other hand, the presented results clearly suggest the interaction of the MFD network with APBs (cf. figures 4.18 and 4.19). Therefore, the coalescence model according to figure 4.21(d) (cf. [197]) is regarded as explanation for the observed shifts.

The predominant detection of TDs at the edges of AlSb islands is unexpected. The coalescence of islands during GaSb overgrowth is assumed to occur midway between two initial AlSb islands. Two scenarios are considered. Either TDs are formed where they are observed, or they move toward these sites. The motion needs to answer the question for the driving force again. The residual stress is regarded as too small in order to extend the dislocation line within the heterostructure interface. The proximity to the presence of APBs (cf. figure 4.19) is emphasized with respect to the first scenario. On the contrary to the assumption on the site of coalescence, a monoatomic step hinders the lateral expansion of the island because the insertion of an APB is required. Hence, the interspace is filled by only one expanding

island and the coalescence occurs at the edge of the AlSb island where the APB must be formed during the closure of the epitaxial film. At this site, a perfect 60° dislocation like in figure 4.22(b) or (c) is forced to bend upwards. The interaction of the dislocation with the APB is treated in chapter 4.3.

The lateral bending of the Lomer dislocations in order to connect MFD of different islands is apparently easier in the high mismatched GaSb/Si system than in, e.g., GaAs on Si because the maximal shift accounts for only 4 GaSb(110) lattice planes. This allows the linkage according to figure 4.21(c). The shift between the networks is smaller than 1 nm in 66 % of the cases. Therefore, the perfection of the MFD network is facilitated by the large mismatch and the small equilibrium MFD distance. Whether the MFD are straightened to minimize the line energy, is difficult to judge from the presented investigation. In fact, this confirmation would give another hint to the mobility of Lomer dislocations at the interface - be it conservative or non-conservative.

4.2.2.3. Technical aspects of the measurements and results

Tomography

Benefits and limitations of the tomographic results partly coincide with the explanations in section 4.1.2.2. Occasionally, this section is referenced for a more detailed description in the following paragraphs. The benefits due to a full tilt by 180° apply to the presented results as well. For instance, the cupping artefact [156] does not occur (cf. $(1\bar{1}0)$ slices in figure 4.14). This situation should enable an easy segmentation by the selection of a small number of discrete grey values. They only need to represent Si, AlSb and GaSb. But neither the direct isosurface presentation of the AlSb layer nor the approach to inherently render the volume with the DART algorithm in TomoJ [202] succeeds for the presented results. Three aspects are mentioned that have to be considered as explanations for this drawback. Firstly, the marker for image alignment is situated far from the region of interest. As outlined in section 4.1.2.2, the blurring of object details increases with the distance to the marker due to image distortions. Secondly, the grey scale calibration is related to the average image intensity (cf. section 3.2). On the other hand, the contrast is not explicitly regarded for the grey scale calibration. For example, the contrast between the amorphous damage layer and the intact specimen depends on the crystal orientation (cf., for instance, [129]). Thirdly, figure 4.24 shows an image from the HAADF tilt series exhibiting periodic contrast features. The micrograph is acquired approximately in the [111] zone axis. The periodic fringes are attributed to Moiré contrast. This effect occurs less pronounced in several images. The tomogram does not exhibit a corresponding, periodic feature. Therefore, the fringes are averaged out as they are not aligned in the stack of tilt series images. An impact on the correct grey value distribution in the tomogram is speculated.

The evaluation of island dimensions from the tomogram is limited by the spatial resolution. The stated uncertainty of 3 nm is based on the Crowther criterion (equation 2.12 and [133]) with an object diameter $D = 100\,\text{nm}$ and the number of $N = 90$ projections. This estimate is rather pessimistic because height differences smaller than 3 nm are clearly observed. The reason is the choice of D which is related to the average specimen diameter. The islands themselves are smaller and, moreover, anisotropically regarding the lateral sizes

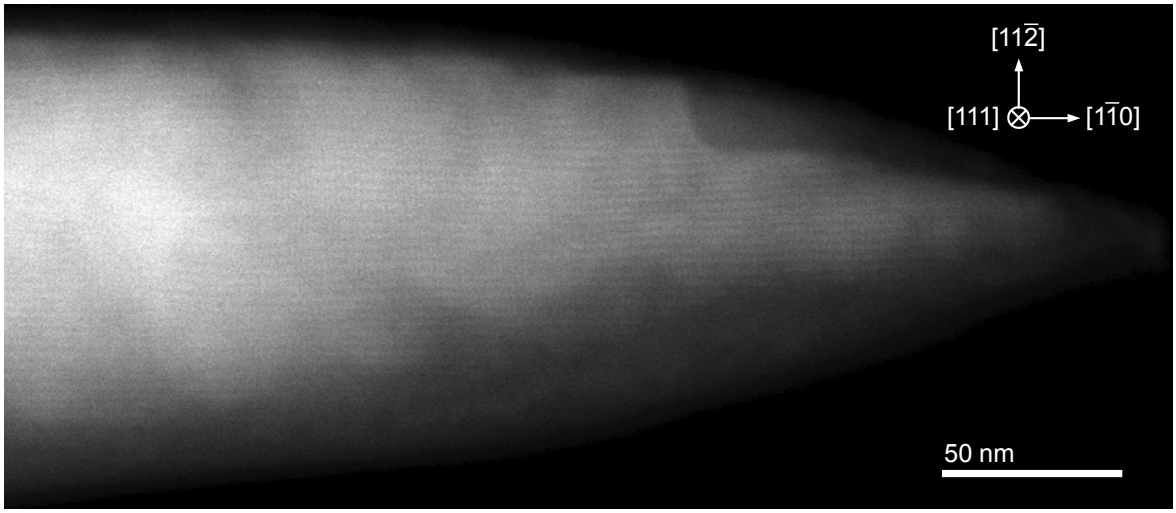

Figure 4.24. The HAADF micrograph is approximately acquired along the [111] viewing direction. The image exhibits short periodic contrast features that are related to Moiré fringes.

and their heights. On the other hand, the resolution downgrades with increasing distance to the tilt axis which is originally expressed by D. Consequently, the uncertainty of 3 nm refers to islands at the specimen edge but it is smaller for those ones located at the centre. It is pointed out that the spatial resolution assessment in electron tomography is currently an open question [142].

A comment on noise in the tomogram is suggested due to the results of this chapter. The section through the tomogram in figure 4.13 appears noisier in the left than in the right part. This gradient is very pronounced because of the reference point for the image alignment. The aligned tilt series is ideal near the specimen tip where the droplet served as marker. The serial image acquisition in STEM mode is prone to image distortions. Short range artefacts, i.e. the random displacement of scan lines with respect to neighbouring lines due to vibrational and magnetic disturbances, are expected over the whole image. Specimen drift will cause a systematic displacement of scan lines on the complete image length leading to a distortion. The goniometer is observed to mainly account for the observed specimen motion which occur with non-uniform drift rates. A delay time after each tilt is applied to reduce the resulting image distortion. The remaining deviations from the ideally undistorted situation accumulate with increasing distance from the reference point of image alignment. As a result, the tomogram exhibits the noise gradient due to the increasing misalignment of images far from the specimen tip.

Microstructure analysis

The relation of the Moiré (figure 4.16) and the WBDF (figure 4.18) image requests a critical consideration. Bollmann [71, p.49f] has outlined that a Moiré pattern provides a direct access to the location of the interfacial MFDs. Obviously, a discrepancy arises because the MFD spacing s is approximately two times larger than the Moiré period d_M. The semi-coherent interface (cf. figure 2.4) is established with respect to the $\{110\}$ lattice planes in the III-Sb/Si(001) heterostructure. Every 8 or 9 lattice planes, respectively, the coherence

is interrupted by one {110} half-plane on the substrate side. The prediction of Bollmann [71] would be valid if the Moiré fringes arose due to the coupling of g_{110} reflections. These reflections are forbidden due to the integral extinction rule of the fcc lattice. Hence, the double period is explained by the coupling of {220} reflections. Only every second MFD coincides with a minimum in the Moiré pattern. Therefore, the half-period shift in the MFD network which has been revealed in the WBDF micrograph, is not detected in the Moiré image.

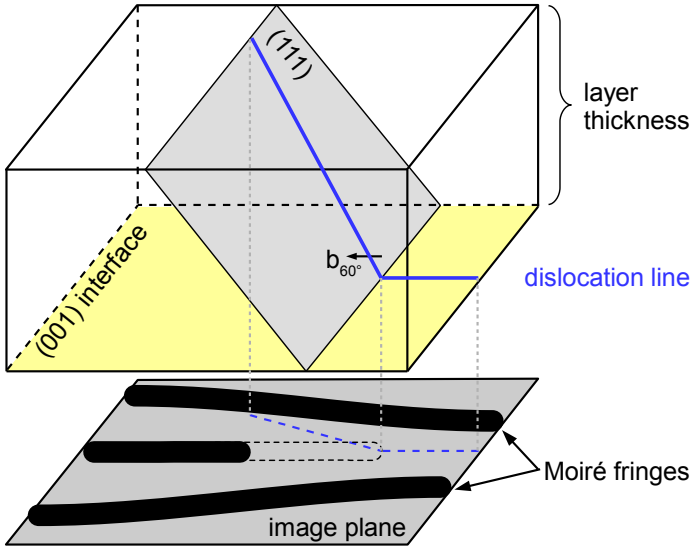

Figure 4.25. A threading dislocation line in the heteroepitaxial layer appears as half-line in the Moiré pattern. The location of the terminating half-line along the projected path of the threading dislocation is unknown (dashed fringe).

The actual position of the TD with respect to the terminating half-line in the Moiré pattern demands a further comment. Figure 4.25 describes the potential position of the Moiré feature along the projected path of the dislocation line. This uncertainty has been explained by Bassett *et al.* [188]. It is quantified with the knowledge of the epitaxial film thickness and of the dislocation habit plane. The III-Sb layer thickness t varies from 15 nm to 30 nm due to the conical specimen shape. The common {111} glide plane embraces an angle of $\theta = 54.7°$ with the (001) plane. Assuming the shortest line toward the surface, the uncertainty amounts to a range of $t/\tan 54.7° = 11$ nm to 21 nm. These values show that the localization of dislocation lines with respect to coalescence sites becomes inappropriate for thick parts of the layer. On the other hand, two arguments support the deduced TD positions. Firstly, the positions are consistent with the WBDF result which is sensitive to the dislocation strain fields. Secondly, it is anticipated that the dislocations run rather perpendicular to the (001) plane than under the angle of 54.7° in case of an interaction with an APB.

4.3. Threading dislocations in III-Sb based laser structures

The investigated functional semiconductor heterostructure is a layered stack of 5.3 µm thickness. The preparation of the lamella guarantees the access to the entire sequence of layers along the growth direction by TEM/STEM (cf. figure 3.5). A needle-shaped specimen does not cover enough sample volume to catch the microstructure in its whole complexity. In this way, the investigation of dislocations propagating through the whole III-Sb heterostructure is feasible. A 3D investigation allows to determine the line directions of dislocations and interaction sites of defects. The decision whether defects intersect, will be ambiguous in 2D projected images. The selection of the BF STEM mode (section 3.2.3) and the purposeful orientation of the sample (section 3.1.2) are indispensable prerequisites for the acquisition of the tilt series. The BF STEM mode allows the penetration of high specimen thicknesses. The orientation ensures contrast along dislocations over the whole tilt range in BF STEM images.

The following sections dwell on the disclosure of the 3D microstructure on the corresponding length scale. The experimental part is divided into three parts. In the first instance, the characterization of microstructural objects by STEM and TEM investigations is presented. These analyses rely on conventional 2D projections with well established methods. Afterwards, the acquisition of the BF STEM tilt series is described. Challenges in addition to the preliminary results which are presented in section 3.2.3 are considered. Subsequently, the 3D arrangement of dislocations and interaction sites are deduced from tomographic data in the third subsection.

In its first part, the subsequent discussion is dedicated to the 3D arrangement of defects. The location on different lattice planes and peculiar line directions are addressed. The final part regards the choice of the BF STEM signal for electron tomography that violates the projection requirement. Furthermore, the impact of the lamella orientation with respect to the asymmetry of the microstructure is discussed.

4.3.1. Experimental results

4.3.1.1. STEM/TEM analysis of microstructural objects

The use of the single tilt axis holder for tomography imposes a general backlash. Usually, the unambiguous characterization of dislocations requires two degrees of freedom in order to realize specific sample orientations. Thus, the control over diffraction conditions enables a quantitative defect analysis. Additional information of further specimens, therefore, complement the later 3D analysis of the tilt series described in the next section.

Dislocations

FIB lamellae prepared parallel to the two orthogonal directions [110] and $[1\bar{1}0]$ are mounted on a grid and investigated with a double-tilt sample holder. The loss of symmetry due to the substrate miscut necessitates to consider both directions. Figure 4.26 presents BF STEM images of two respective specimens. They provide an overview on the variety of TDs. The 9 µm wide field of view meets the requirement of a sufficiently large area for a survey. The indication of [110] and $[1\bar{1}0]$ is held consistent for the sample throughout the chapter.

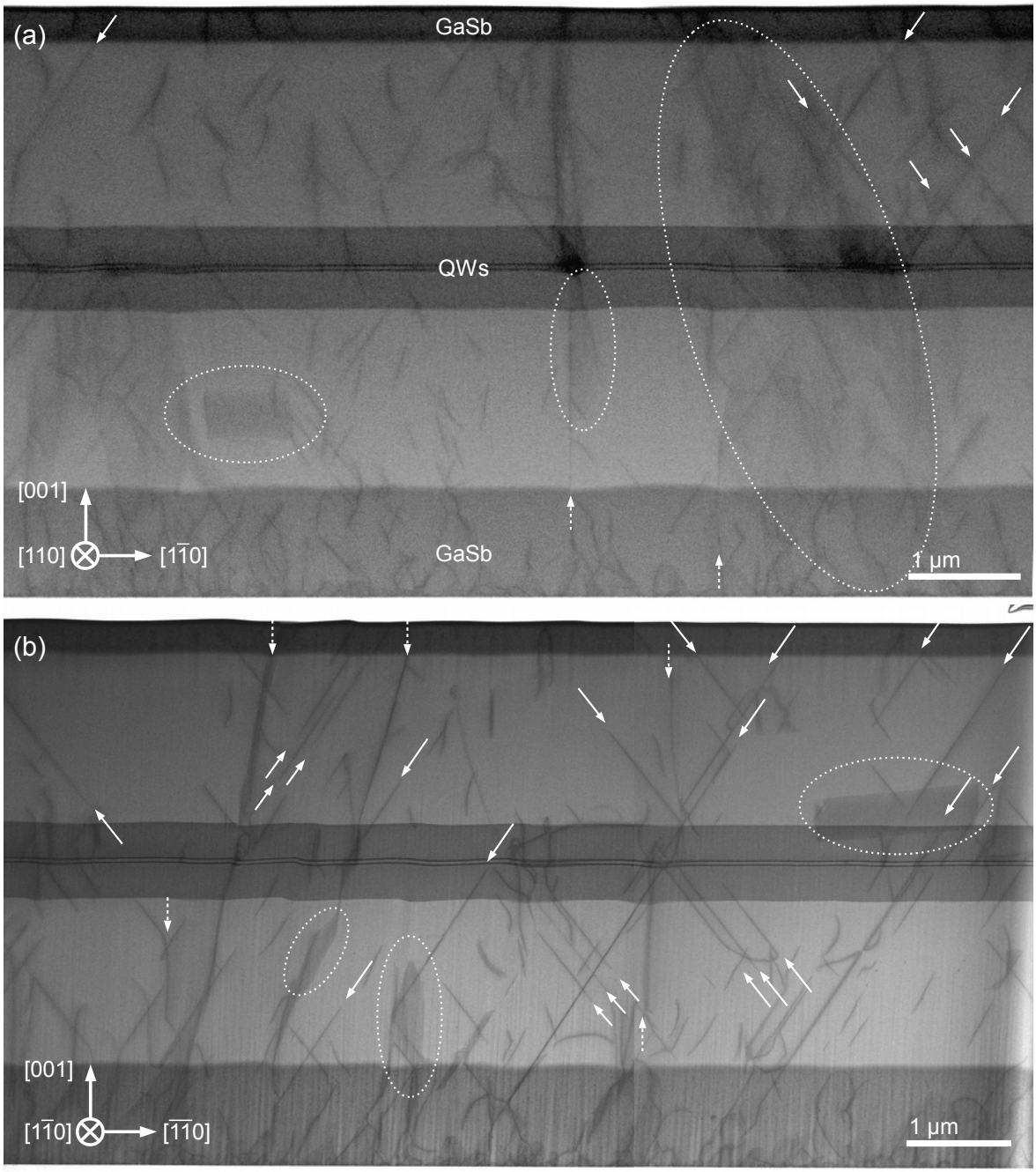

Figure 4.26. BF STEM images along ⟨110⟩ zone axes presenting a large field of view. Specimens of the laser structure are prepared as lamellae parallel to the (110) (a) and to the (1$\bar{1}$0) (b) lattice planes. The defect structure apparently differs in the two orthogonal viewing directions. (White arrows and dotted ellipses are explained in the text.)

The III-Sb polarity is not taken into account by this notation. The brightness and contrast settings in figure 4.26 are enhanced to emphasize dark features caused by line defects. The Si substrate appears as white saturated part at the bottom of the images. The dislocation line segments confined in the lamella differ in orientation, shape, length and density. Different

types are classified in the following. Moreover, the attention is drawn to differences in the two orthogonal directions.

The abundance of long, linear objects is observed to differ in figures 4.26(a) and (b). White arrows highlight straight, black traces that are inclined by approximately $\pm 54.7^\circ$ toward the horizontal interface lines of the heterostructure. They are related to the $\{111\}$ lattice planes which are imaged edge on. The object lengths indicate a confinement within a narrow slab parallel to the $\{110\}$ projection planes. Assuming dislocation lines, they run close to $\langle 112 \rangle$ directions. A confusion with SFs is considered below. These rather long line segments occur more often in the projection onto the $(1\bar{1}0)$ plane. In contrast, short segments with arbitrary directions present a second type. They are more abundant in the orthogonal projection onto the (110) plane. Their length along the [001] direction is in agreement with an appearance on $\{111\}$ lattice planes that belong to the $[1\bar{1}0]$ zone in figure 4.26(a) and to the [110] zone in figure 4.26(b), respectively. A third, distinct type is marked by dashed, white arrows. They point at lines that are predominantly directed in the growth direction. Often these defects are observed to appear in bunches as seen in the upper part of figure 4.26(a). Their lengths within the lamella points to a habit plane different from the usual $\{111\}$ glide planes.

It is remarkable that there are micrometre-sized domains appearing free of defects within parts of the III-antimonide heterostructure. This aspect might explain the successful operation of the device. On the other hand, figure 4.26(a) (cf. also figure 3.6) exhibits parts with a certain dislocation density which coincide with a grey shaded surrounding (large dotted ellipse). Furthermore, sites of exceptionally high dislocation density are observed. The bunches of dislocations predominantly oriented along the [001] direction are one example. Spots of high density near strained layer QWs are another one. Such locations are observed in figure 4.26 as well as in figures 3.6 and 4.28. In general, the dislocation density appears higher near the interface than elsewhere, that is, dislocations partially annihilate within the buffer layer. This fact is in agreement with the intention of the buffer layer. The reduction of the dislocation density to produce templates for growth is well documented, e.g. for the integration of symmetry equivalent diamond structured Ge on Si [203, 204] or for the heteroepitaxy of III-V compound semiconductors with zinc-blende structure on Si [69].

The lamella thicknesses need to be comparable in order to avoid confusion. The thickness of both specimens is estimated to be approximately 300 nm from FIB/SEM measurements during preparation. Slight thickness gradients from the top to the bottom and from the top left to the right bottom in 4.26(a) and (b), respectively, are deduced from the overall intensity change. The appearance of grey shaded areas is emphasized by dotted ellipses. Assuming the horizontally elongated ellipses highlight planar defects parallel to a $\{111\}$ plane, the lamella thickness t is confirmed from the projected height $h_{(001)}$ along the [001] direction:

$$t = h_{(001)} \cdot \tan \gamma.$$

$\gamma = 35.3^\circ$ is the angle between the (111) and the (110) plane. The measured height of (420 ± 10) nm yields (300 ± 10) nm in agreement with the former estimate. Defects extending in the growth direction and those marked by vertically elongated ellipses are reconsidered in respect to figure 4.27.

A comment on the chemical abruptness of the heterostructure interfaces has to be made

with regard to the BF STEM images in figure 4.26 at this point. The [110] view in figure 4.26(a) is oriented onto the prevailing substrate steps introduced by the wafer miscut. Therefore, interfaces are not imaged edge-on. In contrast, interfaces between cladding and wave guide as well as the quantum wells appear more abrupt in figure 4.26(b) because the $[1\bar{1}0]$ direction corresponds to the direction of the substrate steps and it is, therefore, parallel to the surface. Besides, steps parallel to the $[1\bar{1}0]$ zone axis with a height of approximately 10 nm are observed at all interfaces - here, most prominently at the lower transition to the wave guide. The transition from the buffer layer to the cladding appears blurred due to the composition gradient applied during growth.

Planar defects

Grey shaded areas are described with respect to figure 4.26. They are observed in figure 3.6, too. They are related to planar defects approximately parallel to the {110} planes because they partly stretch over the whole layer stack. Planar defects situated predominantly parallel to {110} lattice planes in zinc-blende structure are considered to be APBs. This assumption is proved in the following.

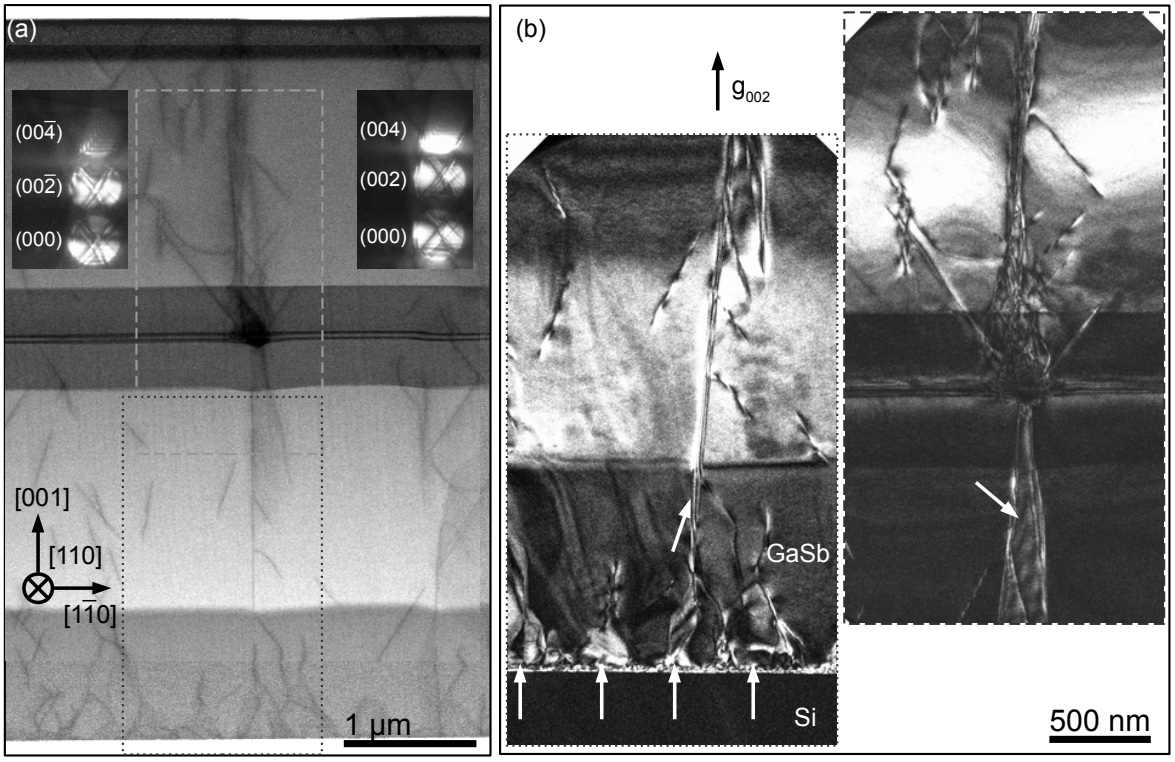

Figure 4.27. (a) The BF STEM image is an excerpt of figure 4.26(a). It focuses on defects that are predominantly stretch along the [001] direction. Interfaces appear to obtain a step at their intersection with these defects (white arrows). The insets show CBED patterns taken from the left and the right of the central defect feature. (b) DF TEM images with the $\vec{g} = (002)$ diffraction condition reveal the presence of planar defects. The images correspond to the framed parts in (a).

The enlarged central part of figure 4.26(a) is presented in figure 4.27(a). The grey dotted and dashed boxes refer to the location of DF TEM images shown in figure 4.27(b). The

insets present CBED patterns which have been recorded with the beam positioned at the lower wave guide layer. The left and the right pattern origin from the right and the left of the central defect feature that extends in the [001] direction, respectively. The superposition of the {002} diffraction discs with odd indexed HOLZ lines allows to discriminate between the (002) and the $(00\bar{2})$ reflection [205]. The dominant pair of crossing lines belong to the $(\bar{3}\bar{3}\bar{5})/(\bar{3}\bar{5}3)$ planes and to the $(\bar{3}\bar{5}5)/(\bar{3}\bar{5}\bar{3})$ planes, respectively. The allocation has succeeded with a respective CBED and HOLZ line calculation applying the JEMS software package [154]. In fact, Taftø and Spence [205] presented an inversion of the cross caused by constructive and destructive interference in the case of thin GaAs TEM foils. The thin film assumption does not apply here. But the qualitative difference seen in the comparison of the (002) and $(00\bar{2})$ discs remains and indicates the existence of anti-phase domains (APD). Therefore, the dark features along the [001] direction are related to the presence of an anti-phase boundary (APB), a planar defect.

The DF TEM images with the (002) reflection excited (figure 4.27(b)) confirm the presence of planar defects. The micrographs are taken from the vicinity of the bunch of threading defects. White arrows point at contrast oscillations. They are caused by planar defects which are inclined to the beam direction as well as to the imaging plane. The high density of such defects near the interface to the Si substrate has to be emphasized. Georgakilas *et al.* [191] applied the g_{002} condition to reveal APDs that self-annihilate during growth of several 10 nm of GaAs on Si. Apparently, there is a residual amount of APBs penetrating the presented antimonide heterostructure with its origin at the beginning stage of the sample growth.

In addition to the considerations of appropriate imaging conditions for tomography of dislocation lines (cf. section 3.2.3), the comparison of figures 4.27(a) and (b) supports the choice of BF STEM imaging. The diffraction conditions are not constant over the whole region of interest due to sample bending and thickness changes. Hence, the DF image suffers from respective contrast contours. Furthermore, the appearance of defect lines depends on the depth within the foil. Therefore, contrast oscillations are observed along defect lines that lie inclined within the TEM lamella. On the shown length scale, these circumstances even obscure the general sensitivity of the g_{002} imaging vector to the chemical composition of different layers in the III-antimonide stack. The structure factor of zinc-blende structures for g_{002} and, hence, the diffracted intensity depends on the difference of atomic scattering factors of the group III element and of Sb reasoning the chemical sensitivity. The integration over diffraction conditions by the convergent beam for STEM imaging effectively attenuates the contrast oscillations (cf. section 2.2.2). In consequence, there are not any thickness or bending contours. The line defects appear as homogeneous dark lines and the suite of layers with different composition is clearly resolved.

On the other hand, the contrast oscillations convey a rough notion about the orientation of defects and interaction of defects. The line defects appear to merge into the APB. The latter exhibits an average habit plane that is slightly inclined toward the $(1\bar{1}0)$ plane. The line defects consequently move out of their original glide plane which is assumed to be of {111} type. A precise determination of the line directions and the localization of potential interaction sites require the 3D investigation by tomography.

Perfect 60° dislocations are prone to the dissociation into a pair of a 90° and a 30° partial dislocation (see equation 2.1 and, e.g., [62]). The terms perfect 60°, partial 90° and partial 30° dislocation are used for convenience as in section 4.2.2. The actual angle is determined

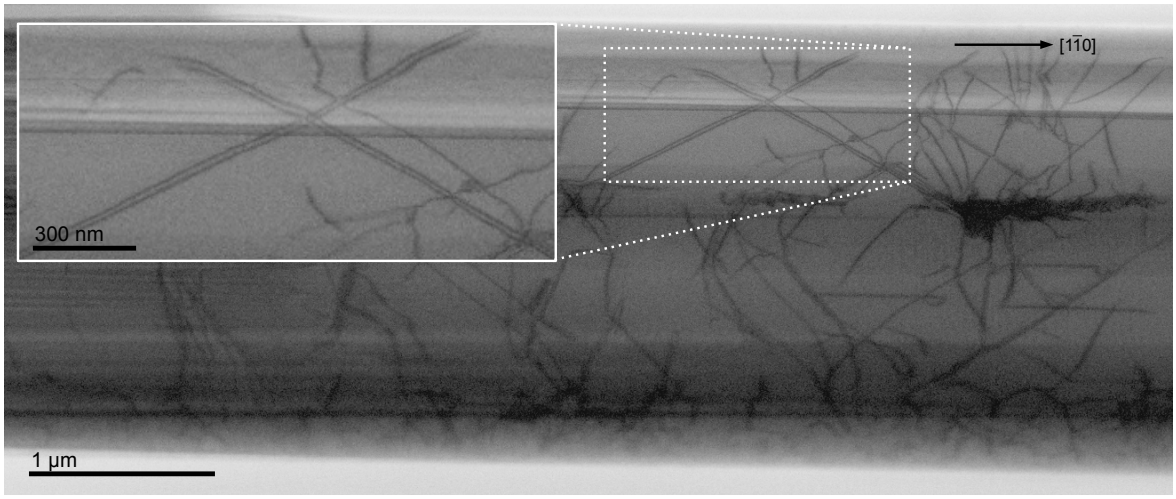

Figure 4.28. The BF STEM image is selected from a tilt series. The specimen is tilted −60° off the [110] zone axis. The magnified part of the image (inset) underlines the resolution of two lines at the high tilt angle.

by the Burgers vector and the line direction. The mentioned dislocations belong to a glide system which is in contrast to the sessile, perfect edge dislocations. The distinction between SF and partial dislocation as well as ruling out a single dislocation line succeeds with the acquisition of a BF STEM image at a high tilt angle (Fig. 4.28). Here, the $(1\bar{1}1)$ and $(\bar{1}11)$ lattice planes are not parallel to the viewing direction anymore. The micrograph clearly depicts two separated lines. Hence, the contrast features represent two partial dislocations that frame a SF. The projected distance of the partials corresponds to $\sqrt{2} \cdot (3 \pm 1)$ pixel. The pixel resolution is 4.8 nm and the inclination of the distance has to be regarded by multiplication with $\cos^{-1}(30°)$. This consideration allows to estimate the order of the distance to be (23 ± 8) nm. The SF width for several III-V semiconductors observed in early works by Gottschalk *et al.* [206] is smaller. On the other hand, there are reports on larger splitting and a high scattering of the width in InP by Luysberg and Gerthsen [207] covering the presently observed value. It is doubted that the measured splitting distance reflects the equilibrium state of bulk material as the SF origin is traced back to the QWs.

Direct contrast from this planar defect is too faint or not present under the imaging conditions. On the other hand, planar defects parallel to a (111) or a $(\bar{1}\bar{1}1)$ plane are supposed to explain features marked by horizontally elongated ellipses in figure 4.26. The allocation of the lattice plane is based on two facts. The calculated lamella thickness assuming a (111) plane and measuring the dimension of the shaded area matches the value from the SEM measurement. The clipping of the (111) plane with the lamella surface results in a straight and horizontal line. In figure 4.26, the lamella surface is not parallel to the $(1\bar{1}0)$ plane due to the substrate offcut. Therefore, the intersection line is inclined with respect to the interface orientations. Bounding dislocation lines are suspected from careful inspection of the planar defects edges. These indications suggest a several 100 nm wide SF to explain the observations. Quantitative BF STEM analysis of SFs have been performed by Phillips *et al.* [105] revealing depth dependent oscillations which blur due to multiple scattering. It is assumed that oscillations vanish for the imaging in a $\langle 110 \rangle$ zone axis and for 300 nm thick sample as presented in figure 4.26.

Dislocation motion

Figure 4.29 shows a BF STEM image that has been acquired from the layer subsequent to the GaSb buffer. The observed dislocations extend the characterization of static dislocation features outlined above. They give hints to the motion of dislocations. White arrows point at curly dark lines which indicate a non-conservative dislocation motion. The scheme next to the micrograph contrasts the different line shapes. Instead of being confined to {111} glide planes, the defect arbitrarily changes its glide plane. Short line segments on varying lattice planes lead to the curly appearance in micrographs. This mode of motion requires point defects accumulating at the defect line [168]. Hence, the climbed dislocations present a proof for the existence of point defects. A conservative motion is impeded after the climb process because the dislocation left its glide plane. This argument imposes the question how other dislocations arrive on non-{111} planes although looking rather straight. Respective cases are observed in figure 4.26.

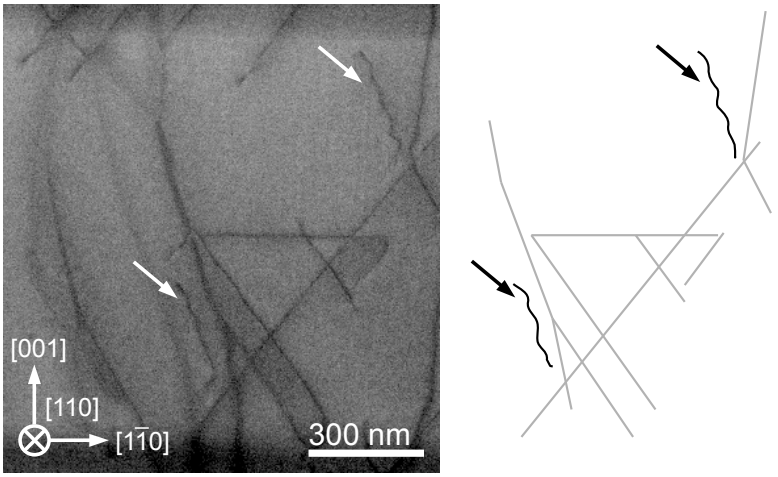

Figure 4.29. The BF STEM image displays a number of dislocations within the layer subsequent to the GaSb buffer. The sample is tilted by 12° from the [110] towards the [010] zone axis. Arrows point at curly dislocation lines. The scheme on the right emphasizes the addressed objects.

The knowledge on the actual line direction and the location of a certain lattice plane provides the information whether a dislocation is able to conservatively move. A further aspect for the mobility is the potential pinning of the dislocation in an interaction node. In the next sections, electron tomography is shown to offer this information. The horizontal line segment on a (001) plane in the centre of figure 4.29 is outlined as peculiar feature. The conservative motion to this state requires the line segment to be oriented along [1$\bar{1}$0].

4.3.1.2. BF STEM tilt series of a micrometre-sized TEM lamella

In contrast to needle-shaped specimens, a further challenge is imposed by TEM lamellae that extend as far as several micrometres. The capability to capture the whole specimen volume along the viewing direction in focus depends on the depth of field D_{obj}. It is related to the convergence semiangle α_c of the STEM probe and the target resolution d_{obj} by (see, e.g., [3])

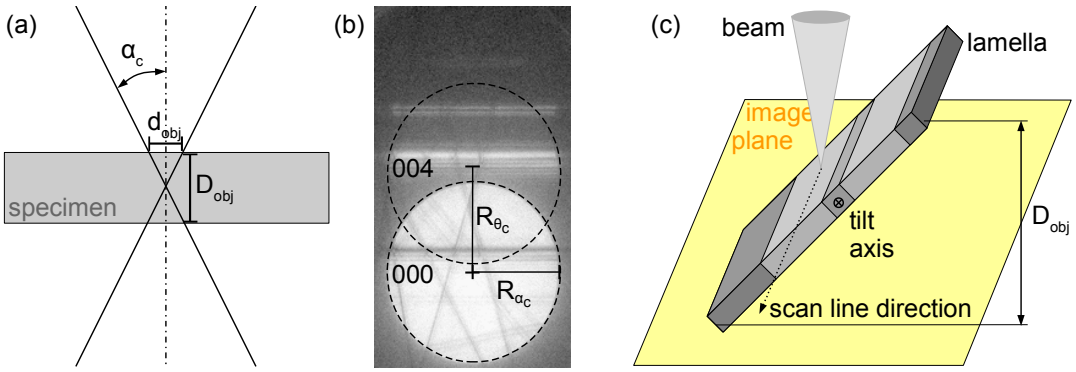

Figure 4.30. (a) The sketch defines the relation of α_c, the target resolution d_{obj} and the depth of field D_{obj}. (b) CBED pattern for the determination of the beam convergence semiangle α_c. (c) The graphic illustrates the impossibility to obtain a focused image of the tilted lamella if the beam focus is static.

$$D_{obj} = \frac{d_{obj}}{\alpha_c}. \tag{4.11}$$

Figure 4.30(a) schematically depicts the geometrical conditions of the specimen illumination by the electron beam. The D_{obj} is regarded to correspond to the specimen thickness along the viewing direction. α_c is determined from the CBED image of Si shown in figure 4.30(b). It has been acquired with the CCD while the microscope is operated in STEM mode.

$$\alpha_c = \theta_B \cdot \frac{R_{\alpha_c}}{R_{\theta_B}} \tag{4.12}$$

θ_B is calculated from the Bragg equation 2.9 for the Si (004) reflection. R_{α_c} and R_{θ_B} are defined in figure 4.30(b). The convergence angle is determined to be $\alpha_c = 17.5$ mrad. A target resolution of $d_{obj} = 4.8$ nm results in a depth of field of $D_{obj} = 274$ nm. The antimonide layer stack exhibits a thickness of 5.3 µm. At a tilt of, for instance, 45° as illustrated in figure 4.30(c), the top and the bottom of the lamella vary by 3.7 µm in height and cannot be focused at the same time. This problem is solved by the "dynamic focus" function implemented in the GMS tomography plug-in. The scanning line direction is set parallel to the tilt axis. The focus is corrected for each scanned line.

A tilt series is acquired over the range from −72° to 72° in steps of 3°. Figure 4.31 displays a choice of BF STEM images from this series. The tilt axis is approximately aligned with the $[1\bar{1}0]$ direction of the cubic layer structure. The closest approach to the [110] zone axis is set to the nominal goniometer tilt angle of 0°. The offset from the [110] direction is smaller than 0.8° which is deduced by comparison to SAD pattern calculation. The imaged field of view has been sampled with 1500 pixels x 1500 pixels corresponding to an area of 5.6 µm × 5.6 µm or a sampling rate of 3.7 nm /pixel, respectively. The dwell time per pixel is chosen to be 40 µs at 0° and is prolonged by $1/\cos\alpha$ for the respective tilt angle α. This option of the acquisition software is used to account for the decreasing intensity at high tilt angles. It is applied to avoid corrections of the contrast and brightness settings during the tilt series acquisition. Nevertheless, images at high tilt angles ($|\alpha| > 60°$) are contrast enhanced in order to illustrate microstructural features in figure 4.31. The other images are unprocessed to demonstrate the orientation dependent changes of the image intensity. The

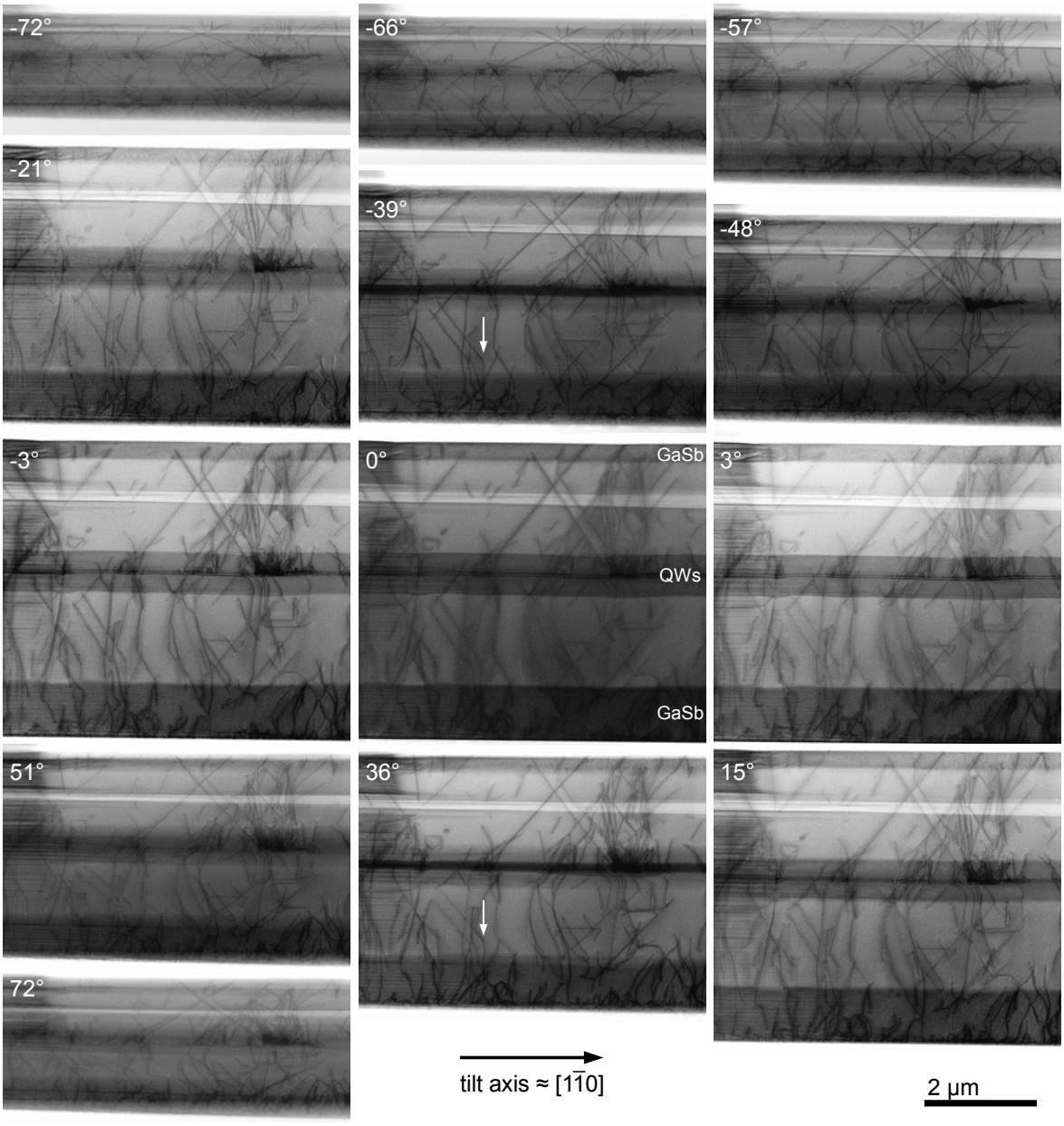

Figure 4.31. The BF STEM images present a choice of micrographs from a tilt series. The imaged part of the TEM lamella is 5.6 µm wide and 5.0 µm high. The white arrows point to a contrast feature that is invisible at most tilt angles.

image alignment is carried out with respect to the QWs and/or the bunch of dislocations at the QW in the right of the images.

Nearly all features assigned to dislocation lines stay in contrast for all tilt angles in accordance to the elaboration in section 3.2.3. One of the rare exemptions is marked by white arrows in figure 4.31. The respective line feature is invisible in most of the tilt series images. It is most clearly visible in the images at −39° and 36°. The BF STEM micrograph at 0° exhibits the best visibility of the shaded areas that are assigned to APB. In the right, a large one reaches from the bottom to the top of the lamella. It gradually expands along the [1$\bar{1}$0]

directions below the QWs and contracts in the upper part of the layer stack. A smaller APB is observed in the left. It is confined to the lower part of the heterostructure. It is bounded by rather parallel sides and annihilates above the QWs.

4.3.1.3. Reconstructed and rendered 3D volume

The 3D reconstruction of the probed volume allows to determine the lamella thickness. The probed part as marked in figure 3.6 is nearly plane-parallel with a thickness of (310 ± 10) nm. The aligned image series is reconstructed by the WBP routine. In fact, the data set does not meet the projection requirements as described in section 2.2.3. Nevertheless, the reconstructed volume contains the necessary information to render the line defects and to obtain a model of the 3D dislocation arrangement. Figure 4.32 illustrates the applied procedure. Intersections of dislocation lines with slices of the reconstructed volume as shown in figures 4.32(a) and (b) result in star like features (A), in short (B) or in long streaks (C). The schemes illustrate the origin of these three objects. The schematic sample volume in figure 4.32(c) contains line defects inclined (red, A), perpendicular (blue, B) and parallel (violet, C) to the tilt axis (dot and dash line). The micrographs represent their traces as dark lines. The intensity values do not show any monotony regarding the tilt angles. But they remain dark with respect to their surrounding throughout the whole tilt series (see figure 4.31). The back-projections of the dark traces into the reconstruction volume appear as dark rays that intersect at the approximate position of the defect line. Due to the violation of the projection requirement, rays caused by micrographs with the highest contrast from line defects remain and cause the star like artefacts. Figure 4.32(d) schematically depicts the expected appearance of the reconstructed objects A, B and C. The orientation of tomogram slices has to be adapted to the respective cases. Figure 4.32(b) demonstrates that the location of object C is difficult in slices parallel to the tilt axis. A sectioning orthogonal to the tilt axis is required in this case. In contrast, the orthogonal slices hardly reveal object B which is observed in parallel slices as shown in figure 4.32(b). Its position is well localized along the direction of

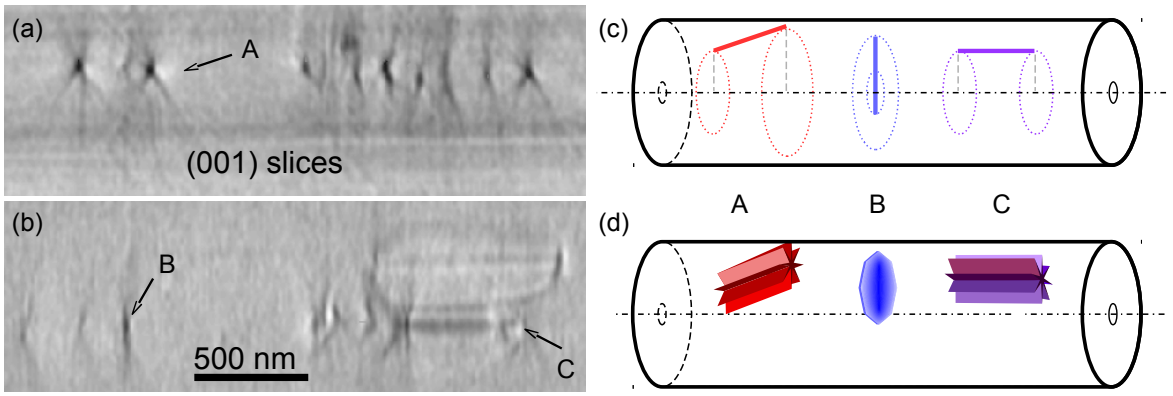

Figure 4.32. The images (a) and (b) exemplify two slices through the reconstructed volume parallel to the (001) lattice planes. The procedure to trace and render line defects in order to create a 3D dislocation model is explained in the text. The schemes in (c) and (d) depict the original and the reconstructed volume, respectively. Different orientations of defect lines with respect to the tilt axis (dot and dash line) are regarded.

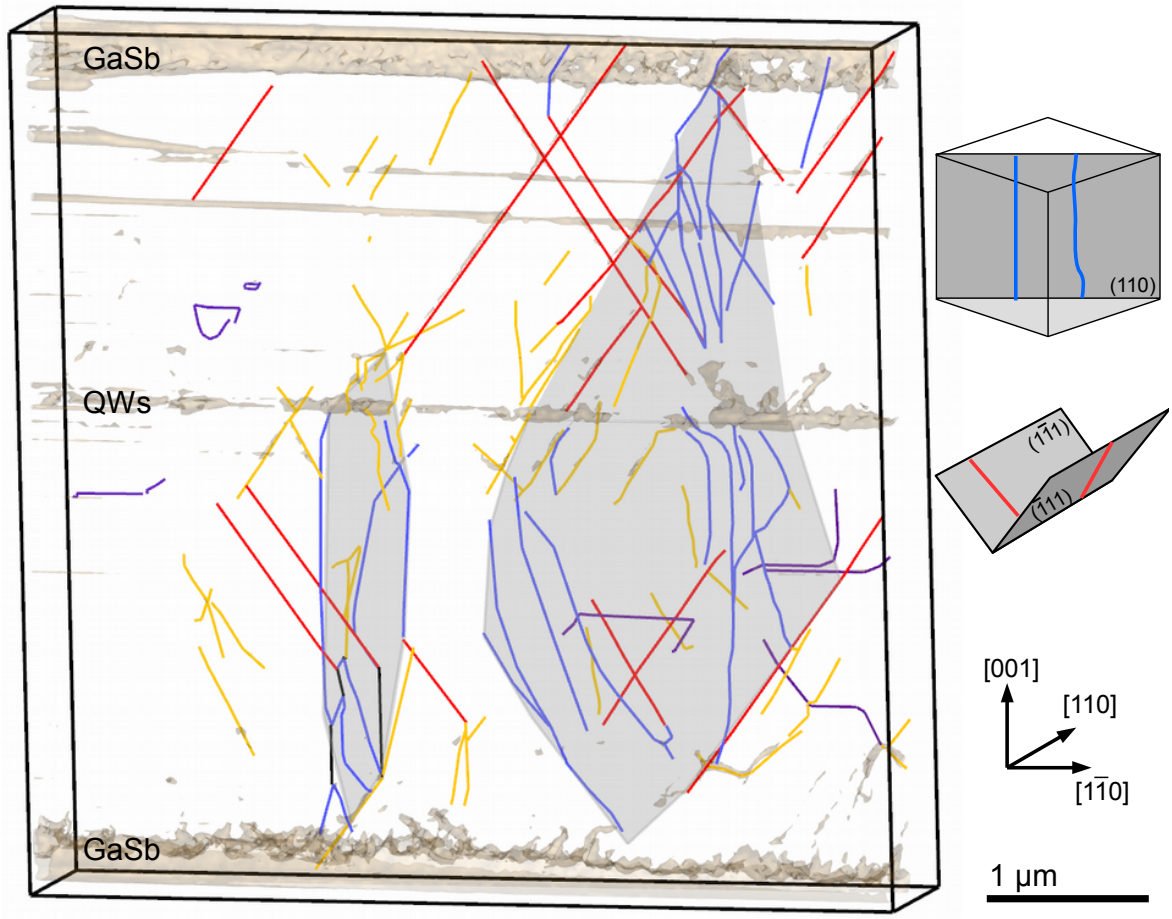

Figure 4.33. Essence from reconstructed volume: View along [110] as in projected BF STEM image at 0°. Transparent isosurface as orientation: top GaSb and GaSb buffer layer, quantum wells (QWs). Manually rendered dislocation lines colored yellow, red, blue, violet and black. Explanations for the color coding in the text.

the tilt axis. The perpendicular direction obviously requires additional information.

The lines are rendered for the analysis of the tomogram. The position of a dislocation is marked and traced while scanning through the suite of slices. The ideal situation is found in case A where lines are easily tracked. Case C works in the same way using slices perpendicular to the line direction. In case B, the tracking will only work if there is a line segment at the top and at the bottom of the lamella which does not run within the plane perpendicular to the tilt axis. The segment within this plane than is assumed to be straight and results from the connection of the points where the line moves into this plane.

Altogether, a volume of $5.7 \times 5.7 \times 0.3$ µm^3 has been reconstructed. The result of the rendered defects is presented in figure 4.33 along with a transparent isosurface of the reconstructed volume. The latter builds a frame for the orientation within the III-Sb layer stack: The GaSb capping and the GaSb buffer layer are visible at the top and at the bottom, respectively. The quantum wells (QWs) are partly resolved in the isosurface representation. Surface features due to the misplaced milling area and due to curtaining appear in the upper and in the left part of the image, respectively (cf. section 3.1.2 and figure 3.6). They are

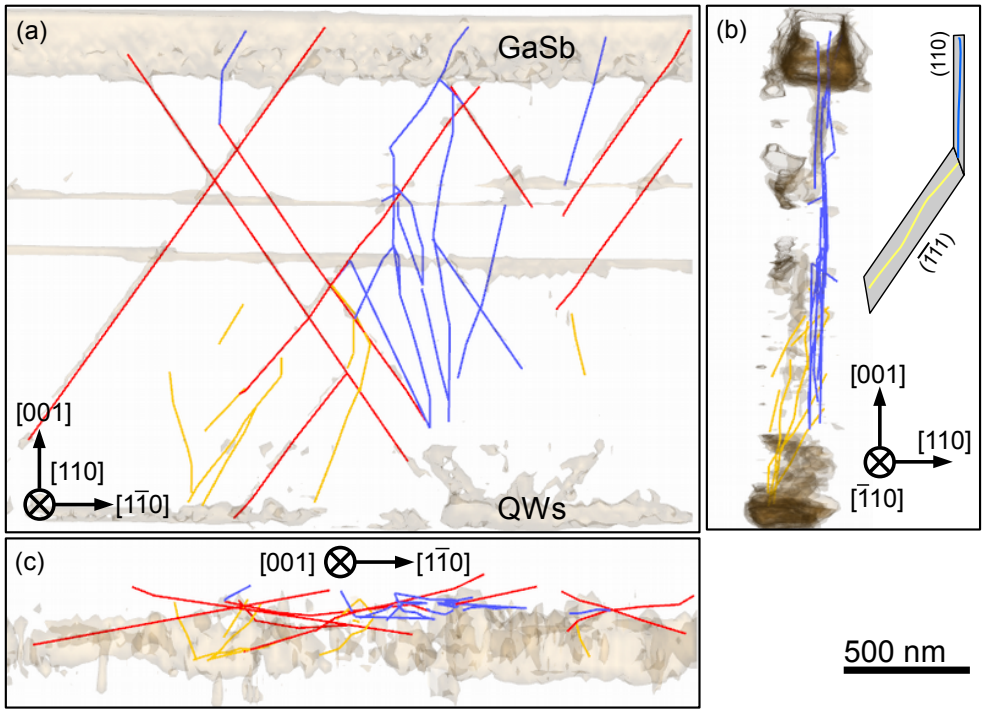

Figure 4.34. Extract of probed volume as represented in Fig. 4.33: upper right part. (a) view along [110], (b) view along [1$\bar{1}$0] without defects hosted on {111} planes and (c) view along [001]. The isosurface is merely presented around the QWS in the latter image.

beneficial to assess the position of the lamella surface. The 3D presentation in figure 4.33 provides an overview of the recorded and rendered volume. The model of dislocations is a selection of the whole amount of line defects. Their density is too high to be resolved near the substrate and, partly, in the vicinity of the QWs. On the other hand, the high density impedes the resolution and reconstruction of parts of the QWs.

The colours of the rendered defects correspond to the classification that has been introduced above. Long, straight lines which are located on (1$\bar{1}$1) and ($\bar{1}$11) planes as already observed in the micrographs of figure 4.26, appear in red. The resolution of the tomogram does not suffice to tell apart the dissociated 60°-dislocation highlighted in figure 4.28. All line defects which are predominantly hosted on (110) planes, are coloured blue. The violet dislocations contain a significant segment that is parallel to the interface toward the substrate. Yellow is chosen to trace so far unspecific dislocations. Dislocations that do not appear in the reconstructed data at all are presented in black. Their existence is inferred from respective tilt series images (see figure 4.31). Their location is deduced from interaction nodes and from dislocations that seem to end within the crystalline material.

In the following, three parts of the volume are considered separately for a detailed analysis. These are located with regard to figure 4.33 in the right top (figure 4.34) and bottom part (figure 4.35) and in the left bottom part (figure 4.36), respectively. Each figure comprises three orthogonal views to convey a notion of the 3D defect configuration.

The strongest accumulation of line defects is observed in the upper right of figure 4.33, i.e. above the strained (In,Ga)(Sb,As) QWs. Here, the region around the QWs seems to

be a source of a high density of threading dislocations. The bunch of defects near the QW that even appears as isosurface, has not been rendered. The blue lines emerging from this bunch show irregular line directions in the projection onto a (110) plane. In contrast, the view along the $[\bar{1}10]$ and the [001] direction in figures 4.34(b) and (c), respectively, reveal a confinement to the (110) plane, i.e. the line direction has no [110] component. Only short segments leave the prevailing confinement and reach the surface. Red lines are left out in figure 4.34(b) for clarity because they are predominantly superimposed over the blue ones. The absence of line defects in the left of the blue defects accumulated parallel to (110) planes has to be highlighted. Straight defects hosted on $(1\bar{1}1)$ and $(\bar{1}11)$ planes will propagate slightly inclined toward the $[1\bar{1}\bar{2}]$ and the $[\bar{1}1\bar{2}]$ orientation, respectively, apart from the area which is dominated by the blue bunch as shown by the projection onto the (001) plane in figure 4.34(c). Bending of dislocations on {111} planes is detected within the accumulation regions. Yellow segments end at the lamella surface, in dislocation interaction nodes or convert into one of the blue line defects. The complex nodes of dislocation reactions are hardly resolved because of many short, parallel line segments in their vicinity. The crossing red lines in the left are indeed the SFs that are described with respect to figure 4.28. They penetrate each other without a detectable disturbance of their course.

Figure 4.35 shows the lower right part of the investigated volume. In addition to the threefold coloured line defects that occurred in figure 4.34, the violet lines with horizontal segments are observed. The blue line defects appear predominantly confined to (110) planes again as seen from the views along the [001] and the $[\bar{1}10]$ direction in figures (b) and (c), respectively. It is worth to mention the dislocations running along the [001] direction until passing the interface from the cladding to the wave guide layer. There, they bend toward the $[\bar{1}10]$ direction. Their trace is lost in the near of the quantum wells. The bending of these dislocations within the wave guide is attributed to the relief of strain. The curved blue ones in the left follow the edge of the shaded area that has been described in accordance to figure 4.31. The {111} bound dislocations (red) exhibit significant bending as observed along the [001] direction in figure 4.35(c). The rightmost one has got a parallel offset in the middle part. The other two tend to bend into the (110) plane. In contrast to the top right part, the area left of the (110) accumulation plane is out of the reconstructed volume in figure 4.35(b). On the right, many yellow segments appear to traverse the lamella from one surface to the other. The $[\bar{1}10]$ view reveals that several of these line defects follow the traces of the (111) and the $(\bar{1}\bar{1}1)$ glide planes which cannot be inferred from the projected images.

Figure 4.35(c) depicts the $[1\bar{1}0]$ line direction of the violet, horizontal dislocation segments, i.e. they are trapped within (110) planes like the blue ones. They are labelled with Roman numbers (i) - (iv). The segments at their ends turn down- or upward. In case of dislocation (i), one segment turns onto the $(\bar{1}11)$ plane while the other one continues on a $(\bar{1}\bar{1}1)$. The reaction with one yellow line at the left turning point is suggested. The ending segments of dislocation (ii) in figure 4.35(a) are directed toward the substrate probably hosted on a $(\bar{1}\bar{1}1)$ plane. The shortness does not allow a reliable allocation of the habit plane. The violet segment (iii) is worth to mention because it turns approximately onto a $(1\bar{1}0)$ plane as seen in figures 4.35(a) and (c).

The last part under investigation in the bottom left in figure 4.33 is presented in figure 4.36. There are several blue line segments moving into the {110} planes where they stretch as straight lines close to the [001] direction. A reaction point marked as "A" most prominently

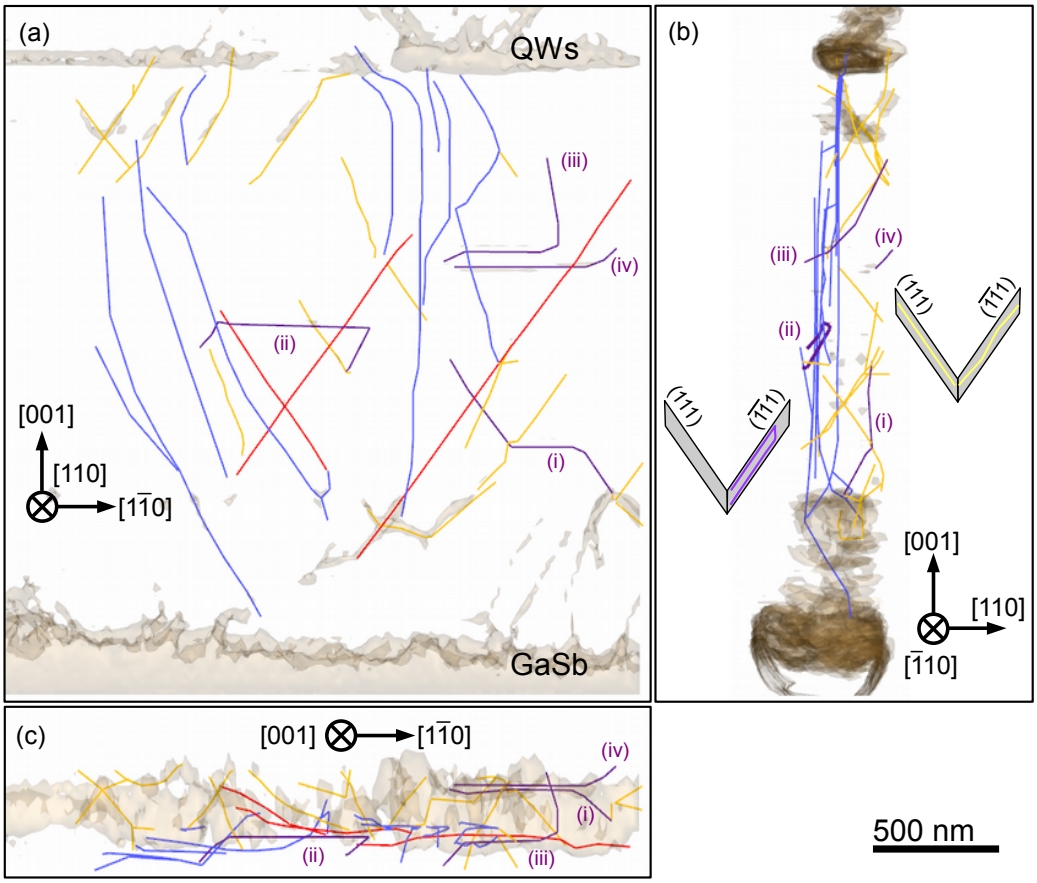

Figure 4.35. Extract of probed volume as represented in Fig. 4.33: lower right part. (a) The horizontal, violet line segments attract attention in the view along the [110] direction. (b) The view along the [1$\bar{1}$0] direction is presented without defects hosted on (1$\bar{1}$1) and ($\bar{1}$11) planes for clarity. Here, red lines depict the traces of indicated lattice planes. (c) The view along the [001] direction is presented with the isosurface only around the QWs.

underlines the challenge of tracing lines perpendicular to the tilt axis. The ending of the red defect on a faint streak (cf. figure 4.32) marks the end of the blue dislocation. Moreover, this particular case highlights the interaction of a line defect on a ($\bar{1}$11) glide plane with a planar defect where it is bend into the (1$\bar{1}$0) plane. The situation is much more complex at the node labelled "B". Here, the existence of a black dislocation is inferred from its occurrence in projected images (white arrows in figure 4.31). The ending of the red dislocation line at "B" has been assumed to be the starting point and the node below as its end. But the exclusive invisibility of the black dislocation points to a change of the Burgers vector $\vec{b}$ at node "B". Regarding the necessary criterion for invisibility [3]

$$\vec{g} \cdot \vec{b} = 0, \tag{4.13}$$

the black dislocation possesses $\vec{b} = [11\ell]$ (ℓ integer) because $\vec{g}$ points along the permanently excited systematic row parallel to the tilt axis or the [1$\bar{1}$0] direction. Contrast from these defects arises only in the vicinity of low-indexed zones during the tilt series when reflections with non-perpendicular vectors are excited. The careful investigation of the raw data reveals

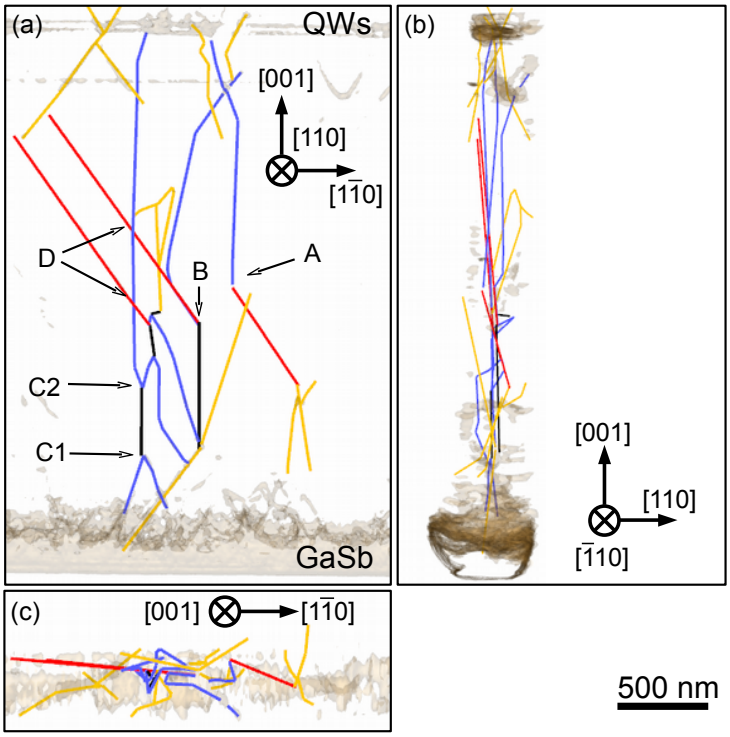

Figure 4.36. Extract of probed volume as represented in Fig. 4.33: lower left part. (a) Capital letters in the viewing direction of [110] mark nodes of defect interactions. Images (b) and (c) present the views along the [1$\bar{1}$0] along the [001] direction, respectively.

a parallel segment to the red dislocation starting at "B". This third segment is necessary as the sum of Burgers vectors at the node has to equal zero, i.e. a change at a dislocation bend is impossible. The parallel segment is not resolved in the tomogram. It bends away as the ascending blue line which is trapped in a (110) plane before turning toward the lamella surface.

There are two more black dislocations which are worth to be mentioned because they explain a peculiar arrangement of line segments. During investigations of various III-Sb samples, dislocations have been found with segments apparently moving back and forth. In fact, there are interaction sites (e.g. "C1" and "C2") that are present at the turning points. Finally, the attention is drawn to the interaction nodes "D". In contrast to the SFs revealed in figure 4.28, the two parallel red dislocations do not exhibit an unresolved partner. The encounter with the blue dislocation along the [001] direction appears to happen without a reaction. Hence, it is assumed that the Burgers vectors are mutually perpendicular. The blue line marks the edge of the APB observed in figure 4.31. It is considered that the right parts of the red dislocations are confined within the APB parallel to the (110) lattice plane and the blue dislocation marks a corner of the APD. Alternatively, the red dislocations have to intersect the APB parallel to the ($\bar{1}$10) lattice plane. The latter case has to be discussed.

4.3.2. Discussion

4.3.2.1. 3D defect arrangement

The discussion of the 3D defect arrangement follows the occurrence of different types of dislocations as outlined in the tomographic data. Dislocation lines on {111} and on {110} planes are considered in the first and second paragraph, respectively. Subsequently, an own paragraph is dedicated to horizontal line segments which are located at both {111} and {110} planes. Finally, the interaction of dislocations with APBs and with other dislocations is addressed.

Dislocations on {111} planes

Dislocations presented in red and most of those in yellow lie on {111} planes. In the following, their mobility and the asymmetry in their density and their shapes are regarded. The formation of TDs at the interface to the substrate is treated in section 4.2. The course of a dislocation line on the {111} plane is the prerequisite for its mobility by means of conservative motion. Dislocation glide will occur if there is a resolved shear stress that acts on the dislocation line. This driving force originates from lattice mismatch. Strain due to the mismatch between the substrate and the layer is, in principle, relieved by the incorporation of MFD networks in the interface plane during lateral island growth. A further location of possible mismatch is presented by each transition from one layer to the next in the III-antimonide heterostructure. The lattice constant of the quaternary alloys has actually been designed to match layers with different compositions [208] and, eventually, to avoid plastic relaxations by MFDs. Merely the In-rich QWs are compressively strained [56]. A pseudomorphic growth is expected due to their small thickness. The different thermal expansion coefficient of III-V materials and Si imposes stress onto the heterostructure during the unavoidable cooling from growth to room temperature. The linear thermal expansion coefficients α_T of Si and GaSb at room temperature are $2.59 \times 10^{-6}\,\mathrm{K}^{-1}$ [209] and $7.75 \times 10^{-6}\,\mathrm{K}^{-1}$ [210]. The lattice constants at room temperature a_{RT} expand with temperature according to

$$a(T) = a_{RT} * (1 + \alpha_T \cdot \Delta T). \tag{4.14}$$

A change of the lattice mismatch f (equation 2.2) for the temperature difference of $\Delta T = 550\,^{\circ}\mathrm{C}$ is estimated to add up to approximately 0.3%. This thermal mismatch is regarded as driving force to move dislocations on {111} planes which is important for the consideration of dislocation reactions. The creation of new dislocations at the surface by the introduction of half-loops that glide to the interface [68] is not expected. The thermal stress does not provide the activation energy to initiate this process. The epitaxial film retains residual strain. Dixon and Goodhew [211] have demonstrated that even 3 µm thick InGaAs layers on GaAs can exhibit residual strain as high as 0.3%. Recently, Rodriguez *et al.* [212] have presented 1 µm thick GaSb films on Si with a residual strain of approximately 0.1%.

The glide systems based on the four {111} planes are symmetry equivalent in the diamond structured Si substrate. In the epitaxial layer, this symmetry is lost due to the application of a vicinal substrate and due to the growth of polar III-V compound semiconductors on non-polar Si wafer. The miscut gives rise to the introduction of additional 60° dislocations in

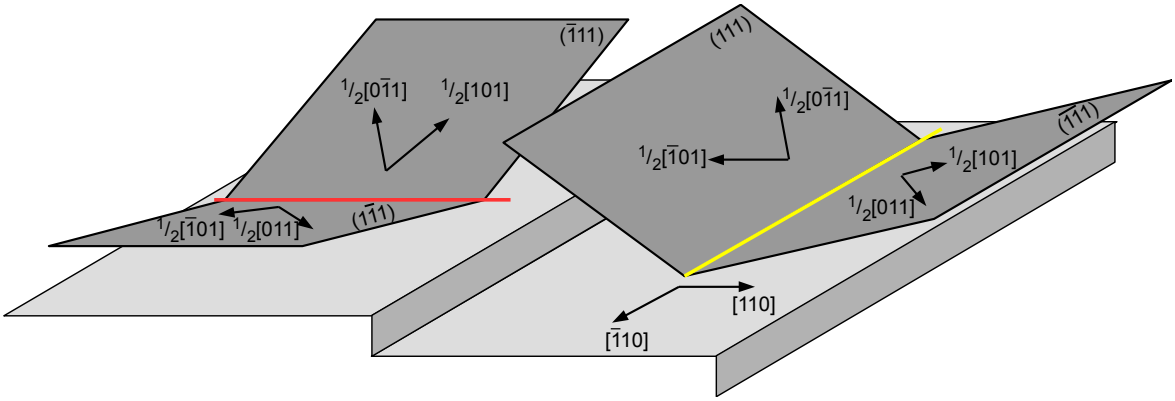

Figure 4.37. The relation between the surface steps, the {111} planes and the Burgers vectors with a $\frac{1}{2}\langle 001\rangle$ is illustrated by this sketch. (Angles between planes are not exact.)

order to compensate the misfit along the [001] direction which is outlined according to figure 4.23(b). Thus, there is a reason for the asymmetry between the two sets of {111} planes that belong to the $[1\bar{1}0]$ and to the [110] zone. The geometrical arrangement is sketched in figure 4.37. Assuming respective dislocations also relieve mismatch along the [110] direction, only the $\frac{1}{2}[101]$ and the $\frac{1}{2}[011]$ Burgers vectors are favourable. They belong to the $(\bar{1}\bar{1}1)$ glide plane regarding the initial line direction parallel to the prevailing $[1\bar{1}0]$ step direction. They exhibit the respective misfit components while the screw components are balanced

$$\frac{1}{2}[101] = \frac{1}{4}[1\bar{1}0]_{screw} + \frac{1}{4}[110]_{misfit} + \frac{1}{2}[001]_{misfit} \tag{4.15}$$

$$\frac{1}{2}[011] = \frac{1}{4}[\bar{1}10]_{screw} + \frac{1}{4}[110]_{misfit} + \frac{1}{2}[001]_{misfit}. \tag{4.16}$$

Hence, a difference in the occupation with dislocations on the (111) and $(\bar{1}\bar{1}1)$ is expected, too. This expectation is in agreement with the study of Mooney *et al.* [204] who considered SiGe layers on vicinal Si substrates.

The chemical difference of the $\{111\}_{\mathrm{A}}$ and $\{111\}_{\mathrm{B}}$ in III-V compounds found the second origin for asymmetry. The Sb terminated $(\bar{1}\bar{1}1)_{\mathrm{B}}$ and $(111)_{\mathrm{B}}$ planes present the faster growth front during the initial 3D growth stage (cf. figure 4.20). A dominant inclusion of defects on these planes explains a difference between the dislocation densities of {111} planes belonging to the $[1\bar{1}0]$ and to the [110] zone. This trend amplifies the effect of strain relief along the [001]. The asymmetry of dislocation densities with respect to the two zones is in accordance with the observations (cf. yellow line segments and figure 4.26).

The chemically different dislocation cores of III-V semiconductors are regarded as source for diverse line shapes. Like-sign {111} half-planes [213] that are intercalated due to the Burgers vector edge component, will exhibit group III or group V terminated cores if the planes belong to orthogonal zones. They are called α- and β- dislocations, respectively. A different abundance of group III and group V interstitials leads to an asymmetry of the non-conservative motion of α- and β- dislocations [214]. As a consequence, the asymmetry of straight {111} bound and irregular shaped dislocations occurs as observed in the tomographic analysis. Besides, the climbed dislocations are pinned after climbing out of there

original glide plane. The presence of point defects/interstitials in the investigated material systems is in agreement with the pores described in section 4.1 and the curly, i.e. climbed, dislocation lines outlined with respect to figure 4.29.

To complete the observed dislocations on {111}, the violet contours in the upper left part of figure 4.33 are mentioned. Point defects are considered as source for the formation of dislocation loops. The nucleation of point defects on densely packed lattice planes results in dislocation loops [215].

Dislocations on {110} planes

The occurrence of dislocation lines on {110} planes in sphalerite structure is uncommon. The experimental data demonstrate a strong correlation to the existence of APBs. Actually, the suppression of APDs is intended by the growth on vicinal Si(001) wafers [69]. The energetically favourable formation of atomic bilayer surface steps promotes an exclusive (2x1) surface reconstruction [193]. Si dimers are formed parallel to the step directions from the dangling bonds that lie in the respectively parallel {110} plane as shown before in figure 4.20(b). Figure 4.38(a) depicts the single crystalline GaSb growth at a Si bilayer step. The initial saturation of the Si surface by Sb atoms is presumed. Residual monoatomic steps lead to the presence of occasional (1x2) domains. Figure 4.38(b) illustrates the formation of an APB due to the monoatomic step. The transform from one domain to the other is described by an inversion or by a 90° rotation followed by a $\frac{a}{4}\langle 111\rangle$ shift. The {110} habit plane conserves the stoichiometry along the interface, i.e. equal atoms are alternately bond to one another. The continuous transition from single to predominant double layer steps has been reported [216] as well as the strong reduction of APDs by using misoriented substrates [191]. Furthermore, Georgakilas *et al.* [191] discussed the annihilation mechanisms of APDs at early stages of growth. If the cancellation of APDs is incomplete, an asymmetric abundance of the two types of domains has to be considered. The presented results prove the existence of residual APDs that traverse the whole epitaxial layer stack.

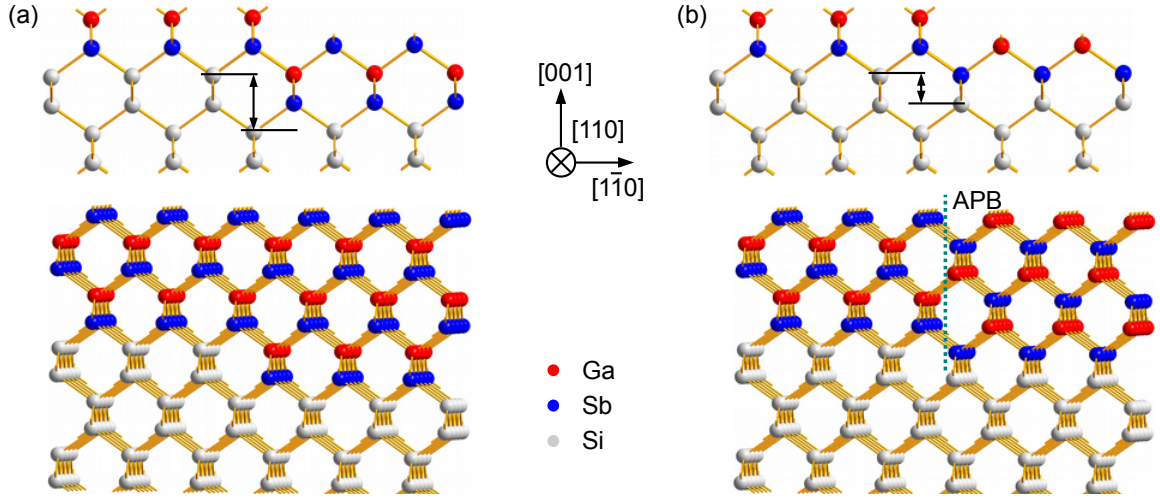

Figure 4.38. (a) Double steps on the vicinal Si(001) surface are intende in order to avoid the formation of APD. (b) The occurrence of monoatomic steps on the Si(001) surface induces the formation of an APD.

The dislocation lines rendered in blue appear to be trapped in the APBs. Figure 4.39 illustrates this situation. The smooth shape and the frequent dislocation lines along the [001] direction raise the question of their formation. The {111} planes do not belong to the [001] zone. Therefore, the dislocations have not reached this orientation by a conservative motion. TDs created at the interface to the substrate continue with the advancing growth front. Here, the length is kept as short as possible under following boundary condition. The energy per unit length is smallest for a dislocation on a densely packed {111} plane [217] because the smallest number of dangling bonds at the dislocation core is introduced. If the dislocation met an APB at the growth front, it could be energetically more favourable to continue a trail within the planar defect. The termination of the dislocation line at the APB is excluded due to the congruence of atom bonds on both sides of the grain boundary. Figure 4.39(a) depicts two dislocation lines (blue dashed) that leave the $(1\bar{1}1)$ plane when meeting an APD during growth. The right one exhibits a sharp bend and continues in the $(1\bar{1}0)$ plane. Such a situation occurs at node "A" in figure 4.36. The other one continues its path within the (110) plane of the APB. The smooth shape is a result of minimizing the length. Alternatively, if motion of dislocations occurs due to climb, the edges of APDs will define the shape. It is suggested that edges of the APDs coin a preferred location for dislocation lines because a maximal number of incorrectly bonded atoms is broken. In that way, dislocations follow the APD corners especially along the [001] direction as illustrated by figure 4.39(b). The atomic arrangement at the corner is schematically presented in figure 4.39(c). Atoms at the corner exhibit more bonds to like partners than atoms along plane parts. An open question concerns the atomic structure of the dislocation core. The answer would clarify the impact of trapped dislocations on the electrical device performance. Furthermore, the experimental findings imply that the notion of the effect of APBs on electrical devices has to be reconsidered regarding the mergers with threading defects.

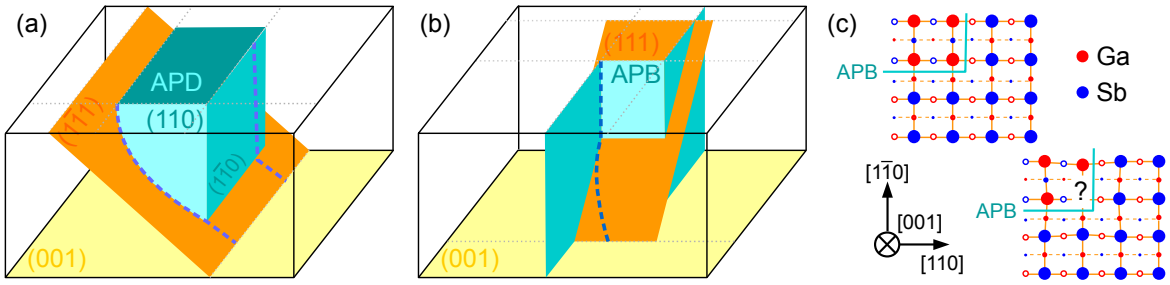

Figure 4.39. (a) The scheme displays the changing line direction of a dislocation that meets an APD. (b) The model illustrates the confinement of a dislocation at an APD edge. (c) The schematic depicts the atom configuration of an APB parallel to the (001) plane. (big filled circles on reference plane, small open circles and small filled $\frac{1}{4}a$ above and below, respectivly, and smallest circles $\frac{1}{2}a$ below the reference plane, with a as lattice constant) The APD exhibits an edge formed by the (110) and $(1\bar{1}0)$ planes. The atomic arrangement of a dislocation core placed at the edge constitutes an open question.

Eventually, the occurrence of steps at interfaces and at the sample surface are explained at this point. On the one hand, dislocations with screw component reaching the sample surface or the growth front involve the formation of spiral-like mounds [218]. On the other hand, studies of GaAs on Si(001) showed like steps in conjunction with the presence of APBs [219, 220]. The second observation is in accordance with the present study of III-Sb on

vicinal Si(001). Cho and Carter [220] mention different growth rates of APD as plausible explanation. Developing this idea further, the annihilation of APB in the beginning happens due to overgrowth. And the inclination of APBs toward the {110} planes as seen in figures 4.26(b) and 4.27 appears due to the lateral expansion of the faster growing domain. The deviation from the {110} plane has to be realized by nano-facets that, for energetic reasons, retain stoichiometry and charge neutrality [197, 221, 222]. The most often observed {110} APBs [70] are exclusively considered for simplicity in this discussion. It is shown in this work that many dislocations are bound to the APBs. Assuming the preferred screw component $\frac{1}{2}[001]$, spiral features and the presence of APBs have to be considered in combination. The surface steps caused by screw components bunch together and explain steps of approximately 10 nm height at the surface and at interfaces. *Hence, tomography reveals and explains the correlation of those steps and the presence of APBs.* The numerous dislocations trapped in the APB are not inferred from 2D projections of common cross-sectional TEM specimen. Finally, it is speculated that the incorporation of dislocations in APB with the advancing growth front prevents the cancellation of APD.

Horizontal dislocations

The presence of horizontal defect segments is explained by the conservative motion of dislocations on {111} planes and the joining with an APB. Figure 4.40(a) and (b) illustrate situations which explain the observations according to figure 4.35. The former case depicts a dislocation that moves on the (111) plane toward the sample surface. It might be a half loop expanding from an interface where it is pinned. When it meets the APB its motion is blocked and the trapped line segment follows the intersection of the (111) and the (110) plane which is parallel to the (001) surface plane.

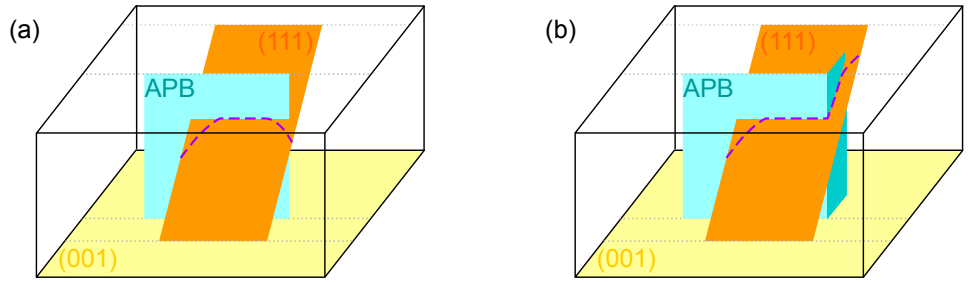

Figure 4.40. The schemes in (a) and (b) illustrate two formation routes of horizontal dislocation line segments (dashed violet).

The notion of a trapped dislocation in a {110} APB is fostered by the tomographic dislocation model where a violet horizontal line with two terminating segments pointing downward approximately parallel to the (111) plane has been revealed. A more complex line course appears at corners of APDs as depicted in figure 4.40(b). An idealized corner of an APD composed of a (110) and a $(\bar{1}10)$ bounding plane is intersected by a (111) plane on which a dislocation is gliding as in the case before. At the corner the horizontal line segment ends and the dislocation turns around the corner in the direction defined by the intersection of the neighbouring, orthogonal APB plane and the habit plane of the dislocation. A respective course of a violet dislocation line has been described in accordance to figure 4.35.

An alternative explanation for the case presented in figure 4.40(a) is based on the termination of a SF at the APB [219]. This scenario allows the formation of the horizontal line segment at the growth front. But an experimental trace like the grey shaded area highlighted by horizontally elongated ellipses in figure 4.26 is missing. Furthermore, the exceptional SF width needs an explanation.

Reactions of dislocations

The presence of horizontal line segments is a first example for the reaction of a dislocation with an APB. Figure 4.41(a) presents a similar situation. The dislocation line in red colour glides on the $(1\bar{1}1)$ plane until it meets APB parallel to the (110) plane. The dislocation line is trapped at the intersection of the planes which points along the $[\bar{1}12]$ direction instead of the horizontal $[\bar{1}10]$ direction. This situation is most prominently observed in figures 4.35 and 4.36. Here, dislocations in red are bend into planes common to the ones rendered in blue. In absence of APBs, straight dislocation lines occur approximately along $\langle 112 \rangle$ directions, too, as observed in figures 4.26(b) and 4.34. This behaviour is attributed to the minimization of the dislocation length which contrasts the preferred direction along $\langle 110 \rangle$ due to a minimum in the Peierls potential [62].

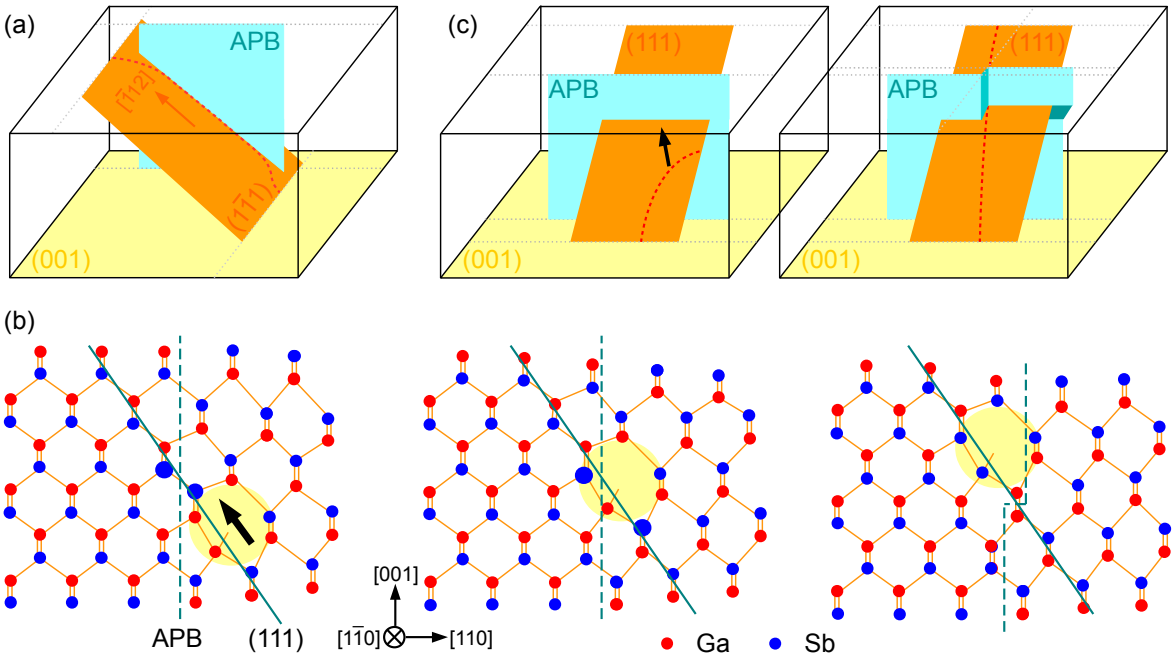

Figure 4.41. (a) A dislocation is trapped along the $[\bar{1}12]$ direction defined by the intersection of the glide plane and the APB. (b) The atomistic models illustrate the interaction of a dislocation gliding on the (111) plane with an APB parallel to the (110) plane. The image plane is parallel to the $(1\bar{1}0)$ plane. (c) The models depict the dislocation line moving on the (111) plane. The right images in (b) and (c) show the formation of a kink in the APB due to the passage of the dislocation line.

In order to discuss the questions why dislocations are trapped in an APB and why they do not penetrate through the APB, an atomistic model of the APB and a dislocation is presented in figure 4.41(b). An overview on the process is provided by the model in figure 4.41(c). A

dislocation glides on a (111) lattice plane as outlined by the black arrow and meets an APB which is parallel to the (110) plane. If the dislocation penetrated the APB, it would leave a kink in the APB due to a Burgers component perpendicular to the (110) plane. The left image of figure 4.41(b) schematically depicts the core of a 60° dislocation (shaded in yellow) on a (111) glide plane before meeting the APB. False bonds between equal atoms (Ga-Ga and Sb-Sb) mark the position of the APB. Two Sb atoms are emphasized (big blue circles) at the intersection of the APB and the glide plane. In the middle image the dislocation has moved into the APB. The wrong Sb-Sb bond is broken which is assumed to be energetically favourable and gives reason to the trapping of dislocations in the APB. Respective Sb atoms are still depicted as big blue circles. Moreover, the wrong Ga-Ga bond of the terminating row of atoms at the dislocation core vanishes, too. In accordance to the observed asymmetry between dislocation lines rendered in yellow and in red, respectively, it is regarded that one trapped type is prone to climb within the APB. In addition to the scenario of ingrown dislocations, this climb process also results in the presence of dislocations in {110} planes following the [001] direction or APD edges. The other type continues as depicted in figure 4.41(a). The pair of initially parallel dislocations starting at node "B" in figure 4.36 could be an example for these types.

The consideration of trapping presumes that a passage of the dislocation through the APB is impossible. This hypothetical event is depicted in the right images of figures 4.41(b) and (c). Kvam [70] investigated the interaction of dislocations with APBs for GaAs grown layer by layer on Si(001). He argues that the passage creates a kink in the APB if $\vec{b} \cdot \vec{n} \neq 0$ ($\vec{n}$ normal of APB). The consequent enlargement of the APB area is energetically unfavourable and, hence, the dislocation movement is blocked. Besides, figure 4.41(b) shows that the dislocation core changes from a Ga- to a Sb-termination during this step and that a two pairs of wrong bonds (Ga-Ga and Sb-Sb) have to be created. On the other hand, Kvam [70] expects dislocations with $\vec{b} \perp \vec{n}$ can pass the APB. None of the perfect glissile dislocations exhibits a Burgers vector parallel to the (110) and $(1\bar{1}0)$ APBs. But an interesting option exists for dissociated dislocations. The dislocation reaction

$$\frac{1}{2}[011] \rightarrow \frac{1}{6}[\bar{1}21] + \frac{1}{6}[112] \tag{4.17}$$

is regarded as an example. A Burgers vector parallel to an APB on a $(1\bar{1}0)$ plane is created. Thus one partial passes the APB and the other one is trapped. An increasing distance of both dislocations implies the creation of a wide SF. These wide SFs are regarded as possible explanation of the planar defects marked by horizontally elongated ellipses in figure 4.26.

The high density of dislocations related to APBs promotes interactions of dislocations. The tangle of blue lines in figure 4.34 is an illustrative example. A detailed analysis would require an improved resolution of this region. Obviously, an APB is an obstacle for gliding dislocations and it affects their line direction. In return, an impact of dislocations on the annihilation of APDs is suggested by many parts of APB that are not parallel to {110} lattice planes. Rules for the vast spectrum of dislocation interactions in fcc materials that have been described by Thompson [63], are assumed to hold at APBs, too. The conservation of Burgers vectors is, for instance, the basis for the interpretation of nodes "A" - "C" in figure 4.36.

4.3.2.2. Experimental limitations and improvements

The tomogram has revealed dislocations and their course through the volume of the lamella. Obviously, a limitation occurs in parts of high dislocation density including the direct environment of a complex dislocation node. The actual position of the dislocation core and the presence of the contrast feature in a DF TEM image depends on the excitation error and the depth of the line defect within the specimen foil [107]. As a consequence, the dislocation image changes its location towards the actual position during a tilt series. Barnard *et al.* [161] have applied the WBDF signal for tomography. They have estimated a lower resolution limit of 5 nm. The reconstruction reproduces the dislocations as cylinders due to the variable location of the dislocation line. The STEM mode averages over several values of the excitation error (cf. section 2.2.2). This averaging leads to a wider intensity peak of the contrast feature in comparison to DF TEM images [161]. The resolution of dissociated dislocation lines (figure 4.28) shows that objects with a distance of approximately 20 nm are easily distinguished. In parts with high dislocation density, it is difficult to decide whether crossing dislocations react or just pass each other. Additional information are exploited to support the analysis. In that sense, junctions with three line segments indicate a reaction. The application of the invisibility criterion allows to conclude a change of Burgers vectors which is a further hint to a reaction. Phillips *et al.* [116] have demonstrated the application of the $g \cdot b$ rule for diffraction contrast in STEM (BF/ADF). An advantage of STEM over DF TEM is the absence of thickness and bend contours.

A valuable improvement for the tomogram would be the removal of the star-like artefacts illustrated in figure 4.32. A relevant algorithm for image processing has been applied to the results of the WBDF tomogram [42, 161]. In that way, the laborious rendering of defects will be avoided if the direct visualization of dislocations in an isosurface is feasible [45]. Typical artefacts that are considered in the previous chapters, are subordinated because the selected STEM signal does not meet the projection requirement. That is, the elongation due to the missing wedge or the cupping artefact are insignificant. The comprised chemical contrast merely provides some useful markers for image alignment and orientation in the tomogram. The common key figures tilt step and tilt range are not critical for an improvement of the tomographic data. But a double-tilt axis tomogram [223] circumvents the uncertainties of the plate-like appearance of dislocations with line directions perpendicular to the tilt-axis (cf. figure 4.32).

A final comment has to address the specimen shape. The tomography lamella represents only a slice parallel to the (110) plane. The results suggest a prevailing elongation of APDs parallel to steps which is in agreement with the initial island anisotropy, i.e. $\{111\}_B$ faces in APDs grow faster along $[1\bar{1}0]$ (cf. figure 4.20). Furthermore, it is clear that dislocations are blocked by APBs and that µm-sized parts of the heterostructure are nearly free of dislocations. Figure 4.42 illustrates the current, idealized notion. The set of APDs works as defect filter for one direction, i.e. dislocations are hindered to ascend on $\{111\}$ planes. They will bend into the APBs in the lower parts of the heterostructure if the density of APD is sufficiently high. In the orthogonal direction, the filter does not work due to the asymmetric elongation of APDs. This aspect might lead to a difference in residual strain along the [110] and the $[1\bar{1}0]$ direction. In order to support the idea according to figure 4.42, lamellae parallel to the $(1\bar{1}0)$ plane and parallel to the (001) plane have to be prepared for future

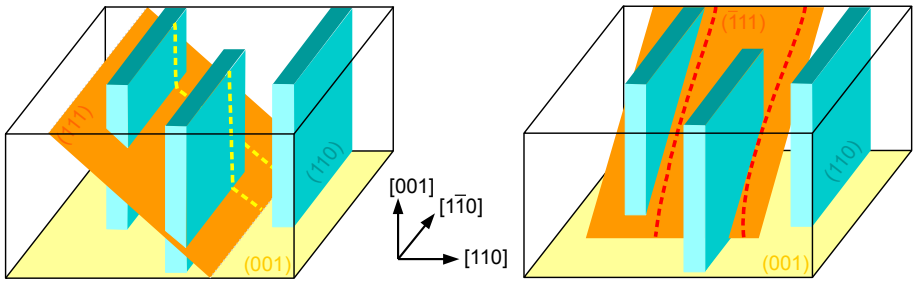

Figure 4.42. The anisotropically elongated APDs (blue) serve as dislocation filter, i.e. they impede the course of dislocation lines on {111} planes. The anisotropy

investigations. The former will show more events where dislocations just turn into an APB. The latter will give an overview about the arrangement of APDs. But it will only contain a limited height of the epitaxial layer stack.

5. Reconstruction of (In,Ga)N insertions in GaN based nanocolumns

In the previous chapter, tomography is used to analyse a pore embedded in GaSb and an AlSb wetting layer enclosed by GaSb and Si. These investigations are tacitly based on the assumption of homogeneous phases, i.e. pure AlSb, GaSb, Si or vacuum. The present chapter is dedicated to the retrieval of (In,Ga)N layers inserted into a 3D grown GaN nanocolumn. Variations in the amount of incorporated indium must be expected that is the simple assumption of a homogeneous (In,Ga)N layer does not hold. The variations are suggested by cathodoluminescence measurements on the investigated sample by Bengoechea-Encabo *et al.* [53]. The authors associated two different emission wavelength to a facet dependent incorporation of indium. The detailed description of the (In,Ga)N insertions inside the GaN nanocolumns is the goal of this chapter. The insights allow to understand the optoelectronic properties of the GaN based heterostructures as they sensitively depend on the indium content and the location of its incorporation. Part of the presented results is published in [224].

5.1. Tilt series acquisition

The investigation of the spatial distribution of indium in a (In,Ga)N/GaN nanocolumn is carried out on a 1.3 µm wide lamella. The result of the target preparation which is described in section 3.1.3, is shown in the HAADF STEM image in the left of figure 5.1. The approximate crystallographic orientation is given in the micrograph. Several nanocolumns are confined within the specimen. Remains of nanocolumns in the rearmost row are faintly

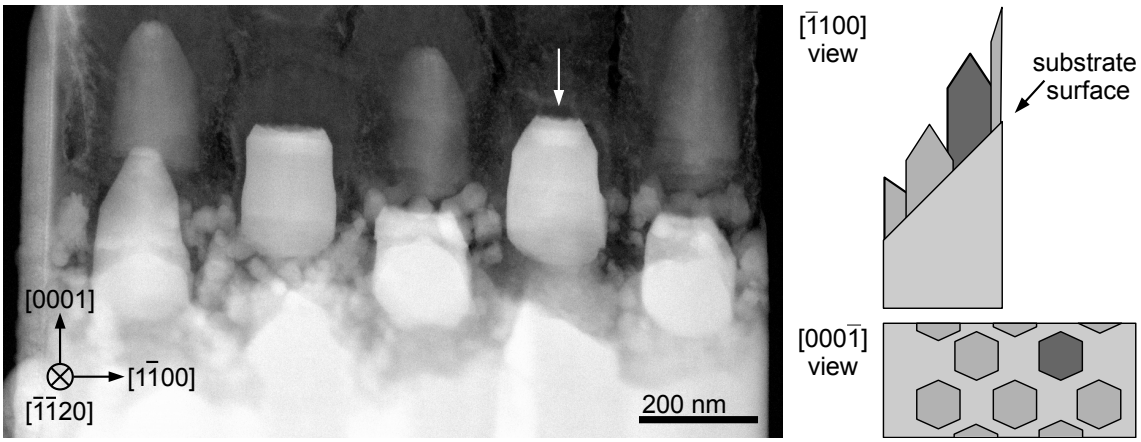

Figure 5.1. The HAADF STEM image presents the specimen of isolated (In,Ga)N/GaN nanocolumns. The arrow points at the nanocolumn under investigation. The schematics illustrate the position of the selected nanocolumn (dark grey) among the neighbouring ones.

captured in the images. Besides, parasitically grown crystallites on top of the Ti mask are discerned between the nanocolumns. The schematics show the lamella in two orthogonal viewing directions. In that way, the relation of 3D objects and the original substrate surface is illustrated. The GaN surface is inclined toward the imaging plane which becomes clear from the $[\bar{1}100]$ view. The GaN template presents a wedge with an increasing thickness in vertical direction. Consequently, the overall HAADF intensity increases toward the bottom of the micrograph. The presence of parasitic crystallites renders the extension of the substrate surface. The contrast of the HAADF micrograph is enhanced in order to reveal the carbon layer covering the nanocolumns.

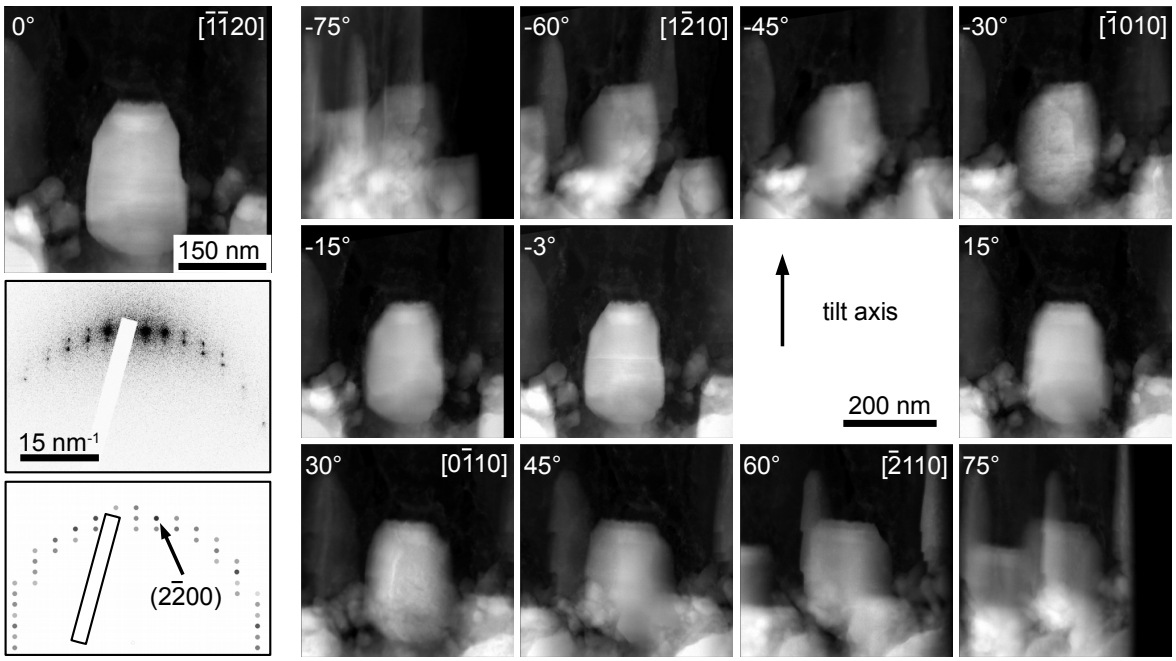

Figure 5.2. The choice of HAADF STEM images from the tilt series presents the target selected nanocolumn in different viewing directions. The images are labelled with respective tilt angles. The left column shows the Z-contrast image at 0° along with an experimental (middle) and a calculated SAD pattern (lowest).

The target object is marked with a white arrow in figure 5.1. The micrographs of the tilt series are restricted to the surrounding of this target. A selection of acquired images at different tilt angles is presented in figure 5.2. The choice of the nanocolumn respects the requirements for the tomographic reconstruction. It exhibits the least overlap with substrate material while being complete. A superposition with remains of the upper row of nanocolumns occurs at high tilt angles. The lower row interferes only with the bottom of the target object. The neighbouring column in the same row does not overlap for the maximum tilt angles of $\pm 75°$. The actual lamella thickness of approximately 400 nm is carefully considered. Electrons have to penetrate circa 1.5 µm of material at the highest tilt. It is assumed that the contribution of carbon to the HAADF signal will be negligible in comparison to GaN and (In,Ga)N if a sufficiently high HAADF collection angle is selected. The detection angle range of 150 mrad to 400 mrad is applied. The dimension of the targeted GaN nanocolumn is well in the validity range for a linear dependence of the intensity on the thickness (cf. figure 3.11). On the other hand, a long dwell time of 320 µs per pixel is used in order to obtain

a reasonable SNR. The total acquisition time for one frame of 1024 x 1024 pixels sums up to 336 s. Such a slow scan is prone to image distortions. The specimen drift after each tilt step is identified as predominant problem. A 300 s delay of the image acquisition after each movement of the goniometer slightly reduces the effect. The resulting image distortion is assumed to be equal in each frame and is counteracted during image processing. Finally, the tilt series comprises 51 images taken over a tilt range of 150° in steps of 3°. The pure time for image capture and goniometer delay adds up to 9 h. The consideration of object tracking and refocussing after each tilt step is not included. The actual measurement has lasted more than 15 h. It is remarked that the STEM alignment is stable on that time scale with respect to the applied magnification.

The HAADF signal allows to detect specimen volumes with high indium content. The enlarged STEM image taken at 0° is shown on top left of figure 5.2. The contrast settings focus on intensity variations in the projection of the target object. The bright trapezoid field below the apex of the nanocolumn is interpreted as region with high indium content indicating the chemical sensitivity. The possibility of misinterpretations due to thickness changes is excluded because the nanocolumn is isolated and thickness change according to its own morphology is too weak in order to explain the brighter feature. In contrast, the detection of (In,Ga)N layers on side facets is hardly inferred from this micrograph. Moreover, the superposition with other nanocolumns, for instance in images taken at −60° and 60°, is misleading. The occurrence of contrast from a dislocation running along the nanocolumn axis in images at −30° and 30° is pointed out as undesirable effect. Beyond, contrast from SFs in the lower half of the selected column is visible in the image acquired at −3°.

The quantitative description of the morphology by means of faceting requires the orientation of the nanocolumn as described according to figure 3.10. A 4.4° deviation of the low indexed [0001] direction from the tilt axis is suggested due to the limited tilt range of the sample stage during preparation (see above). The SAD pattern (contrast inverted) in the middle left of figure 5.2 highlights the remarkable effect in contrast to the rather ideal cases encountered for the antimonides on Si. The rectangular object represents the beam stopper which blanks the central beam. The calculated diffractogram below is obtained for the hexagonal GaN crystal structure with an inclination of the $[11\bar{2}0]$ zone axis of 3.2° toward the $[000\bar{1}]$ and of 0.3° toward the $[1\bar{1}00]$ direction. This determination allows to allocate the approximate orientations to the tilt angles as seen in figure 5.2.

5.2. Analysis of the 3D reconstruction

The 3D reconstructed data set is based on the tilt series presented in figure 5.2. The limited tilt range of 150° causes artefacts due to the missing wedge. The resulting elongation of the reconstructed volume is counteracted by a compression along the direction corresponding to 0° goniometer tilt or approximately the $[\bar{1}\bar{1}20]$ zone axis. The volume is squeezed by the factor 0.9 according to equation 2.13. The result of the 3D reconstruction is found to sensitively depend on the image alignment and to parameters of the SIRT algorithm. Information on the (In,Ga)N layer beyond the apparent part near the apex is only available in optimized 3D analyses. The careless suppression of high spatial frequencies during the SIRT process causes oscillations near the nanocolumn surface which obscure any layer structure. The tilt

series lacks in a prominent and sufficiently small marker that allows an accurate alignment. The images are sheared by 9.5° to account for the drift induced distortion. This angle is chosen to establish a right-angle between the basal top and the prismatic side facets. Eventually, plural attempts of manual image alignment led to the 3D data which are presented in the following.

In the first section, the outer morphology of the nanocolumn is described in detail and the correlation to the shape of the insertion is established. For this purpose, isosurface representations are shown that are based on the binned 3D data set. The binning smooths the surface and reduces the noise related roughness. In the second section, a qualitative analysis of the indium concentration with respect to the different facets is carried out. It is based on slices through the reconstructed volume.

5.2.1. Morphology of GaN nanocolumns and (In,Ga)N insertions

The three-dimensional data set of the reconstructed nanocolumn is visualized as isosurface in figure 5.3. The object extends to 260 nm along the preferential [0001] growth direction and to 150 nm and 170 nm along the orthogonal $[1\bar{1}00]$ and the $[11\bar{2}0]$ direction, respectively. The the ratio of the latter dimensions is in accordance with a regular equilateral hexagon. A

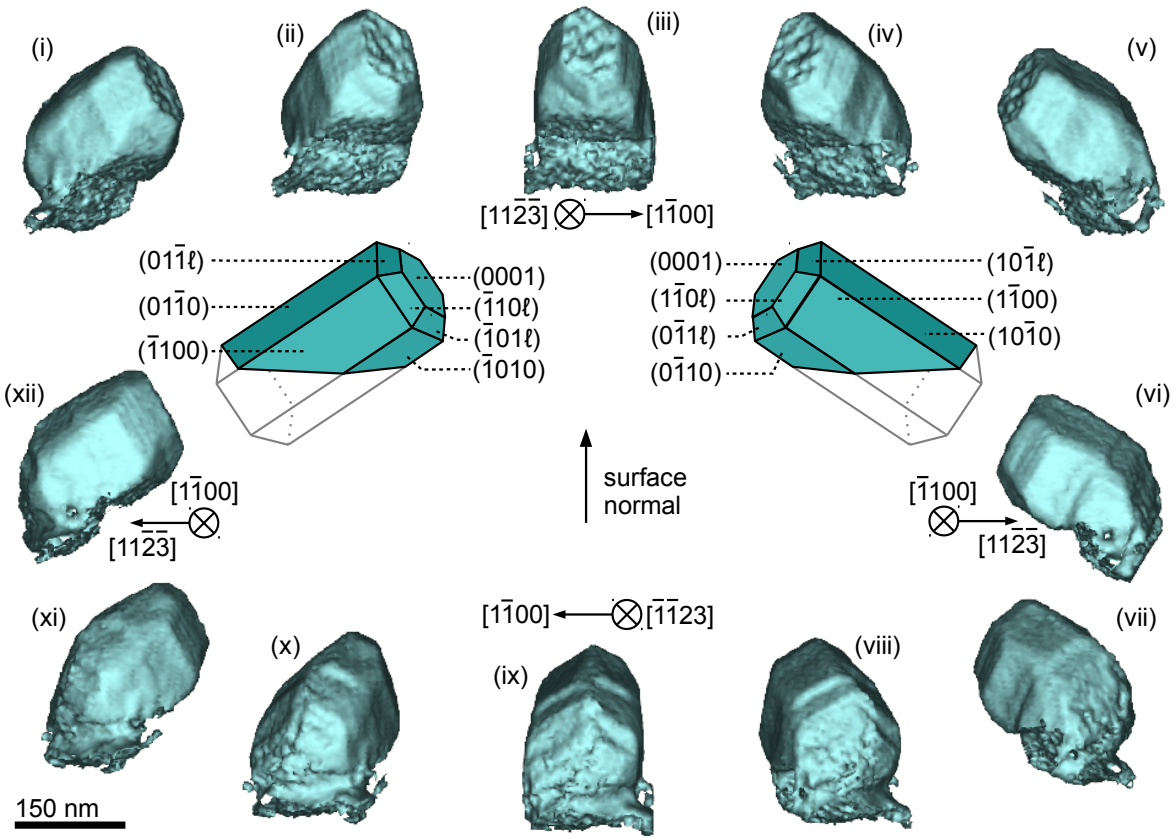

Figure 5.3. The isosurface rendered volume represents the morphology of the nanocolumn. The object is rotated around the original template surface normal in steps of 30° to convey a notion of the 3D shape. The schematics show an idealized hexagonal nanocolumn in order to illustrate the location of indexed facets.

suite of representations from different orientations frames the figure 5.3. The orientations correspond to the full rotation of the inclined nanocolumn around the original surface normal in steps of 30°. This suite conveys a notion of the three-dimensional object and highlights the complex outer shape. The schemes of the nanocolumn from two diametrical directions in the centre of the figure are used to outline the indexation of occurring facets. The facet determination is carried out with the "3dmod" routine of the IMOD software package [157]. The volume has been tilted around a low indexed zone axis starting with the (0001) plane edge on. Then, the tilt angle is determined as soon as a further facet is positioned edge on. In that way, the facet is deduced applying equation B.17.

The apex of the nanocolumn is parallel to the (0001) facet which is perpendicular to the axis of the column. The indexation of the hexagonal crystal structure as outlined in the schemes of figure 5.3 is consistently applied throughout the thesis. To be precise, the polarity has not been determined, i.e. the indexation is incomplete with respect to a possible inversion operation. The views (i) to (v) allow the look onto the (0001) plane. Obviously, the surface exhibits a roughness that is, in contrast, not observed on any other facet. The

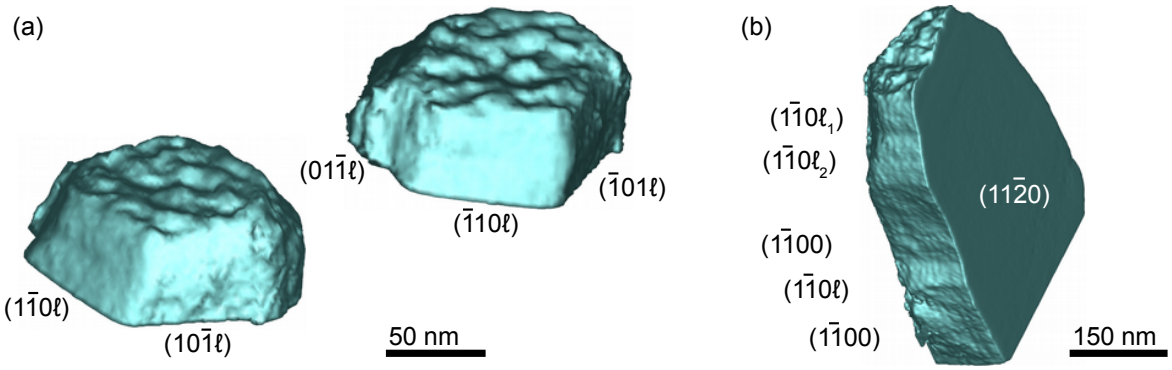

Figure 5.4. (a) The enlarged part of the isosurface illustrates the roughness of the nanocolumn apex. It is viewed in two different bird's eye perspectives. (b) The isosurface representation of the intersected volume highlights steps that interrupt the (1$\bar{1}$00) side facet. The occurrence of different pyramidal facets is outlined.

enlarged part of the apex is shown in figure 5.4(a). It highlights the surface topography which is solely accessible by tomography. The actual roughness is blurred in the projected images of the tilt series (cf. figure 5.2). Further crystallographic forms are summarized as prismatic and pyramidal facets. The former belong to the $\{1\bar{1}00\}$- or m-planes. The latter belong to the $\{1\bar{1}0\ell\}$ family of planes. Prismatic facets parallel to the surface normal, i.e. ($\bar{1}$100) and (1$\bar{1}$00), as well as the (0$\bar{1}$10) and (10$\bar{1}$0) are smooth except for some interruptions by surface steps. These steps are probably formed by pyramidal facets. The intersected isosurface in figure 5.4(b) emphasises these surface steps. The prismatic facets leaned toward the substrate surface are cut during sample preparation or, alternatively, the pyramidal facets originally have had contact to the substrate. The rough appearance of the nanocolumn bottom will be addressed below in section 5.3.2. The pyramidal facets $\{1\bar{1}0\ell\}$ near the apex ($\ell > 0$) are differently developed. Views (vi) and (xii) depict that (10$\bar{1}\ell$) and (01$\bar{1}\ell$) are very small, i.e. the prismatic sides almost touch the basal plane at the apex. The other pyramidal faces are clearly pronounced. In views (ii) and (iv) as well as in (vi) and (xi), ripples on these planes are clearly observed. The enlarged and intersected isosurface in figure 5.4(b) shows

pyramidal facets with different inclination toward the nanocolumn axis which is discerned by the different indices ℓ_1 and ℓ_2. The ripples are attributed to a microfaceting which compromises the indexation of pyramidal facets. The resolution is not sufficient to determine the microfacets. Therefore, the last index of pyramidal facets ℓ has been left undetermined. Prismatic facets are shown to end at the template surface in the schemes in figure 5.3 as simplification. In fact views (v) to (viii) as well as views (x) to (xii) document the presence of pyramidal $\{1\bar{1}0\ell\}$ facets with ($\ell < 0$).

The outer shape of the nanocolumn is compared with the morphology of the (In,Ga)N insertion in figure 5.5. The lower row of isosurface representations repeats views (vi), (v) and (i) from figure 5.3. They are labelled as view onto $(1\bar{1}00)$, onto $(1\bar{1}01)$ and onto $(\bar{1}101)$, respectively. Besides, a view onto the (0001) plane is added which depicts the plan FIB cut of the column about 80 nm below the apex at the side leaned toward the template surface, i.e. approximately parallel to the $(\bar{1}\bar{1}20)$ lattice plane. The upper row represents a montage of two isosurfaces. The outer shape that has been describe beforehand, is presented semi-transparently but still in turquoise colour. In addition, a red opaque isosurface is shown. This corresponds to the (In,Ga)N insertion. GaN covers the whole (In,Ga)N insertion as depicted by the semi-transparent wrap.

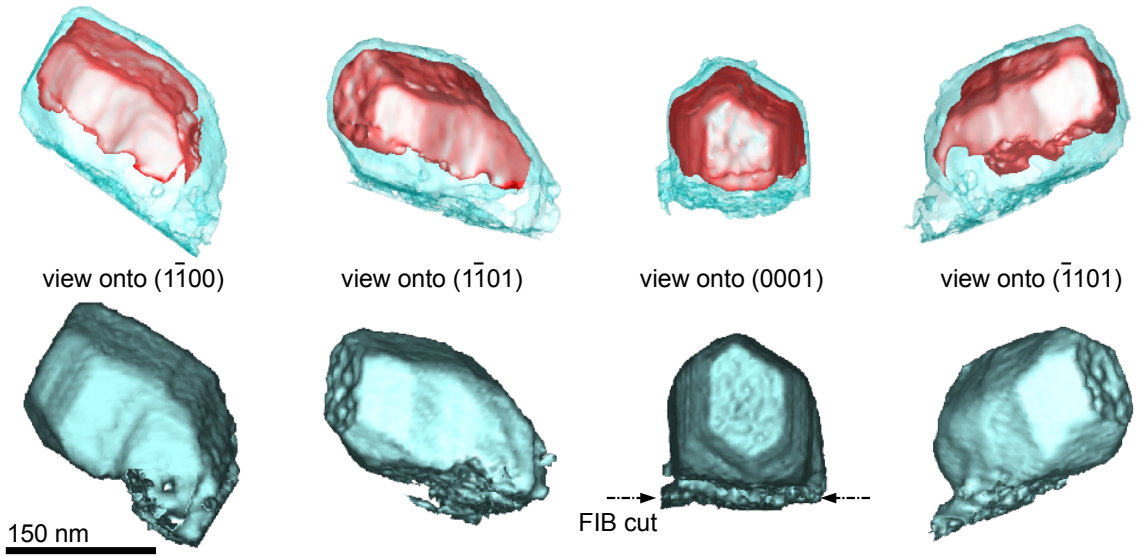

Figure 5.5. The isosurface visualizations of the 3D data set allow the comparison of nanocolumn shape and the morphology of the (In,Ga)N insertion. The upper row shows the insertion as an opaque red isosurface along with the semitransparent, turquoise nanocolumn shape. The lower row presents the opaque, turquoise nanocolumn as isosurface like in figure 5.3.

In general, the (In,Ga)N inclusions mimics the crystallographic facets of the outer shape. Hence, the (In,Ga)N forms a core-shell like coverage (cf. figure 5.5). Obviously, the shell is not completed on the side leaned toward the substrate. This is trivial for the lower part of the column due to the preparative clipping. But a deviation is observed already regarding the prismatic side facets and the pyramidal facets near the template surface. The shell does not reach the clipping of the nanocolumn. This finding is fostered and discussed in the next section.

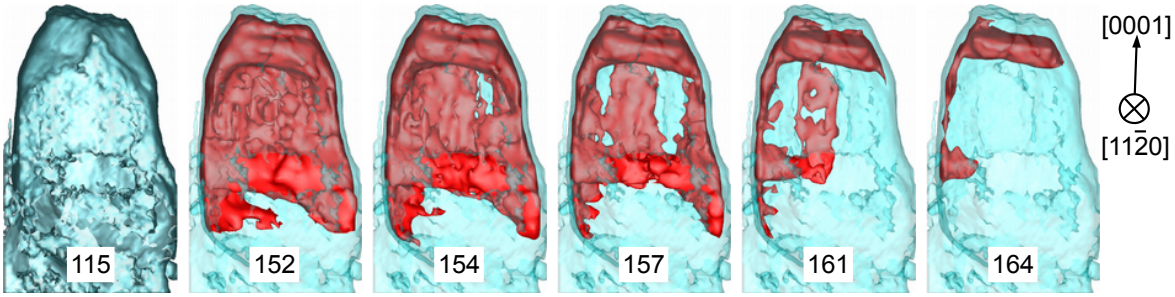

Figure 5.6. Red, opaque isosurfaces represent the grey values pasted at the bottom of the respective nanocolumns. The reference value 115 corresponds to the outer shape of the nanocolumn (turquoise). It is semitransparently drawn as a reference in the presentation of the red isosurfaces.

The presentation of the (In,Ga)N insertion as an isosurface in figure 5.5 needs some explanatory comments. The indium concentration is expected to vary in the (In,Ga)N layer with respect to different facets. The HAADF signal and, eventually, the grey value in the tomogram alter due to this variation. Hence, the morphology of the whole (In,Ga)N insertion cannot be correctly visualized by only one grey value. Figure 5.6 demonstrates the red opaque isosurface for different grey values. The nanocolumn is viewed along the [11$\bar{2}$0] direction, i.e. a view into the shell-like (In,Ga)N insertion is provided. The leftmost image describes the outer nanocolumn shape (grey value 115) as opaque, turquoise isosurface. Afterwards this isosurface appears semitransparently as a reference in subsequent presentations. This procedure is the same as applied for figure 5.5 where the red isosurface corresponds to the selected grey value 152. The correct threshold to present the insertion on the basal plane is certainly higher. Intensity changes in the reconstruction caused by abrupt changes in the object density or the average atomic number appear blurred due to several reasons: The application of a low-pass filter for noise reduction in the tomogram smears out abrupt changes in the intensity. The missing wedge artefact and inaccuracies in image alignment as well as image distortions further contribute to this blurring. The resulting intensity gradient around the volume of the highest indium concentration allows to roughly represent the morphology of the whole (In,Ga)N insertion with only one grey value. But the interference with morphological features at the nanocolumn apex evokes the idea of a roughened (In,Ga)N layer on the basal planes in figure 5.5. The visualization of isosurfaces for increasing grey values in figure 5.6 emphasizes that the insertion is smooth and the roughening occurs in the overgrown GaN layer. It has to be remarked that the access on the roughness of the buried interface is a unique benefit of tomography.

5.2.2. Indium concentration in (In,Ga)N layers parallel to different facets

The qualitative analysis of different indium concentrations in the (In,Ga)N insertions on different facets is obtained from sections through the reconstructed volume. Moreover, differences in the (In,Ga)N layer thickness and morphological changes of the nanocolumn tip are retrieved from the extracted data. Figure 5.7 shows six significant sections together with two isosurface representations. The latter two allow to indicate the positions of the sections through the nanocolumn (dashed lines). The line labels correspond to the designations of the

sections. The grey values of the reconstructed volume are colour coded in order to facilitate the observation of faint intensity variations. Black and dark grey appears in blue. Grey and light grey appear green and yellow, respectively. The highest intensities, i.e. nearly white voxels, are red. The colour scale bar outlines the qualitative dependence on the average atomic number $\bar{Z}$. Carbon of the embedding appears in blue, GaN predominantly in green and (In,Ga)N with the highest indium concentration in red. An absolute determination of the indium fraction in the (In,Ga)N layer is not intended in this work. The value of 26% for the maximal indium concentration is mentioned to provide an order of magnitude. It has been deduced from cathodoluminescence measurements by Bengoechea-Encabo *et al.* [53]. In sections parallel to $\{11\bar{2}0\}$ planes, the chemical interpretation of the intensity is only valid in the upper part. Artefacts in the tomographic reconstruction occur below the white dashed lines. They are discussed in section 5.3.2.

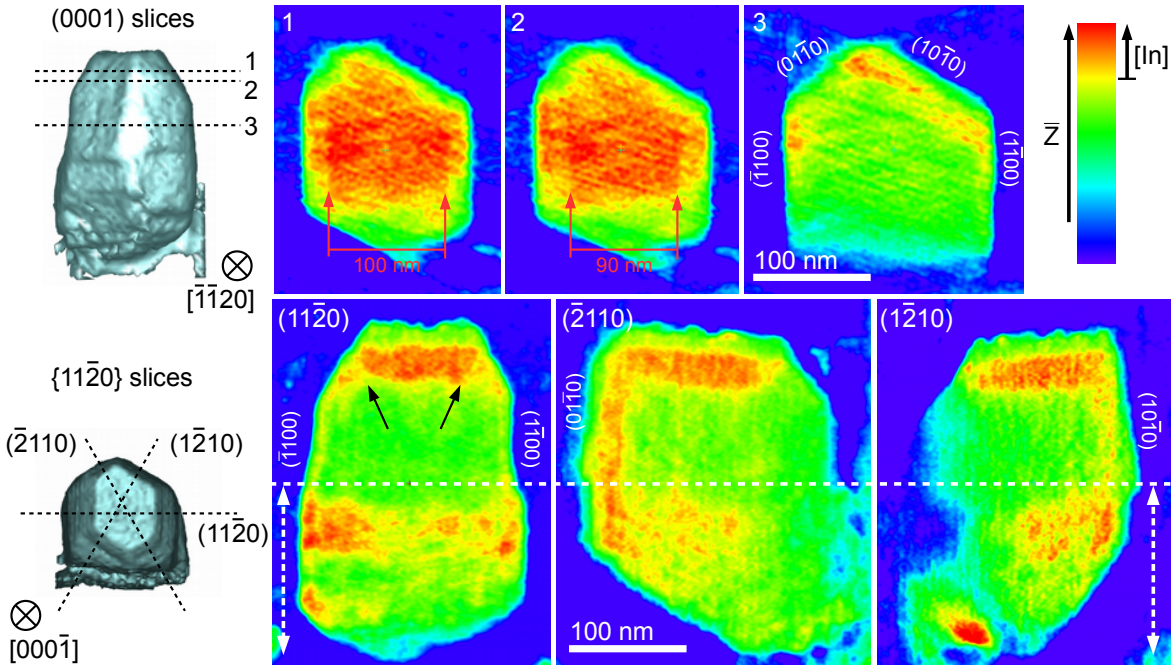

Figure 5.7. The sections through the reconstructed volume of the nanocolumn (right) allow the detailed analysis of the relative indium concentration [In] in (In,Ga)N insertions parallel to different facets. The intersection lines of $\{1\bar{1}00\}$ facets with the slicing planes are outlined. The isosurface rendered volumes in the left are viewed along the $[\bar{1}\bar{1}20]$ and along the $[000\bar{1}]$ direction. The origin of the presented sections and their labels are depicted by black dashed lines.

In figure 5.7, sections 1 to 3 originate from the upper half of the nanocolumn. They are parallel to the (0001) lattice planes. The first two sections cut the pronounced (In,Ga)N insertion which is already visible in the HAADF micrograph projected along the $[11\bar{2}0]$ direction (cf. figure 5.2). Red arrows mark an abrupt change in the indium content. Their distance is higher near the apex. Hence, the region of highest indium content laterally expands towards the top of the nanocolumn. The rim containing a smaller amount of indium shrinks in consequence of the expanding centre part and the reducing tip cross-section. The small coverage by the GaN capping appears at the very edge. The third section is located well below the apex. It reflects the GaN core partially surrounded by the (In,Ga)N insertion on the $\{1\bar{1}00\}$

type facets. The indium concentration fades until complete disappearance before the $(1\bar{1}00)$ and the $(\bar{1}100)$ faces meet the trimmed side in the lower image part. Therefore, the (In,Ga)N insertion does not form a complete shell. The view into the $[000\bar{1}]$ direction exemplifies the unique access to a perspective that is unobtainable for any sample tilt.

Sections that are parallel to the $\{11\bar{2}0\}$ type lattice planes, i.e. orthogonal to the $\{1\bar{1}00\}$ side facets, are presented in the bottom row of figure 5.7. The sections allow to recognize several familiar features from the figures 5.3 and 5.5. A GaN layer encloses the (In,Ga)N insertions. Traces of the smooth pyramidal and prismatic facets follow the silhouette of the nanocolumn. Beyond, information on the (In,Ga)N layer thickness and the qualitative indium concentration are extracted. The highest abundance of indium is found in the layer parallel to the basal planes. The amount of indium in the layer parallel to $\{1\bar{1}00\}$ facets and the layer thickness varies according to the proximity of their surface normal toward the substrate normal. Parallel to the $(01\bar{1}0)$ and the $(10\bar{1}0)$ facet, the indium content is smaller than in the insertion parallel to the basal plane. The layer thickness on these prismatic facets is approximately 5 nm smaller than on the basal plane which is estimated to the value of (30 ± 2) nm. The uncertainty is dominated by artefacts introduced in the tomogram. The $(1\bar{1}00)$ and the $(\bar{1}100)$ side facets exhibit a small indium content and the layers are much thinner than on the symmetry equivalent facets. The (In,Ga)N layer on pyramidal facets is distinguished in the $(11\bar{2}0)$ slice. They are also thicker and contain more indium than the $(1\bar{1}00)$ and the $(\bar{1}100)$ side facets. Black arrows mark the expansion of the basal plane (In,Ga)N insertion along the growth direction which is already suggested by slices 1 and 2. This behaviour is not observed in sections parallel to $(1\bar{2}10)$ and $(\bar{2}110)$, i.e., the hardly developed pyramidal $(01\bar{1}\ell)$ and $(10\bar{1}\ell)$ facet at the outer nanocolumn shape are not pronounced at the GaN core either. The $(\bar{2}110)$ section clearly indicates the absence of an (In,Ga)N layer on pyramidal facets that are faced toward the substrate surface. Besides, these facets are not affected by the FIB cut. The extend of roughness at the apex of the nanocolumn is not present at the termination of the (In,Ga)N insertion on the (0001) plane in accordance with the isosurface consideration in figure 5.6.

The intensities within the insertions on different facets exhibit short range fluctuations in all slices of figure 5.7. A correlation to fluctuations in the indium concentration is not intended in this work. Nevertheless a comment on the potential origin of these fluctuations has to be made because the clustering of indium in (In,Ga)N layers during electron beam irradiation is a well known effect [225, 226]. Consequently, a potential error due to this beam sensitivity of (In,Ga)N has been carefully regarded in experiments that have revealed the indium distribution within a layer as, for instance, done by Schulz *et al.* [227]. In contrast, the presented results are deduced for the insertion on different facets, i.e., the differences of the indium content is considered on a larger length scale. Besides, reconstruction artefacts as a further origin for short range fluctuations of the intensity impede the direct correlation.

5.3. Discussion of experimental results

5.3.1. Implications for (In,Ga)N incorporation

The investigation by electron tomography revealed morphological details which occur due to specific growth conditions. The rough surface at the apex of the nanocolumn is formed

during the deposition of the GaN cap at 625 °C under nitrogen-rich condition (growth details see [53]). Tarsa *et al.* [228] demonstrated the roughening of planar GaN layers that are homoepitaxially grown on (0001) surfaces by plasma-assisted MBE. They have applied comparable growth parameters, i.e. 650 °C and a beam equivalent pressure of nitrogen that has been twelve times higher than the one of Ga.

The nanofaceting which is observed on the pyramidal side facets, is assumed to be composed of low-index facets. These are energetically favourable over vicinal high-index facets. Theoretical calculations by Mutombo and Romanyuk [229] demonstrated that a mixture of $\{1\bar{1}01\}$ and $\{1\bar{1}00\}$ facets is energetically preferred over the semi-polar GaN $\{20\bar{2}1\}$ facets. This case is experimentally confirmed by HAADF STEM observations presented in a work of Zhao *et al.* [230].

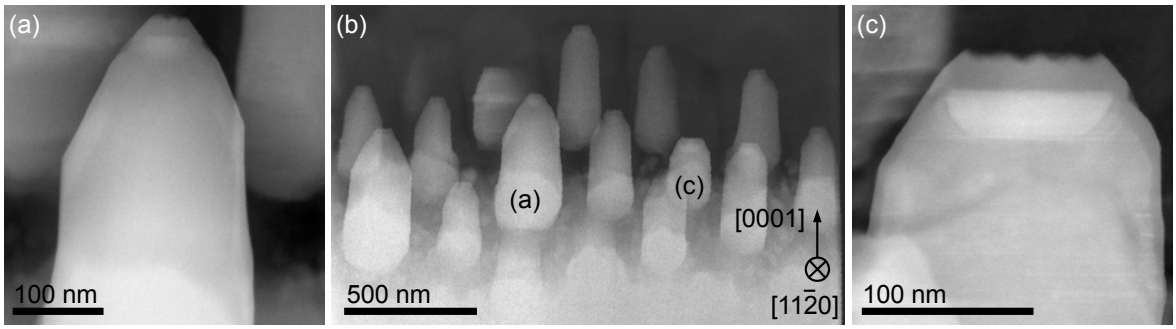

Figure 5.8. The HAADF STEM images give an overview on the nanocolumn morphologies. The different ratio between pyramidal and basal facets characterizes the enlarged areas in (a) and (c) along with their overall different size.

Figure 5.8 broadens the view onto the nanocolumn morphology near the apex. The HAADF STEM micrographs are taken from a lamella that comprises several nanocolumns. Two extreme examples of variable shapes are captured at a higher magnification. They represent the generally observed differences. There are nanocolumns with a more or less pronounced pyramidal habit. Those ones with the hardly developed pyramidal facets are shorter than the others. Albert *et al.* [231] have elaborated on the control of the nanocolumn tip shape. They have fabricated GaN nanocolumns by MBE applying SAG on GaN (0001) templates. The array of 3D objects has appeared homogeneous in contrast to the presented case which is depicted in figures A.3(a) and (b). Beside the different template orientations, the substrate patterning has been carried out with electron beam lithography instead of the colloidal approach applied for the here investigated sample. Hence, morphological heterogeneities could originate from variations in the patterning. For instance, variable hole diameters induce the different nanocolumn sizes. Once the objects passed the mask, the strongly anisotropic material supply in MBE promotes heterogeneities. Then, shadowing affects the morphology of the outer shape as well as of the (In,Ga)N insertions. This effect is described for example by Grandal *et al.* [153]. A further aspect is considered because nanocolumns are roughly classified in two types. The occurrence of inversion domains or the formation of columns with opposite polarity, respectively, could explain different sizes, too. The growth velocity of GaN along the [0001] and the $[000\bar{1}]$ direction is different [232]. The promotion of heterogeneities due to anisotropic material supply remains.

It is shown that the insertion of a core-shell like (In,Ga)N layer on inclined GaN columns grown on the semi-polar GaN (11$\bar{2}$2) substrate is principally feasible. The incorporation of indium and the (In,Ga)N growth rate are highest on the basal plane. The consideration of figure 5.8 shows that a more pronounced pyramidal habit reduces the size of the insertion on the (0001) plane. Consequently, a control of the apex shape is desirable in order to suppress the growth along the polar [0001] axis (cf. section A.2 and [233–235]). Albert *et al.* [231] have manipulated the apex shape of SAG grown GaN columns on (0001) substrates by growth temperature and the ratio of Ga and nitrogen supply. The presented tomogram reveals a mixture of prismatic and pyramidal facets around the tip of the GaN core. Hence, the geometry of the inclined nanocolumns requires further consideration of the growth parameters to control the apex shape. Furthermore, the (In,Ga)N insertion on the basal plane is shown to laterally expand during growth (cf. figure 5.7). It has to be considered whether a (0001) facet evolves during (In,Ga)N growth on a purely pyramidal tip.

The revealed domination of the (01$\bar{1}$0) and the (1$\bar{1}$00) facets (cf. figure 5.3) opens a further possibility to enhance the prevalence of non-polar surfaces. The coalescence of nanocolumns is expected after continued growth resulting in a closed GaN surface. This surface is assumed to be predominantly composed of micrometre-sized {1$\bar{1}$00} facets.

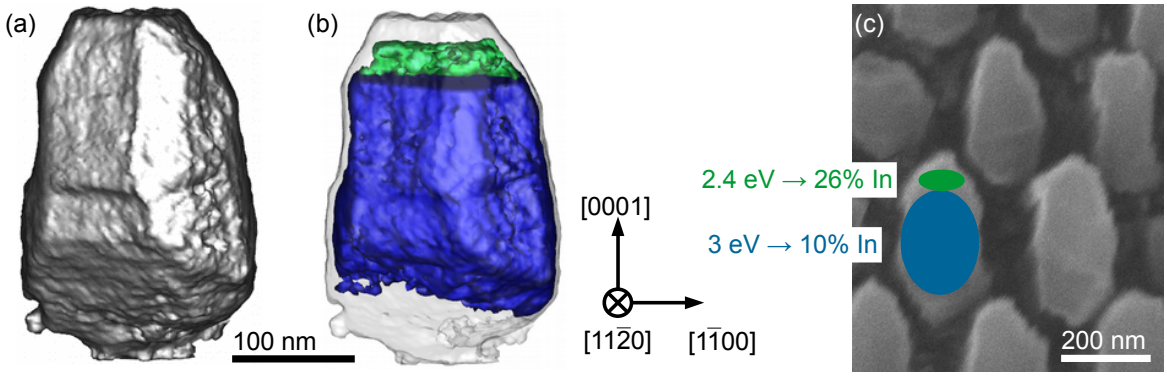

Figure 5.9. (a) The isosurface represents the morphology of the investigated nanocolumn. (b) The outer shape appear as semi-transparent isosurface. The opaque green and blue isosurfaces correspond to (In,Ga)N insertions with a higher and lower indium concentration, respectively. (c) The SEM image is superimposed with the schematically presented cathodoluminescence emission of a nanocolumn according to the results presented in the publication of Bengoechea-Encabo *et al.* [53]. All images show the nanocolumns in the same viewing direction.

Finally, the presented results confirm and extend the ideas on the indium incorporation from the work of Bengoechea-Encabo *et al.* [53]. The tomographic data proves the different indium concentrations on the basal and prismatic facets. The correlation is illustrated in figure 5.9. The isosurface of the nanocolumn and a montage of three different isosurfaces are shown next to an SEM image. The opaque grey isosurface reflects the nanocolumn morphology in 5.9(a). It reappears semi-transparently in figure 5.9(b). The green and blue opaque parts represent the (In,Ga)N insertions on the basal plane and on two of the prismatic planes. The blue isosurface is cropped below the green one. The schematic presentation of CL results as adapted from the respective publication [53] is superimposed on the SEM image in figure 5.9(c). In addition to this principal correlation, a core-shell like morphology of the (In,Ga)N insertion is unveiled. Pronounced pyramidal {1$\bar{1}$0ℓ} facets exhibit an (In,Ga)N

layer, too. They are expected to cause a separate photoluminescence peak according to the work of Albert *et al.* [231]. Furthermore, the tomogram reveals layer thickness variations between the differently developed facets of the complex nanocolumn morphology.

5.3.2. Benefits and limitations of the tomographic data

Three major sources lead to artefacts in the presented tomographic results which are faced in the first instance. They must be carefully considered in order to avoid misinterpretations. The violation of the projection requirement explains the artefacts outlined in the lower halves of the $\{11\bar{2}0\}$ slices in figure 5.7. The first and most important effect originates from a too high thickness of GaN at tilt angles higher than 30°. Nanocolumns in the lower row and parasitic crystallites start to overlap with the bottom of the target object as shown in figure 5.1. This situation qualitatively leads to a wrong distribution of intensity in the tomogram. GaN seems to be missing in the left part of slice $(1\bar{2}10)$ which appears blue (figure 5.7). On the other hand, the red areas in the left of slice $(1\bar{2}10)$ as well as in the right of slice $(\bar{2}110)$ pretend the existence of (In,Ga)N in the core of the column.

The second source is related to the limited tilt range of 150° resulting in the missing wedge artefact. The resulting elongation has been removed but a correction of the intensity spread along the direction of elongation remains. This is schematically depicted in figure 5.10(a). This effect questions the result from figure 5.7 that the (In,Ga)N layer is not grown on the pyramidal $(01\bar{1}\ell)$ and $(10\bar{1}\ell)$ facets. Figure 5.10(b) shows a 2D model corresponding to a section through the insertion near the apex and parallel to the basal plane. It assumes a complete rim of lower indium concentration around the central (In,Ga)N insertion with the highest amount of incorporated indium. A grey scale depth of 256 values is applied. The difference of the grey values is 10 which is smaller than the averaged change visible in figure 5.7 (marked by red arrows). A tilt series of projections in steps of 3° and about a total tilt of 150° is calculated. It serves as input for the tomographic reconstruction with the SIRT algorithm. The resulting tomogram exhibits still the complete ring in addition to the expected blurring of the intensity. Consequently, the result is regarded as reliable.

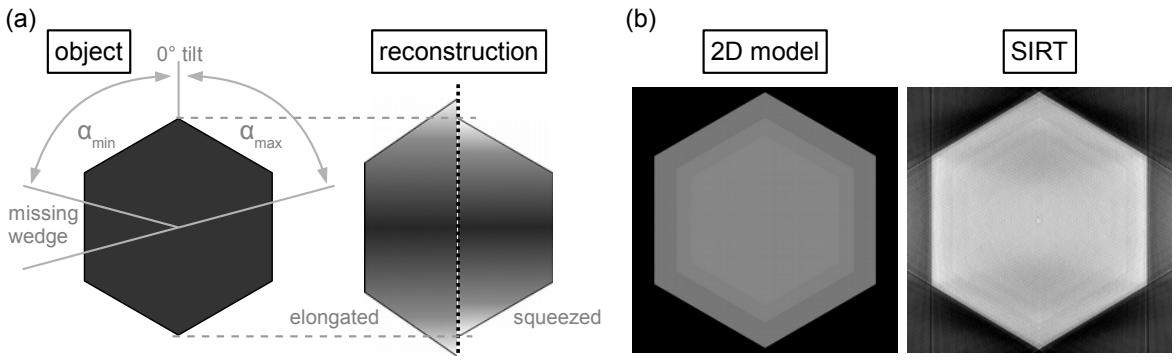

Figure 5.10. (a) The limited tilt-range $\alpha_{max} - \alpha_{min} < 180°$ leads to artefacts in the tomogram due to a lack of information from the "missing wedge". One consequence is the object elongation which is counteracted by a compression of the reconstructed volume. The blurring of intensity along the direction of elongation remains. (b) Projections from the 2D model are calculated and used for the reconstruction with the SIRT algorithm.

The third source of artefacts is the presence of noise in the tomogram. Random image distortions and inaccuracies in the alignment of the tilt series are considered as major origin. A minor contribution is attributed to residual contrast from dislocations and SFs (cf. figure 5.2, e.g. image at 30°). The latter predominantly occur in the bottom half of the nanocolumn. They merely add noise in the part of the tomogram which is already outlined as erroneous. As a consequence, short range, random variations in the intensity of the slices must not be treated as fluctuations in the indium distribution within the (In,Ga)N layer.

In order to avoid the limitations described here and to retain more information from the tomographic results in future investigations, it is suggested to acquire a full tilt series about 180° in steps smaller than 3°. This suggestion implies the isolation of a single nanocolumn in a tomographic specimen. A refinement of the position control during target preparation will be indispensable for this purpose.

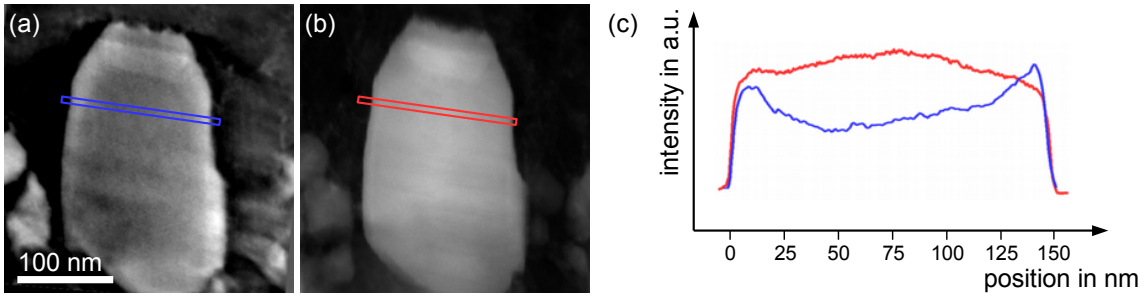

Figure 5.11. The images show (a) a slice through the tomogram and (b) a HAADF STEM micrograph of the target nanocolumn. Both image planes are (approximately) parallel to the $(11\bar{2}0)$ plane. (c) The line profiles are taken from the marked positions in images (a) and (b). They allow to qualitatively compare the information on the (In,Ga)N layer gained from the tomogram and from the projection in a STEM image, respectively.

The unique benefits of tomography in contrast to simple HAADF STEM projections (cf. figure 5.2) and to conventional plan-view and cross-section specimens are outlined in the following. Figure 5.11 compares a slice through the 3D volume parallel to the $(11\bar{2}0)$ lattice plane with a HAADF STEM projection of the original nanocolumn parallel to the same lattice plane. Both images reveal the (In,Ga)N insertion on the basal planes near the apex of the nanocolumn. Beyond this pronounced feature, most information on the remaining (In,Ga)N insertion is superposed with thickness contrast in the HAADF STEM image. The graphs in figure 5.11(c) demonstrate two intensity profiles across the nanocolumn. The increasing intensity toward the nanocolumn centre is observed in the projection. The intensity includes the signal from (In,Ga)N on facets inclined toward the image plane as well as the changing thickness of the projected object. Only a hint to the (In,Ga)N layer on the $(1\bar{1}00)$ facet is found at the left edge of the profile. The tomogram provides the unfolded information on the object thickness and the (In,Ga)N presence.

Alternatively, sections through the nanocolumn must be prepared in order to get rid of the variable thickness. If these specimens allow to image the (In,Ga)N-GaN interfaces edge-on along a low indexed zone axis, the HAADF projection will provide the respective information on the (In,Ga)N layers. But a single, conventionally prepared plan-view or cross-section specimen of a 3D core-shell object offers only a limited insight in the overall shell morphology. A highly symmetric shape has to be assumed in order to draw conclusions on the

whole insertion from the projection information (see e.g. [151–153]). These assumptions do not hold in the case of the presented asymmetric object. Moreover the preparation of several, representative sections on an adequate scale is not feasible. Consequently, tomography provides the only access to the (In,Ga)N layer thicknesses and qualitative variation in the indium fraction on different facets and it conveys a notion of the whole (In,Ga)N insertion around the GaN core. The possibility to arbitrarily rotate and section the reconstructed object constitutes the key to these insights.

The determination of the absolute, quantitative indium fraction in the (In,Ga)N layer is mentioned as outlook for future electron tomography experiments that are based on HAADF STEM tilt series. Quantitative HAADF measurements on layer-by-layer grown (In,Ga)N-GaN heterostructures have been carried out on 2D projections by different groups [236, 237]. The transfer to the third dimension could benefit from their experiences.

6. Conclusion and outlook

The limited spread of electron tomography in materials science with regard to compact, crystalline heterostructures has motivated the introduction of electron tomography at the Paul-Drude-Institut (PDI) für Festkörperelektronik within the frame of the presented work. An increasing 3D design of devices and the continuing shrinkage of structures demands an understanding of the microstructure based on a 3D characterization. The epitaxially fabricated material systems impose two major challenges for the tomographic studies. A target preparation has to be carried out with respect to specimen shape and crystallographic orientation and a suitable (scanning) transmission electron microscopy ((S)TEM) signal has to be found for the acquisition of tomographic tilt series. The first challenge is tackled by the versatile focused ion beam (FIB)-scanning electron microscope (SEM) dual-beam device which has also been introduced at the PDI in the course of this work. The site specific preparation of relevant objects and their confinement in an adequate specimen shape are demonstrated at different examples. The purposeful orientation of a specimen is carried out in order to guarantee a specific imaging condition for a whole tilt series.

Electron tomography is rigorously applied to reveal the 3D arrangement of extended defects and their interaction in complex device-like heterostructures. The 3D representation of defects constitutes the initial information which is not accessible by other experimental techniques. The correlation with complementary measurements on the same specimen and location exceeds the mere 3D representation of defects. In that way, an understanding of the microstructure and its relation to device properties is attained for the investigated semiconductor heterostructures.

The investigation of materials with high atomic number (e.g. antimony) by electron tomography requires a careful selection of a suitable STEM signal. The collection angle range for high-angle annular dark-field imaging is adapted to the maximal specimen thickness and the material under investigation. In that way, chemical information from the Z-contrast micrographs of a tilt series are spatially reconstructed in the tomogram. The access to the 3D arrangement of dislocations is realized with the bright-field STEM signal and the alignment of the $[1\bar{1}0]$ direction to the tilt axis for tomography. In contrast, weak-beam dark-field (WBDF) and annular dark-field (ADF) STEM signals have been applied in the only three electron tomography studies on dislocations in homogeneous semiconductors. The complex microstructure of the investigated antimonide based laser structure demands a representative specimen volume. The resulting thickness rules out the application of the WBDF and the ADF STEM mode. Moreover, it is emphasized that adequate lamella-shaped specimens are uniquely realized with the FIB-SEM device.

The comprehensive investigation of several micrometre thick, epitaxial III-Sb films on Si composed of layers with various composition conveys an idea of the complex 3D microstructure of this material system. At first, pores are revealed in the GaSb buffer layers which are unexpected in these heterostructures grown by molecular beam epitaxy (MBE). They are

generally located below an AlSb layer. Their formation is explained by the accumulation of excess point defects that are introduced during MBE growth. The AlSb layer seems to present an obstacle to the migration of these point defects. The tomographic analysis of the pore shape reveals an unexpected faceting. The minimization of the ratio between surface and volume and a chemical deviation from a clean GaSb surface are regarded.

Secondly, the interface between the III-Sb layer and the Si substrate is addressed. Electron tomography allows to access the buried AlSb initiation layer which forms islands during growth. The island shapes and locations within the subsequently grown GaSb buffer layer are revealed. The asymmetric elongation of islands is related to the prevailing surface domains of the vicinal Si substrate. Complementary TEM and STEM measurements enable a correlation of islands to the misfit dislocation (MFD) networks and to the presence of threading dislocations (TDs). The coalescence of islands and the match of MFD networks appears to work, in principal, without the formation of TDs. This notion is based on the low number of TDs in comparison to the occurrence of coalescence sites and their poor correlation. It is considered that 60° dislocations have to be formed at the interface in addition to perfect 90° dislocations during the initial 3D growth. The missing counterpart to those 60° dislocations in merging islands leads to the TDs. It is argued that 60° dislocations are required to relieve the mismatch along the [001] direction which occurs at the vicinal substrates. Therefore, Burgers vectors with a $\frac{1}{2}$[001] component are assumed to prevail. A strong interference of the presence of TDs, AlSb island edges and APB is suggested by the correlation of tomographic data and complementary measurements.

In the last section on the III-Sb heterostructure, electron tomography is applied to reveal the 3D arrangement of TDs through the epilayer stack. The interaction of dislocations with APBs is inferred from the tomographic reconstruction. APBs appear to be a sink for TDs. Their course is ruled by the planar defect which forces dislocation lines predominantly onto {110} planes. As a consequence, the dislocation distribution is very heterogeneous. Beside the accumulation of dislocations at APBs, there are micrometre-sized parts in the heterostructure that are free of TDs. This aspect might be crucial for the functionality of the heterostructure in a laser device. Furthermore, light is shed on peculiar line directions, i.e. horizontal dislocation segments and line defects that appear to move back and forth. They are explained by means of interaction with APBs and other dislocations. Finally, it has to be emphasized that this comprehensive insight is based on the fabrication of a plane-parallel FIB lamella with a representative sample volume and the capability to image a several micrometres wide field of view by STEM.

The unique access to geometrically complex 3D heterostructures by electron tomography and a dedicated FIB specimen preparation is demonstrated at MBE grown (In,Ga)N/GaN nanocolumns. The 3D objects are elongated along the [0001] direction which is inclined toward the semi-polar $(11\bar{2}2)$ GaN substrate surface. This geometrical constraint precludes a conventional specimen preparation and TEM analysis. The insertion of (In,Ga)N layers on different facets of the nanocolumn is disclosed from the tomogram. Relative differences in the amount of incorporated indium and different layer thicknesses are found for the various facets which are accessed in arbitrary directions and sections through the reconstructed volume. This information is inaccessible for any projection of the nanocolumn in the TEM/STEM. The results provide a detailed understanding of the nanocolumns' optoelectronic properties.

The investigation of material systems regarded in this thesis demonstrates the potential of electron tomography. The future promotion of electron tomography in the research on epitaxial semiconductor heterostructures will meet the requirements to understand the relation between structure and properties of ever shrinking opto-/electronic devices. The visualization of 3D defect arrangements overcomes limitations of 2D micrographs. Most of all, it avoids misinterpretations due to the projection of overlapping microstructural features along the viewing direction.

Some examples for future investigations are implicitly suggested throughout the thesis. For instance, the interaction of pores with dislocations could be unambiguously revealed. It is questioned whether pores nucleate at reaction nodes of dislocations or whether a possible relation to APBs has to be regarded. A further example concerns the initial 100 nm of the GaSb buffer layer on the Si substrate. Lots of dislocations as well as APDs appear to annihilate in this region. Electron tomography would provide valuable details to understand the respective reactions.

Beyond, the tomographic results motivate complementary TEM/STEM studies. Part of TDs are trapped in APBs with line directions predominantly along the [001] direction. Their atomic core structure has to be revealed by high-resolution TEM/STEM experiments. The information would allow to understand the effect of APBs and/or of TDs on device performances.

A. Samples under investigation

Basic principles of heteroepitaxy based on III-V materials are introduced in section 2.1.2. The investigated samples are grown by the molecular beam epitaxy (MBE) technique which is covered, for instance, by the textbook of Herman and Sitter [238]. The following sections describe the two material systems which are chosen as case studies for the presented thesis. The first material system is an example for the cube-on-cube growth of III-Sb layers on Si, i.e. Si(001)$\|$ III-V(001) and $[100]_{\mathrm{Si}}\|[100]_{\mathrm{III\text{-}V}}$, except for one sample that is fabricated on Si(111). The second material system is based on the 3D growth of GaN in the first instance. Afterwards, (In,Ga)N is inserted into the resulting nanocolumns.

A.1. III-Sb on Si(001)

Antimonide based multilayer structures are considered for the realization of infrared laser diodes. The III-As_xSb_{1-x} compounds ($x < 0.1$) allow the engineering of the band gap as well as the lattice constant [56, 57, 208]. The detailed knowledge of quaternary (Ga,In)(As,Sb) and (As,Ga)(As,Sb) alloys with a lattice constant matching GaSb have preceded these goals. Initial studies have been carried out in the thermodynamic limit by applying liquid phase epitaxy [52, 239]. Limitations due to miscibility gaps can be circumvented by non-equilibrium growth methods like chemical or physical vapour deposition techniques [240]. The integration of photonics materials in silicon technology has been demonstrated [241]. Nearly twenty years passed between these achievements. The realization of a GaSb template on Si has been a prerequisite to this work.

The direct deposition of GaSb on Si(001) by MBE results in a 3D growth mode. Akahane *et al.* [181] present a low density of GaSb islands leaving a vast part of the Si surface uncovered. The continued growth leads to a rough layer surface and voids at the heterostructure interface [165]. The introduction of a preliminary AlSb layer of ideally 5 nm nominal thickness [242] changes the situation dramatically. AlSb forms smaller islands with a higher density and better coverage of the substrate [181, 182]. Besides, the interface is chemically stabilized. The direct deposition of GaSb on Si at 600 °C causes a surface roughening that is attributed to the low melting point of the eutectic of Si and Ga [165]. In contrast, the low temperature growth is not an alternative as it results in poor film crystallinity [243]. It has been observed that, firstly, interspaces of AlSb islands are filled with GaSb and the film becomes increasingly smooth during GaSb overgrowth [165, 182, 242]. This has been explained by a strong reduction of the Ga diffusion length in the case of an initial AlSb layer and the preferential growth of GaSb on {111} facets. After the GaSb growth of nominally several tenths of nanometres a smooth film is realized with AlSb islands embedded [57]. A recent study on the application of Al as nucleation layer instead of AlSb points to an alternative approach [212].

The smooth GaSb template conceals a further challenge for the continuation with the

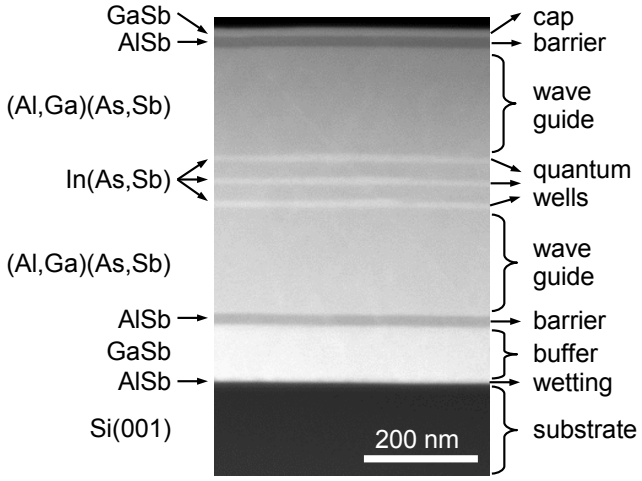

Figure A.1. The III-Sb stacking sequence of design I is depicted along with the HAADF STEM image of sample A.

sample	A	B	C	D	E	F
Si substrate	(001)	4° off (001)	6° off (001)	(111)	4° off (001)	4° off (001)
GaSb buffer [nm]	100	100	1000	1000	1000	1000
AlSb barrier	yes	yes	yes	yes	no	no
design	I	I	I	I	II	II

Table A.1. Overview of III-Sb/Si samples that are under consideration throughout the present thesis.

multilayer structure. The established GaSb buffer contains numerous types of defects. There are threading dislocations (TDs) and planar defects like stacking faults (SFs), twin and anti-phase boundaries (APBs). TDs and APBs are investigated and discussed in sections 4.2 and 4.3. The formation of twin boundaries and SFs in GaSb layers grown directly or with an AlSb wetting layer on Si(001) has been reported [165, 182].

The investigated samples have been grown by MBE in the group of E. Tournié at the Université Montpellier 2, France. Two different designs of III-Sb stacks are considered in this thesis (see figures A.1 and A.2). Both start with an GaSb buffer grown on an AlSb wetting layer as described above. An AlSb barrier layer follows the buffer layer in the first design (I) (figure A.1). Afterwards, two thick (Al,Ga)(As,Sb) wave guide layers enclose the active region of three In(As,Sb) quantum wells (QW) which are separated by (Al,Ga)(As,Sb) layers. A further AlSb barrier follows and an GaSb cap terminates the epitaxial III-Sb layer stack. The capping is necessary because AlSb is prone to oxidation at air [183]. The stacking sequence is illustrated in the HAADF image of sample A in figure A.1. The group V components are dominated by Sb in all layers. Therefore, the HAADF intensity is representative for the Z number of the metal. AlSb appears darkest and In(As,Sb) brightest. The wetting layer is not resolved in the presented image.

The second design (II) exhibits a graded buffer that realizes the transition from GaSb to an Al-rich (Al,Ga)(As,Sb) cladding layer (figure A.2). The (Al,Ga)(As,Sb) wave guide layers embed the active region which is composed of two (Ga,In)(As,Sb) QW separated by

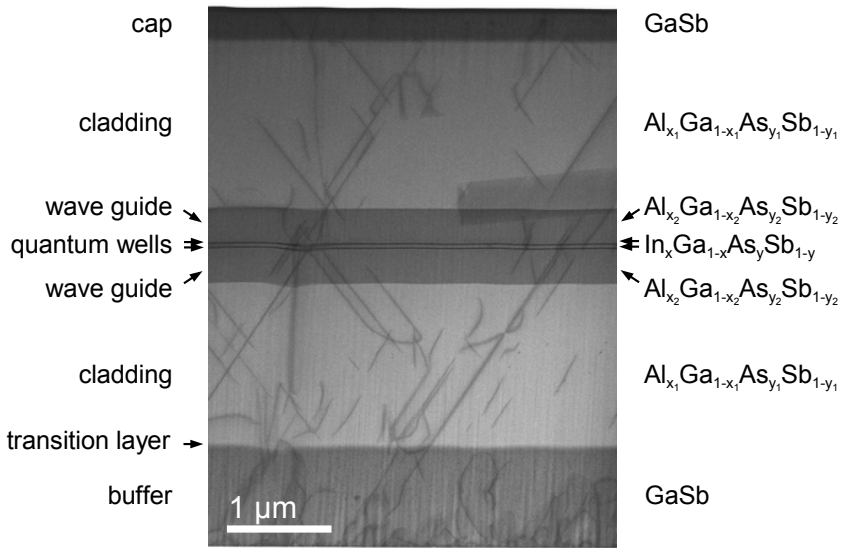

Figure A.2. The III-Sb stacking sequence of design II is depicted along with the BF STEM image of sample F.

an (Al,Ga)(As,Sb) layer. A cladding layer is repeated thereafter. A protective GaSb film terminates the stack. The aluminium content in the cladding layer is higher than in the wave guide, i.e. $x_1 > x_2$. The BF STEM image in figure A.2 reflects this relation by the higher intensity in the cladding layer which is opposite to the HAADF image in figure A.1. Sample E exhibits a superlattice of GaSb layers that alternates with a short period AlSb-GaSb superlattice as difference to the growth begin of the other samples.

Nominal and vicinal Si(001) and Si(111) substrates have been used. The surface normal of vicinal wafers has been inclined toward the [110] direction. Information on the chemical layer structures have been communicated by Cerutti and Tournié [244]. Investigated samples that occur in this thesis, are listed in table A.1. HAADF images of samples A, B, C, D and E are shown in figure 4.7. Sample F is subject of the investigations presented in section 4.3. The fabrication of similar structures is reported by Reboul *et al.* [241] and Rodriguez *et al.* [57]. The process of substrate preparation is described and MBE deposition parameters are given.

A.2. (In,Ga)N/GaN nanocolumns on semi-polar GaN(11$\bar{2}$2)

The impact of GaN based heterostructures is emphasized by the physics Nobel prize 2014 [245]. The realization of efficient white LEDs for everyday application has been awarded. Recent trends outline a route of further improvements: In order to obtain more active surface for light emission per unit area of a wafer, the 3D growth of GaN is pursued [75]. Promising steps toward mass production are already undertaken as they are of industrial interest [246]. The ultimate economic efficiency includes the application of a glass support instead of a single crystalline wafer. A deposited metal film as contact and growth template and the subsequent 3D object fabrication has been demonstrated by Choi *et al.* [247]. According to figure 2.2(a), the band gap of (In,Ga)N alloys is tunable over the whole visible spectrum

(1.59 eV to 3.26 eV) in order to provide white light. Beyond, applications in the ultraviolet and infrared regime are feasible at the wavelength limits of 360 nm (3.44 eV) and 1.9 µm (0.65 eV) for GaN and InN, respectively [49]. The miscibility gap of the solid solution of In in GaN has been successfully overcome by non-equilibrium growth modes. The tunable wavelength and, hence, the complete range of In compositions in (In,Ga)N has been shown by Kuykendall *et al.* [248].

The match of the nitrides to binary sphalerite or elemental diamond structure semiconductors by means of symmetry and lattice constants is difficult. The quest for adequate substrates for the heteroepitaxy of planar GaN films is reviewed by Liu and Edgar [249]. The 3D growth is beneficial in this regard, too. A small contact area to the substrate reduces the abundance of mismatch related threading defects (cf. section 2.1.2). The 3D growth is implemented either by a self-organized manner or by the application of a patterned substrate [75]. The reactivity of nitrogen with potential substrates imposes further challenges to the heteroepitaxy and necessitates substrate treatments in advance of the growth [249]. Finally, the internal piezoelectric field induced along the polar axis of the wurtzite structure has to be considered because it deteriorates the performance of LEDs. Therefore, non- and semi-polar growth directions have been regarded [233–235].

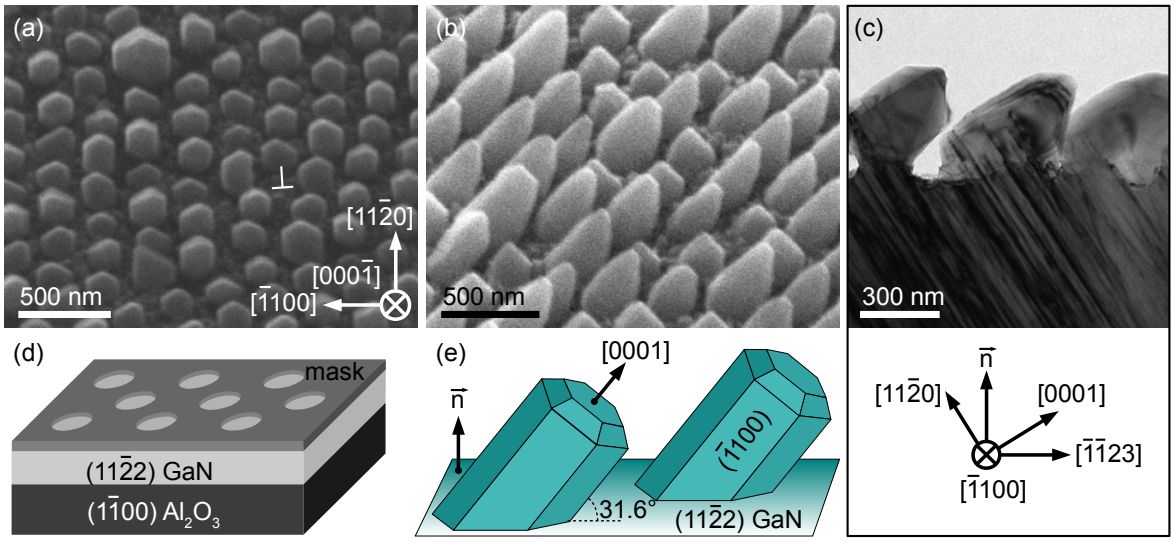

Figure A.3. The secondary electron SEM image along the [000$\bar{1}$] direction highlights the hexagonal symmetry of the nanocolumn morphology (a) and the one in a bird's eye view showing the inclined growth (b). (c) The BF STEM image (courtesy of A. Trampert) presents a cross-section through the nanocolumns viewed along the [$\bar{1}$100] direction. The dark contrast features origin from defects that are predominantly bound to the (0001) planes. The growth geometry obviously serves as defect filter. (d) The schematic depicts the structure of the patterned sample with the Al_2O_3 substrate, the GaN template and the mask. (e) The geometric situation of the sample is sketched with relevant crystallographic planes and directions.

The investigated sample is depicted in figure A.3. It has been grown in the group of E. Calleja in Madrid, Spain, by MBE applying a selected area mask. Growth conditions are published in the work of Bengoechea-Encabo *et al.* [53]. Their goal has been the fabrication of GaN nanocolumns on a semi-polar (11$\bar{2}$2) GaN template and the inclusion of (In,Ga)N in a subsequent step. The SEM images taken with the JIB4501 give a survey of the GaN based

columns in the [000$\bar{1}$] viewing direction (a) and in a bird's eye view (b). The orientation relation in (a) is inferred from the hexagonal symmetry of columns revealed by tilting the sample stage by approximately 54° off the surface normal and aligning the azimuthal stage rotation with a side wall facet. In contrast, a rotation around the surface normal by 90° at a tilt angle of 52° results in the perspective of (b) highlighting the inclined growth with an elongation in the [0001] direction. Regarding equation B.17, the angle between the surface normal of (11$\bar{2}$2) and the [0001] direction is 90°-31.6° = 58.4°, i.e. the maximum tilt of the stage only approaches the [000$\bar{1}$] direction in figure A.3(a). Furthermore, a first idea of the tip morphology is conveyed: There is a basal facet at the apex surrounded by differently pronounced pyramidal facets. Generally, there are rather flat and more pencil-like column tips.

The patterned substrate is schematically depicted in figure A.3(d). A (11$\bar{2}$2) GaN template has been deposited on a (1$\bar{1}$00) Al_2O_3 wafer. A mask for the SAG has been created by colloidal lithography [53, 250]. This procedure relies on the arrangement of spheres in a densely packed mesh. Occasionally, defects are introduced in the hexagonal arrangement of spheres leading, for instance, to "dislocations" (see mark in figure A.3(a)). The approach to design the mask by electron beam lithography allows to avoid such irregularities as shown in samples grown on (0001) GaN templates (see, for instance, [231]).

Figure A.3(e) depicts the geometric situation of the inclined nanocolumns as a schematic model. The normal $\vec{n}$ on the (11$\bar{2}$2) GaN template is parallel to the ($\bar{1}$100) side facet. The preferential [0001] growth direction and the template surface enclose an angle of 31.6°. The impinging material of the molecular beam arrives from directions that describe a cone around the surface normal because the source is not aligned with $\vec{n}$, there is a certain beam divergence and the sample is rotated. Nevertheless, the material is supplied anisotropically and not homogeneously from all directions on a half sphere. Consequently, neither the morphology nor the incorporation of indium are expected to follow the hexagonal symmetry of GaN.

B. Calculations for cubic and hexagonal crystal systems

This appendix lists crystallographic relations that are employed throughout the thesis. Any introductory textbook on solid state physics presents the concepts of Miller indices, crystal coordinate systems and the reciprocal space (see, e.g., [48, 251]). The textbook of Kelly and Knowles [60] is named as reference book for the algebra of crystallographic calculations. Beyond, the publication of Frank [252] provides an instructive description of the hexagonal crystal system and conversion rules to alternative selections of the unit cell: the rhombohedral and the orthorhombic one.

Cubic crystal system

The relations of the Cartesian coordinate system apply to the cubic crystal system. The basis vectors are orthogonal and equally long

$$\vec{a} = a\vec{e}_x \qquad \vec{b} = a\vec{e}_y \qquad \vec{c} = a\vec{e}_z \tag{B.1}$$

where a is the lattice constant and $\vec{e}_i$ are the orthogonal unit vectors. The reciprocal space basis $\left\{\vec{a}^*\ \vec{b}^*\ \vec{c}^*\right\}$ is formed as usual by

$$\vec{a}^* = \frac{\vec{b}\times\vec{c}}{V} \qquad \vec{b}^* = \frac{\vec{c}\times\vec{a}}{V} \qquad \vec{c}^* = \frac{\vec{a}\times\vec{b}}{V} \tag{B.2}$$

with V the volume of the unit cell spanned. The reciprocal basis vectors are orthogonal, too, and they are $1/a$ long. A reciprocal space vector $\vec{g}$ has the Miller indices h, k and l as coordinates

$$\vec{g} = h\vec{a}^* + k\vec{b}^* + l\vec{c}^* = \begin{pmatrix} h \\ k \\ l \end{pmatrix}. \tag{B.3}$$

and corresponds to the set of lattice planes $\{h\ k\ l\}$ in real space. The Miller indices are obtained by the inverse value of the intersection position of the lattice plane $(h\ k\ l)$ with the respective coordinate axes and the distance d_{hkl} from the origin of coordinates. The length of $\vec{g}$ is defined by

$$|\vec{g}| = \frac{1}{a}\sqrt{h^2+k^2+l^2}. \tag{B.4}$$

The reciprocal value is equal to the spacing d of two subsequent $(h\ k\ l)$ lattice planes.

$$d_{hkl} = \frac{1}{|\vec{g}|} \tag{B.5}$$

The angle between two vectors is defined by the inner product

$$\vec{g}_1 \cdot \vec{g}_2 = |\vec{g}_1| \cdot |\vec{g}_2| \cdot \cos \measuredangle(\vec{g}_1, \vec{g}_2). \tag{B.6}$$

The case of the cubic coordinate system allows the trivial calculation of the inner product by

$$\vec{g}_1 \cdot \vec{g}_2 = h_1 h_2 + k_1 k_2 + l_1 l_2. \tag{B.7}$$

and it exhibits the convenient circumstance that the real space direction $[u\ v\ w]$ = $[h\ k\ l]$ is perpendicular to the $(h\ k\ l)$ lattice plane. Hence, the cross product of two directions

$$\begin{bmatrix} u_1 \\ v_1 \\ w_1 \end{bmatrix} \times \begin{bmatrix} u_2 \\ v_2 \\ w_2 \end{bmatrix} = \begin{bmatrix} v_1 w_2 - w_1 v_2 \\ w_1 u_2 - u_1 w_2 \\ u_1 v_2 - v_1 u_2 \end{bmatrix} = \begin{bmatrix} h \\ k \\ l \end{bmatrix} \tag{B.8}$$

yields the lattice plane and its normal.

Hexagonal crystal system

The 4-symbol Miller-Bravais indices h, k, i and l are applied to describe lattice planes in the hexagonal crystal system. Their reciprocal values represent the intersections with the axes $\vec{a}_1$, $\vec{a}_2$, $\vec{a}_3$ and $\vec{c}$ as the usual Miller indices. Figure B.1 illustrates the axes parallel to the

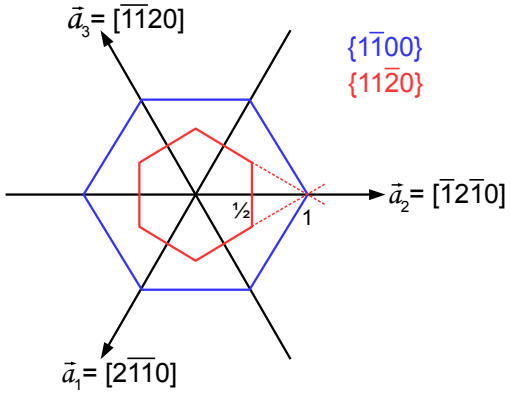

Figure B.1. The description of the hexagonal crystal system is based on a 4-axes system. The 4-symbol Miller-Bravais indexation of lattice planes $(hkil)$ follows the usual rules for Miller indices regarding intersections with the coordinate axes.

basal plane (0001). The c axis is perpendicular to the image plane. It is obvious that $\vec{a}_1$, $\vec{a}_2$ and $\vec{a}_3$ are not independent. The comparison to figure B.1 shows that they are related by

$$\vec{a}_1 + \vec{a}_2 + \vec{a}_3 = 0. \tag{B.9}$$

Likewise, the Miller-Bravais indices are related by $i = -(h+k)$. The benefit of the 4-symbol $(h\ k\ i\ l)$ and the 4 basis vectors is the immediate perceptibility of symmetry equivalent lattice planes. The permutation of h, k and i produces respective planes while l is independent.

Furthermore, the choice of the basis conserves the validity of the zone law in 4-symbol notation

$$uh + vk + ti + wl = 0 \tag{B.10}$$

which has been underlined by Weber [253]. Usually, the calculation of lattice spacings and angles between planes and directions requires the transformation of the 4-symbol into the 3-symbol expression. The respective transformation rules for planes are

$$(h\ k\ i\ l) \rightarrow (h\ k\ l) \tag{B.11}$$

$$(h\ k\ l) \rightarrow (h\ k\ -(h+k)\ l). \tag{B.12}$$

Although the argument for symmetry equivalence applies to direction symbols $[u\ v\ t\ w]$, too, the transformation for directions is different.

$$[u\ v\ t\ w] \rightarrow [(u-t)\ (v-t)\ w] \tag{B.13}$$

$$[u\ v\ w] \rightarrow [(2u-v)\ (2v-u)\ \ -(u+v)\ 3w] \tag{B.14}$$

Using the 3-symbol notation, the plane common to two zones results from the ratio of the direction symbols $h : k : l = (v_1w_2 - w_1v_2) : (w_1u_2 - u_1w_2) : (u_1v_2 - v_1u_2)$. Replacing the two directions by two planes, the equation yields their common zone, i.e. $u : v : w = (k_1l_2 - l_1k_2) : (l_1h_2 - h_1l_2) : (h_1k_2 - k_1h_2)$. The calculation rule is easily remembered by the scheme proposed by Kleber [251] or in analogy to equation B.8. The spacing of the lattice planes $(h\ k\ i\ l)$ is given by

$$d_{hkil}^{-1} = \sqrt{\frac{4}{3a^2}(h^2 + k^2 + hk) + \frac{l^2}{c^2}}. \tag{B.15}$$

The calculation of the angle α between a lattice plane and a direction applying the 4-symbols is derived by Frank [252].

$$\sin\alpha = \frac{uh + vk + it + wl}{\sqrt{(u^2 + v^2 + i^2 + \lambda^2w^2)}\sqrt{(h^2 + k^2 + i^2 + l^2/\lambda^2)}} \tag{B.16}$$

$$\lambda = \sqrt{\frac{2}{3}}\frac{c}{a} \tag{B.17}$$

The factor λ relates the hexagonal lattice constants a and c. A special case occurs for

$$\frac{c}{a} = \sqrt{\frac{3}{2}} \tag{B.18}$$

because the 4-symbol directions and planes

$$[h\ k\ i\ l] \perp (h\ k\ i\ l) \tag{B.19}$$

are orthogonal which is in general not the case.

Bibliography

[1] D.J. DeRosier and A. Klug. Reconstruction of Three Dimensional Structures from Electron Micrographs. *Nature*, 217:130–134, 1968.

[2] J. Frank, editor. *Electron Tomography*. Springer, 1992.

[3] D.B. Williams and C.B. Carter. *Transmission Electron Microscopy*. Springer Science+Business Media, LLC, 1996.

[4] G.N. Hounsfield. Computerized transverse axial scanning (tomography): Part I. Description of system. *British Journal of Radiology*, 46:1016–1022, 1973.

[5] G. Möbus and B.J. Inkson. Nanoscale tomography in materials science. *materialstoday*, 10:18–25, 2007.

[6] A.J. Koster, U. Ziese, A.J. Verkleij, A.H. Janssen, and K.P. de Jong. Three-Dimensional Transmission Electron microscopy: A Novel Imaging and Characterization Technique with Nanometer Scale Resolution for Materials Science. *Journal of Physical Chemistry B*, 104:9368–9370, 2000.

[7] P.A. Midgley and M. Weyland. 3D electron microscopy in the physical sciences: the development of Z-contrast and EFTEM tomography. *Ultramicroscopy*, 96:413–431, 2003.

[8] K. Lepinay, F. Lorut, R. Pantel, and T. Epicier. Chemical 3D tomography of 28 nm high K metal gate transistor: STEM XEDS experimental method and results. *Micron*, 47:43–49, 2013.

[9] P.G. Kotula, L.N. Brewer, J.R. Michael, and L.A. Giannuzzi. Computed Tomographic Spectral Imaging: 3D STEM-EDS Spectral Imaging. *Microscopy and Microanalysis*, 13:1324–1325, 2007.

[10] Z. Saghi, X. Su, Y. Peng, B. Inkson, and G. Möbus. Three-dimensional chemical analysis of tungsten probes by energy dispersive x-ray nanotomography. *Applied Physics Letters*, 91:251906, 2007.

[11] M. Weyland and P.A. Midgley. Electron tomography. *materialstoday*, 7:32–40, 2004.

[12] C. Kübel, A. Voigt, R. Schoemakers, M. Otten, D. Su, T.-C. Lee, A. Carlsson, and J. Bradley. Recent Advances in Electron Tomography: TEM and HAADF-STEM Tomography for Materials Science and Semiconductor Applications. *Microscopy and Microanalysis*, 11:378–400, 2005.

[13] H. Friedrich, P.E. de Jongh, A.J. Verkleij, and K.P. de Jong. Electron Tomography for Heterogeneous Catalysts and Related Nanostructured Materials. *Chemical Reviews*, 109:1613–1629, 2009.

[14] P.A. Midgley and E. Dunin-Borkowski. Electron tomography and holography in materials science. *Nature Materials*, 8:271–280, 2009.

[15] G. Möbus and Z. Saghi. Tomography of nanostructures. In K.D. Sattler, editor, *Handbook of Nanophysics*. Taylor & Francis, 2010.

[16] H.S. Kim, Y. Myung, Y.J. Cho, D.M. Jang, C.S. Jung, and J. Park. Three-Dimensional Structure of Twinned and Zigzagged One-Dimensional Nanostructures Using Electron Tomography. *Nano Letters*, 10:1682–1691, 2010.

[17] I. Arslan, A.A. Talin, and G.T. Wang. Three-Dimensional Visualization of Surface Defects in Core-Shell Nanowires. *Journal of Physical Chemistry C*, 112:11093–11097, 2008.

[18] J. Wu, S. Padalkar, S. Xie, E.R. Hemesath, J. Cheng, G. Liu, A. Yan, J.G. Connell, E. Nakazawa, X. Zhang, L.J. Lauhon, and V.P. Dravid. Electron Tomography of Au-Catalyzed Semiconductor Nanowires. *Journal of Physical Chemistry C*, 117:1059–1063, 2012.

[19] M.A. Verheijen, R.E. Algra, M.T. Borgström, G. Immink, E. Sourty, W.J.P. van Enckevort, E. Vlieg, and E.P.A.M. Bakkers. Three-Dimensional Morphology of GaP-GaAs Nanowires Revealed by Transmission Electron Microscopy Tomography. *Nano Letters*, 7:3051–3055, 2007.

[20] S. Conesa-Boj, S. Estradé, J.M. Rebled, J.D. Prades, A. Cirera, J.R. Morante, F. Peiró, and J. Arbiol. Advanced Electron Microscopy Techniques on Semiconductor Nanowires: from Atomic Density of States Analysis to 3D Reconstruction Models. In Paola Prete, editor, *Nanowires*. InTech, 2010.

[21] G. Tourbot, C. Bougerol, A. Grenier, M. Den Hertog, D. Sam-Giao, D. Cooper, P. Gilet, B. Gayral, and B. Daudin. Structural and optical properties of InGaN/GaN nanowire heterostructures grown by PA-MBE. *Nanotechnology*, 22:075601, 2011.

[22] T. Echigo, N. Monesegue, D.M. Aruguete, M. Murayama, and M.F. Hochella. Nanopores in hematite (α-Fe_2O_3) nanocrystals observed by electron tomography. *American Mineralogist*, 98:154–162, 2013.

[23] I. Arslan, J.R. Tong, and P.A. Midgley. Reducing the missing wedge – High-resolution dual axis tomography on inorganic materials. *Ultramicroscopy*, 106:994–1000, 2006.

[24] Z. Saghi, X. Xu, and G. Möbus. Three-dimensional metrology and fractal analysis of dendritic nanostructures. *Physical Review B*, 78:205428, 2008.

[25] S. Van Aert, K.J. Batenburg, M.D. Rossell, R. Erni, and G. Van Tendeloo. Three-dimensional atomic imaging of crystalline nanoparticles. *Nature*, 470:374–377, 2011.

[26] B. Goris, S. Bals, W. Van den Broek, E. Carbó-Argibay, S. Gómez-Gra na, L.M. Liz-Marzán, and G. Van Tendeloo. Atomic-scale determination of surface facets in gold nanorods. *Nature materials*, 11:930–935, 2012.

[27] M.C. Scott, C.-C. Chen, M. Mecklenburg, C. Zhu, R. Xu, P. Ercius, U. Dahmen, B.C. Regan, and J. Miao. Electron tomography at 2.4-ångström resolution. *Nature*, 483: 444–447, 2012.

[28] C.-C. Chen, C. Zhu, E.R. White, C.-Y. Chiu, M.C. Scott, B.C. Regan, L.D. Marks, Y. Huang, and J. Miao. Three-dimensional imaging of dislocations in a nanoparticle at atomic resolution. *Nature*, 496:74–77, 2013.

[29] H.L. Xin, P. Ercius, K.J. Hughes, J.R. Engstrom, and D.A. Muller. Three-dimensional imaging of pore structures inside low-κ dielectrics. *Applied Physics Letters*, 96: 223108, 2010.

[30] L. Roiban, L. Sorbier, C. Pichon, C. Pham-Huu, M. Drillon, and O. Ersen. 3D-TEM investigation of the nanostructure of a δ-Al_2O_3 catalyst support decorated with Pd nanoparticles. *Nanoscale*, 4:946–954, 2012.

[31] T. Uusimäki, G. Margaris, K. Trohidou, P. Granitzer, K. Rumpf, M. Sezen, and G. Kothleitner. Three-dimensional quantitative characterization of magnetite nanoparticles embedded in mesoporous silicon: local curvature, demagnetizing factors and magnetic Monte Carlo simulations. *Nanoscale*, 5:11944–11953, 2013.

[32] A.K. Shukla, P. Ercius, A.R.S. Gautam, J. Cabana, and U. Dahmen. Electron Tomography Analysis of Reaction Path during Formation of Nanoporous NiO by Solid State Decomposition. *Crystal Growth and Design*, 14:2453–2459, 2014.

[33] T.J.V. Yates, L. Laffont, M. Weyland, D. Zhi, and P.A. Midgley. 3D analysis of semiconductor structures using HAADF STEM tomography. *Institute of Physics: Conference Series*, 179:31–34, 2003.

[34] T. Inoue, T. Kita, O. Wada, M. Konno, T. Yaguchi, and T. Kamino. Electron tomography of embedded semiconductor quantum dot. *Applied Physics Letters*, 92:031902, 2008.

[35] J. Hernández-Saz, M. Herrera, D. Alonso-Álvarez, and S.I. Molina. Analysis of the 3D distribution of stacked self-assembled quantum dots by electron tomography. *Nanoscale Research Letters*, 7:681, 2012.

[36] G. Möbus and B.J. Inkson. Three-dimensional reconstruction of buried nanoparticles by element-sensitive tomography based on inelastically scattered electrons. *Applied Physics Letters*, 79:1369–1371, 2001.

[37] X.Y. Zhong, B. Kabius, D.K. Schreiber, J.A. Eastman, D.D. Fong, and A.K. Petford-Long. Three-dimensional quantitative chemical roughness of buried ZrO_2/In_2O_3 interfaces via energy-filtered electron tomography. *Applied Physics Letters*, 100: 101604, 2012.

[38] H. Stegmann, H.-J. Engelmann, and E. Zschech. Characterization of barrier/seed layer stacks of Cu interconnects by electron tomographic three-dimensional object reconstruction. *Microelectronic Engineering*, 65:171–183, 2003.

[39] P. Ercius, M. Weyland, D.A. Muller, and L.M. Gignac. Three-dimensional imaging of nanovoids in copper interconnects using incoherent bright field tomography. *Applied Physics Letters*, 88:243116, 2006.

[40] S. Kudo, Y. Hirose, T. Yamaguchi, K. Kahihara, K. Maekawa, K. Asai, N. Murata, T. Katayama, K. Asayama, N. Nattori, T. Koyama, and K. Nakamae. Analysis of Junction Leakage Current Failure of Nickel Silicide Abnormal Growth Using Advanced Transmission Electron Microscopy. *IEEE Transactions on Semiconductor Manufacturing*, 27:16–21, 2014.

[41] G. Haberfehlner, R. Serra, D. Cooper, S. Barraud, and P. Bleuet. 3D spatial resolution improvement by dual-axis electron tomgraphy: Application to tri-gate transistors. *Ultramicroscopy*, 136:144–153, 2014.

[42] J.S. Barnard, A.S. Eggeman, J. Sharp, T.A. White, and P.A. Midgley. Three-dimensional analysis of dislocation networks in GaN using weak-beam dark-field electron tomography. *Philosophical Magazine*, 86:4901–4922, 2006.

[43] M. Tanaka, K. Higashida, K. Kaneko, S. Hata, and M. Mitsuhara. Crack tip dislocations revealed by electron tomography in silicon single crystals. *Scripta Materialia*, 59:901–904, 2008.

[44] M. Tanaka, M. Honda, M. Mitsuhara, S. Hata, K. Kaneko, and K. Higashida. Three-Dimensional Observation of Dislocations by Electron Tomography in a Silicon Crystal. *Materials Transactions*, 49:1953–1956, 2008.

[45] A. Mussi, P. Cordier, S. Demouchy, and C. Vanmansart. Characterization of the glide planes of the [001] screw dislocations in olivine using electron tomography. *Physics and Chemistry of Minerals*, 41:537–545, 2014.

[46] O. Madelung and M. Schulz, editors. *Landolt-Börnstein Numerical Data and Functional Relationships in Science and Technology*, Volume III/22. Springer-Verlag Berlin Heidelberg New York, 1987.

[47] T. Hahn, editor. *International Tables of Crystallography*, Volume A: Space-group symmetry. Springer, 2005.

[48] N.W. Ashcroft and D.N. Mermin. *Festkörperphysik*. Oldenbourg Wissenschaftsverlag GmbH, 2007.

[49] J. Wu. When group-III nitrides go infrared: New properties and perspectives. *Journal of Applied Physics*, 106:011101, 2009.

[50] H. Föll. Semiconductors I, 2015. "http://www.tf.uni-kiel.de/matwis/amat/semi_en/index.html", accessed: 2015-11-16.

[51] F. Thuselt. *Physik der Halbleiterbauelemente*. Springer-Verlag Berlin Heidelberg, 2005.

[52] E. Tournié, F. Pitard, A. Joullié, and R. Fourcade. High temperature liquid phase epitaxy of (100) oriented GaInAsSb near the miscibility gap boundary. *Journal of Crystal Growth*, 104:683–694, 1990.

[53] A. Bengoechea-Encabo, S. Albert, J. Zuñiga-Perez, P. de Mierry, A. Trampert, F. Barbagini, M. A. Sanchez-Garcia, and E. Calleja. Selective area growth and characterization of GaN nanocolumns, with and without an InGaN insertion, on semi-polar (11-22) GaN templates. *Applied Physics Letters*, 103:241905, 2013.

[54] L.Y. Kuritzky and J.S. Speck. Lighting for the 21st century with laser diodes based on non-basal plane orientations of GaN. *MRS Communications*, 5:463–473, 2015.

[55] H. Kroemer. The 6.1 Å family (InAs, GaSb, AlSb) and its heterostructures: a selective review. *Physica E*, 20:196–203, 2004.

[56] J.B. Rodriguez, L. Cerutti, and E. Tournié. GaSb-based, 2.2 µm type-I laser fabricated on GaAs substrate operating continuous wave at room temperature. *Applied Physics Letters*, 94:023506, 2009.

[57] J.B. Rodriguez, L. Cerutti, P. Grech, and E. Tournié. Room-temperature operation of a 2.25 µm electrically pumped laser fabricated on a silicon substrate. *Applied Physics Letters*, 94:061124, 2009.

[58] M. Wienold, B. Röben, L. Schrottke, R. Sharma, A. Tahraoui, K. Biermann, and H. T. Grahn. High-temperature, continuous-wave operation of terahertz quantum-cascade lasers with metal-metal waveguides and third-order distributed feedback. *Optics Express*, 22:3334–3348, 2014.

[59] N.Z. Yahaya, M.B.K. Raethar, and M. Awan. Review on Gallium Nitride HEMT Device Technology for High Frequency Converter Applications. *Journal of Power Electronics*, 9:36–42, 2009.

[60] A. Kelly and K.M. Knowles. *Crystallography and Crystal Defects*. John Wiley & Sons, Ltd., 2012.

[61] J. Weertman and J.R. Weertman. *Elementary Dislocation Theory*. Oxford University Press, New York, 1992.

[62] J.P. Hirth and J. Lothe. *Theory of Dislocations*. John Wiley & Sons Inc., 1982.

[63] N. Thompson. Dislocation Nodes in Face-Centred Cubic Lattices. *Proceedings of the Physical Society of London B*, 66:481–492, 1953.

[64] Y.-Y. Wong, E.Y. Chang, T.-H. Yang, J.-R. Chang, J.-T. Ku, M.K. Hudait, W.-C. Chou, M. Chen, and K.-L. Lin. The Roles of Threading Dislocations on Electrical Properties of AlGaN/GaN Heterostructure Grown by MBE. *Journal of The Electrochemical Society*, 157:H746–H749, 2010.

[65] M. Moseley, A. Allerman, M. Crawford, J.J. Wierer, M. Smith, and L. Biedermann. Electrical current leakage and open-core threading dislocations in AlGaN-based deep ultraviolet light-emitting diodes. *Journal of Applied Physics*, 116:053104, 2014.

[66] F.C. Frank and J.H. van der Merwe. One-dimensional dislocations. II. Misfitting monolayers and oriented overgrowth. *Proceedings of the Royal Society (London) A*, 198:216–225, 1949.

[67] E.A. Fitzgerald. Dislocations in strained-layer epitaxy: theory, experiment, and applications. *Materials Science Reports*, 7:87–142, 1991.

[68] J.W. Matthews and A.E. Blakeslee. Defects in epitaxial multilayers: I Misfit dislocations. *Journal of Crystal Growth*, 27:118–125, 1974.

[69] Y.B. Bolkhovityanov and O.P. Pchelyakov. GaAs epitaxy on Si substrates: modern status of research and engineering. *Physics-Uspekhi*, 51:437–456, 2008.

[70] E.P. Kvam. Interaction of Dislocations and Antiphase (Inversion) Domain Boundaries in III-V/IV Heteroepitaxy. *Journal of Electronic Materials*, 23:1021–1026, 1994.

[71] W. Bollmann. *Crystal Defects and Crystalline Interfaces*. Springer Verlag, Berlin, 1970.

[72] A. Trampert. Heteroepitaxy of dissimilar materials: effect of interface structure on strain and defect formation. *The Journal of Physical Chemistry C*, 115:529–533, 2011.

[73] Q. Wan and A. Trampert. Atomic Configuration of the MnAs/GaAs (110) Interface Analyzed by High-Resolution Electron Microscopy. *Journal of Power Electronics*, 9: 36–42, 2009.

[74] J.P. Hirth and R.W. Balluffi. On grain boundary dislocations and ledges. *Acta Metallurgica*, 21:929–942, 1973.

[75] S. Li and A. Waag. GaN based nanorods for solid state lighting. *Journal of Applied Physics*, 111:071101, 2012.

[76] J. Orloff, M. Utlaut, and L. Swanson. *High Resolution Focused Ion Beams - FIB and Its Applications*. Kluwer Academic/Plenum Publishers, New York, 2003.

[77] L.A. Giannuzzi and F.A. Stevie. A review on focused ion beam milling techniques for TEM specimen preparation. *Micron*, 30:197–204, 1999.

[78] M.W. Phaneuf. FIB for materials science applications - a review. In L.A. Giannuzzi and F.A. Stevie, editors, *Introduction to Focused Ion Beams*, pages 143–172. Springer Science+Business Media, Inc., 2005.

[79] B.W. Ward, J.A. Notte, and N.P. Economou. Helium ion microscope: A new tool for nanoscale microscopy and metrology. *Journal of Vacuum Science and Technology B*, 24:2871–2874, 2006.

[80] D.C. Bell, M.C. Lemme, L.A. Stern, J.R. Williams, and C.M. Marcus. Precision cutting and patterning of graphene with helium ions. *Nanotechnology*, 20:455301, 2009.

[81] M.M.V. Taklo, A. Klumpp, P. Ramm, L. Kwakman, and G. Franz. Bonding and TSV in 3D IC Integration: Physical Analysis with a Plasma FIB. *Microscopy and Analysis*, 25:9–12, 2011.

[82] J. Jiruše, T. Hrnčiř, F. Lopour, M. Zadražil, A. Delobbe, and O. Salord. Combined plasma FIB-SEM. *Microscopy and Microanalysis*, 18 (Suppl 2):652–653, 2012.

[83] L. Reimer. *Scanning electron microscopy - Physics of Image Formation and Microanalysis*. Springer-Verlag Berlin Heidelberg, 1998.

[84] DENKA Inc. "DENKA L-MION". product data sheet, 2003.

[85] G. Benassayag, P. Sudraud, and B. Jouffrey. *In situ* high voltage TEM observation of an electrohydrodynamic (EHD) ion source. *Ultramicroscopy*, 16:1–8, 1985.

[86] R.G. Forbes. Understanding how the liquid-metal ion source works. *Vacuum*, 48: 85–97, 1996.

[87] G.D. Alton and P.M. Read. Emittance measurement of gallium liquid-metal ion sources. *Nuclear Instruments and Methods in Physics Research B*, 54:7–11, 1991.

[88] B.I. Prenitzer, C.A. Urbanik-Shannon, L.A. Giannuzzi, S.R. Brown, R.B. Irwin, T.L. Shofner, and F.A. Stevie. The Correlation between Ion Beam/Material Interactions and Practical FIB Specimen Preparation. *Microscopy and Microanalysis*, 9:216–236, 2003.

[89] L.A. Giannuzzi, B.I. Stivie, and B.W. Kempshall. Ion-Solid Interactions. In L.A. Giannuzzi and F.A. Stevie, editors, *Introduction to Focused Ion Beams*, pages 13–52. Springer Science+Business Media, Inc., 2005.

[90] W. Demtröder. *Experimentalphysik 4*. Springer-Verlag Berlin Heidelberg, 2005.

[91] B.W. Kempshall, S.M. Schwarz, B.I. Prenitzer, L.A. Giannuzzi, R.B. Irwin, and F.A. Stevie. Ion channeling effects on the focused ion beam milling on Cu. *Journal of Vacuum Science and Technology B*, 19:749–754, 2001.

[92] L. Frey, C. Lehrer, and H. Ryssel. Nanoscale effects in focused ion beam processing. *Applied Physics A*, 76:1017–1023, 2003.

[93] I. Utke, P. Hoffmann, and Melngailis. Gas-assisted focused electron beam and ion beam processing and fabrication. *Journal of Vacuum Science and Technology B*, 26: 1197–1276, 2008.

[94] N.I. Kato. Reducing focused ion beam damage to transmission electron microscopy samples. *Journal of Electron Microscopy*, 53:451–458, 2004.

[95] J. Hernández-Saz, M. Herrera, and S.I. Molina. A methodology for the fabrication by FIB of needle-shape specimens around sub-surface features at the nanometre scale. *Micron*, 43:643–650, 2012.

[96] H. Yamaguchi, A. Shimase, S. Haraichi, and T. Miyauchi. Characteristics of silicon removal by fine focused gallium ion beam. *Journal of Vacuum Science and Technology B*, 3:71–74, 1985.

[97] D.J. Stokes, T. Vystavel, and F. Morrissey. Focused ion beam (FIB) milling of electrically insulating specimens using simultaneous primary electron and ion beam irradiation. *Journal of Physics D: Applied Physics*, 40:874–877, 2007.

[98] E. Montoya, S. Bals, M.D. Rossell, D. Schryvers, and G. Van Tendeloo. Evaluation of Top, Angle, and Side Cleaned FIB Samples for TEM Analysis. *Microscopy Research and Technique*, 70:1060–1071, 2007.

[99] M. Schaffer, B. Schaffer, and Q. Ramasse. Sample preparation for atomic-resolution STEM at low voltages by FIB. *Ultramicroscopy*, 114:62–71, 2012.

[100] M.C. Dolph and C. Santeufemio. Exploring cryogenic focused ion beam milling as a Group III–V device fabrication tool. *Nuclear Instruments and Methods in Physics Research B*, 328:33–41, 2014.

[101] J.W. Ward, R.L. Kubena, and M.W. Utlaut. Transverse thermal verlocity broadening of focused beams from liquid metal ion sources. *Journal of Vacuum Science and Technology B*, 6:2090–2094, 1988.

[102] L.A. Giannuzzi, B.W. Kempshall, S.M. Schwarz, J.K. Lomnes, B.I. Prenitzer, and F.A. Stivie. FIB Lift-Out Specimen Preparation Techniques. In L.A. Giannuzzi and F.A. Stevie, editors, *Introduction to Focused Ion Beams*, pages 201–228. Springer Science+Business Media, Inc., 2005.

[103] T. Kamino, T. Yaguchi, T. Hashimoto, T. Ohnishi, and K. Umemura. A FIB micro-sampling technique and a site specific TEM specimen preparation method. In L.A. Giannuzzi and F.A. Stevie, editors, *Introduction to Focused Ion Beams*, pages 229–246. Springer Science+Business Media, Inc., 2005.

[104] M. Jublot and M. Texier. Sample preparation by focused ion beam micromachining for transmission electron microscopy imaging in front-view. *Micron*, 56:63–67, 2014.

[105] P.J. Phillips, M. De Graef, and M. Mills. STEM stacking fault analysis in Ni-based super alloys. *Microscopy and Microanalysis*, 16:746–747, 2010.

[106] P. Hirsch, R. Nicholson, A. Howie, and D.W. Pashley. *Electron Microscopy of thin crystals*. Butterworth, London, 1965.

[107] L. Reimer. *Springer Series in Optical Sciences: Transmission Electron Microscopy*. Springer Verlag Berlin Heidelberg, 1984.

[108] S.J. Pennycook and P.D. Nellist, editors. *Scanning Transmission Electron Microscopy - Imaging and Analysis*. Springer Science+Business Media, LLC, 2011.

[109] A.V. Crewe, J. Wall, and L.M. Welter. A High-Resolution Scanning Transmission Electron Microscope. *Journal of Applied Physics*, 39:5861–5868, 1968.

[110] O.L. Krivanek, M.F. Chisholm, V. Nicolosi, T.J. Pennycook, G.J. Corbin, N. Dellby, M.F. Murfitt, C.S. Own, Z.S. Szilagyi, M.P. Oxley, S.T. Pantelides, and S.J. Pennycook. Atom-by-atom structural and chemical analysis by annular dark-field electron microscopy. *Nature*, 464:571–574, 2010.

[111] M. Bosman, V.J. Keast, J.L. García-Muñoz, A.J. D'Alfonso, S.D. Findlay, and L.J. Allen. Two-Dimensional Mapping of Chemical Information at Atomic Resolution. *Physical Review Letters*, 99:086102, 2007.

[112] JEOL Ltd. JEM-2100F - Field Emission Electron Microscope, 2003. User Manual.

[113] C.J. Humphreys. Fundamental concepts of STEM imaging. *Ultramicroscopy*, 7:7–12, 1981.

[114] D.M. Maher and D.C. Joy. The formation and interpretation of defect images from crystalline materials in a scanning transmission electron microscope. *Ultramicroscopy*, 1:239–253, 1976.

[115] P.J. Phillips, M.J. Mills, and M. De Graef. Systematic row and zone axis STEM defect image simulations. *Philosophical Magazine*, 91:2081–2101, 2011.

[116] P.J. Phillips, M.C. Brandes, M.J. Mills, and M. DeGraef. Diffraction contrast STEM of dislocations: Imaging and simulations. *Ultramicroscopy*, 111:1483–1487, 2011.

[117] P.J. Phillips, M. DeGraef, L. Kovarik, A. Agrawal, W. Windl, and M.J. Mills. Atomic-resolution defect contrast in low angle annular dark-field STEM. *Ultramicroscopy*, 116:47–55, 2012.

[118] V.E. Cosslett. Penetration and Resolution of STEM and CTEM in Amorphous and Polycrystalline Materials. *Physica Status Solidi A*, 55:545–548, 1979.

[119] EM-24560 Dark field image observation device, 2007. Instructions of the annular dark field detector.

[120] D.S. He and Z.Y. Li. A practical approach to quantify the ADF detector in STEM. *Journal of Physics: Conference Series*, 522:012017, 2014.

[121] P. Hartel, H. Rose, and C. Dinges. Conditions and reasons for incoherent imaging in STEM. *Ultramicroscopy*, 63:93–114, 1996.

[122] S.J. Pennycook. Structure Determination Through Z-Contrast Microscopy. *Advances in Imaging and Electron Physics*, 123:173–206, 2002.

[123] Y. Peng, P.D. Nellist, and S.J. Pennycook. HAADF-STEM imaging with sub-angstrom probes: a full Bloch wave analysis. *Journal of Electron Microscopy*, 53: 257–266, 2004.

[124] B.F. Buxton, J.E. Loveluck, and J.W. Steeds. Bloch waves and their corresponding atomic and molecular orbitals in high energy electron diffraction. *Philosophical Magazine A*, 38:259–278, 1978.

[125] P. Geuens and D. Van Dyck. The S-state model: a work horse for HRTEM. *Ultramicroscopy*, 93:179–198, 2002.

[126] J.M. Cowley and Y. Huang. De-channeling contrast in annular dark-field STEM. *Ultramicroscopy*, 40:171–180, 1992.

[127] D.D. Perovic, A. Howie, and C.J. Rossouw. On the image contrast from dislocations in high-angle annular dark-field scanning transmission electron microscopy. *Philosophical Magazine Letters*, 67:261–272, 1993.

[128] V. Grillo. The effect of surface strain relaxation on HAADF imaging. *Ultramicroscopy*, 109:1453–1464, 2009.

[129] Z. Yu, D.A. Muller, and J. Silcox. Relative contrast in a-Si and c-Si in ADF-STEM imaging. *Microscopy and Microanalysis*, 9:848–849, 2003.

[130] J. Radon. Über die Bestimmung von Funktionen durch ihre Integralwerte längs gewisser Mannigfaltigkeiten. *Berichte der Sächsischen Akademie der Wissenschaften*, 69:262–277, 1917.

[131] S.R. Deans. *The Radon Transform*. Dover Publications Inc., 2007.

[132] P.W. Hawkes. The Electron Microscope as a Structure Projector. In J. Frank, editor, *Electron Tomography*. Plenum Press, New York, 1992.

[133] R.A. Crowther, D.J. de Rosier, and A. Klug. The reconstruction of a three-dimensional structure from projections and its application to electron microscopy. *Proceedings of the Royal Society of London A*, 317:319–340, 1970.

[134] M. Radermacher and W. Hoppe. Properties of 3-D reconstructions from projections by conical tilting compared to single-axis tilting. *Proceedings of the Seventh European Congress on Electron Microscopy*, 1:132–133, 1980.

[135] D.J. DeRosier and P.B. Moore. Reconstruction of Three-dimensional Images from Electron Micrographs of Structures with Helical Symmetry. *Journal of Molecular Biology*, 52:355–369, 1970.

[136] P.R. Smith, T.M. Peters, and R.H.T. Bates. Image reconstruction from finite numbers of projections. *Journal of Physics A: Mathematical, Nuclear and General*, 6:361–382, 1973.

[137] R.G. Hart. Electron Microscopy of Unstained Biological Material: The Polytropic Montage. *Science*, 159:1464–1467, 1968.

[138] P.W. Hawkes. Weighted Back-Projection Methods. In J. Frank, editor, *Electron Tomography*. Plenum Press, New York, 1992.

[139] P. Gilbert. Iterative Methods for the Three-dimensional Reconstruction of an Object from Projections. *Journal of Theoretical Biology*, 36:105–117, 1972.

[140] R. Gordon, R. Bender, and G.T. Herman. Algebraic Reconstruction Techniques (ART) for Three-dimensional Electron Microscopy and X-ray Photography. *Journal of Theoretical Biology*, 29:471–481, 1970.

[141] J. Miao, F. Förster, and O. Levi. Equally sloped tomography with oversampling reconstruction. *Physical Review B*, 72:052103, 2005.

[142] J.-J. Fernandez. Computational methods for electron tomography. *Micron*, 43:1010–1030, 2012.

[143] X. Ke, S. Bals, D. Cott, T. Hantschel, H. Bender, and G. Van Tendeloo. Three-Dimensional Analysis of Carbon Nanotube Networks in Interconnects by Electron Tomography without Missing Wedge Artifacts. *Microscopy and Microanalysis*, 16: 210–217, 2010.

[144] K.J. Batenburg, S. Bals, J. Sijbers, C. Kübel, P.A. Midgley, J.C. Hernandez, U. Kaiser, E.R. Encina, E.A. Coronado, and G. Van Tendeloo. 3D imaging of nanomaterials by discrete tomography. *Ultramicroscopy*, 109:730–740, 2009.

[145] T. Roelandts, K.J. Batenburg, E. Biermans, C. Kübel, S. Bals, and J. Sijbers. Accurate segmentation of dense nanoparticles by partially discrete electron tomography. *Ultramicroscopy*, 114:96–105, 2012.

[146] J.F. Ziegler. SRIM - The Stopping and Range of Ions in Matter, 2016. "http://www.srim.org", accessed: 2016-02-08.

[147] A. Rosenauer, K. Gries, K. Müller, A. Pretorius, M. Schowalter, A. Avramescu, K. Engl, and S. Lutgen. Measurement of specimen thickness and composition in $Al_xGa_{1-x}N$/GaN using high-angle annular dark field images. *Ultramicroscopy*, 109: 1171–1182, 2009.

[148] J.-Y. Igaki, K. Kanda, Y. Haruyama, M. Ishida, Y. Ochiai, J.-I. Fujita, T. Kaito, and S. Matsui. Comparison of FIB-CVD and EB-CVD growth characteristics. *Microelectronic Engineering*, 83:1225–1228, 2006.

[149] S. Hata, H. Sosiati, N. Kuwano, M. Itakura, T. Nakano, and Y. Umakoshi. Removing focused ion-beam damages on transmission electron microscopy specimens by using a plasma cleaner. *Journal of Electron Microscopy*, 55:23–26, 2006.

[150] R. Pérez and P. Gumbsch. Directional Anisotropy in the Cleavage Fracture of Silicon. *Physical Review Letters*, 84:5347–5350, 2000.

[151] T.-W. Yeh, Y.-T. Lin, L.S. Stewart, P.D. Dapkus, R. Sarkissian, J.D. O'Brien, B. Ahn, and S.R. Nutt. InGaN/GaN Multiple Quantum Wells Grown on Nonpolar Facets of Vertical GaN Nanorod Arrays. *Nano Letters*, 12:3257–3262, 2012.

[152] J.-R. Chang, S.-P. Chang, Y.-J. Li, Y.-J. Cheng, K.-P. Sou, J.-K. Huang, H.-C. Kuo, and C.-Y. Chang. Fabrication and luminescent properties of core-shell InGaN/GaN multiple quantum wells on GaN nanopillars. *Applied Physics Letters*, 100:261103, 2012.

[153] J. Grandal, M. Wu, X. Kong, M. Hanke, E. Dimakis, L. Geelhaar, H. Riechert, and A. Trampert. Plan-view transmission electron microscopy investigation of GaAs/(In,Ga)As core-shell nanowires. *Applied Physics Letters*, 105:121602, 2014.

[154] JEMS - Electron Microscopy Software Java Version, 2012. © Pierre Stadelmann 1999-2012, CIME - EPFL Switzerland.

[155] E.A. Fischione Instruments, Ltd. Model2050 - on-axis rotation tomography holder, 2015. "www.fischione.com/products/holders/model-2050-axis-rotation-tomography-holder", accessed: 2015-11-12.

[156] W. Van den Broek, A. Rosenauer, B. Goris, G.T. Martinez, S. Bals, S. Van Aert, and D. Van Dyck. Correction of non-linear thickness effects in HAADF STEM electron tomography. *Ultramicroscopy*, 116:8–12, 2012.

[157] J.R. Kremer, D.N. Mastronarde, and J.R. McIntosh. Computer visualization of three-dimensional data using IMOD. *J. Struct. Biol.*, 116:71–76, 1996.

[158] D.N. Mastronarde. Dual-axis tomography: an approach with alignment methods that preserve resolution. *J. Struct. Biol.*, 120:343–352, 1997.

[159] J.S. Barnard, J.H. Sharp, J.R. Tong, and P.A. Midgley. Weak-beam dark-field electron tomography of dislocations in GaN. *Journal of Physics: Conference Series*, 26:247–250, 2006.

[160] J.S. Barnard, J. Sharp, J.R. Tong, and P.A. Midgley. High-Resolution Three-Dimensional Imaging of Dislocations. *Science*, 313:319, 2006.

[161] J.S. Barnard, A.S. Eggeman, J. Sharp, T.A. White, and P.A. Midgley. Dislocation electron tomography and precession electron diffraction - minimizing the effects of dynamical interactions in real and reciprocal space. *Philosophical Magazine*, 90: 4711–4730, 2010.

[162] S. Hata, H. Miyazaki, S. Miyazaki, M. Mitsuhara, M. Tanaka, K. Kaneko, K. Higashida, K. Ikeda, H. Nakashima, S. Matsumura, J.S. Barnard, J.H. Sharp, and P.A. Midgley. High-angle triple-axis specimen holder for three-dimensional diffraction contrast imaging in transmission electron microscopy. *Ultramicroscopy*, 111:1168–1175, 2011.

[163] M. Niehle and A. Trampert. Electron tomography on nanopores embedded in epitaxial GaSb thin films. *Micron*, 73:54–62, 2015.

[164] M. Rühle and M. Wilkens. Defocusing contrast of cavities I. Theory. *Crystal Lattice Defects*, 6:129–140, 1975.

[165] S.H. Vajargah, S. Ghanad-Tavakoli, J.S. Preston, R.N. Kleiman, and G.A. Botton. Growth mechanisms of GaSb heteroepitaxial films on Si with an AlSb buffer layer. *Journal of Applied Physics*, 114:113101, 2013.

[166] S.P. Murarka and M.C. Peckerar. *Electronic Materials - Science and Technology*. Academic Press Inc., 1989.

[167] H.A. Tahini, A. Chroneos, H. Bracht, S.T. Murphy, R.W. Grimes, and U. Schwingenschlögl. Antisites and anisotropic diffusion in GaAs and GaSb. *Applied Physics Letters*, 103:142107, 2013.

[168] R. Vardya and S. Mahajan. Mechanism of dislocation climb in binary and mixed III-V semiconductors. *Philosophical Magazine A*, 71:465–472, 1995.

[169] S.H. Huang, G. Balakrishnan, M. Mehta, L.R. Dawson, D.L. Huffaker, and P. Li. Arsenic-induced etched nanovoids on GaSb (100). *Journal of Applied Physics*, 102: 044312, 2007.

[170] C. Jäger and W. Jäger. Defect formation and dopant diffusion in III-V semiconductors: zinc diffusion in GaP. *Journal of Physics: Condensed Matter*, 14:12865–12870, 2002.

[171] J.W. Cahn and R.E. Hannemann. (111) surface tension of III-V compounds and their relationship to spontaneous bending of thin crystals. *Surface Science*, 1:387–398, 21964.

[172] W.A. Harrison. Electronic structure and the properties of interfaces. *Ultramicroscopy*, 14:85–88, 1984.

[173] H. Lüth. *Solid Surfaces, Interfaces and Thin Films*. Springer-Verlag Berlin Heidelberg, 2015.

[174] J. Houze, S. Kim, S.-G. Kim, S.C. Erwin, and L.G. Whitman. Structure of AlSb(001) and GaSb(001) surfaces under extreme Sb-rich conditions. *Physical Review B*, 76: 205303, 2007.

[175] K. Matoba, J. Takagi, T. Yasunaga, H. Jinnai, and K. Iwasaki. Tilt-angle measurement of a sample stage using a capacitive liquid-based inclinometer. *Journal of Electron Microscopy*, 61:193–198, 2012.

[176] R.F. Egerton, P. Li, and M. Malac. Radiation damage in the TEM and SEM. *Micron*, 35:399–409, 2004.

[177] H. Yasuda, A. Tanaka, K. Matsumoto, N. Nitta, and H. Mori. Formation of Porous GaSb Compound Nanoparticles by Electronic-Excitation-Induced Vacancy Clustering. *Physical Review Letters*, 100:105506, 2008.

[178] A. Lugstein, J. Bernardi, C. Tomastik, and E. Bertagnolli. Synthesis of nanowires in room temperature ambient: a focused ion beam approach. *Applied Physics Letters*, 88:163114, 2006.

[179] A. Lugstein, C. Schoendorfer, M. Weil, C. Tomastik, A. Jauss, and E. Bertagnolli. Study of focused ion beam response of GaSb. *Nuclear Instruments and Methods in Physics Research B*, 255:309–313, 2007.

[180] M. Hayashida, T. Iijima, M. Tsukahara, and S. Ogawa. High-precision alignment of electron tomography tilt series using markers formed in helium-ion microscope. *Micron*, 50:29–34, 2013.

[181] K. Akahane, N. Yamamoto, S.-I. Gozu, A. Ueta, and N. Ohtani. Initial growth stage of GaSb on Si(001) substrates with AlSb initiation layer. *Journal of Crystal Growth*, 283:297–302, 2005.

[182] Y.H. Kim, Y.K. Noh, M.D. Kim, J.E. Oh, and K.S. Chung. Transmission electron microscopy study of the initial growth stage of GaSb grown on Si (001) substrate by molecular bema epitaxy method. *Thin Solid Films*, 518:2280–2284, 2010.

[183] T. Shibata, J. Nakata, Y. Nanishi, and M. Fujimoto. A Rutherford Backscattering Spectroscopic Study of the Aluminum Antimonide Oxidation Process in Air. *Japanese Journal of Applied Physics*, 33:1767–1772, 1994.

[184] J.M. García, G. Medeiros-Ribeiro, K. Schmidt, T. Ngo, J.L. Feng, A. Lorke, J. Kotthaus, and P.M. Petroff. Intermixing and shape changes during the formation of InAs self-assembled quantum dots. *Applied Physics Letters*, 71:2014–2016, 1997.

[185] R. Songmuang, S. Kiravittaya, and O.G. Schmidt. Shape evolution of InAs quantum dots during overgrowth. *Journal of Crystal Growth*, 249:416–421, 2003.

[186] K. Song, L.R. Comolli, and M. Horowitz. Removing high contrast artifacts via digital inpainting in cryo-electron tomography: An application of compressed sensing. *Journal of Structural Biology*, 178:108–120, 2012.

[187] S.H. Vajargah, M. Couillard, K. Cui, S.G. Tavakoli, B. Robinson, R.N. Kleiman, J.S. Preston, and G.A. Botton. Strain relief and AlSb buffer layer morphology in GaSb heteroepitaxial films grown on Si as revealed by high-angle annular dark-field scanning transmission electron microscopy. *Applied Physics Letters*, 98:082113, 2011.

[188] G.A. Bassett, J.W. Menter, and D.W. Pashley. Moiré patterns on electron micrographs, and their application to the study of dislocations in metals. *Proceedings of the Rocyal Society of London A*, 246:345–368, 1958.

[189] J.E. Angelo, J.N. Kuznia, A.M. Wowchak, P.I. Cohen, and W.W. Gerberich. Identification of the misfit dislocations at an FeAl/AlAs/GaAs interface using moiré fringe contrast in a transmission electron microscope. *Applied Physics Letters*, 59:63–65, 1991.

[190] A. Rocher and E. Snoeck. Misfit dislocations in (001) semiconductor heterostructures grown by epitaxy. *Materials Science and Engineering*, B67:62–69, 1999.

[191] A. Georgakilas, J. Stoemenos, K. Tsagaraki, P. Komninou, N. Flevaris, P. Panayotatos, and A. Christou. Generation and annihilation of antiphase domain boundaries in GaAs on Si grown by molecular beam epitaxy. *Journal of Material Research*, 8: 1908–1921, 1993.

[192] R.L. Schwöbel and E.J. Shipsey. Step Motion on Crystal Surfaces. *Journal of Applied Physics*, 37:3682–3686, 1966.

[193] D.J. Chadi. Stability of Single-Layer and Bilayer Steps on Si(001) Surfaces. *Physical Review Letters*, 59:1691–1694, 1987.

[194] J.M. Kang, M. Mouaoura, L. Lassabatère, and A. Rocher. Accomodation of lattice mismatch and threading of dislocations in GaSb films grown at different temperatures on GaAs (001). *Journal of Crystal Growth*, 143:115–123, 1994.

[195] F. Ernst and P. Pirouz. The formation mechanism of planar defects in compound semiconductors grown epitaxially on {100} silicon substrates. *Journal of Materials Research*, 4:834–842, 1989.

[196] J.G. Zhu and C.B. Carter. 60° dislocations in (001) GaAs/Si interfaces. *Philosophical Magazine A*, 62:319–328, 1990.

[197] P. Komninou, J. Stoemenos, G.P. Dimitrakopulos, and T. Karakostas. Misfit dislocations and antiphase domain boundaries in GaAs/Si interface. *Journal of Applied Physics*, 75:143–152, 1993.

[198] A. Bourret and P.H. Fuoss. Structure of GaAs=GaSb incoherent interface after epitaxial growth. *Applied Physics Letters*, 61:1034–1036, 1992.

[199] A. Korner and H.P. Karnthaler. The study of glide dislocation loops on {001} planes in a f.c.c. alloy. *Philosophical Magazine A*, 42:753–762, 1980.

[200] W. Qian, M. Skowronski, R. Kaspi, M. De Graef, and V.P. Dravid. Nucleation of misfit and threading dislocations during epitaxial growth of GaSb on GaAs(001) substrates. *Journal of Applied Physics*, 81:7268–7272, 1997.

[201] K. Madiomanana, M. Bahri, J.B. Rodriguez, L. Largeau, L. Cerutti, O. Mauguin, A. Castellano, G. Patriarche, and E. Tournié. Silicon surface preparation for III-V molecular beam epitaxy. *Journal of Crystal Growth*, 413:17–24, 2015.

[202] C. Messaoudil, T. Boudier, C.O. Sanchez Sorzano, and S. Marco. TomoJ: tomography software for three-dimensional reconstruction in transmission electron microscopy. *BMC Bioinformatics*, 8:288, 2007.

[203] G. Capellini, M. De Seta, Y. Busby, M. Pea, F. Evangelisti, G. Nicotra, C. Spinella, M. Nardone, and C. Ferrari. Strain relaxation in high Ge content SiGe layers deposited on Si. *Journal of Applied Physics*, 107:063504, 2010.

[204] P.M. Mooney, F.K. LeGoues, J. Tersoff, and J.O. Chu. Nucleation of dislocations in SiGe layers grown on (001)Si. *Journal of Applied Physics*, 75:3968–3977, 1994.

[205] J. Taftø and J.C.H. Spence. A Simple Method for the Determination of Structure-Factor Phase Relationships and Crystal Polarity Using Electron Diffraction. *Journal of Applied Crystallography*, 15:60–64, 1982.

[206] H. Gottschalk, G. Patzer, and H. Alexander. Stacking Fault Energy and Ionicity of Cubic III-V Compounds. *Physica Status Solidi A*, 45:207–217, 1978.

[207] M. Luysberg and D. Gerthsen. On the Dissociation of Dislocations in InP. *Physica Status Solidi A*, 146:157–172, 1994.

[208] A. Salhi, Y. Rouillard, A. Pérona, P. Grech, M. Garcia, and C. Sirtori. Low-threshold GaInAsSb/AlGaAsSb quantum well laser diodes emitting near 2.3 μm. *Semiconductor Science and Technology*, 19:260–262, 2004.

[209] Y. Okada and Y. Tokumaru. Precise determination of lattice parameter and thermal expansion coefficient of silicon between 300 and 1500 K. *Journal of Applied Physics*, 56:314–320, 1984.

[210] M.E. Straumanis and C.D. Kim. Lattice Parameters, Thermal Expansion Coefficients, Phase Width, and Perfection of the Structure of GaSb and InSb. *Journal of Applied Physics*, 36:3822–3825, 1965.

[211] R.H. Dixon and P.J. Goodhew. On the origin of misfit dislocations in InGaAs/GaAs strained layers. *Journal of Applied Physics*, 68:3263–3168, 1990.

[212] J.B. Rodriguez, K. Madiomanana, L. Cerutti, A. Castellano, and E. Tournié. X-ray diffraction study of GaSb grown by molecular beam epitaxy on silicon stubstrates. *Journal of Crystal Growth*, 439:33–39, 2016.

[213] M.S. Abrahams, J. Blanc, and C.J. Buiocchi. Like-sign asymmetric dislocations in zinc-blende structure. *Applied Physics Letters*, 21:185–186, 1972.

[214] A. Trampert, K.H. Ploog, and E. Tournié. Anisotropic misfit dislocation nucleation in two-dimensional grown InAs/GaAs(001) heterostructures. *Applied Physics Letters*, 73:1074–1076, 1998.

[215] T.P. Chen, L.J. Chen, T.S. Huang, and Y.D. Guo. Transmission electron microscope investigation of dislocation loops in Si-doped GaAs crystals. *Semiconductor Science and Technology*, 7:A300–A303, 1992.

[216] B.S. Schwartzentruber, N. Kitamura, M.G. Lagally, and M.B. Webb. Behavior of Steps on Si(001) as a function of vicinality. *Physical Review B*, 47:13432–13441, 1993.

[217] P. Kightley, P.J. Goodhew, R.R. Bradley, and P.D. Augustus. A mechanism of misfit dislocation reaction for GaInAs strained layers grown onto off-axis GaAs substrates. *Journal of Crystal Growth*, 112:359–367, 1991.

[218] B. Brar and D. Leonard. Spiral growth of GaSb on (001) GaAs using molecular beam epitaxy. *Applied Physics Letters*, 66:463–465, 1995.

[219] Z. Liliental-Weber, E.R. Weber, L. Parechanian-Allen, and J. Washburn. On the use of CBED for identification of APBs in GaAs grown on Si. *Ultramicroscopy*, 26:59–63, 1988.

[220] N.-H. Cho and C.B. Carter. Formation, faceting, and interaction behaviors of antiphase boundaries in GaAs thin films. *Journal of Materials Sciences*, 36:4209–4222, 2001.

[221] P.M. Petroff. Nucleation and growth of GaAs on Ge and the structure of antiphase boundaries. *Journal of Vacuum Science and Technology B*, 4:874–877, 1986.

[222] D. Vanderbilt and C. Lee. Energetics of antiphase boundaries in GaAs. *Physical Review B*, 45:11192–11201, 1992.

[223] P. Penczek, M. Marko, K. Buttle, and J. Frank. Double-tilt electron tomography. *Ultramicroscopy*, 60:393–410, 1995.

[224] M. Niehle, A. Trampert, S. Albert, A. Bengoechea-Encabo, and E. Calleja. Electron tomography of (In,Ga)N insertions in GaN nanocolumns grown on semi-polar ($11\bar{2}2$) GaN templates. *APL Materials*, 3:036102, 2015.

[225] T.M. Smeeton, M.J. Kappers, J.S. Barnard, M.E. Vickers, and C.J. Humphreys. Electron-beam-induced strain within InGaN quantum wells: False indium "cluster" detection in the transmission electron microscope. *Applied Physics Letters*, 83:5419–5421, 2003.

[226] T. Li, E. Hahn, D. Gerthsen, A. Rosenauer, A. Strittmatter, L. Reissmann, and D. Bimberg. Indium redistribution in an InGaN quantum well induced by electron-beam irradiation in a transmission electron microscope. *Applied Physics Letters*, 86:241911, 2005.

[227] T. Schulz, T. Remmele, T. Markurt, M. Korytov, and M. Albrecht. Analysis of statistical compositional alloy fluctuations in InGaN from aberration corrected transmission electron microscopy image series. *Journal of Applied Physics*, 112:033106, 2012.

[228] E.J. Tarsa, B. Heying, X.H. Wu, P. Fini, S.P. DenBaars, and J.S. Speck. Homoepitaxial growth of GaN under Ga-stable and N-stable conditions by plasma-assisted molecular beam epitaxy. *Journal of Applied Physics*, 82:5472–5479, 1997.

[229] P. Mutombo and O. Romanyuk. *Ab initio* density functional theory study of non-polar $(10\bar{1}0)$, $(11\bar{2}0)$ and semipolar $\{20\bar{2}1\}$ GaN surfaces. *Journal of Applied Physics*, 115: 203508, 2014.

[230] Y. Zhao, F. Wu, T.-J. Yang, Y.-R. Wu, S. Nakamura, and J.S. Speck. Atomic-scale nanofacet structure in semipolar $(20\bar{2}\bar{1})$ and $(20\bar{2}1)$ InGaN single quantum wells. *Applied Physics Express*, 7:025503, 2014.

[231] S. Albert, A. Bengoechea-Encabo, P. Lefebvre, F. Barbagini, M.A. Sanchez-Garcia, E. Calleja, U. Jahn, and A. Trampert. Selective area growth and characterization of InGaN nano-disks implemented in GaN nanocolumns with differetn top morphologies. *Applied Physics Letters*, 100:231906, 2012.

[232] L.T. Romano and T.H. Myers. The influence of inversion domains on surface morphology in GaN grown by molecular beam epitaxy. *Applied Physics Letters*, 71:3486, 1997.

[233] P. Waltereit, O. Brandt, A. Trampert, H.T. Grahn, J. Menniger, M. Ramsteiner, M. Reiche, and K.H. Ploog. Nitride semiconductors free of electrostatic fields for efficient white light-emitting diodes. *Nature*, 406:865, 2000.

[234] F. Bernardini and V. Fiorentini. Non-linear macroscopic polarization of III-V nitride alloys. *Physical Review B*, 64:085207, 2001.

[235] M. Leroux, N. Grandjean, M. Laügt, J. Massies, B. Gil, P. Lefebvre, and P. Bigenwald. Quantum confined Stark effect due to built-in internal polarization fields in (Al,Ga)N/GaN quantum wells. *Physical Review B*, 58:R13371, 1998.

[236] K. Pantzas, G. Patriarche, D. Troadec, S. Gautier, T. Moudakir, S. Suresh, L. Lareau, O. Mauguin, P.L. Voss, and A. Ougazzaden. Nanometer-scale, quantitative composition mappings of InGaN layers from a combination of scanning transmission electron microscopy and energy dispersive x-ray spectroscopy. *Nanotechnology*, 23:455707, 2012.

[237] T. Mehrtens, M. Schowalter, D. Tytko, P. Choi, D. Raabe, L. Hoffmann, H. Jönen, U. Rossow, A. Hangleiter, and A. Rosenauer. Measuring composition in InGaN from HAADF-STEM images and studying the temperature dependence of Z-contrast. *Journal of Physics: Conference Series*, 471:012009, 2013.

[238] M.A. Herman and H. Sitter. *Molecular Beam Epitaxy*. Springer-Verlag Berlin Heidelberg, 1996.

[239] J.L. Lazzari, J.L. Leclercq, P. Grunberg, A. Joullié, B. Lambert, D. Barbusse, and R. Fourcade. Liquid phase epitaxial growth of AlGaAsSb on GaSb. *Journal of Crystal Growth*, 123:465–478, 1992.

[240] A. Ghiti and E.P. O'Rilly. Antimony-based strained-layer 2–2.5 μm quantum well lasers. *Semiconductor Science and Technology*, 8:1655–1661, 1993.

[241] J.R. Reboul, L. Cerutti, J.B. Rodriguez, P. Grech, and E. Tournié. Continuous-wave operation above room temperature of GaSb-based laser diodes grown on Si. *Applied Physics Letters*, 99:121113, 2011.

[242] K. Akahane, N. Yamamoto, S.-I. Gozu, and N. Ohtani. Heteroepitaxial growth of GaSb on Si(001) substrates. *Journal of Crystal Growth*, 264:21–25, 2004.

[243] K.G. Eyink, M.L. Seaford, T.W. Haas, D.H. Tomich, W.V. Lampert, S.D. Walck, J.S. Solomon, W.C. Mitchel, and L.F. Eastman. Characterization of low-temperature grown AlSb and GaSb buffer layers. *Journal of Vacuum Science and Technology B*, 15:1187–1190, 1997.

[244] L. Cerutti and E. Tournié. private communication, 2014.

[245] I. Akasaki and H. Amano and S. Nakamura. The nobel prize in physics, 2014. "www.nobelprize.org/nobel_prizes/physics/laureates/2014/", accessed: 2015-12-04.

[246] M. Vogel. Licht aus der dritten Dimension. *Physik Journal*, 10/2014:16–17, 2014.

[247] J.H. Choi, A. Zoulkarneev, S.I. Kim, C.W. Baik, M.H. Yang, S.S. Park, H. Suh, U.J. Kim, H.B. Son, J.S. Lee, M. Kim, J.M. Kim, and K.Kim. Nearly single-crystalline GaN light-emitting diodes on amorphous glass substrates. *Nature Photonics*, 5:763–769, 2011.

[248] T. Kuykendall, P. Ulrich, S. Aloni, and P. Yang. Complete composition tunability of InGaN nanowires using a combinatiorial approach. *Nature materials*, 6:951–956, 2007.

[249] L. Liu and J.H. Edgar. Substrates for gallium nitride epitaxy. *Materials Science and Engineering R*, 37:61–127, 2002.

[250] A. Bengoechea-Encabo, S. Albert, M.A. Sanchez García, L.L. López, S. Estradé, J.M. Rebled, F. Peiró, G. Nataf, P. de Mierry, J. Zuniga-Perez, and E. Calleja. Selective area growth of a- and c-plane GaN nanocolumns by molecular beam epitaxy using colloidal nanolithography. *Journal of Crystal Growth*, 353:1–4, 2012.

[251] W. Kleber. *Einführung in die Kristallographie*. VEB Verlag Technik, Berlin, 1965.

[252] F.C. Frank. On Miller-Bravais Indices and four-dimensional Vectors. *Acta Crystallographica*, 18:862–866, 1965.

[253] L. Weber. Das viergliedrige Zonensymbol des hexagonalen Systems. *Zeitschrift für Kristallographie*, 57:200–203, 1922.

Eidesstattliche Erklärung

Ich erkläre hiermit an Eides statt, dass ich die Dissertation selbständig und nur unter Verwendung der von mir gemäß §7 Abs. 3 der Promotionsordnung der Mathematisch-Naturwissenschaftlichen Fakultät I, veröffentlicht im Amtlichen Mitteilungsblatt der Humboldt-Universität zu Berlin Nr. 21/2009 am 06.07.2009, angegebenen Hilfsmittel angefertigt habe.

Berlin, den 10.03.2016